ABSTRACT

In this golden era of multi-messenger astronomy, with highly sensitive telescopes detecting spectacular transients almost nightly, a whole new window is now wide open to study the universe on all timescales. Typically, these events are generated from the total or partial destruction of an astrophysical object and emit electromagnetic waves of all different wavelengths, neutrinos and gravitational waves–carrying important physics that was previously inaccessible. Therefore, it is of utmost importance to take advantage of this tremendous progress in observation with analytic and simulation tools to explain the physics of exotic astrophysical events. This thesis aims to do so by studying the hydrodynamics of some of the most exotic high-energy astrophysical phenomena, ranging from tidal disruption events, shock physics, accretion, and gravitational wave emission from core collapse supernovae, and dynamic stability of the giant planetary atmosphere. We have developed novel analytical tools, primarily using classical hydrodynamics and general relativity, and have utilized computational techniques (numerical and simulations). Our study on giant planets shows how the presence of a solid core can save the planet from being unstable when due to ionization it is expected to be, and thus solves a puzzle in the "core-accretion" theory of giant planet formation. We have presented a general relativistic modification for the accretion solution on a neutron star through stalled shock, which is useful in understanding weak or failed supernovae and can potentially impact the much-discussed standing accretion shock instability–which we restudied and in the process uncovered a new variant impacting the explosion mechanism and gravitational-wave signature. We have also studied the oscillation modes of a nascent proto-neutron star to show how they can contribute to the gravitational wave signature emitted. Our study of deep-tidal disruption events (events in which stars approach black holes closely) refutes the widely speculated possibility of nuclear detonation arising in such events.

HYDRODYNAMICS, STABILITY AND ACCRETION: FROM PLANETS, TO STARS, TO SUPERMASSIVE BLACK HOLES

By

Suman Kumar Kundu

M.Sc, Syracuse University, 2020

B.Sc, Bangladesh University of Engineering & Technology, 2011

Dissertation

Submitted in Partial Fulfillment of the Requirements

for the degree of

Doctor of Philosophy in Physics

Syracuse University

August 2023

ACKNOWLEDGEMENTS

I express my sincere gratitude to my advisor, Eric Coughlin, for taking me on as his first graduate student. When I started, I immediately understood the depth of this person's knowledge and passion on high-energy astrophysics; but the fact that now I can understand our discussions far better indicates to me that I have grown as a scientist over the years. I am thankful to him for being supportive and understanding all the things that I did not know how to express, for being there when I was struggling. Again, I will not be able to articulate properly but let me put it this way – he took me with absolutely zero knowledge on astrophysics and has made me the astrophysicist I am now.

Next, I thank Professor Duncan Brown (the person with a big enough head that fits so many hats); I have learned so many little things from him that I am sure have improved my presentation skill by a great deal. Professor Brown guided me one semester when Eric was on leave and involved me in work on aspects of supernovae physics. I could resonate better with the bottom-up approach Professor Brown adapts in discussing any problems.

I thank Professor Carl Rosenzweig; we have similar tests and aspirations in physics. This man breaths physics, I will continue trying my best to inherit that quality. He has been my guardian here, in professional and more so in personal life. I also thank Mrs. Rosenzweig for having me and my family several times at her place and, more importantly, for letting us steal her retired husband for hours.

I found an excellent friend in my colleague Chaitanya. We used to discuss physics and life in our office and could complement each other well. All the other people in the Gravitational Wave Astrophysics group including Ananya Bandopadhyay, Daniel Paradiso, Matt Cufari, Keisi Kacanj, and Matt Todd have considered me as one of them and made me feel that I belong. I thank Kesavan and Pan, with whom I survived the qualifying exam and beyond. I thank my other friends from the Physics department Arnab, Asad, Emtiaz bhai, Manu and Sarthak for their constant support and motivations.

Many thanks to all of my other collaborators including Andrew Youdin, Adam Burrows, and David Vartanyan. Special thanks to Chris Nixon of the University of Leeds and Phil Armitage of StonyBrook University for writing about a hundred recommendation letters for me.

I thank my parents for tolerating me for all the troubles I have caused, including this one of leaving the country and the comfort of a government service to pursue physics. I thank all my teachers from the school days to the university for the unconditional love they have shown me. I would specifically mention my school teacher, Mr. Anupam Bhattachariya, he taught me the Euclids among other things and I miss him utterly every time I write up my works. I thank Professor Ashim Chakraborti, my physics teacher at college, who used to say that I am the best student he got in his career who loved me as his son (and I owe him many sorry).

I would like to thank my defense committee members, William Wylie, Stefan Ballmer, and Alex Nitz, for taking the time to review and critique this thesis.

Finally, I would mention my other half, my wife Aparazita, for taking care of everything other than Physics in our households and keeping me, Leo & John (to be born) running.

Contents

List of Tables ix

List of Figures xv

Preface xvi

1 Introduction 1

2 Preliminaries 12

2.1 Eulerian and Lagangian view-points . . . 12
2.2 Fluid equations: conservation laws . . . 12
2.3 Shocks . . . 13
2.4 Linear Perturbation theory . . . 14
2.4.1 Hydrostatic equilibrium . . . 14
2.4.2 Linear adiabatic wave eqution (LAWE) . . . 15
2.4.3 Eigenmodes . . . 18
2.5 Smoothed Particle Hydrodynamics (SPH) . . . 18

3 Stability of giant planetary atmosphere with a solid core 21

3.1 Atmospheric model . . . 23
3.1.1 Fluid equations . . . 23
3.1.2 Hydrostatic Solutions . . . 26
3.2 Perturbation Analysis . . . 30
3.2.1 Eigenmode Equations . . . 30
3.2.2 Solutions . . . 34
3.2.3 Region of Instability . . . 34
3.2.4 Non-radial perturbations . . . 36
3.3 Summary and Implications . . . 37
3.4 Varying adiabatic index . . . 40

4 General relativistic settling solutions in the context of a core-collapse supernovae **42**
4.1 Equations . . . 44
4.1.1 Metric . . . 44
4.1.2 Fluid Equations . . . 44
4.1.3 Ambient Fluid . . . 45
4.1.4 Jump Conditions . . . 46
4.1.5 Bernoulli, mass, and entropy conservation equations . . . 47
4.2 General Relativistic Accreting Solutions . . . 47
4.2.1 Impact of varying the ambient fluid velocity . . . 47
4.2.2 Impact of varying the adiabatic index . . . 48
4.2.3 Asymptotic behavior of the general relativistic solutions near the horizon . . . 51
4.3 Physical Interpretation . . . 53
4.4 Summary . . . 54

5 Asteroseismology on a proto-neutron star **57**
5.1 Simulations . . . 58
5.2 Linear Perturbation Analysis . . . 59
5.3 Spectrogram Analysis . . . 62
5.4 Results . . . 65

6 Standing Accretion Shock Instability **69**
6.1 Background Flow and linearized equations . . . 71
6.1.1 Shock jump conditions . . . 73
6.1.2 Background Soluion . . . 75
6.1.3 Linearized Equations for general ℓ . . . 76
6.1.4 Neutron star Boundary conditions . . . 78
6.1.5 Background Flow With Cooling Functions . . . 79
6.2 Numerical determination of eigenfrequencies . . . 79
6.2.1 $\ell = 0$, the radial modes . . . 80
6.2.2 Non-radial modes: Oscillation in the *eigenspectrum* . . . 80
6.2.3 $\ell = 1$, the *classic* SASI at low oscillation frequency . . . 81
6.2.4 $\ell = 2$, the surprise? . . . 81
6.2.5 $\ell > 2$ . . . 83
6.3 Implications for explodability . . . 85
6.4 Implications for Gravitational Waves . . . 85
6.5 Summary . . . 87

7 Star crushed by black hole **89**
7.1 Analytic Estimates 90
7.2 Numerical simulations 96
7.2.1 Simulation setup 96
7.2.2 Simulation Results 98
7.2.3 Effects of General Relativity 102
7.3 Summary 103

8 Conclusions **106**

Bibliography **142**

List of Tables

1 The square of the lowest-order eigenvalue σ_1^2 and the auxiliary variable K_0 for each of the configurations shown in Figure (7). 32

2 The table summarizes the details of the simulations, including the progenitor mass, equation of state, initial core rotation, and explosion status within the simulated time interval. 60

3 Summary of some of the major previous work investigating SASI. 72

4 The real and imaginary parts of eigenvalues corresponding to few representative eigenmodes of solutions specified by ℓ. We have set $\gamma = 4/3$ and $\xi_{ns} = 0.1$ for these results. 80

5 The maximum central density and temperature, normalized to their original values, obtained from the SPH simulations, predicted by LC86, and predicted by CN22 for the β range analyzed here. For $\beta = 1$ and 2, the density and temperature at the center of the star monotonically decline with time in the numerical simulations, hence their values of identically 1 from the simulations. 101

6 For the β given in the first column, the maximum central density relative to its original value is given in columns 2, 3, and 5 for 10^5, 10^6 and 10^7 SPH particles, respectively. The relative error between successive resolutions, calculated as the difference between the higher and lower-resolution values normalized by the higher-resolution result, is shown in the fourth and sixth column. 102

List of Figures

1 A cartoon to visualize the canonical tidal disruption process. The "penetration factor" is defined as $\beta \equiv r_t/r_p$, the ratio of the tidal radius to the pericenter distance, as defined in the text. 8

2 Plot of Numerical Solutions to the Lane-Emden equation for γ ranging from 1.0 to 2.0 15

3 Plot of density $\frac{\rho}{\rho_c}$ vs ξ for γ ranging from 1.0 to 2.0 16

4 The first 5 eigenfunctions of a $\gamma = 5/3$ polytrope. 19

5 Schematic view of the SPH convolution using a smoothing kernel W in 2D space. The l_2 distance between the two points i around which the kernel is centered and the other particle j is shown. This figure is adapted from [1] 20

6 A qualitative illustration of our model of a giant planet, which is a spherical object that consists of a core of radius $R_{\rm c}$ and mass $M_{\rm c}$ and a compressible envelope that extends from $R_{\rm c}$ to R. The envelope has a mass of $M_{\rm e}$, such that the total mass of the planet is $M_{\rm c} + M_{\rm e}$ and the relative mass of the core is $\mu = M_{\rm c}/(M_{\rm c} + M_{\rm e})$. 23

7 Left: The unperturbed and dimensionless density g_0 as a function of radius for the relative core masses μ shown in the legend and a polytropic index $\gamma = 1.3$ and a core radius of $\xi_{\rm c} = 0.05$. Middle: Identical to the left panel but with fixed $\gamma = 1.3$ and $\mu = 0.05$ and the inner radii shown in the legend. Right: Identical to the left panel but with fixed $\mu = 0.05$, fixed $\xi_{\rm c} = 0.05$, and variable adiabatic indices as shown in the legend. 28

8 Top-left panel: The lowest-order eigenfunctions as a function of the dimensionless radius for the polytropic index $\gamma = 1.3$ and core radius $\xi_c = 0.05$ for different values of the fractional core mass μ shown in the legend. . . 28

9 The square of the lowest-order eigenvalue as a function of the adiabatic index, γ. The left panel corresponds to a core mass of $\mu = 0.05$, while in the right panel we set $\mu = 0.1$. 29

10 The curve that delimits where $\sigma_1^2 = 0$ in the $\gamma - \xi_c$ plane that separates the stable and unstable behavior. The left panel fixes $\mu = 0.05$ and the shaded region denotes where the solutions are unstable, while the right panel varies the core mass. 32
11 The $\sigma_1^2 = 0$ curve separating stable and unstable behavior. We have simulated three model planetary configurations having similar properties to the gas-giants in our solar system: Jupiter(Blue), Saturn(Green), Neptune(Orange). The model parameters are shown in legends. 33
12 The ratio between the post-shock fluid velocity to the ambient fluid velocity (U_s/U_a) at the location of the shock as a function of the ambient fluid velocity, U_a, in both the Newtonian and General Relativistic settings for $\gamma = 4/3$. Note that U_a is the freefall speed at the shock normalized by the speed of light, and hence the relativistic solution approaches the non-relativistic one when $U_a \ll 1$; in the Newtonian limit, the entire problem is self-similar and U_a can be set to one without loss of generality. 46
13 The normalized fluid velocity (the radial component of four-velocity in the top-left and the three-velocity as seen by local static observer in the top-right), comoving density (bottom-left), and comoving pressure (bottom-right) for the ambient speeds (at the location of the shock) shown in the legends as functions of radius (in km). Here we set the neutron star mass to be $3\,M_\odot$ to convert to physical units. The black dashed line indicates the surface of the neutron star whereas the colored dashed lines indicate the location of the stalled shock appropriate to the respective ambient velocity. Newtonian limits are given by the dashed curves in each panel. 49
14 The normalized three-velocity as seen by a static and locally flat observer for the ambient speeds (at the location of the shock) shown in the legend as functions of normalized radial coordinate by the shock radius (r/R); the black dashed line at $r/R = 1$ indicates the fixed location of the shock in this coordinate and the colored dashed lines indicate the location of the neutron star surface, assumed to be at 10 km. The Newtonian solution, which is self-similar (i.e., it does not depend on v_a), is shown by the solid black curve. 50

15 Left: The Newtonian solution for the fluid velocity as a function of radius normalized by the shock radius for the adiabatic indices in the legend; the solid curves show the numerical solution from the Bernoulli equation in the Newtonian limit, while the dashed curves give the analytic, asymptotic scalings, arbitrarily offset by a factor of 0.9 so that they can be differentiated from the exact solutions when $r/R \ll 1$. Right: The fluid velocity derived from the relativistic Bernoulli equation (solid curves) and the Newtonian Bernoulli equation (dashed curves) for an ambient velocity of $U_{\rm a} = 0.2$ and the adiabatic indices in the legend. The two solutions agree well near the shock front but disagree strongly near the horizon, which occurs at $r/R = 0.04$ in this case. 52

16 The figure shows the energy (in $10^{-8} M_{\odot} c^2$) obtained for the simulation `s19-3D` as a function of the sampling rate used to resample the data from the simulations. The solid blue curve represent the case when Cubic interpolation is used whereas the orange curve shows the case when Linear interpolation is used. The corresponding dashed curves show the difference between energy values obtained for a particular sampling frequency and the one lower. We can see that the values converge as the sampling frequency is increased. 67

17 The figure shows the strain (top) and its spectrogram (bottom) of the 3D simulation `s19-3D`. The strain data has been uniformly sampled at 16,384 Hz. The ends have been tapered to zero by applying half cosine windows to the first and last 1024 points of the data. Then, the data are zero-padded by 0.04 seconds on either end. The spectrogram of this signal is shown on the bottom panel. The $f-$mode frequencies, obtained from linear perturbation analysis, start at 200ms and go from 500 Hz to 1000 Hz at 0.6 seconds after the core bounce, and are shown as red crosses in the bottom panel. The vertical orange line shows the time $t_0 = 200$ ms after the core bounce. The two orange parabolic curves define the frequency range within which the algorithm looks for the peak in the spectra. . . . 68

18 The modulus of the dimensionless, radial velocity ($f_{\rm r}$, left), the dimensionless density (g, middle), and the dimensionless pressure (h, right) as functions of $\xi = r/R$. 76

19 The real (left) and imaginary (right) parts of $\tilde{f}_{\rm n}$ for the first five radial ($l = 0$) eigenmodes with $\gamma = 4/3$ and $\xi_{\rm NS} = 0.1$. 80

20 Left:The growth rate σ_r against the oscillation frequency σ_i for different values of ℓ as shown by the legends. Right: The real and imaginary parts of the first order perturbation to the post-shock fluid radial velocity corresponding to the maximally unstable mode with $\ell = 2$. 81

21 Left: $\ell = 2$ eigen spectrum while the adiabatic index γ is being varied while keeping ξ_{ns} fixed at 0.1. Right: $\ell = 2$ eigen spectrum, while the neutron star radius, ξ_{ns} is varied while the adiabatic index γ is kept fixed at 4/3. 82

22 The modulus of the dimensionless, radial velocity ($f_{\rm r}$, left), the dimensionless density (g, middle), and the dimensionless pressure (h, right) as functions of $\xi = r/R$. With $\alpha < \beta$ ($\alpha > \beta$) the gas reaches the surface of the accretor in finite (infinite) time. 84

23 The modulus of the dimensionless, radial velocity ($f_{\rm r}$, left), the dimensionless density (g, middle), and the dimensionless pressure (h, right) as functions of $\xi = r/R$. Cooling with $\alpha < \beta$ ($\alpha > \beta$) boosts (weakens) the instability, which agrees well when we examined the same effect by varying the adiabatic index, γ. 84

24 Data obtained from a 2-D simulation of a $10M_\odot$ progenitor of [2]. Top-Left: The oscillatory eigenspectrum of $\ell = 2$ modes at $t = 0.6155$s with $\xi_{NS} := R_{NS}/R = 0.394389$ and $\gamma_{mean} = 1.38631$ is calculated over the radial extent. Top-Right: The identification of the unstable modes with lowest, highest and the most unstable mode on the spectrogram. Bottom-Left: the strain times distance of GW, $h_+ D$, bottom-right: the time-frequency representation (that is, spectrogram) of the strain signal. The pink line indicates the f-mode evolution obtained in asteroseismology, the black line with dots indicates the unstable SASI modes with the highest frequency, the black line with diamonds indicates the unstable SASI modes with the lowest frequency, and the black line with the squares on it indicates the unstable modes with maximum instability. 86

25 The integrated column density at the time when the center of mass of the star reaches pericenter. The value of β is shown in the top-left of each panel. The left panels show the distribution of stellar material in the orbital plane, and the corresponding right panels show the view perpendicular to that plane. In the convention we adopt, both the initial x, y coordinate of the center of mass of the star starts with negative values, and arrives the pericenter with a positive x-coordinate value and $y = 0$. Thus, any fluid element with a positive (negative) y-value has already (not yet) passed through its pericenter. Increasing β clearly leads to an increase in the flattening, or "crushing" of the star, into the orbital plane near pericenter. 91

26 Left:The Solution for H, considering gas pressure and self gravity (solid curves) along with the solutions obtained when the gas free-falls in the tidal field (dashed curves). This shows that the self-gravity and pressure of the gas starts to play significant roles to counter the compression at much earlier times than when the star would be compressed to zero height ($H = 0$) in the free-fall case (i.e this time is to be read when the dashed curves goes vertical). Right: The ratio of the central density normalized to its original value as a function of time normalized by the dynamical time of the star. As β increases, the time of the maximum density achieved approaches 0, the time when the center of mass reaches the pericenter and the compression increases significantly. 96

27 The maximum central density (temperature) normalized to the original density (temperature) at the center as a function of the penetration factor, β in the left (right) panel. The blue dashed lines indicate the large-β behavior of our solution while the black dashed lines indicate the corresponding scalings predicted by [3]. 97

28 Left: The ratio of gas pressure to the ram pressure of the freely falling fluid as a function of time normalized by the dynamical time of the star. The ratio being much smaller to 1 indicates the fact that the gas pressure succeeds in resisting the compression much before it becomes comparable to the ram pressure. Right: The velocity of the fluid element normalized to the escape velocity as the function of time normalized to the dynamical time of the star. 97

29 The central density normalized to its original value as a function of time normalized by the dynamical time of the star. The different curves are appropriate to the β in the legend, with solid (dashed) curves resulting from the numerical simulations (analytic model). The magnitude of the compression and time of the maximum compression agrees reasonably well between the SPH and analytic results. 98
30 The maximum value of the central stellar density (left) and temperature (right) as a function of β normalized by their initial values. The dashed curves represent the scalings derived by [4] (olive) and [5] (teal), the solid, teal curves are from the analytic model (also in [5]), and the solid, orange curves are from the numerical simulations. 99
31 The ratio of the maximum to the original density at the geometric center of the star as a function of β. The different solid curves are obtained by varying the spatial resolution, with the corresponding number of particles shown in the legend. The analytic prediction is shown by the dashed curve. 99
32 The ratio of maximum central density to the original central density against the dynamic time of the star with $\beta = 7$. The resolution and gravity are specified by the legend (solid-blue and dotted-orange use the Schwarzschild metric for the gravitational field of the SMBH). The compression is stronger (by a factor of $\lesssim 1.5$) with relativistic effects included, and the time of maximum compression occurs later in comparison to the Newtonian case; the latter effect arises from time dilation (note that the horizontal axis is coordinate time, i.e., time as measured by an observer at infinity) normalized by the dynamic time of the star. 104

Preface

Chapter 3 is based on material from:
Suman Kumar Kundu, Eric R. Coughlin, Andrew N. Youdin and Philip J. Armitage, "Dynamical stability of giant planets: the critical adiabatic index in the presence of a solid core," **Monthly Notices of the Royal Astronomical Society, Volume 507, Issue 4, Pages 6215-6224 (2021)**
https://academic.oup.com/mnras/article/507/4/6215/6368867.

Chapter 4 is based on material from:
Suman Kumar Kundu and Eric R. Coughlin, "Spherically symmetric accretion on to a compact object through a standing shock: the effects of general relativity in the Schwarzschild geometry," **Monthly Notices of the Royal Astronomical Society, Volume 516, Issue 4, Pages 4814-4821 (2022)**
https://academic.oup.com/mnras/article/516/4/4814/6691706.

Chapter 5 is based on material from:
Chaitanya Afle, *Suman Kumar Kundu*, Jenna Cammerino, Eric R. Coughlin, Duncan A. Brown, David Vartanyan, and Adam Burrows, "Measuring the properties of $f-$mode oscillations of a protoneutron star by third-generation gravitational-wave detectors," **Physical Review D, Volume 107, Pages 123005, Issue 12 (2023)**
https://link.aps.org/doi/10.1103/PhysRevD.107.123005.

Chapter 7 is based on material from:
Suman Kumar Kundu, Eric R. Coughlin and Chris J. Nixon, "Stars Crushed by Black Holes. III. Mild Compression of Radiative Stars by Supermassive Black Holes," **The Astrophysical Journal, Volume 107, Pages 71, Issue 2 (2022)**
https://iopscience.iop.org/article/10.3847/1538-4357/ac9734.

Late Anupam Bhattachariya, my high school teacher, I am sure he would have read this with unbound joy and enthusiasm.

Chapter 1

Introduction

$\pi\alpha\nu\tau\alpha\ \rho\epsilon\iota$ (everything flows)

Heraclitus

The universe is vast; the length scale starts with the Planck length at $\sim 10^{-32}cm$ and goes all the way to $\sim 10^{26}cm$–the size of the observable universe. While on earth we are used to dealing with energies of the order of joules ($10^{-7}ergs$), a supernova releases energy of the order 10^{44} joules! Similarly, in space astronomy the temperatures that we deal with run from a few degrees above absolute zero, with particles moving very slowly, to billions of degrees Celsius, with particles moving with velocities close to the speed of light. High-energy astrophysics studies the dynamic, energetic, and often violent physical processes operating in the extreme universe. Therefore, supernovae, neutron stars, pulsars, active galactic nucleus (AGN), and black holes are the typical protagonists in the story of high-energy astrophysics. Some other major players are stellar winds, jets crushing their way through the Interstellar or Intergalactic medium (ISM or IGM), and accretion disks around compact bodies that come in a wide range of length scales [6].

Typically events where an astrophysical object suffers either partial or total destruction (e.g. Supernovae–the spectacular explosion in the violent death of massive stars, Tidal Disruption Events–where stars are crushed by supermassive black holes) or events where a compact object accretes stellar material–emit electromagnetic waves of all different wavelengths, neutrinos, and gravitational waves. With telescopes (e.g., Swift [7], Chandra [8] , James Web Space Telescope (JWST) [9], XMM-Newton [10]) picking spectacular electromagnetic transients (astrophysical events that last from fractions of a second to weeks or years) almost nightly, a whole new window is now wide open to study the universe on all timescales. Moreover, with the Laser Interferometer Gravitational-Wave Observatory (LIGO) [11, 12] and it's sister facilities VIRGO [13], KAGRA [14] and the prospect of third-generation detectors as Cosmic Explorer [15] and Einstein Telescope

[16] coming online in near future the universe is now glowing in gravitational waves too, marking the dawn of a new era of multi-messenger astrophysics. This reality necessarily places the arena of high-energy processes at the very heart of modern astrophysics [17]. Now stars are gaseous bodies, powered by central nuclear engines. ISM and IGM are also composed of gases. Therefore, we are dealing with fluids here, *things that flow*. Compact objects like neutron stars and white dwarfs are also modeled with fluids with a stiffer equation of state.

Matter is discontinuous if it is fine-grained. But when all we care about is long-wavelength (low-frequency) dynamics of a many-body system, as in most astrophysical scenarios, we can instead opt for a coarse-grained description. *Fluid dynamics* is such a *effective* description suitable for studying the dynamics of continuous and deformable media such as gases, liquids, and plasma [18]. One describes such a medium by specifying the velocity field $\vec{v} = \vec{v}(\vec{r}, t)$, and two independent thermodynamic properties, most commonly the pressure $p = p(\vec{r}, t)$ and the mass density $\rho = \rho(\vec{r}, t)$, at every point in space and time in a region [19]. The validity of such a description depends upon two basic length-scale associated with such many-body systems. The first of these two length scales is the *microscopic* mean free path, $\lambda_{collision}$–the mean distance traveled by individual particles between molecular collisions. This length-scale determines the rate at which any generic disturbances imposed on the fluid relaxes through molecular collisions. The other important length-scale is the length scale L over which bulk fluid properties such as mass density ρ (or temperature) change through collective motion of the fluid. Hence, this length scale increases as the length scale associated with the disturbances, i.e. $L \sim \lambda_{disturbance}$ The fluid description is valid in the limit $\lambda_{collision} << L \sim \lambda_{disturbance}$ [20].

To describe the dynamics of fluid bodies, one typically associates the stress tensor with the body as $\Pi_{ij} := \rho v_i v_j + p\delta_{ij} + \delta\Pi_{ij}$, $p = p(\rho, \mathcal{E}_0)$ is the equation of state, and $\delta\Pi_{ij}$ the gradient term. Fluids with $\delta\Pi_{ij} = 0$ are *ideal* fluids and in this thesis we will deal only with such fluids. The relative importance between the remaining two terms in Π_{ij} can be weighted by defining the Mach number $Ma := v/c_s$ where the sound speed $c_s : (\partial p/\partial \rho)\,|_s$, s being the specific entropy (entropy per unit mass). Flows with $Ma \sim 1$ are compressible; on the other hand, flows with $Ma << 1$ are *incompressible*. The fluids encountered in astrophysics are mostly *compressible* and will be the subject matter of this. In most cases, the viscosity is subdominant and can be safely neglected (accretion disks being the major exclusion). Astronomical objects are often self-gravitating; therefore, in *astrophysical fluid dynamics* gravitation is utterly important (the same with the magnetic field, in cases); whereas in *terrestrial/engineering* fluid dynamics these effects are often neglected [21]. For example, a very common scenario in astrophysics is when materials accelerate

and attain supersonic velocity under the gravitational influence of a central body (and eventually get accreted onto it); then, because of the high compressibility, strong shock fronts are often formed, as we will explore in greater detail in this thesis. When gravitation is dealt with in Newtonian theory, the resulting theory is called *hydrodynamics or gas dynamics* and *relativistic hydrodynamics* when relativity is used[19]. The equations of hydrodynamics, which are conservation statements of mass, momentum, and energy, are reviewed in Chapter 2 of this thesis.

The equations of hydrodynamics for systems in states far from equilibrium are notoriously hard to solve, the chief complaint being the inherent non-linearity. Although the advent of computational power enables us to solve for nonlinear systems that were unthinkable a decade ago, still the use of *perturbation techniques* continues to remain powerful in providing useful insights into system behavior. The strategy is to first describe some sort of equilibrium for the system and then to *perturb* the equilibrium ever so slightly so that one can get away by neglecting the non-linearity as much as possible. We will present a rough sketch of this algorithm known as *linear perturbation theory* in Chapter 2. Although it sounds like a good fairy tale that a fluid remains steady; the typical steady state considered, specifically, in stellar astrophysics, is a state with $\partial/\partial t = 0$ everywhere inside the fluid body. Now, if we apply small perturbations to this configuration and find that they grow over time, we say that the configuration is *unstable* with respect to those perturbations. On the other hand, if we find those perturbations becoming weaker and weaker and eventually dying out over time or the perturbations cause the configuration to oscillate with time, then the configuration is *stable* in response to those perturbations. We can thus define *instabilities* as mechanism that initiate processes of energy exchange ("energy release"). They feed off free energy in the system and ultimately makes "great things happen". A Few famous instabilities in astrophysics are the Kelvin-Helmholtz instability, which is caused by stellar jets moving at high speed with respect to the ambient medium [22], the gravitational (Jeans) instability, which is thought to be responsible for formation of giant planets and stars [23], the various thermal instabilities that play a key role in determining the temperature structure of ISM in the galaxy [24] and the one that will appear throughout this thesis in this thesis arises in the context of core-collapse supernovae, the "standing accretion shock instabilies (SASI)"[25, 26, 27].

The next major focus of this thesis is *accretion*–the phenomenon of the fall of matter (fluid) onto some compact body. The absence of angular momentum of the falling material will lead to a spherically symmetric accretion, and the presence of sufficient angular momentum leads to the formation of an accretion disc [28]. Accretion is attractive to astrophysicists– because of the rich physics involved and to astronomers– because a significant fraction of the total rest mass energy of the material accrued transforms into

radiation making it the prime target for their observation.

Core-collapse supernovae are the places where hydrodynamics, stability, and accretion play major role in the overall physics and will constitute a major portion of this thesis. When a massive star (with mass $\gtrsim 8M_{\odot}$) exhausts all its nuclear fuel reserve and collapses under its own weight, the sea of electrons, stripped out of the atoms due to the extreme temperature and density at the core, momentarily resists the gravitational collapse. But in such a dense environment, the protons capture electrons to produce neutrons, and the collapse carries on until the neutrons can supply enough degeneracy pressure to reestablish equilibrium again. This moment is proclaimed by the *bounce* of the proto-neutron star (PNS) (of typical size $\sim$ 10 Km) that launches a shock in the ambient stellar medium. This shock wave passes through the overlaying infalling stellar envelope, ionizing it, losing energy in the process, and stalls at a distance of $\sim 100 - 150$ Km. In various phases of the procedure mentioned above detectable electromagnetic, gravitational, and neutrino signals are emitted, making core-collapse supernovae the prototypical multi-messenger source [29].

In Chapter 4, we present novel relativistic accretion solutions that match the boundary conditions at the location of the stalled shock and the surface of the compact object. In the model, we have considered the Schwarzschild geometry to model gravity around the accreting neutron star and treated the ambient stellar material as pressureless dust and the post-shock fluid as a $\gamma = 4/3$ polytrope. In this setting, we first derive the extent of discontinuities in fluid properties (e.g. velocity, density, and pressure) across the shock. Similarly to previous work carried out in the Newtonian limit, we find that the gas 'settles' interior to the stalled shock [30, 25]; in the relativistic regime analyzed here, the velocity asymptotically approaches zero near the Schwarzschild radius. These solutions can represent accretion on a material surface if the radius of the compact object is outside of its event horizon, such as a neutron star; we also discuss the possibility that these solutions can approximately represent the accretion of gas on a newly formed black hole following a core-collapse event. Hence, they provide novel generalizations to earlier work and highlight the importance of general relativity, which becomes essential when the shock is pushed to very small radii (as in failed or nearly failed scenarios). We point out that these solutions are different from the relativistic generalizations of the Bondi accretion solution [31] as the latter ones do not account for the presence of a pre-existing shock. A significant fraction of the kinetic energy of the free-falling fluid is transformed into its internal energy when it passes through an existing strong shock. This effect cannot be considered as a small perturbation on top of a pure free-fall solution.

Despite efforts since the 1950s, the question of "What causes the stalled shock to revive

and ultimately give rise to the explosion?" continues to remain unanswered. Hydrodynamic instability, specifically the SASI discovered in the early 2000's showed promise of explaining that question and created some stir in the community [25, 26, 32, 33, 34, 35]. In present days the neutrino mechanism–where the emitted neutrinos deposit enough energy behind the shock to revive it is favored by most over SASI. Nevertheless, the community agrees on the fact that SASI contributes to the asymmetric explosion seen in supernovae by aiding the neutrino mechanism by enhancing the neutrino heating area. Our analysis of SASI in Chapter 6 takes a fresh look at SASI and, in addition to reconfirming the traditional attributes, we also find a *new* set of unstable modes in the $\ell = 2$ eigenmode spectra. The oscillation frequency corresponding to the maximally unstable mode (among those unstable modes) is strikingly similar to the frequency associated with the free-fall time of the PNS , *which is high, while SASI is traditionally associated with relatively low-frequency oscillations*. We claim that these unstable modes will soon add up and cascade into other unstable modes. Then the non-linear coupling between various unstable modes can create *turbulent* motion in the cavity between the shock front and the neutron star, fueling the asymmetric explosion [36, 37, 38].

In Chapter 5 we do asteroseismology–the study of oscillation modes of stars–neutron star in our case. By modeling the neutron star as a fluid body with appropriate equation of state, we perturb the configuration and work with the linear terms. We first work in the Cowling approximation [39]–without perturbing the space-time metric and eventually relax the approximation. By adopting numerical methods, we solve the perturbation equations and obtain the frequencies corresponding to the various oscillation modes of the PNS. The fundamental mode (f-mode) of the oscillations found by this method is then shown to be the dominant supplier of power in the gravitational wave signature obtained in the state-of-the-art supernovae simulations [2, 40]. Now what might cause the neutron star to oscillate? We discuss the possibility that the aforementioned $l = 2$ unstable modes may act as the *hammer* to set the neutron star *bell* ringing? The following observation bolster our argument: although the f-modes of oscillation of the neutron star contribute in the gravitational waves; other modes of oscillations (e.g. the pressure modes (p-mode), the gravity modes (g-mode)) do not! A resonance between the SASI cavity and the neutron star oscillation explains this– *only* the f-mode frequencies line up with the SASI unstable modes and hence are activated, not the others!

Chapter 3 analyzes the hydrodynamics of a giant planetary atmosphere with a solid core. There are a couple of theories explaining the formation of giant planets. The "gravitational instability" models describe the formation as a result of gravitational instabilities in the protoplanetary disc [23, 41]. On the other hand, the "core accretion" paradigm advocates the gradual formation of a solid core and then run-away gas accretion by it from

the disc [42, 43]. During this run-away gas accretion phase, the material heats up and gets ionized. This can lead the adiabatic index, γ, of the gas to fall below 4/3–a limiting value known as the "Chandrasekhar limit" due to the famous work of Chandrasekhar showing any spherical polytropic structure becoming dynamically unstable when the adiabatic index falls below 4/3 [44]. We claim that the presence of the solid core would impact the *naive* Chandrasekhar limit which should not be invoked here. Rather, we map out a region in the plane of adiabatic index - normalized radius of the core (to the radius of the planet) for different normalized core mass (to the total mass of the planet), where the configuration is unstable. The core is shown to essentially provide stability for the configuration, which remains stable even when the adiabatic index γ falls well below 4/3. Our result solves a mystery in the formation process of giant planets.

In conjunction with analytic methods to attack hydrodynamics in astrophysical scenarios, simulation tools are becoming more and more indispensable now-a-day (for very valid reasons that will be exemplified) to simulate the fluid flow in various high-energy astrophysical events; one such premise is the "tidal disruption events (TDEs)": events where stars reaching close proximity to supermassive black holes get either partially or completely teared apart in the tidal field of a black hole. There are strong theoretical and observational evidence that nearly every galaxy in the universe hosts at least one supermassive black hole (SMBH) at its center [45, 46, 47, 48, 49] as a scientific fact. Virtually all of these behemoths are surrounded by a star cluster, the members of which interact with each other and with the SMBH through random gravitational encounters [50]. Such interactions occasionally fetch a star so close to the black hole that the tidal force it experiences in the tidal field of the hole causes either partial or full disruption of the star.

Theoretical prediction of TDEs, mainly proposed as a possible mechanism to explain active galactic nuclei (AGN), dates back to the 1970s [51, 52, 53, 54, 55]. Although those efforts were not successful in explaining AGN's; the idea of disruption of stars by black holes thrived. Solid theoretical groundworks were laid down by the 1990s to explain the specifics of such processes and possible signatures arising from them [56, 57, 58, 59, 60, 61]. The first observational TDE candidate, detected in X-rays, emerged in the late 1990s [62, 63, 64] and since then multiple TDE candidates have also been detected in other wavebands, including radio, optical, UV and hard X-rays [65, 66, 67, 68, 69, 70]. The number of definitive detections now exceeds 50 in relatively quick time and this accelerating trend in detection is expected to continue with current (e.g. Chandra, Swift, SRG/eROSITA) and upcoming high cadence wide-field all sky surveys (e.g. SKA, LSST , Einstein probe) (see [71] for a detailed review of the observational status). In addition to being a very intricate physical phenomenon to be scrutinized in its own right, the wider

astrophysics community continues to utilize TDEs as valuable tools to dig into several other areas of their interests, for example, physics of compact objects [72, 73, 74, 75], black hole demographics [76, 77, 78], galaxy formation and mergers [79, 80], stellar dynamics in otherwise quiescent galactic center [81], and accretion physics [82, 83]. All these intriguing physics interests, in addition to the aforementioned progress in observation, have triggered a new generation of analytic and semi-analytic works supplemented well with a plethora of simulation-based works [84, 85, 86, 87, 88, 89, 90, 91, 92, 5, 93] to venture into different stages of TDE evolution under various conditions [94, 95, 96, 97, 98, 99] and this trend is expected to continue in coming decades. These studies have utilized a rich profusion of analytic, numerical, and simulation techniques while incorporating the appropriate stellar and gravity models. Naturally, main-sequence stars are thought to predominantly participate in TDEs. Hence, the polytropic stellar models and to account for the radiative diffusive processes present in a sunlike star more realistically, a variant of the polytropic models– Eddington's standard models [100] are the two leading stellar models utilized in the TDE literature [57, 3, 4, 101, 5]. Depending upon the context and accuracy desired, the Newtonian and/or General Relativistic (GR) prescription has been adopted to treat gravity of such processes (around the hole and the self-gravity of the star) [102, 5]. Simulation techniques have played an important role in TDE research since the early days. These simulations have adapted Lagrangian smoothed particle hydrodynamics (SPH) [103] or Eulerian adaptive mesh refinement (AMR) [104] methods. Very recently, a fusion between the two methods, arbitrary Lagrangian-Eulerian (also known as moving-mesh scheme) is also being tried [105].

In the description of canonical TDEs, typically a one-solar-mass star is considered to approach a supermassive black hole from infinity; a schematic of the process is presented in Figure 1. The orbit of such a star is parabolic [85, 106]. The nature of such tidal interactions and the signatures that arise from them largely depend on how close to the black hole the star reaches. An implicit measure of this *closeness* is the "penetration factor", $\beta \equiv r_t/r_p$, where $r_t := R_\star \left(M_\bullet/M_\star\right)^{1/3}$, the tidal radius, is roughly the distance at which the tidal force exerted by the black hole on the star, trying to disrupt it, becomes equal to the self-gravity of the star, which holds it gravitationally, and r_p, is the point of closest approach between the two bodies [51]. TDEs with a low value of β ($\beta \lesssim 1$) are inherently different from those having high-β value ($\beta \gg 1$) both in the qualitative and quantitative sense [107, 91]. While in $\beta \lesssim 1$ events, the tides cannot completely destroy the star; in events with $\beta >> 1$, the tidal force engulfs the self-gravity of the star and it suffers serious tidal compression.

The first significant understanding of this tidal compression suffered by a star in course of a TDE came from [108]; although in that work they only considered low-β

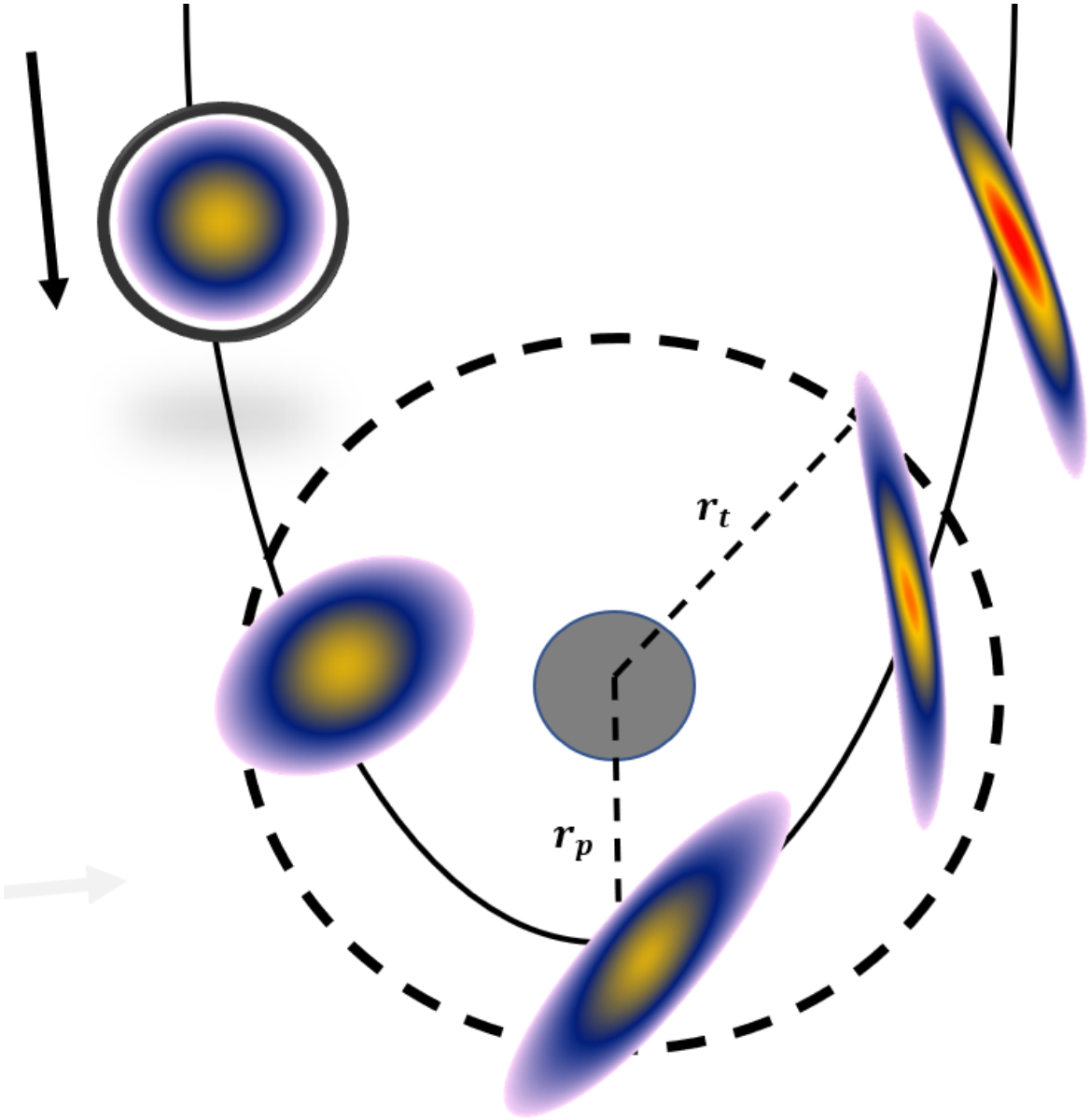

Figure 1: A cartoon to visualize the canonical tidal disruption process. The "penetration factor" is defined as $\beta \equiv r_t/r_p$, the ratio of the tidal radius to the pericenter distance, as defined in the text.

($\beta \sim 1$) encounters, in which just the stellar envelope is affected, not the core. They reported that the star suffers from tidal compression until it reaches the pericenter (the closest approach), after which it rebounds, which leads to ejection of stellar material in all directions. In particular, [108] identified ejection in *orthogonal* directions to the orbital plane as a possibility, contrasting major previous works of that time, which advocated the idea that the stellar material disperses only in directions lying *within* the orbital plane (the so-called "toothpaste-tube effect"; see, for example, [109, 110]). Following the same line of reasoning as in [108], [4], in a series of papers, we examined the tidal compression that arises in moderate ($5 < \beta \lesssim 15$) to more deep plunging ($15 < \beta < 30$) encounters, where not only the envelope but also the core of the star is affected [57, 3, 111, 4]. They argued that the compression the star suffers within the orbital plane, in the direction orthogonal to the line connecting the center of the star to the hole, gets approximately canceled by the stretching it suffers, towards the center of the black hole. Thus, they concluded that the overall compression, i.e. rise in the central density of the star, is largely due to the compression suffered in the orthogonal out of plane direction. To quantitatively estimate the extent of the tidal compression suffered by the star as it passes through $\sim$ the pericenter, [4] approximated the star to retain its hydrostatic equilibrium until it reaches the tidal sphere. To analyze the perturbed configuration, they proposed considering a linear relationship between the perturbed and the original position of particular fluid elements. Such approximations, packaged under the name the *affine* star model - enabled them to analyze the TDE dynamics by dealing with only a finite number of internal degrees of freedom of the star. Then, they asserted that at the point of maximum compression, all the internal energy of the compressed gas comes from the transformation of its kinetic energy gained by falling freely in the gravitational field of the hole. In other words, at the point of maximum compression, they equate the thermal pressure of the gas to the ram pressure of the freely infalling gas. Furthermore, adopting the polytropic equation of state $p \propto \rho^{\gamma}$, p the gas pressure, ρ the density and γ the adiabatic index of the stellar material, they found that the maximum density varies according to $\rho_{max} \propto \beta^{2/(\gamma-1)}$, in moderately penetrating encounters (roughly, $5 < \beta \lesssim 15$). Then, they confirmed, the same scaling continues to hold for the run of maximum density with the change in penetration factor, even in deeply penetrating tidal encounters having β values of roughly $\beta > 15$). As a possible ramification of this sharp rise in central density and correspondingly temperature, they proposed the possibility of igniting a thermonuclear runaway in the core of the star in these deep TDEs.

Almost immediate criticism of [4]'s work came from [58], who argued that the disruption of the stellar envelope will be followed by formation of a shock and that will prematurely stop the adiabatic compression. Through smoothed particle hydrodynamics

(SPH) simulations, they reinforced their claim, by showing the maximum density to follow a much shallower β-scaling. Similarly, they found a factor of $2-3$ below the increase in the maximum temperature than that mediated by the β^2 scaling as predicted by [4]. Since then, there have been a multitude of analytic and simulation works trying to resolve this apparent dispute: some confirming and some disagreeing with their prediction. An unanimous answer to the question of the maximum density and temperature reached at the stellar center and, as a consequence, of how probable a thermonuclear detonation of the stellar core in deep TDEs–remains eluding.

Recently, [5] have launched a new investigation into this by proposing a hydrodynamical model to trace the evolutionary pathway of the star during the process of a deep tidal interaction. The model incorporates all the valid assumptions of the *affine*-star model of [4], while rectifying and refines some of its core physics. [5]'s model retains the same elegance of only dealing with a finite number of independent degrees of freedom of the *affine*-star model while identifying the *affine* approximation with the first-order terms in an infinite series solution to the fluid equations. Next, they question the use of globally conserved quantities in order to determine the temporal evolution of the connections (between current and initial Lagrangian coordinates) in [4]'s work. [5] rightfully identify, such use of globally conserved quantities brings in contributions from parts of the star, where the very assumption of linear relationship between initial and perturbed fluid coordinates itself is not valid. They note that although the *affine* assumption works well in modeling the density variation at the stellar core, it inevitably fails to do so in the rarefied outer envelope. Thus, the use of conserved quantities, derived by integrating over the whole volume (which includes the envelope) is guilty of collecting contributions from regions where the assumption goes wrong. It is worth noting that [4] too were aware of this fact that, in the envelope of the star, the fundamental assumption of their model breaks down, but failed to acknowledge the fact that the use of globally conserved quantities was bringing undue contributions in their formalism from the envelope, where the *affine* assumption fails. To rectify this, [5] resort to using fluid equations in their differential form and then equate the leading-order terms in the initial Lagrangian coordinates. This allows them to relate fluid quantities locally, making the formalism now self-consistent with the assumptions of the *affine*-model. Another refinement of the [4]'s work is accomplished while deriving the expression for the maximum density in the [5]'s work. Instead of equating the thermal pressure of the fluid with the *ram pressure* of the infalling fluid as done by [4], [5] equate the thermal pressure of the compressed gas with the *pressure gradient*, rightfully pointing out that it is not the pressure itself but the pressure gradient that is responsible for stopping compression.

These modifications result in a maximum density scaling of $\rho_{max} \propto \beta^{3/(\gamma+1)}$, much

shallower than the scaling of $\rho_{max} \propto \beta^{2/(\gamma-1)}$ obtained by [4]. [5] apply their techniques to analyze TDEs that range from a variety of stellar models, including the omnipresent standard polytropic models and also, in cases, the Eddington standard model (with the polytropic index $\Gamma = 4/3$ and the adiabatic index $\gamma \simeq 5/3$), which is a crude but reasonable representation of radiative stars [100]. [5]'s results [1] differ significantly from that of [4]'s. For stars modeled by the standard model, [4] found that the normalized central density varies as $0.22\beta^3$ in the large-β ($\beta \gtrsim 20$) regime, while [5] concludes that the same scaling goes as $5.4 \times 10^{-3}\beta^3$. The improved logical consistency of [5]'s model and the dramatic difference in the large-β ($\beta \gtrsim 20$) scaling of the maximum density and temperature resulting from that allude us to launch a follow-up investigation. In Chapter 7, we present an estimate of the maximum density and thus the extent of compression experienced by a sun-like star, modeled with the Eddington standard model, in the course of a deep disruption process ($\beta >> 1$) through high-resolution SPH simulations. We simulate encounters in the range of $\beta = 2 - 10$ and analyze the results to obtain the maximum density achieved. We conclude that the compression we find is mild compared to [4] in the range of our investigation, and *nuclear detonation is highly unlikely to arise from such an event.*

[1] see Figure. 18 of [5], which shows that the results obtained for standard model stars

Chapter 2

Preliminaries

2.1 Eulerian and Lagangian view-points

Before we write the fluid equations, we introduce two different viewpoints adopted in typical discussion in fluid dynamics–the *Eulerian* and *Lagrangian* viewpoints. In the Eulerian viewpoints, one chooses to describe the variations of fluid properties at a *fixed* point in space; hence the *Eulerian time derivatives* would simply be the partial differential operator, $\partial/\partial t$. On the other hand, from the *Lagrangian point of view* one chooses to describe how the fluid properties of an infinitesimal bit of fluid change over time as one *rides on* it. The *Lagrangian time-derivative* is then

$$\frac{d}{dt} := \frac{\partial}{\partial t} + \vec{v}.\nabla \tag{2.1}$$

2.2 Fluid equations: conservation laws

The equations of hydrodynamics are respectively–the continuity that describes the conservation of mass density, the Navier-Stokes equation that describes the conservation of momentum density and the energy equation that describes conservation of energy. We consider a fluid with following stress tensor, $\Pi_{ij} := \rho v_i v_j + p\delta_{ij} + \delta\Pi_{ij}$, the pressure $p = p(\rho, \mathcal{E}_0)$ as a function of the density ρ and energy $\mathcal{E}_0$ is the equation of state, and $\delta\Pi_{ij}$ the gradient term. Fluids with $\delta\Pi_{ij} = 0$ are *ideal* fluids and in this thesis we will deal only with such fluids. $\vec{\pi} := \rho\vec{v}$ denotes the momentum density of the fluid and the energy current j^ϵ is defined as $j^\epsilon := (p + \mathcal{E}).\vec{v}$. The conservation laws are surmised as the equations of hydrodynamics and are as follows:

1. **Conservation of mass: the continuity equation**

$$\frac{\partial\rho}{\partial t} = -\nabla.\vec{\pi} \tag{2.2}$$

Equation (2.2) is a simple statement that says that the mass cannot be created or destroyed.

2. **Conservation of momentum: the Navier-Stokes equations**

$$\frac{\partial \pi_i}{\partial t} = -\nabla_j . \vec{\Pi}_{ij} \tag{2.3}$$

this is essentially a rewrite of Newton's second law of motion.

3. **Conservation of energy**

$$\frac{\partial \mathcal{E}}{\partial t} = -\nabla . \vec{j^{\epsilon}} \tag{2.4}$$

Invoking the first laws of thermodynamic,

$$d\mathcal{E} = Tds - pd\left(\frac{1}{\rho}\right) \tag{2.5}$$

Taking the time-derivative of this equation and upon utilizing the continuity equation we obtain,

$$\frac{d\mathcal{E}}{dt} = T\frac{ds}{dt} - \frac{p}{\rho}\nabla . \vec{v} \tag{2.6}$$

which implies,

$$T\frac{ds}{dt} = 0 \tag{2.7}$$

the *Lagrangian derivative* used here is to signify the fact that the statement says, specific entropy of a gas parcel is conserved along its path of motion. Although we emphasize the fact that this is only true for regions of smooth flow, as we will show, the discontinuities in the flow (shocks) do not conserve entropy.

2.3 Shocks

Under normal conditions, fluid parcels along their path of motion conserve entropy, and the conservation of energy equation implies conservation of entropy. But there are conditions under which this is not true and the fluid element experiences an abrupt change in entropy (and other associated properties), resulting in a *shock wave*. One way to understand a shock wave is to think of a very strong sound wave. Because the wave is strong, the temperature at the top of the wave would be *significantly higher* than in the valley. The phase speed being proportional to the temperature, the top of the wave moves faster than the valley; hence the top part *outruns* the valley and a pile-up effect occurs in the direction of propagation. Therefore, the wave will steepen like waves on the beach and form a discontinuity, a shock. In principle, every sound wave is expected to form shocks, but those shocks are very *weak*. For example, the shock wave resulting from an explosion expands spherically, loses its strength, and eventually becomes just a sound wave. People

on the ground hear *sonic booms*, the weakening shock wave resulting from supersonic airplanes. The presence of a shock in a medium is described by *jump conditions*– which state the amount of discontinuity in the properties of the fluid after passing through a shock wave [112].

2.4 Linear Perturbation theory

The program of linear perturbation theory is well described by this quote from Ledoux [113]: "Essentially, two approaches exist for the discussion of the stability of a system. We can apply a small perturbation to it, so small that, in the equations that govern the evolution of this perturbation, we can content ourselves with keeping only the terms of the first degree in this perturbation. The equations so obtained are said to be linearized and their solution describes the behavior of the perturbation. "

As an example of the basic ideas involved, here we outline the method by applying this method to describe the adiabatic oscillation modes of a star.

2.4.1 Hydrostatic equilibrium

Although, in practice, a static configuration of a fluid body is impossible to achieve, nevertheless, a quasi-static state is assumed–where the *macroscopic* motion of the fluid element is negligible, that is, $v = 0$, $\partial/\partial t = 0$ on any fluid properties.

Under this condition, the continuity and energy (entropy) equation is trivially satisfied. The star is assumed to be in layer-by-layer *hydro-static equilibrium* between the gas pressure and the self-gravity. Hence, the momentum equation reads,

$$\frac{1}{\rho}\frac{\partial p}{\partial r} = -\frac{\partial \phi}{\partial r} \tag{2.8}$$

Here, ϕ is the gravitational potential to be solved from the Poisson equation,

$$\nabla^2 \phi = 4\pi G\rho \tag{2.9}$$

For a spherically symmetric star the above two equations are combined into,

$$\frac{1}{r^2}\frac{\partial}{\partial r}\left(\frac{r^2}{\rho}\frac{\partial \phi}{\partial r}\right) = -4\pi G\rho \tag{2.10}$$

This equation describes the hydro-static structure of a spherically symmetric star. Now to solve the equation we need to specify an equation of state, which we take to be polytropic, as $p = K\rho^\gamma$, $\gamma = 1 + \frac{1}{n}$ being the adiabatic index of the gas. It is convenient to switch to the following dimensionless quantities,

$$r = \alpha\xi, \;\; \rho = \rho_c \theta^n \tag{2.11}$$

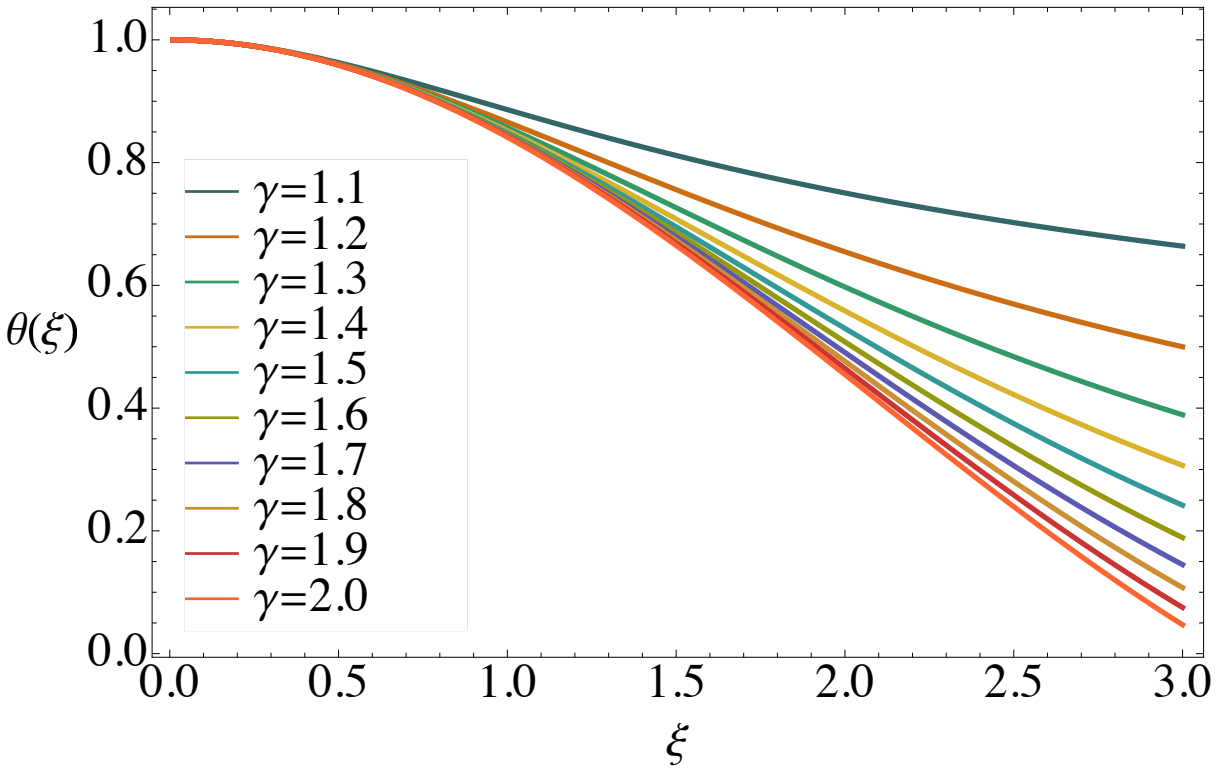

Figure 2: Plot of Numerical Solutions to the Lane-Emden equation for γ ranging from 1.0 to 2.0

Here, $\alpha^2 = \frac{\gamma}{\gamma-1}\frac{K\rho_c^{\gamma-2}}{4\pi G}$ is some fixed length scale, ρ_c being the central density. This definitions put Equation (2.10) into the following dimensionless form:

$$\frac{1}{\xi^2}\frac{\partial}{\partial\xi}\left(\xi^2\frac{\partial\theta}{\partial\xi}\right) = -\theta^n \tag{2.12}$$

The above equation is known as the "Lane-Emden" equation and admits numerical solutions and is being displayed in Figure 2 for a range of values of the adiabatic index, γ. Now this immediately gives us to solve for the density profiles of the star as shown in Figure 3.

2.4.2 Linear adiabatic wave eqution (LAWE)

In this section, we will analyze what happens to the hydrostatic structure of the star if we apply small perturbations to it. We choose to work in *Lagrangian* framework, where the continuity equation is written as,

$$\frac{d}{dt}(\delta m) = 0, \tag{2.13}$$

where $\delta m = \rho\delta V$, the mass contained in a spherically symmetric thin shell of δV. Now the continuity equation becomes,

$$\frac{d}{dt}(\rho r^2 dr) = 0, \tag{2.14}$$

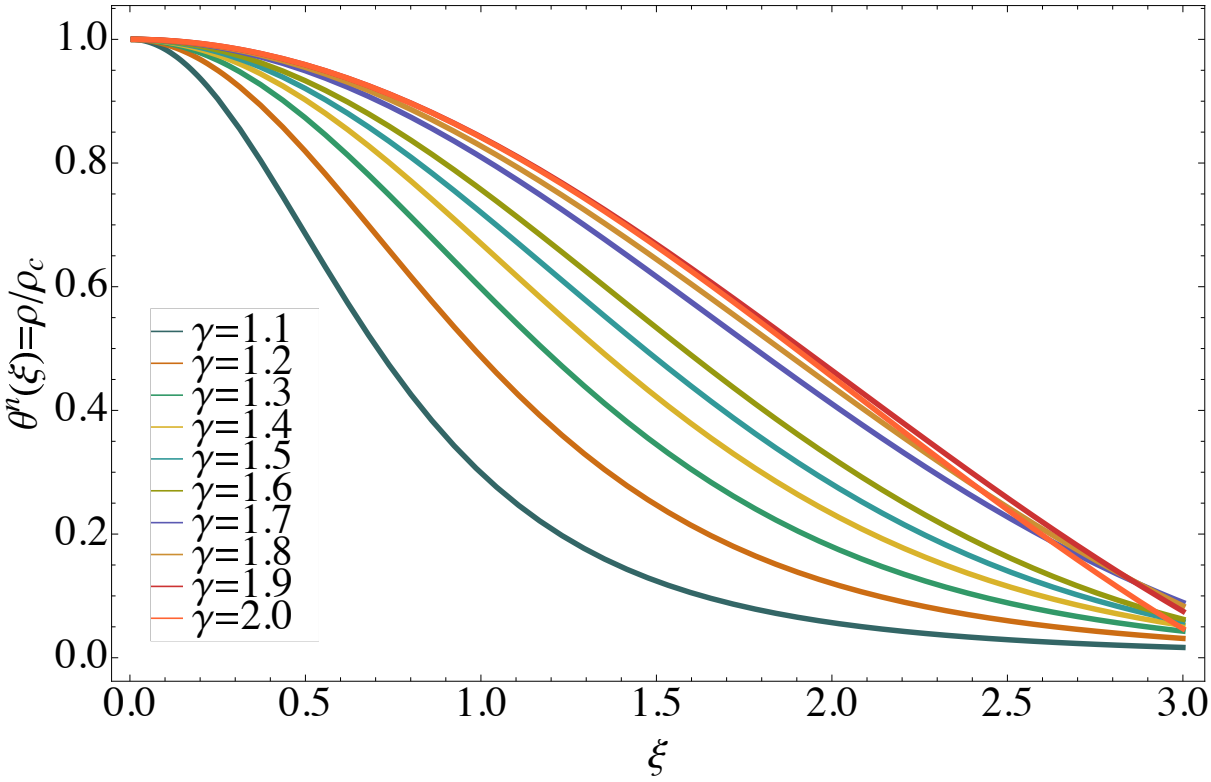

Figure 3: Plot of density $\frac{\rho}{\rho_c}$ vs ξ for γ ranging from 1.0 to 2.0

At an *initial time*, when the fluid elements under consideration was at a location r_0, the density is given by some initial density profile ρ_0, i.e. $\rho(r, t = 0) = \rho_0(r_0)$. Hence,

$$\rho(r,t)r^2dr = \rho_0(r_0)r_0^2dr_0, \tag{2.15}$$

which immediately gives, the time-dependent solution for the density as,

$$\rho(r,t) = \rho_0(t_0)\left(\frac{r}{r_0}\right)^{-2}\left(\frac{\partial r}{\partial r_0}\right)^{-1} \tag{2.16}$$

Now, we perturb the fluid configuration ever so slightly from its initial configuration as,

$$r(r_0,t) = r_0 + r_1(r_0,t) \tag{2.17}$$

Plugging in this definition in Equation (2.16),

$$\rho(r,t) = \rho_0(r_0)\left(1 - \frac{1}{r_0^2}\frac{\partial}{\partial r_0}[r_0^2 r_1]\right) + \mathcal{O}[r_1^2] \tag{2.18}$$

This is solution for the density in the linear order of the perturbed position of the Lagrangian fluid elements. Keeping terms only the linear order in perturbation equation yields,

$$\rho_1 = -\rho_0\frac{1}{r_0^2}\frac{\partial}{\partial r_0}[r_0^2 r_1] \tag{2.19}$$

Similarly to linear order the momentum equation, (2.10) becomes,

$$\frac{\partial^2 r_1}{\partial t^2} + \frac{1}{\rho_0}\left(\frac{\partial p_1}{\partial r_0} - \left(\frac{\rho_1}{\rho_0} + \frac{\partial r_1}{\partial r_0}\right)\frac{\partial p_0}{\partial r_0}\right) = 2\frac{Gm_0(r_0)}{r_0^3}r_1 \tag{2.20}$$

Linearization of the equation of state implies,

$$p_1 = \gamma p_0(r_0)\frac{\rho_1}{\rho_0} \tag{2.21}$$

In Equation (2.19)-(2.21) we have three unknowns ρ_1,p_1 and r_1 and we do algebraic manipulation to reduce them into a single equation in r_1:

$$\frac{\partial^2 r_1}{\partial t^2} - \mathcal{L}[r_1] = 0, \tag{2.22}$$

this equation is known as the linear adiabatic wave equation (LAWE). Here the operator is given by,

$$\mathcal{L} = \frac{1}{\rho}\frac{\partial}{\partial r_0}\left[\frac{\gamma p_0}{r_0^2}\frac{\partial}{\partial r_0}[r_0^2 r_1]\right] + \frac{1}{\rho_0}\frac{\partial p_0}{\partial r_0}\left(\frac{\partial r_1}{\partial r_0} - \frac{1}{r_0^2}\frac{1}{r_0^2}\frac{\partial}{\partial r_0}[r_0^2 r_1]\right) + \frac{2Gm_0(r_0)}{r_0^3}r_1, \tag{2.23}$$

the initial density and pressure profile of the star are respectively $\rho_0(r_0)$, $p_0(r_0)$ and $m_0(r_0)$is the initial mass profile given by,

$$m_0(r_0) = 4\pi\int_0^{r_0}\rho_0 r_0^2 dr_0) \tag{2.24}$$

To numerically solve Equation (2.23), we normalize the variables to have numbers in the range of 0 to ~ 1 by adopting the following re-definitions:

$$\rho_0 = \rho_c g_0(\xi_0),\ p_0 = p_c h_0(\xi_0),\ r_0 = \alpha\xi_0,\ \tau = \sqrt{4\pi G\rho_c}t \tag{2.25}$$

This transforms the LAWE into the following dimensionless form:

$$\begin{aligned}\frac{\partial^2\xi_1}{\partial\tau^2} - \Bigg[\frac{\gamma-1}{g_0}\frac{\partial}{\partial\xi_0}\left[\frac{h_0}{\xi_0^2}\frac{\partial}{\partial\xi_0}[\xi_0^2\xi_1]\right] + \frac{\gamma-1}{\gamma}\frac{1}{g_0}\frac{\partial h_0}{\partial\xi_0}\left(\frac{\partial\xi_1}{\partial\xi_0} - \frac{1}{\xi_0^2}\frac{\partial}{\partial\xi_0}[\xi_0^2\xi_1]\right)\\ + \frac{2}{\xi_0^3}\left(\int_0^{\xi_0} g_0(\xi_0)\xi_0^3 d\xi_0\right)\xi_1\Bigg] = 0\end{aligned} \tag{2.26}$$

At $\tau = 0$, we *seed* perturbations into the star by giving it some non-zero velocity that may depend on where we are within the star. We define this initial velocity profile in the star as

$$V_0(\xi_0) = \frac{\partial\xi_1}{\partial\tau}|_{\tau=0}. \tag{2.27}$$

Now we Laplace transform Equation (2.26) by adopting following definition of a quantity f,

$$L[f(\xi_0,\tau)] = \tilde{f}(\xi_0,\sigma) = \int_0^{\infty} f(\xi_0,\tau)\exp -\sigma\tau d\tau \tag{2.28}$$

This gives,

$$\sigma^2\tilde{\xi_1} - \mathcal{L}[\tilde{\xi_1}] = V_0(\xi_0), \tag{2.29}$$

where

$$\begin{aligned}\mathcal{L}[\tilde{\xi_1}] = \frac{\gamma-1}{g_0}\frac{\partial}{\partial\xi_0}\left[\frac{h_0}{\xi_0^2}\frac{\partial}{\partial\xi_0}[\xi_0^2\xi_1]\right] + \frac{\gamma-1}{\gamma}\frac{1}{g_0}\frac{\partial h_0}{\partial\xi_0}\left(\frac{\partial\xi_1}{\partial\xi_0} - \frac{1}{\xi_0^2}\frac{\partial}{\partial\xi_0}[\xi_0^2\xi_1]\right) \\ + \frac{2}{\xi_0^3}\left(\int_0^{\xi_0} g_0(\xi_0)\xi_0^3 d\xi_0\right)\xi_1\end{aligned} \tag{2.30}$$

2.4.3 Eigenmodes

To illustrate the power of this method let's consider the initial velocity profile of the star is

$$V_0(\xi_0) = VE_n(\xi_0), \tag{2.31}$$

where V is a constant with value $<< 1$ and the function E_n satisfies,

$$\mathcal{L}[E_n] = -\sigma_n^2 E_n, \tag{2.32}$$

and are called the *eigenfunctions* with *eigenfrequencies* σ_n. Physically, we expect the perturbation to the density to remain non-divergent; hence we demand that the eigenfunction would satisfy $E_n(\xi_0) = 0$ and since the eigenvalue equation is linear we can always rewrite Equation 2.32 by dividing it by $\frac{\partial E_n}{\partial\xi_0}|_{\xi_0=0}$ and define some new function $E_n \to E_n/\frac{\partial E_n}{\partial\xi_0}|_{\xi_0=0}$. Hence we now have the following eigen system,

$$\mathcal{L}[E_n] = -\sigma_n^2 E_n,\ E_n(0) = 0,\ \frac{\partial E_n}{\partial\xi_0}|_{\xi_0=0} = 1, \tag{2.33}$$

with

$$\begin{aligned}\mathcal{L}[E_n] = \frac{\gamma-1}{g_0}\frac{\partial}{\partial\xi_0}\left[\frac{h_0}{\xi_0^2}\frac{\partial}{\partial\xi_0}[\xi_0^2 E_n]\right] + \frac{\gamma-1}{\gamma}\frac{1}{g_0}\frac{\partial h_0}{\partial\xi_0}\left(\frac{\partial\xi_1}{\partial\xi_0} - \frac{1}{\xi_0^2}\frac{\partial}{\partial\xi_0}[\xi_0^2 E_n]\right) \\ + \frac{2}{\xi_0^3}\left(\int_0^{\xi_0} g_0(\xi_0)\xi_0^3 d\xi_0\right)E_n\end{aligned} \tag{2.34}$$

In Figure 4, we present the first 5 eigenfunctions by numerically solving the eigensystem (2.33) for a $\gamma = 5/3$ polytrope.

2.5 Smoothed Particle Hydrodynamics (SPH)

Smoothed particle hydrodynamics (SPH) is a particle-based Lagrangian method to solve the equations of hydrodynamics [114, 115]. But as Price points out, SPH aims to answer

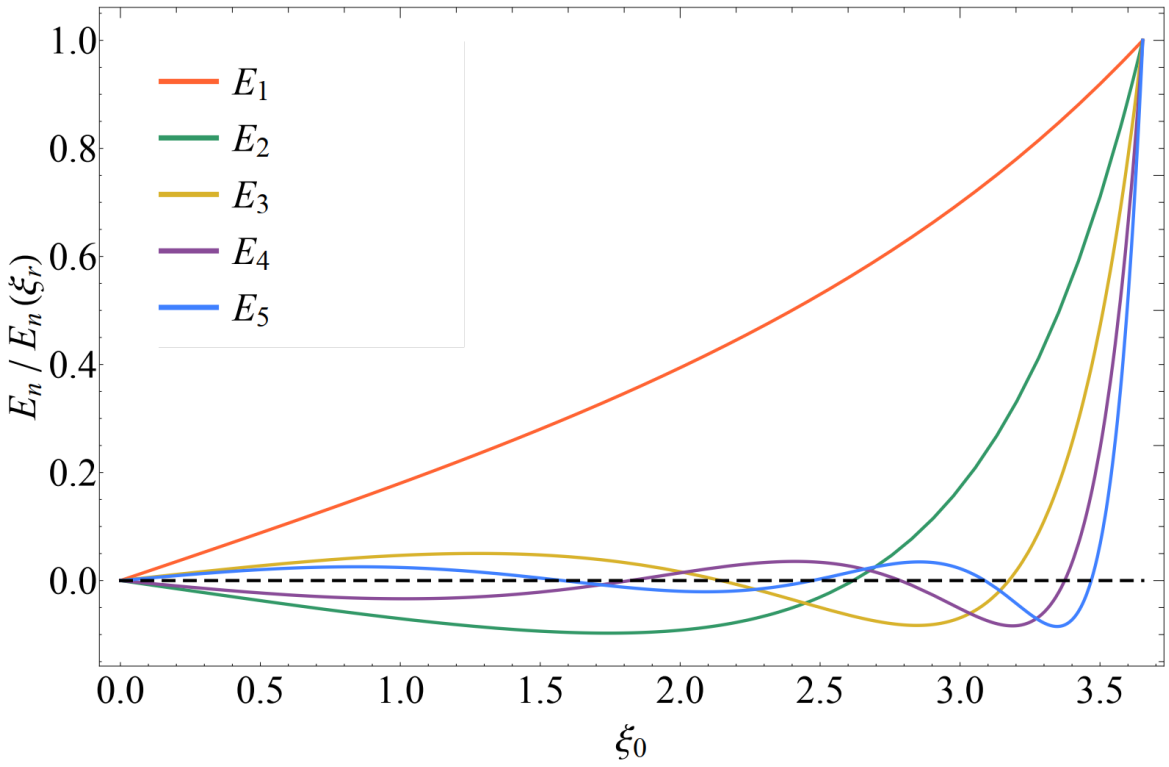

Figure 4: The first 5 eigenfunctions of a $\gamma = 5/3$ polytrope.

the question: "How does one compute the density from an arbitrary distribution of point-mass particles?" [116]. SPH calculates the density (and other fluid properties) using a weighted summation over nearby particles, give by,

$$A(\vec{r}) = \Sigma_i A_i \frac{m_i}{\rho_i} W\left(||\vec{r} - \vec{r_i}||_2, h\right) \tag{2.35}$$

Figure 5 illustrates the concept of a smoothing kernel W, which has dimensions of inverse volume and h is a scale parameter that determines the fall-off of W as a function of particle spacing. Although the early SPH implementations used to employ a constant resolution length h, now-a-days the smoothing length is set in an adaptive way, for example, making h proportional to the density. Since the density itself is a function of the smoothing length, through iterative summation one simultaneously obtains the mutually dependent $h(r)$ and $\rho(r)$ [117, 118, 115]. The gradient operator reads,

$$\nabla_i A_i = \rho_i \Sigma_j m_j \left(\frac{A_i}{\rho_i^2} + \frac{A_j}{\rho_j^2}\right) \nabla_{\vec{r_i}} W\left(||\vec{r} - \vec{r_i}||_2, h\right) \tag{2.36}$$

This allows one to implement the fluid equations in the following way:

$$\frac{d\vec{v}}{dt} = -\frac{1}{\rho}\nabla p + \vec{g}, \;\; p = B\left(\left(\frac{\rho}{\rho_0}\right)^{\gamma} - 1\right) \tag{2.37}$$

The SPH simulation cycle operates broadly in this three steps:

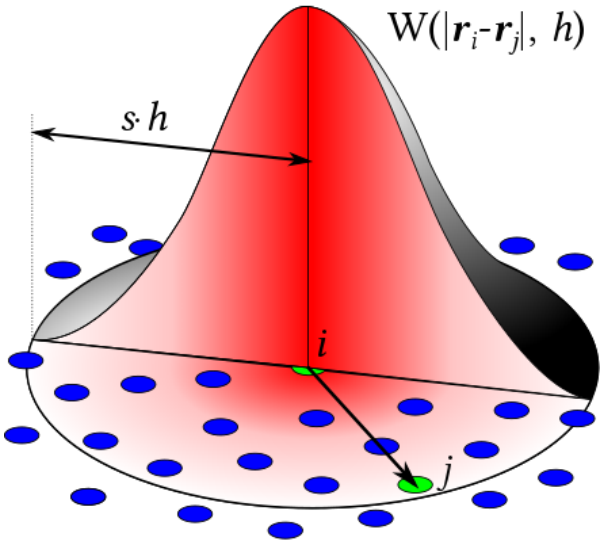

Figure 5: Schematic view of the SPH convolution using a smoothing kernel W in 2D space. The l_2 distance between the two points i around which the kernel is centered and the other particle j is shown. This figure is adapted from [1]

1. For each particle i, it computes ρ_i as $\rho_i = \Sigma_j m_j$ W $(||\vec{r} - \vec{r_i}||_2, h)$

2. For each particle i, it computes ∇p_i

3. Integrates in Euler step:

$$\begin{aligned} \vec{v}_{t+1} &= \vec{v}_t + \Delta t \frac{d\vec{v}}{dt}, \\ \vec{r}_{t+1} &= \vec{r}_t + \Delta t \vec{v}_{t+1} \end{aligned} \tag{2.38}$$

To ensure numerical stability SPH uses the Courant-Friedrichs-Lewy (CFL) condition,$C = \frac{v_{max}\Delta t}{\Delta r} \lesssim C_{max} \sim 1$ to calculate the allowed time step in explicit time integrations.

Chapter 3

Stability of giant planetary atmosphere with a solid core

One of the ways by which giant planets are thought to form is through "core accretion" (CA[1]; e.g., [42, 122, 123, 124, 125, 126]), a sequential process whereby the planet is assembled from a solid core that builds a surrounding, gaseous envelope through accretion from a protoplanetary disc. Quantitative studies of the CA model show that it proceeds via two or three evolutionary phases [127]. In the first phase planetesimals form [128, 129, 130, 131] and then grow into larger rocky cores by the accretion of pebbles and/or other planetesimals and growing cores [132, 133, 134, 135, 136]. In the second phase the core accretes a low mass (relative to the core) gas envelope from the circumstellar disc by radiative cooling on the Kelvin-Helmholtz (KH) timescale, which causes the envelope to contract and permits further gaseous accretion [137, 138]. Initially, the KH timescale increases as the envelope grows in mass, and thus the evolution is slow. The recycling of gas between the disc and the bound envelope, a three-dimensional effect that is not captured in classical models, may modify the cooling timescale at this stage [139, 140, 141]. If and when the atmospheric mass becomes comparable to that of the core, the self-gravity of the gas envelope becomes significant, and the KH timescale decreases. This transition leads to the third phase of rapid "runaway growth" of the gas envelope, which (in classical one-dimensional models) begins as a more rapid, but still hydrostatic, KH contraction (e.g., [126, 142]. The end of runaway growth again involves hydrodynamics, as the growing planet carves a gap in the disk, which lowers gas accretion and eventually sets the final planet mass [143, 144, 145].

[1]The other paradigm for giant-planet formation is through instabilities in the protoplanetary disk – the "disc instability" model (e.g., [41, 119, 23]). We will cast our discussion within the framework of the CA model, but many of our conclusions would also apply to the disk instability model. See [120, 121] for discussions of these models.

Qualitative and potentially observable changes to the giant planet formation process would occur if, at any point, the planet became dynamically unstable. This is in principle possible if the effective adiabatic index of the gaseous envelope, which we denote as γ, drops below a critical value. [44] demonstrated that for a gaseous, self-gravitating spherical body, dynamical instability to radial perturbations occurs if $\gamma < 4/3$. This result has well-studied implications for the stability of massive stars, which are dominated by radiation pressure and hence have $\gamma \approx 4/3$, but it can also come into play for cooler, gas pressure dominated bodies. As a gas envelope contracts and its temperature rises, molecular hydrogen first dissociates, and is then ionized. These two transitions can reduce the adiabatic index from 7/5 (appropriate to a diatomic molecular gas) to values near unity [146]. In the star formation context is has long been suggested that this drop in adiabatic index as gas heats up leads to dynamical instability and collapse [147], and it is natural to ask whether the same phenomenon can occur in planet formation. Early work on core accretion noted that the existence of low γ regions could bring proto-planets close to dynamical instability [122], which could lead to pulsations [148]. More recently, [145] speculated that the presence of $\gamma < 4/3$ regions in enough of the planet might accelerate planet formation. We emphasize that this potential *dynamical* instability is distinct from the established effect that dissociation has in reducing gas accretion rates during the slow, hydrostatic phase [149].

The key difference between the structure of a star and that of a forming giant planet is that the latter possesses a rocky or icy core that is much less compressible than the gaseous envelope. It is thus inaccurate to treat the entire planet as a single adiabatic gas, and Chandrasekhar's simple $\gamma < 4/3$ criterion for instability need not apply. A more realistic – though still highly idealized – model is to treat the planet as having a gaseous envelope of fixed adiabatic index, that is truncated radially at a finite inner core radius. Our goal in this work is to calculate a modified Chandrasekhar-like stability criterion for this model system, which will depend on the size and mass of the rocky core. We consider the outer radius of the planet embedded in the disc to be less than the smaller of the Hill radius or the Bondi radius, and ignore any non-radial perturbation from the stellar tidal force.

In Section 3.1.1 we describe the model and write down the fluid equations that govern the evolution of the planetary envelope in the presence of the massive core, and in Section 3.1.2 we present hydrostatic solutions to these equations in the limit that the envelope can be modeled as polytropic. In Section 3.2 we derive the equations that describe the response of the envelope to radial perturbations and we delimit the region of instability as a function of the core properties. We discuss the implications of our findings and directions for future work in Section 7.3.

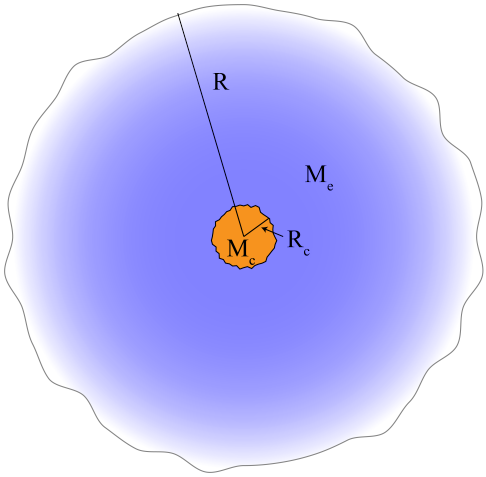

Figure 6: A qualitative illustration of our model of a giant planet, which is a spherical object that consists of a core of radius R_c and mass M_c and a compressible envelope that extends from R_c to R. The envelope has a mass of M_e, such that the total mass of the planet is $M_\mathrm{c} + M_\mathrm{e}$ and the relative mass of the core is $\mu = M_\mathrm{c}/(M_\mathrm{c} + M_\mathrm{e})$.

3.1 Atmospheric model

We model a giant planet as a spherical object that consists of an incompressible core of radius R_c and a compressible envelope that extends from R_c to R, outside of which the density is zero (see Figure 6). As we noted in Section **??**, the processes of ionization and molecular dissociation that occur within the envelope imply that energy can be transferred from one species to another. Instead of modeling these processes explicitly, we treat the gas as adiabatic with an *effective* adiabatic index that – owing to these processes – can be less than 4/3. In this way, we do not account for the time dependence that accompanies these non-ideal processes, but instead gain some understanding as to the combined effects of the smaller adiabatic index and the presence of the incompressible core on the hydrodynamic stability of the envelope.

3.1.1 Fluid equations

With this set of assumptions, the hydrodynamical evolution of the envelope is governed by the continuity of mass, radial momentum, and entropy, the conservation laws for which read respectively:

$$\frac{\partial \rho}{\partial t} + \frac{1}{r^2}\frac{\partial}{\partial r}\left(r^2 \rho v\right) = 0, \tag{3.1}$$

$$\frac{\partial v}{\partial t} + v\frac{\partial v}{\partial r} + \frac{1}{\rho}\frac{\partial p}{\partial r} = -\frac{GM_\mathrm{c}}{r^2} - \frac{GM}{r^2}, \tag{3.2}$$

$$\frac{\partial}{\partial t}\ln\left(\frac{p}{\rho^\gamma}\right) + v\frac{\partial}{\partial r}\ln\left(\frac{p}{\rho^\gamma}\right) = 0. \tag{3.3}$$

Here ρ is the gas density within the envelope, v is the radial velocity, r is spherical radius from the origin, p is the gas pressure, and γ is the adiabatic index. On the right-hand side of Equation (3.2) we accounted for the gravitational presence of the core that has mass $M_{\rm c}$, and

$$M = \int_{r_{\rm c}}^{r} 4\pi r^2 \rho \, dr \tag{3.4}$$

is the total atmospheric mass contained within radius r. It is mathematically convenient to write the continuity equation (3.1) in terms of M, which is (upon using Equation (3.4) to write ρ in terms of M):

$$\frac{\partial M}{\partial t} + v \frac{\partial M}{\partial r} = 0. \tag{3.5}$$

While we did not write it explicitly, all of the fluid variables are functions of both spherical radius r and time t; we do not consider angular perturbations here.

We anticipate finding solutions to Equations (3.2) – (3.5) that are hydrostatic, such that the radial velocity v and time dependence are identically zero, on top of which we impose perturbations that induce radial motion and temporal evolution. The solutions for the fluid variables are therefore characterized by the existence of a surface $R(t)$ that, when the perturbations are small and the motions are subsonic, is approximately independent of time and separates the planetary interior from the ambient gas (which is assumed to have a negligible impact on the dynamics of the envelope). In our model we neglect accretion from the surrounding, protoplanetary disc, and hence the total mass of the planet $M_{\rm c} + M_{\rm e}$ is conserved, where $M_{\rm c}$ is the core mass and $M_{\rm e}$ is the total mass of the gaseous envelope. The characteristic speed within the envelope is governed by the sound speed $c_{\rm s}$, which – owing to the approximately hydrostatic nature of the envelope – is comparable to the freefall speed, or $c_{\rm s} \simeq \sqrt{G\left(M_{\rm c} + M_{\rm e}\right)/R}$. The characteristic timescale that parameterizes the temporal evolution of the planet is then the sound crossing time, being $R/c_{\rm s} \simeq R^{3/2}/\sqrt{G\left(M_{\rm c} + M_{\rm e}\right)}$.

Given these considerations, we analyze the fluid equations in terms of the following (dimensionless) space-like and time-like variables:

$$\xi = \frac{r}{R(t)}, \tag{3.6}$$

$$d\tau = \frac{1}{R}\left(\sqrt{\frac{G(M_c + M_e)}{R}}\right) dt. \tag{3.7}$$

We further non-dimensionalize the mass coordinate by defining

$$M = M_{\rm e} m(\xi, \tau), \tag{3.8}$$

from which it follows that

$$\rho = \frac{M_{\rm e}}{4\pi R^3}\frac{1}{\xi^2}\frac{\partial m}{\partial \xi} \equiv \frac{M_{\rm e}}{4\pi R^3} g(\xi,\tau), \tag{3.9}$$

where

$$g(\xi,\tau) = \frac{1}{\xi^2}\frac{\partial m}{\partial \xi}. \tag{3.10}$$

Similarly, we non-dimensionalize the pressure p and the radial velocity v by introducing the functions h and f, defined via

$$\begin{aligned} p &= \left(\frac{GM_e(M_c+M_e)}{4\pi R^4}\right) h(\xi,\tau), \\ v &= \left(\sqrt{\frac{G(M_c+M_e)}{R}}\right) f(\xi,\tau). \end{aligned} \tag{3.11}$$

We can now write the hydrodynamic equations (3.2), (3.3) and (3.5) in dimensionless form by introducing these coordinate transformations. To further simplify the resulting equations, we maintain that the fluid motions are subsonic, such that the dimensionless function f satisfies $f \ll 1$ and $\partial R/\partial t \ll c_{\rm s}$. In this limit, we can also linearize the hydrodynamic equations in the assumed-small quantities f and $1/c_{\rm s}\times\partial R/\partial t$, such that we keep only leading-order terms in these quantities and omit any non-linear contributions. Doing so yields the following three dimensionless, fluid equations:

$$\frac{\partial m}{\partial \tau} + (f - V\xi)\frac{\partial m}{\partial \xi} = 0, \tag{3.12}$$

$$\frac{\partial f}{\partial \tau} + \frac{1}{g}\frac{\partial h}{\partial \xi} = -\frac{\mu}{\xi^2} - (1-\mu)\frac{m}{\xi^2}, \tag{3.13}$$

$$\frac{\partial}{\partial \tau}\ln\left(\frac{h}{g^\gamma}\right) + V(3\gamma - 4) + (f - V\xi)\frac{\partial}{\partial \xi}\ln\left(\frac{h}{g^\gamma}\right) = 0. \tag{3.14}$$

Here we defined

$$\mu \equiv \frac{M_{\rm c}}{M_{\rm c}+M_{\rm e}} \tag{3.15}$$

as the ratio of the mass of the core to the total mass of the planet, and

$$V \equiv \frac{\partial R}{\partial t}\left(\frac{G\left(M_{\rm c}+M_{\rm e}\right)}{R}\right)^{-1/2} \tag{3.16}$$

is the ratio of the velocity of the surface of the envelope to the escape speed.

In the absence of conduction, the surface of the planet is a contact discontinuity that separates the planetary interior from the ambient gas, across which the pressure and fluid velocity (in the comoving frame of the contact discontinuity) are continuous. We further

reduce the parameter space of our solutions by assuming that the ambient gas does not play a dominant role in providing further pressure confinement of the planetary envelope, and therefore the ambient pressure is set to zero. With these assumptions, the boundary condition on the fluid velocity at the surface is

$$v(\xi = 1, \tau) = \frac{\partial R}{\partial t} \quad \Rightarrow \quad f(\xi = 1, \tau) = V. \tag{3.17}$$

In addition, the pressure perturbation at the surface must vanish to smoothly match onto the surrounding medium, and if the planet is subject to only radial perturbations, the fluid velocity at the core radius must be zero. In the next two sections, we seek solutions to the above set of equations that satisfy these boundary conditions by treating the envelope as a hydrostatic medium with small, time-dependent perturbations, where "small" implies that the radial velocity is subsonic. As such, we write

$$h(\xi, \tau) = h_0(\xi) + h_1(\xi, \tau), \tag{3.18}$$

$$g(\xi, \tau) = g_0(\xi) + g_1(\xi, \tau), \tag{3.19}$$

$$f(\xi, \tau) = f_1(\xi, \tau) \tag{3.20}$$

with subscript-0 quantities representing the unperturbed, hydrostatic solutions and subscript-1 quantities the perturbations. Note that, because the background upon which we impose such perturbations is hydrostatic, there is no zeroth-order velocity (i.e., f_0 is absent from the above expressions). Below we will also work with the functions m_0 and m_1, which are directly related to g_0 and g_1 via Equation (3.10).

3.1.2 Hydrostatic Solutions

The hydrostatic solutions to Equations (3.12) - (3.14) are independent of time and possess no radial velocity, meaning that $V \equiv 0$ and $f_0 = 0$. In this case, the continuity and entropy equations are trivially satisfied, and the radial momentum equation yields the dimensionless equation of hydrostatic balance that relate the subscript-0 functions:

$$\frac{1}{g_0}\frac{\partial h_0}{\partial \xi} = -\mu\frac{1}{\xi^2} - (1-\mu)\frac{m_0}{\xi^2}, \tag{3.21}$$

To close this system, we need a relationship between the hydrostatic pressure and the density, for which we adopt a polytropic equation of state and let

$$h_0 = K_0 g_0^{\gamma}, \tag{3.22}$$

where K_0 is the dimensionless specific entropy of the atmospheric gas. The equation for m_0 is then

$$\frac{\gamma}{\gamma-1}K_0\frac{\partial}{\partial\xi}\left[\left(\frac{1}{\xi^2}\frac{\partial m_0}{\partial\xi}\right)^{\gamma-1}\right]=-\frac{\mu}{\xi^2}-(1-\mu)\frac{m_0}{\xi^2}. \tag{3.23}$$

Note that, if the first term on the right-hand side of this equation were absent, this would just be the Lane-Emden equation written in terms of the enclosed mass m_0. When $\mu \neq 0$, the first term represents the gravitational contribution from the core.

We can numerically solve Equation (3.23) by following the procedure outlined in [150]: the solutions to this equation must satisfy the requirement that the total mass of the envelope be equal to M_e, so that $m_0(1) = 1$. We can therefore expand the function m_0 in powers of $(1-\xi)$ and equate like powers on the left and right sides of Equation (3.23); this results in the following, leading-order approximation to m_0 near the surface of the planet:

$$m_0(\xi)=1-\frac{\gamma-1}{\gamma}\left(\frac{\gamma-1}{\gamma}\frac{1}{K_0}\right)^{\left(\frac{1}{\gamma-1}\right)}(1-\xi)^{\left(\frac{\gamma}{\gamma-1}\right)} \times\left[1-\left(\frac{2\gamma-3}{2\gamma-1}\right)(1-\xi)\right]. \tag{3.24}$$

This expression can be used to evaluate $m_0(\xi \simeq 1)$ and $dm_0/d\xi(\xi \simeq 1)$, which can be used as boundary conditions to integrate Equation (3.23) inward for a given, dimensionless specific entropy K_0. When the polytropic envelope is assumed to extend to the geometric center of the planet, K_0 is fixed by requiring that the enclosed mass equal zero at the origin. For a given γ, there is then a unique value of K_0 for which the density terminates at the surface ($\xi \simeq 1$) and the enclosed mass equals zero at the origin, which is just the usual solution to the Lane-Emden equation (e.g., [151, 152]). This value of K_0 can be determined iteratively through a brute-force, trial-and-error method in which one successively changes the value of K_0 until the boundary condition near the origin is satisfied (see the discussion in Section 2 of [150]).

For our application here, however, the existence of an incompressible core of relative mass μ modifies the solution from the usual, Lane-Emden function. In particular, if we let the core have some associated, relative radius ξ_c (i.e., ξ_c is the radius of the core, R_c, divided by the total radius of the planet R), then the total enclosed mass of the envelope must instead be zero at ξ_c. In addition to the relative mass of the core μ, there is thus an additional, free parameter contained in these solutions, which is the inner radius ξ_c (presumed greater than zero) at which the core terminates and the envelope begins. The solutions to Equation (3.23) are therefore determined by three parameters, being the core mass μ, core radius ξ_c, and adiabatic index γ; once these three parameters are fixed, the

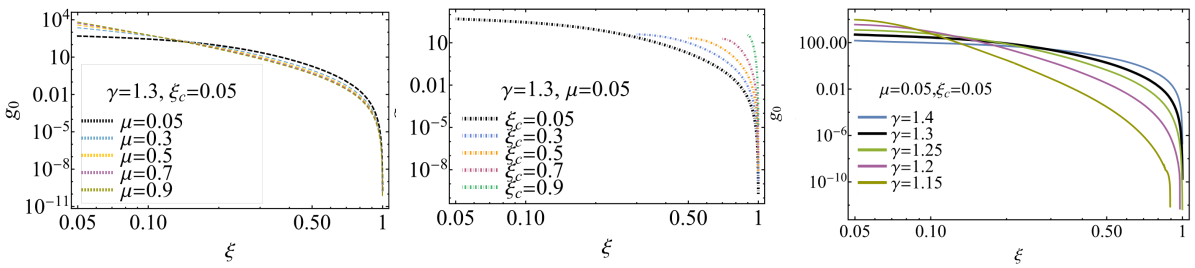

Figure 7: Left: The unperturbed and dimensionless density g_0 as a function of radius for the relative core masses μ shown in the legend and a polytropic index $\gamma = 1.3$ and a core radius of $\xi_c = 0.05$. Middle: Identical to the left panel but with fixed $\gamma = 1.3$ and $\mu = 0.05$ and the inner radii shown in the legend. Right: Identical to the left panel but with fixed $\mu = 0.05$, fixed $\xi_c = 0.05$, and variable adiabatic indices as shown in the legend.

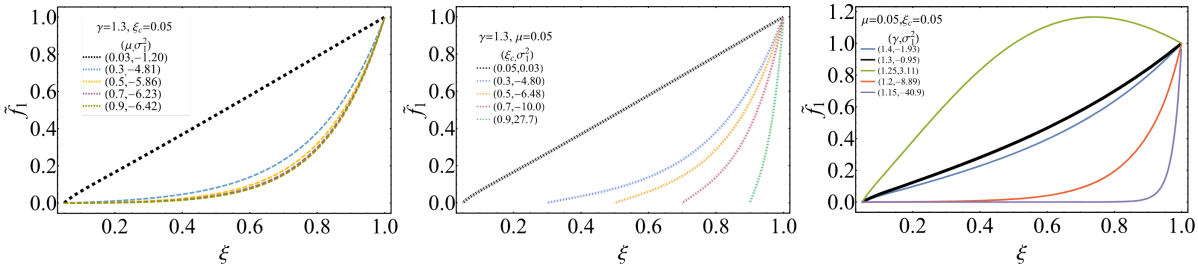

Figure 8: Top-left panel: The lowest-order eigenfunctions as a function of the dimensionless radius for the polytropic index $\gamma = 1.3$ and core radius $\xi_c = 0.05$ for different values of the fractional core mass μ shown in the legend.

value of K_0 that satisfies the inner boundary condition ($m_0(\xi_c) = 0$) can be determined by – as for the standard Lane-Emden equation described above – iteratively looping over K_0 in a trial-and-error manner.

In principle, the solutions for the envelope extend asymptotically close to $\xi = 1$ where the density is exactly zero and the mass satisfies $m \equiv 1$. However, the envelope becomes extremely tenuous near the surface once γ nears unity – the case of interest here – owing to the fact that the density declines approximately as $\propto (1 - \xi)^{1/(\gamma-1)}$ (e.g., for $\gamma = 1.1$, the density reaches $\sim 10^{-10}$ at $\xi = 0.9$). In practice and to avoid any numerical artifacts associated with initializing the integration of Equation (3.23) too close to the surface, we integrate Equation (3.23) from the location where leading-order solution for the unperturbed density (i.e., using Equation 3.24) satisfies $g_0 = 10^{-8}$, and outside of this location we replace the numerically obtained solution with the leading-order, series expansion given in Equation (3.24). We have verified that increasing or decreasing the threshold, lower limit on the density that sets the outer boundary does

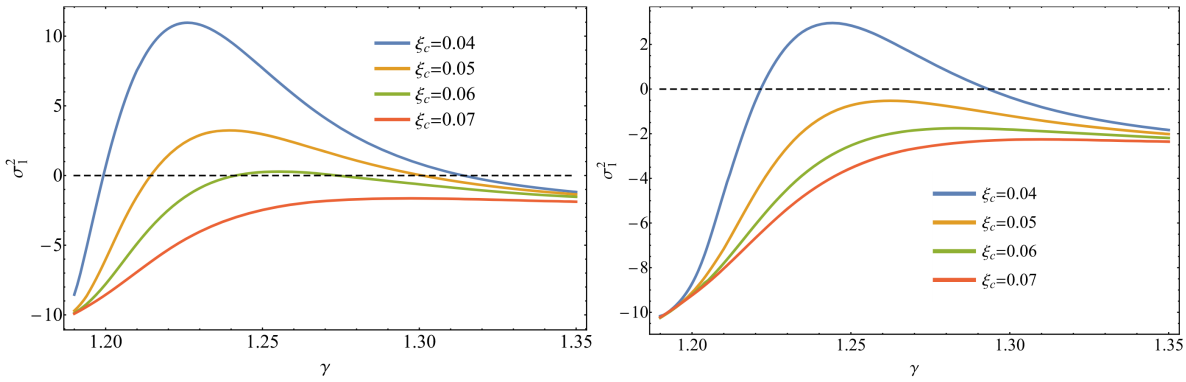

Figure 9: The square of the lowest-order eigenvalue as a function of the adiabatic index, γ. The left panel corresponds to a core mass of $\mu = 0.05$, while in the right panel we set $\mu = 0.1$.

not noticeably change the hydrostatic solution or the eigenmodes (see below). Examples of the hydrostatic solutions are shown in Figure (7). To isolate the impact of the relative core mass (μ), radius (ξ_c), and polytropic index (γ) on the hydrostatic solutions, we fix all but one parameter for each of the plots. The left panel of Figure (7) shows five different solutions for the dimensionless density g_0 (on a logarithmic scale) as a function of the normalized spherical radius variable ξ, obtained by setting the adiabatic index $\gamma = 1.3$, the dimensionless core radius $\xi_c = 0.05$ and varying the fractional core mass μ, successively for each curve. Comparing these five curves (as we move from $\mu = 0.9$ to $\mu = 0.05$) we observe two contrasting behaviors: the configuration that receives the highest contribution from core to its total mass ($\mu = 0.9$), is the densest configuration near the core ($\xi \approx \xi_c$) and as we move toward the outer edge ($\xi \approx 1$) its density ranks to be the least dense one. This is due to the fact that the gravitational field is more centrally concentrated for a larger core mass, and all the material piles up near the inner boundary.

In the middle panel of this figure we show solutions obtained by varying the size of the core (successively as we move from one curve to the next) while maintaining $\gamma = 1.3$ and $\mu = 0.05$. We see that the envelope is denser on average, for a more voluminous core. This trend is expected because as the core grows in size, it leaves less space to be occupied by the envelope that – for the same μ – contains the same mass, resulting in an increase in density.

In the right panel of this figure we vary the adiabatic index γ while maintaining a fixed dimensionless core radius $\xi_c = 0.05$ and fractional core mass $\mu = 0.05$. We see the same contrasting behavior between regions near the inner and outer boundaries. We notice the most compressible envelope (the one with the smallest adiabatic index $\gamma = 1.15$), ranks to be the densest, closer to the core ($\xi \approx \xi_c$), and the least dense near the outer edge of

the planet ($\xi \approx 1$). This behavior occurs because the increased compressibility of the gas causes more matter to pile up near the core.

The non-dimensionalized equations we derived demonstrate that hydrostatic solutions to the fluid equations in the absence of an entropy gradient are manifestly scale-free; this is exploited in the standard analysis of the Lane-Emden equation by defining

$$\alpha^2 = \frac{\gamma}{\gamma - 1} \frac{K \rho_{\rm c}^{\gamma - 1}}{4\pi G \rho_{\rm c}}, \tag{3.25}$$

where K is the adiabatic constant related to the central pressure p_c and density $\rho_{\rm c}$ as $\frac{p_c}{\rho_c^\gamma}$. The surface of the planet then occurs at some fixed number times α. However, it is a choice to work in coordinates normalized by α and the central properties of the planet, and we can instead – as we have done here – choose to work with a radial coordinate that is relative to the surface and the average properties of the planet. In this case the *dimensionless* entropy variable K_0 that ensures the regularity of the solutions at the center of the planet is a function of the adiabatic index, and here it is also a function of the core mass and radius. Owing to the self-similarity of the equations, the same solution is valid for any choice of physical planet radius R provided that the radius is scaled by R, the pressure is scaled by M/R^{-4}, and the density by M/R^{-3}.

3.2 Perturbation Analysis

3.2.1 Eigenmode Equations

With the polytropic solution as the unperturbed state, the perturbation equations are

$$\frac{\partial m_1}{\partial \tau} = (V\xi - f_1) \frac{\partial m_0}{\partial \xi}, \tag{3.26}$$

$$\frac{\partial f_1}{\partial \tau} - \frac{g_1}{g_0^2} \frac{\partial h_0}{\partial \xi} + \frac{1}{g_0} \frac{\partial h_1}{\partial \xi} = -(1-\mu) \frac{m_1}{\xi^2}, \tag{3.27}$$

$$\frac{\partial}{\partial \tau} \left[\frac{h_1}{h_0} - \frac{\gamma g_1}{g_0} \right] - V(4 - 3\gamma) = 0. \tag{3.28}$$

Note that, in the last of these expressions, the Brunt-Vaisala frequency is identically zero – and the solutions are therefore buoyantly neutral – because of the isentropic nature of the envelope. We can now take the Laplace transform of Equations (3.26)–(3.28), where the Laplace transform of f_1 is

$$\tilde{f}_1(\xi, \sigma) = \int_{-\infty}^{\infty} f_1(\xi, \tau) \exp(-\sigma\tau)\, d\tau \tag{3.29}$$

and similarly for all other fluid variables. We can understand the linear response of the envelope to a given perturbation by letting there be, for example, an initial, non-zero

velocity with some underlying radial dependence; this function then appears on the right-hand side of the Laplace-transform of Equation (3.27) and serves to initialize the motion of the gas. The resulting response is then able to be written as a sum over the *eigenmodes* of the set of Laplace-transformed equations, where the eigenmodes are solutions to this set of equations that possess *eigenvalues*. The eigenvalues are complex numbers that we denote $\sigma_{\rm n}$ where the perturbations to the fluid variables diverge as simple poles in the complex plane. Importantly, even though the coefficients in such an eigenmode expansion depend on the nature of the initial perturbation, the fact that the fluid variables diverge at the eigenvalues implies that the eigenmodes themselves do not (see [150] for explicit expressions for the coefficents). Defining $\tilde{f}_{\rm n} = \tilde{f}_1/\tilde{V}$ as the ratio of the perturbation to the fluid velocity to the perturbation to the surface velocity and taking the limit as $\sigma \to \sigma_{\rm n}$, a single, second-order equation for $\tilde{f}_{\rm n}$ can be derived by combining the Laplace-transformed equations; the equation is

$$\sigma_{\rm n}^2 \tilde{f}_{\rm n} + \frac{\partial}{\partial \xi}\left[\frac{\gamma h_0}{g_0}\frac{1}{g_0 \xi^2}\frac{\partial}{\partial \xi}\left[\left(\xi - \tilde{f}_{\rm n}\right)\frac{\partial m_0}{\partial \xi}\right]\right] + (4-3\gamma)\frac{1}{g_0}\frac{\partial h_0}{\partial \xi} + \frac{1-\mu}{\xi^2}(\xi - \tilde{f}_{\rm n})\frac{\partial m_0}{\partial \xi} = 0. \quad (3.30)$$

The fluid velocity must be continuous across the surface of the planet, which gives the first boundary condition on the eigenfunction (cf. Equation 3.17)

$$\tilde{f}_{\rm n}(\xi = 1) = 1. \quad (3.31)$$

We also demand that the solutions for the eigenmodes be non-trivial and expandable about the surface; taking the leading-order terms in the series expansion of Equation (3.30) then shows that the derivative of $\tilde{f}_{\rm n}$ satisfies

$$\left.\frac{\partial \tilde{f}_{\rm n}}{\partial \xi}\right|_{\xi=1} = \frac{1}{\gamma}\left(\sigma_{\rm n}^2 + 2\left(\gamma - 2\right)\right). \quad (3.32)$$

Finally, the fluid velocity must be equal to zero at $\xi_{\rm c}$ owing to the incompressible nature of the core, which gives the additional boundary condition

$$\tilde{f}_{\rm n}(\xi_{\rm c}) = 0. \quad (3.33)$$

This third boundary condition determines the eigenvalues $\sigma_{\rm n}$, as we start with some initial guess for the eigenvalue, integrate equation (3.30) inward from a point near the surface ($\xi \simeq 1$) using boundary conditions (3.31) and (3.32) with this guess, and determine the value of $\tilde{f}_{\rm n}(\xi_{\rm c})$. We then perturb the guess for $\sigma_{\rm n}$, calculate the new function and the corresponding residual of $\tilde{f}_{\rm n}(\xi_{\rm c})$, and continue to iterate on the value of $\sigma_{\rm n}$ until we satisfy the third boundary condition $\tilde{f}_{\rm n}(\xi_{\rm c}) = 0$. The set of eigenvalues $\sigma_{\rm n}$ then delimit

$\gamma = 1.3$, $\xi_c = 0.05$			$\gamma = 1.3$, $\mu = 0.05$			$\mu = 0.05$, $\xi_c = 0.05$		
μ	K_0	σ_1^2	ξ_c	K_0	σ_1^2	γ	K_0	σ_1^2
0.1	0.202	-1.20	0.05	0.190	0.03	1.4	0.136	-1.93
0.3	0.238	-4.81	0.3	0.108	-4.80	1.33	0.168	-0.95
0.5	0.263	-5.86	0.5	0.0633	-6.48	1.25	0.246	3.11
0.7	0.282	-6.23	0.7	0.0303	-10.0	1.2	0.333	-8.89
0.9	0.298	-6.42	0.9	0.00683	-27.7	1.15	0.439	-40.9

Table 1: The square of the lowest-order eigenvalue σ_1^2 and the auxiliary variable K_0 for each of the configurations shown in Figure (7).

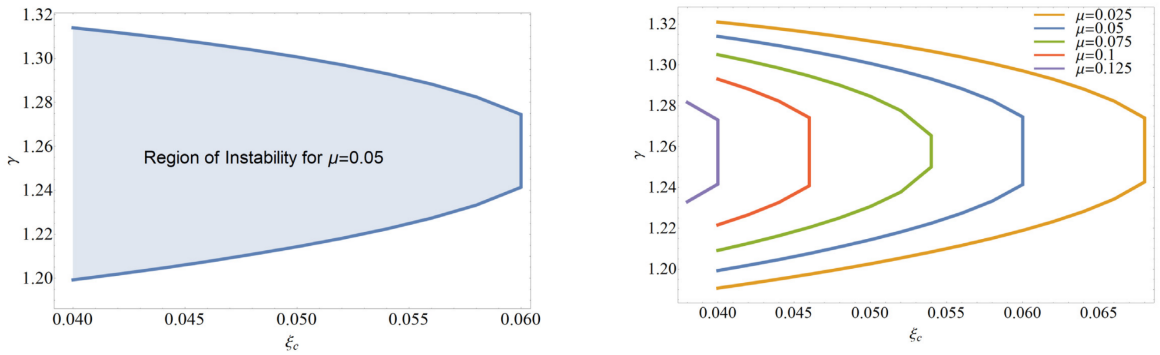

Figure 10: The curve that delimits where $\sigma_1^2 = 0$ in the $\gamma - \xi_c$ plane that separates the stable and unstable behavior. The left panel fixes $\mu = 0.05$ and the shaded region denotes where the solutions are unstable, while the right panel varies the core mass.

the solutions that satisfy the boundary conditions near the surface of the planet and at the inner core. Since Equation (3.30) is in the form of a Hermitian operator equation (e.g., [153]), the eigenvalue squares σ_n^2, are purely real, and the corresponding solutions vary as $\propto \exp(\sigma\tau)$. Thus, if $\sigma_n^2 < 0$, the solutions are stable and oscillate in time, whereas if $\sigma_n^2 > 0$ the envelope is unstable and small perturbations grow exponentially rapidly with time. The lowest-order mode $\tilde{f}_1$ has no zero crossings, and each higher-order mode has one more zero crossing than the previous one.

As for the hydrostatic solutions, we set the outer boundary (at which we evaluate the boundary conditions 3.31 and 3.32) at the location within the hydrostatic envelope at which the dimensionless, unperturbed density satisfies $g_0 = 10^{-8}$. We have verified that changing this small parameter by an order of magnitude (increasing or decreasing) has no effect on the eigenvalues or the eigenfunctions. To further mitigate any numerical errors, in practice in the eigenmode equation (3.30) we replace any derivatives of m_0 higher

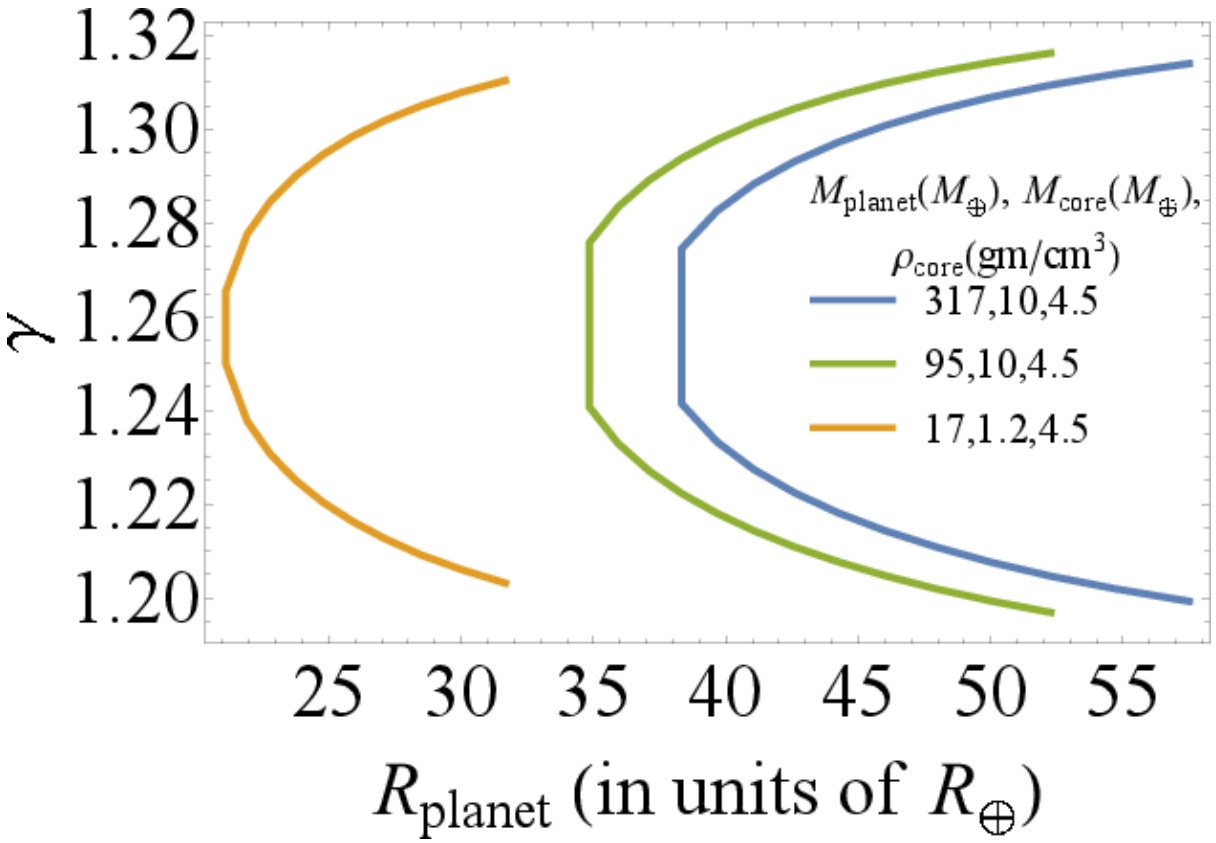

Figure 11: The $\sigma_1^2 = 0$ curve separating stable and unstable behavior. We have simulated three model planetary configurations having similar properties to the gas-giants in our solar system: Jupiter(Blue), Saturn(Green), Neptune(Orange). The model parameters are shown in legends.

than the first with the lower-order values that result from the equation of hydrostatic equilibrium (3.23).

3.2.2 Solutions

In Figure 8 we present the lowest-order eigenfunction for the hydrostatic solutions presented in Figure 7; the eigenvalues that characterize these solutions are given in Table 3 (along with other properties of the hydrostatic envelope). We see from this figure that, as the eigenvalue appropriate to the lowest-order mode becomes increasingly negative, the eigenfunction decreases more rapidly from the surface of the envelope (which can be seen directly from the boundary condition on the derivative of $\tilde{f}_{\rm n}$ in Equation 3.32). This feature is a familiar property of the p-modes of linearly stable stars (e.g., [153]), and illustrates that the majority of the power of these modes resides in the outer layers of the planetary envelope. Thus, a solution that is characterized by only very negative eigenvalues responds to a homologous initial velocity perturbation (i.e., such that the initial velocity profile is $\propto \xi$) by oscillating violently and stochastically – albeit stably and sinusoidally in time – in its outermost extremities (see the end of Section 3.1 of [150] for further discussion).

On the other hand, as the lowest-order eigenvalue becomes less negative, the eigenfunction is better approximated by a linear function of ξ that extends from the core to the planet radius. Indeed, if $\gamma = 4/3$ and the inner boundary extends to the origin, then an exact solution to Equation (3.30) and the boundary conditions (3.31)–(3.33) is $\tilde{f}_n = \xi$ with $\sigma_n^2 = 0$, which is just the familiar Chandrasekhar limit. Thus, a linear initial velocity perturbation for this specific case retains its linear profile, and the entire envelope expands or contracts homologously with time. As the square of the eigenvalue becomes positive, the leading-order eigenfunction attains a relative maximum in the interior of the envelope. This feature illustrates that a contraction of the envelope results in the acceleration of the fluid in the interior of the planet, which increases the gravitational potential and further accelerates contraction, resulting in a runaway collapse of the gas that proceeds exponentially rapidly with time. In the opposite scenario of an initial expansion, the very slow decline of the pressure results in the outward acceleration of the envelope.

3.2.3 Region of Instability

It is clear from Figure 8 and Table 3 that, in addition to the singular case of the Chandrasekhar instability where $\sigma^2 = 0$ for $\xi_{\rm c} = \mu = 0$ and $\gamma = 4/3$, there is a region of parameter space within which the leading-order eigenvalue is positive and the envelope

is dynamically unstable to radial perturbations. Qualitatively we expect that as the adiabatic index softens, the envelope should become more susceptible to instability, as the increase in the gas pressure is less pronounced (and less able to resist the increase in self-gravity) for an initial, radial contraction; an analogous argument for the existence of the instability exploits the less rapid decline in the pressure for an initial expansion of the envelope. Eventually, for a fixed core mass and radius, we expect this Chandrasekhar-like instability to arise once the adiabatic index crosses a sufficiently small, threshold value. To support this prediction, Figure 9 shows the square of the leading-order eigenvalue as a function of γ for a fixed core mass ($\mu = 0.05$ for the left panel and $\mu = 0.1$ for the right panel). Each curve in this figure is for a different value of the core radius ξ_c, with the core radii appropriate to each curve given in the legend. We observe from the left panel that as we go to smaller values of γ, the leading-order eigenvalue becomes less negative, and provided that the core radius satisfies $\xi_c \lesssim 0.06$, crosses $\sigma^2 = 0$ and the envelope becomes unstable. This zero crossing represents the generalization of the Chandrasekhar limit to a envelope that possesses a core (modeled as incompressible) in its interior.

For finite (i.e., non-zero) ξ_c and μ, the γ at which the envelope transitions from stable to unstable in going from large to small γ is always less than $\gamma = 4/3$ (e.g., for $\xi_c = \mu = 0.05$, from Figure 9 the adiabatic index that separates stable and unstable envelopes is $\gamma \simeq 1.3$). This finding demonstrates that the effect of an incompressible core in the planetary interior is to *stabilize* the envelope against the Chandrasekhar-like instability. This stabilizing influence arises from the fact that, because it is incompressible, there is no change in the gravitational potential associated with the core when we impose a perturbation to the planet. Thus, the destabilizing increase in self-gravity is always lessened in comparison to a core-less envelope, implying that the critical γ that yields an unstable envelope must be less than the one that characterizes an envelope without a solid core.

Interestingly, Figure 9 also shows that the leading-order eigenvalue does not increase monotonically as the adiabatic index decreases, and instead there is a *most unstable envelope* that is characterized by a largest σ_1^2. As γ continues to decrease below this most-unstable value, the square of the eigenvalue starts to decline, and crosses below zero to yield *stable solutions* once γ is sufficiently small. Moreover, for values of the core radius that are large enough, the envelope *never becomes unstable*, even for very small values of γ, which disagrees with our naive expectation that sufficiently small adiabatic indices should give rise to an unstable envelope.

This behavior arises because as γ decreases, all of the mass of the envelope becomes increasingly concentrated near the core, as can be seen from the right-most panel of Figure 7. However, since the fluid cannot penetrate the planetary core, any perturbation

to such an envelope cannot result in a large change in the distribution of its mass and its corresponding gravitational potential (i.e., the eigenfunction satisfies $\tilde{f}_1(\xi_c) = 0$, hence the vast majority of the mass is not displaced when acted upon by any perturbation, and the resulting change in the gravitational potential – proportional to the change in the mass *interior to radius* r – is likewise small). Therefore, for sufficiently small γ, the envelope can effectively be considered a non-self-gravitating fluid with the entirety of the planetary mass located at the edge of the core; since the change in the self-gravity of this configuration must be effectively zero for any physical perturbation that does not displace the core, such an envelope cannot exhibit any Chandrasekhar-like instability.

The shaded region in the left-hand panel of Figure 10 shows the range of adiabatic indices within which the envelope is unstable as a function of the inner radius ξ_c when $\mu = 0.05$, and the curve that encloses this region delimits the combination of γ and ξ_c – for a fixed μ – at which the eigenvalue crosses the $\sigma_1^2 = 0$ instability threshold. As the inner radius decreases, a larger range of adiabatic indices is unstable. The right-hand panel of this figure shows a set of such curves (within each of which the envelope is unstable) for a range of core masses. As the core mass increases, the envelope becomes stable to a larger range of inner radii, which arises from the fact that the perturbation to the self-gravity of the planet declines as more of the planetary mass is contributed by the incompressible core. To show our results in explicit astrophysical units, we map out the instability region in Figure 11 for planetary parameters (the parameters shown in legends) similar to those appropriate to the gas giants in our solar system.

3.2.4 Non-radial perturbations

We consider the analysis of non-radial perturbations to be beyond the scope of this work, but it may be useful to outline some of the considerations. To study angular perturbations with rigor, one can treat the solutions we obtained due to radial perturbations as the radial component of a total solution of the form $f(\xi, \theta, \phi, \tau) = f_r(\xi) Y_\ell^m(\theta, \phi) \exp(\sigma\tau)$ [150], where $Y_\ell^m(\theta, \phi)(\ell = 0, 1, 2, ...; m = -\ell, -\ell + 1, ..., \ell - 1, \ell)$ is a spherical harmonic; the angular dependence of non-radial velocities can be written as derivatives of spherical harmonics (e.g., [154, 153]). In general, the surfaces will neither move uniformly nor oscillate in and out regularly because the displacement of a typical mass element from its unperturbed state is not radial. Thus, the motion can be complicated, for example, some regions of the surface expanding and some other region contracting at the same instant of time. In non-radial oscillations gravity is also a restoring force, implying that the spectrum will have both gravity (g-mode) and pressure (p-mode) eigenmodes (unless the envelope is modeled as a pure polytrope, in which case the vanishing of the entropy gradient removes the presence of g-modes). The detail of these considerations demand

separate study and will be analyzed in future works. We also ignored the gravitational presence of the host star here, and hence the tidal force – which will contribute an $\ell = 2$ perturbation to the envelope – was not accounted for in our analysis.

3.3 Summary and Implications

The formation of giant planets generically involves regions where hydrogen becomes dissociated and then ionized, leading to a reduction in the average adiabatic index of the envelope. In this work, we analyzed the stability (to radial perturbations) of hydrostatic solutions for a class of models, composed of an incompressible core and a polytropic envelope, that capture to leading-order how a reduced γ affects planetary stability. We demonstrated that the presence of a core within a planetary interior supplies a net stabilizing effect, relative to the usual Chandresekhar criterion of $\gamma = 4/3$ that is calculated for polytropic gaseous spheres with no central mass. The stabilizing effect of the incompressible solid core is due to the fact that the core-occupied region does not contribute to the self-gravity variations, while the pressure remains approximately the same compared to the core-less configuration. Stability depends upon the core-to-total-planet mass ratio μ, the core radius relative to the planetary radius $\xi_c = r_c/R$, and the adiabatic index γ. As shown in Figure 10, depending upon the values of these parameters the core can either fully stabilize the envelope, or lead to a strip of unstable γ values whose upper boundary lies below the classical value of $\gamma = 4/3$.

Our model considers a single, effective adiabatic index for the entire envelope, though the motivating physics for treating small values of the adiabatic index – partial ionization and dissociation – implies that should, more physically, change as a function of radius and time. A radially varying adiabatic index implies that the background state is no longer polytropic, and buoyancy terms will modify the eigenvalues. In Section 3.4 we derive the eigenvalue equation that accounts for the effects of a time-dependent (perturbed) adiabatic index, and demonstrate that such effects can be quite important in determining the stability of a planetary envelope. We have also adopted inner boundary conditions for the envelope that correspond to a strictly incompressible core. In reality, rocky cores are compressible (e.g., [155]) and may not have a sharp boundary [156, 157], and this finite compressibility becomes increasingly important as the majority of the gas piles up near the core surface (as occurs for the small-γ solutions and that eventually inhibits the formation of the Chandrasekhar-like instability). When the core is compressible, its stabilizing influence on the envelope lessens, as more mass is able to penetrate deeper into the interior of the planet and increase the perturbation to self-gravity (which is ultimately responsible for generating the instability). At the outer envelope boundary,

we have ignored any effects that the ambient disc gas might have on either the stability of the envelope to radial perturbations, or to the generation of Kelvin-Helmholtz-like interface instabilities alongside the Chandrasekhar-like instability analyzed here.

The possibility of dynamical instability in the envelope of planets that form via core accretion is distinct from the existence of a maximum (or "critical") core mass within that theory. Generically, in core accretion, solutions to the planetary structure exhibit a maximum in a plot of core mass versus total mass [122, 41, 124, 127, 158]. This class of solution is derived by matching the interior structure to background disc conditions at the Bondi or Hill radius, in contrast to the zero-pressure outer boundary conditions considered here. [158] included detailed structure calculations (with energy transport by both radiation and mixing length theory convection), as well as a detailed disc model to specify how planet envelope conditions vary with disc radius. They noted that the core instability – which occurs in steady state calculations – would not directly cause dynamical collapse, but would instead give an enhanced rate of cooling and Kelvin-Helmholtz contraction, as in the time-dependent structure calculations of [126] and as noted in the introduction. Simpler adiabatic models of the "core accretion instability" show that it does depend on the adiabatic index e.g.[159], but there is no straightforward reason to expect that the two types of instability would show similar trends or thresholds in γ.

The outcome of a Chandrasekhar-like dynamical instability, were it to occur in a forming giant planet, cannot be addressed in linear theory. It appears likely, however, that any nascent collapse would change the interior density and temperature sufficiently as to restore a stable value of γ. As a consequence, we expect the maximum degree of radial compression of the envelope to be bounded, and gas that initially collapses will rebound and exhibit a large-scale oscillation. In principle, this could lead to the formation of an outward-propagating shock wave at some depth in the interior of the planetary envelope. Depending on its strength, this shock could then eject a fraction of the planetary envelope. Alternatively, the planet could exhibit "breathing modes," or large-amplitude oscillations, formed analogously to the oscillations of classical Cepheids [148].

Our model does not include the accretion of material onto the core or the gaseous envelope. Accounting for the accretion of mass onto the core, and the corresponding loss of mass from the envelope, could be relatively simply accomplished by changing the inner boundary condition from $f_1(\xi_c) = 0$ to some non-zero value. The change in the envelope mass then comes out of the continuity equation self-consistently by integrating from ξ_c to ξ and imposing a non-zero $f_1(\xi_c)$, and there would then be an additional perturbation that arises from the time-dependent mass of the core (which arises from the finite flux at

the core radius) that appears in the momentum equation. This change in the boundary condition would likely serve to further stabilize the envelope, as self-gravitating mass is lost to the core, the time dependence of which serves as a source term in the equations (and hence doesn't affect the eigenvalues). Alternatively, one could simply impose a time-dependent core mass and neglect the complicating issue of self-consistently accounting for the flux from the envelope. In this case the eigenvalues are unaltered as the time-dependent core mass is just a source term in the equations.

Allowing for accretion onto the planet from the surrounding disc is not as straightforward because our hydrostatic solutions terminate at a radius where the density is zero. To maintain a finite mass flux at the surface would therefore require an infinite velocity there, which, in addition to being obviously non-physical, cannot be done self-consistently in our model where the velocity is considered a perturbation. One would therefore need to change the background solution such that either the gaseuos envelope extends out indefinitely, or that the envelope terminates at a location with finite density and that is not a contact discontinuity (to permit accretion). A natural way to do the latter would be to join the envelope onto an accretion shock, meaning that the hydrostatic nature of the envelope would only be approximate[2]. Doing the former could be possible if the adiabatic index is small enough (e.g., $\gamma = 1.2$ in the core-less case leads to an envelope of infinite radius), though the eigenvalues describing the perturbations to such a system would be continuous, further complicating the analysis. In either case the problem differs substantially from the one considered here, and the eigenvalues would likewise be quite different. For example, a non-zero initial velocity gradient in the unperturbed solution leads to complex eigenvalues because the operator equation is no longer Hermitian (e.g., [160]).

Our stability maps – or more refined versions of them that included some of the neglected effects discussed above – would need to be combined with planetary evolution models to fully assess whether dynamical instability occurs during giant planet formation. It is immediately obvious, however, that the formation of a Jupiter-like planet via a standard core accretion channel is rendered highly stable by the presence of its core. The diversity of proto-planetary interior structures that can be formed, whether by standard core accretion, its variants, or via gravitational instability, is broad. It remains possible that the evolutionary tracks of some giant proto-planets cross into the instability strip that we have defined, leading to potentially observable time-dependent dynamics.

[2]There is a time-steady, self-similar solution that does this and that has been studied in the context of neutron star accretion; see [30, 25].

3.4 Varying adiabatic index

When the adiabatic index of the fluid is non-uniform and variable in time, the entropy equation takes a slightly different form that incorporates derivatives of the adiabatic index. In particular, if we start with the gas-energy equation in spherical symmetry,

$$\frac{de}{dt} + (e+p)\,\frac{1}{r^2}\frac{\partial}{\partial r}\left[r^2 v\right] = 0, \tag{3.34}$$

where $d/dt = \partial/\partial t + v\partial/\partial r$ is the advective derivative, then using the continuity equation turns this into

$$\frac{de}{dt} - (e+p)\,\frac{d}{dt}\ln\rho = 0. \tag{3.35}$$

We now define

$$e = \frac{1}{\gamma - 1}p, \tag{3.36}$$

and let γ (the adiabatic index) vary with both space and time. Then the previous equation becomes, after some algebraic rearranging,

$$\frac{d}{dt}\ln\left[\frac{1}{\gamma-1}\frac{p}{\rho^\gamma}\right] + \ln\rho\frac{d\gamma}{dt} = 0. \tag{3.37}$$

We now introduce the non-dimensionalized density, pressure, and velocity as we did in Section 3.1.1 and we perturb the variables about a background, hydrostatic state. We also allow variation in the adiabatic index and therefore write

$$\gamma = \gamma_0(\xi) + \gamma_1(\xi,\tau), \tag{3.38}$$

Since the continuity and momentum equations are unaltered, the linearized versions of these equations are also unchanged from those found in Section 3.2 (specifically Equations 3.26 and 3.27). The linearized entropy equation is recovered by inserting our definitions for the velocity, density, and pressure into Equation (6.5), changing variables to τ and ξ, and maintaining first-order terms. The result is

$$\begin{aligned} \frac{\partial}{\partial\tau}\left[\frac{h_1}{h_0} - \frac{\gamma_0 g_1}{g_0}\right] + f\left(\frac{1}{h_0}\frac{\partial h_0}{\partial\xi} - \frac{\gamma_0}{g_0}\frac{\partial g_0}{\partial\xi} - g_0\frac{\partial\gamma_0}{\partial\xi}\right) \\ -(4-3\gamma_0)\,V = \left(\frac{1}{\gamma_0-1} - \ln g_0\right)\frac{\partial\gamma_1}{\partial\tau} + (f - V\xi)\frac{1}{\gamma_0-1}\frac{\partial\gamma_0}{\partial\xi}. \end{aligned} \tag{3.39}$$

We notice now the entropy equation is indeed modified accommodating the variability of the adiabatic index γ. The Equation 3.39 collapses into Equation (3.28) when the gradient of entropy vanishes.We can now take Laplace transformation of our perturbed equations and combine them into a single, second-order equation for $\tilde{f}_1$; upon dividing

by $\tilde{V}$ – the Laplace transform of the velocity of the surface relative to the escape speed – this equation for the eigenmodes is

$$\sigma_n^2 \tilde{f}_1 + \frac{1}{g_0^2 \xi^2} \frac{\partial h_0}{\partial \xi} (\gamma_0 - 1) \frac{\partial}{\partial \xi} \left((\xi - \tilde{f}_1) \frac{\partial m_0}{\partial \xi} \right) + \frac{h_0}{g_0} \frac{\partial}{\partial \xi} \left(\frac{\gamma_0}{g_0 \xi^2} (\xi - \tilde{f}_1) \frac{\partial m_0}{\partial \xi} \right) = - \frac{1 - \mu}{\xi^2} (\xi - \tilde{f}_1) \frac{\partial m_0}{\partial \xi} - \frac{1}{g_0} \frac{\partial}{\partial \xi} \left[\tilde{f}_1 \left(\frac{\partial \gamma_0}{\partial \xi} \left(\frac{1}{\gamma_0 - 1} + g_0 h_0 \right) - \left(\frac{\partial h_0}{\partial \xi} - \frac{\gamma_0 h_0}{g_0} \frac{\partial g_0}{\partial \xi} \right) \right) + h_0 \left(\sigma_n \left(\frac{1}{\gamma_0 - 1} - \ln g_0 \right) \frac{\tilde{\gamma}_1}{\tilde{V}} - \xi \frac{1}{\gamma_0 - 1} \frac{\partial \gamma_0}{\partial \xi} + (4 - 3\gamma_0) \right) \right] \quad (3.40)$$

Without an additional expression that relates the perturbation to the adiabatic index to the other fluid variables, which could, for example, come from a microphysical model, we cannot make further progress on Equation (3.40). However, in general we expect changes in the adiabatic index to be most sensitive to changes in the gas temperature; if we therefore assume that the fractional change in the adiabatic index, γ_1/γ_0, is proportional to the fractional change in the temperature, T_1/T_0, then we can use our definitions of the fluid quantities to construct an additional relationship among $\tilde{\gamma}_1$ and the Laplace-transformed (dimensionless) fluid variables. The result is that the eigenmode equation is no longer Hermitian, and hence the eigenvalue squares σ^2 are no longer (in general) purely real. Time-dependent changes in the adiabatic index of the fluid can therefore generate distinct instabilities in the planetary interior, as is derived (much) more rigorously in [154]. We also see that, in the area of interest here where γ_0 is close to one, the importance of time-dependent changes to the adiabatic index is amplified by the factor of $1/(\gamma_0 - 1)$ on the right-hand side of Equation (3.40). Changes to the adiabatic index can be quite important for understanding the generic stability of a giant-planet envelope.

Chapter 4

General relativistic settling solutions in the context of a core-collapse supernovae

At the end of the life of a massive star, where it has exhausted its supply of nuclear fuel, the core collapses $\sim$ dynamically under its own self-gravity. The process of inverse-β decay during the collapse removes electron pressure, further destabilizing the core and producing an abundance of neutrons; this de-leptonized, collapsing core is the proto-neutron star (PNS). The PNS "bounces" due to the nucleon-nucleon interaction potential (that is, the equation of state of the nuclear material stiffens) and launches an outward-propagating shock wave. The shock dissociates heavy nuclei as it propagates outward, loses energy, and eventually stalls under the ram pressure of the infalling envelope [161, 162, 163, 164, 165, 166].

Some mechanism revives the shock and yields the powerful and luminous explosion that is the supernova. This "supernova problem," being the stall and eventual revival (in successful explosions) of the shock wave launched by the bounce of the PNS, has eluded a conclusive theoretical explanation for decades. Two likely mechanisms for accelerating the stalled shock are the neutrino mechanism [164, 167, 168, 169, 170, 171] and the standing accretion shock instability [25, 26, 32, 172, 173]. The neutrino mechanism, first laid out in the 1960s [161, 174] and revived in the mid-1980s by works such as [164, 175], propose that some fraction of the neutrino flux radiated from the nascent neutron star is absorbed by the abundant free neutrons and protons in the post-shock layer; the energy and momentum deposited by the absorbed neutrinos then revives the stalled shock. The standing accretion shock instability arises from the fact that some of the large-angle (i.e., small spherical harmonic number ℓ), oscillatory modes of the accretion shock can be dynamically unstable, the instability drives the shock outward leading to an asymmetric

explosion [25]. Subsequent work (e.g., [176]) has shown that hydrodynamic instabilities can aid the neutrino mechanism if not independently capable of driving the explosion.

Independent of the mechanism responsible for reviving the shock, it has been found to stall in many numerical calculations. Newtonian solutions describing the velocity, density, and pressure of the post-shock gas were found by [177, 178, 30]. In these solutions, the gas "settles" and the velocity of the fluid approaches zero asymptotically close to the origin for sufficiently small values of the adiabatic index (see the left panel of Figure 15 below). [25] obtained these solutions in the adiabatic limit ([30] included the effects of cooling) and analyzed their response to angular perturbations. These solutions and the numerical work of [25] were in the Newtonian limit, and the gravitational field around the central compact object (PNS) was described as a Newtonian point mass.

However, for a neutron star with mass M ($\sim 1.4 M_\odot$) and radius R ($\sim$ 10 km), the gravitational radius is $GM/(Rc^2) \simeq 0.2$, and the free-fall speed of the shock radius at $R_{\rm sh} \simeq 100$ km is $\sqrt{2GM/R_{\rm sh}} \simeq 0.2\,c$. Relativistic effects therefore introduce order-unity corrections to the behavior of the gas within the shock and will non-trivially modify the Newtonian settling solutions. [179] expanded the classic work of [180] on spherically symmetric accretion by incorporating the effects of general relativity in the Schwarzschild metric (see also [181] who expanded [179]'s work to non adiabatic equations of state). Bondi accretion (and its relativistic generalization) does not account for the existence of a shock[1]. When the freely falling fluid passes through an existing strong shock, a substantial fraction of its kinetic energy is converted into internal energy – an effect that cannot be considered a small perturbation on top of a pure freefall solution. Subsequent work (e.g., [182, 183, 184, 185]) has also explored similar topics. However, the generalization of the [177], adiabatic settling solution through an existing standing shock to the Schwarzschild metric incorporating the appropriate jump conditions – for which there are exact solutions (as we show below) – does not appear to have been detailed in the literature (but see [186]).

Here, we present and analyze the relativistic generalization of adiabatic settling solutions for the post-standing accretion shock flow that were studied numerically in [25]. In Section 4.1.2 we describe the model and write down the fluid equations. The ambient fluid – assumed to be freely falling and effectively pressureless – is analyzed in Section 4.1.3, and we give the relativistic jump conditions in Section 4.1.4. Stationary solutions to the fluid equations that satisfy the relativistic jump conditions and are adiabatic are

[1] [181] briefly discuss the possibility of a shock transition in the critical flow, which is different from the flow through an existing shock. It is also worth noting that those same authors used special relativistic shock jump conditions, which are inconsistent with the Schwarzschild background (see Equations 4.12,4.13, and 4.14 below).

presented in Section 4.2, where we also discuss the variation of the solutions with the shock radius (effectively the ambient velocity at the location of the shock), the variation with the adiabatic index and the behavior of the flow near the horizon. We present the physical interpretation of these solutions in Section 4.3, discuss the implications of our findings, and identify directions for future work in Section 4.4.

4.1 Equations

4.1.1 Metric

We assume that there is a compact object (without spin) that dominates the gravitational field of the infalling fluid. With these assumptions, the metric describing the spacetime is given by the Schwarzschild metric:

$$\begin{aligned} ds^2 &= g_{\mu\nu} dx^\mu dx^\nu \\ &= -\left(1 - \frac{2M}{r}\right) dt^2 + \left(1 - \frac{2M}{r}\right)^{-1} dr^2 + r^2 d\Omega^2, \end{aligned} \tag{4.1}$$

where M is the mass of the compact object. We have adopted the Einstein summation convention (as we will throughout the remainder of the work) so that repeated upper and lower indices imply summation, and we have let $G = c = 1$.

4.1.2 Fluid Equations

We let the accreting gas – which has passed through the standing shock – be a relativistic perfect fluid with total energy e', pressure p' and rest-mass density ρ'. For simplicity, we assume that the gas is adiabatic, with $e' = p'/(\gamma - 1)$ and γ the adiabatic index. With U^μ the four-velocity of the fluid, the energy-momentum tensor is [187]

$$T^{\mu\nu} = \left(\rho' + \frac{\gamma}{\gamma - 1} p'\right) U^\mu U^\nu + p' g^{\mu\nu}. \tag{4.2}$$

Energy-momentum conservation is expressed as

$$\nabla_\mu T^{\mu\nu} = 0 \tag{4.3}$$

where ∇_μ is the covariant derivative. Conservation of mass (or particle number) is

$$\nabla_\mu [\rho' U^\mu] = 0, \tag{4.4}$$

and from Equation (4.1) we have the conservation of the norm of the four-velocity:

$$U_\mu U^\mu = -1. \tag{4.5}$$

It is useful to work with the time and space-like projections of Equation (4.3) [187, 160]. Taking the contraction of Equation (4.3) with U_ν yields

$$U^\mu \nabla_\mu e' = -(e' + p')\nabla_\mu U^\mu. \tag{4.6}$$

We now introduce the projection tensor $\Pi^\beta_\nu = U^\beta U_\nu + g^\beta_\nu$, which projects the components of Equation (4.3) onto the 3-space orthogonal to U^μ; contracting Equation (4.3) with the projection tensor then gives the momentum equations,

$$(e' + p')U^\mu \nabla_\mu U^\nu + \Pi^{\mu\nu}\nabla_\mu p' = 0. \tag{4.7}$$

One can also re-express the energy equation in the following convenient form using the continuity Equation (4.4),

$$U^\mu \nabla_\mu S' = 0, \tag{4.8}$$

where $S' = \ln(p'/\rho'^\gamma)$. This equation demonstrates that S', which we interpret as the entropy of the gas, is a conserved Lagrangian quantity in adiabatic regions of the flow. Since we assume that the flow is spherically symmetric and irrotational, there are only two components of the four-velocity that are related by Equation (4.5); we will refer to the radial component of the four-velocity by U.

4.1.3 Ambient Fluid

Pressure support is lost from the core, and a rarefaction wave travels through the overlying stellar envelope, which causes shells of material at successively larger radii to fall inward. If the density and pressure of the ambient medium fall off as power-laws with distance from the core, one can show that there exists a self-similar solution to the fluid equations that describes the propagation of the rarefaction wave and the fluid interior to the wave [188]; the wave travels at the local sound speed, and the gas pressure of the fluid interior to the wave is much lower than the ram pressure. Therefore, the infalling gas can be treated effectively as pressureless. We denote the four-velocity of the ambient fluid by $U_{\rm a} = (U^{\rm t}_{\rm a}, U_{\rm a}, 0, 0)$. The radial momentum equation, Equation (4.7) gives

$$U_{\rm a}\frac{\partial U_{\rm a}}{\partial r} = -\frac{M}{r^2} \tag{4.9}$$

Integrating the above equation and assuming that the gas is weakly bound, so the binding energy is ~ 0, then gives

$$U_{\rm a} = -\sqrt{\frac{2M}{r}}. \tag{4.10}$$

The time-steady solution to the continuity equation (4.4) is then

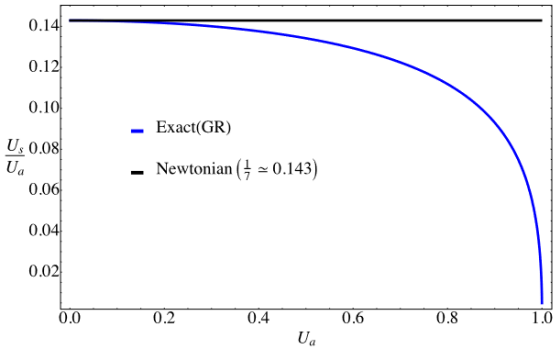

Figure 12: The ratio between the post-shock fluid velocity to the ambient fluid velocity ($U_{\rm s}/U_{\rm a}$) at the location of the shock as a function of the ambient fluid velocity, $U_{\rm a}$, in both the Newtonian and General Relativistic settings for $\gamma = 4/3$. Note that $U_{\rm a}$ is the freefall speed at the shock normalized by the speed of light, and hence the relativistic solution approaches the non-relativistic one when $U_{\rm a} \ll 1$; in the Newtonian limit, the entire problem is self-similar and $U_{\rm a}$ can be set to one without loss of generality.

$$\rho'_{\rm a} = \bar{\rho}_{\rm a} \left(\frac{r}{R}\right)^{-3/2}, \tag{4.11}$$

where R is the shock radius and $\bar{\rho}_{\rm a}$ is the density of the ambient gas at $r = R + \epsilon$ in the limit that $\epsilon \rightarrow 0$.

4.1.4 Jump Conditions

In the adiabatic limit the energy, mass, and momentum fluxes must be conserved across the shock, which give the strong-shock jump conditions – assuming the ambient gas pressure is negligible – in the lab frame (which equals the rest frame of the shock by assumption):

$$\rho'_{\rm s} U_{\rm s} = \rho'_{\rm a} U_{\rm a}, \tag{4.12}$$

$$\left(\rho'_{\rm s} + \frac{\gamma}{\gamma - 1} p'_{\rm s}\right) U_{\rm s} \sqrt{1 - (U_{\rm a})^2 + (U_{\rm s})^2} = \rho'_{\rm a} U_{\rm a} \tag{4.13}$$

$$\left(\rho'_{\rm s} + \frac{\gamma}{\gamma - 1} p'_{\rm s}\right) (U_{\rm s})^2 + (1 - (U_{\rm a})^2) p'_{\rm s} = \rho'_{\rm a} U_{\rm a}^2 \tag{4.14}$$

The subscript "s" indicates that these are the properties of the post-shock fluid at the shock radius.

Equations (4.12), (4.13) and (4.14) can be combined into the following cubic [2] to be

[2] This equation reduces to the special relativistic jump conditions obtained in [160] (Equation 23 therein with $U_2^{''} = U_{\rm s}$ and $U_a^{''} = U_{\rm a}$).

solved for U_s:

$$\begin{aligned}\gamma^2 U_s^3 + (2U_a\gamma - U_a\gamma^2)U_s^2 + \left(-1 + U_a^2 + \gamma^2 - U_a^2\gamma^2\right) \\ + \left((1 - U_a^2)U_a + 2U_a\gamma - 2U_a^3\gamma - U_a\gamma^2 + \gamma^2\right) = 0.\end{aligned} \tag{4.15}$$

Figure 12 shows the ratio U_s/U_a resulting from Equation (4.15) as a function of the ambient four-velocity. We see that the ratio is nearly equal to its Newtonian value (~ 0.14) for $U_a \lesssim 0.2$, but as the ambient velocity becomes more relativistic, the ratio deviates significantly from the Newtonian value.

4.1.5 Bernoulli, mass, and entropy conservation equations

Combining Equations (4.4) and (4.6) yields the conservation of the radial energy flux,

$$\left(1 + \frac{\gamma}{\gamma - 1}\frac{p'}{\rho'}\right)^2 \left(1 - \frac{2M}{r} + U^2\right) = \dot{E} \tag{4.16}$$

We use the continuity Equation (4.4) to express the density of the post-shock fluid in terms of the four-velocity as

$$r^2\rho' U = \dot{M}, \tag{4.17}$$

while entropy conservation gives

$$p' = K(\rho')^\gamma. \tag{4.18}$$

With these results, we can write Equation (4.16) as

$$\left(1 + \frac{\gamma}{\gamma - 1}K\left(\frac{\dot{M}}{r^2 U}\right)^{\gamma-1}\right)^2 \left(1 - \frac{2M}{r} + U^2\right) = \dot{E}. \tag{4.19}$$

Equation (4.19) is the relativistic generalization of the Bernoulli equation, to which it manifestly reduces in the limit that the velocity is small (see Equation 4 in [25]).

4.2 General Relativistic Accreting Solutions

4.2.1 Impact of varying the ambient fluid velocity

Here, we discuss the effects of varying the velocity of the ambient fluid, U_a, while keeping γ fixed at 4/3. Given the fluid velocity U_a, we can calculate the entropy $K = p'/(\rho')^{4/3}$, the radial energy flux $\dot{E}$ and the radial mass flux $\dot{M}$ by using the jump conditions and we can then solve Equation (4.19) numerically for the post-shock fluid velocity $U(r)$. We can then calculate the fluid three-velocity as seen by an observer who is stationary with

respect to the compact object and who employs locally flat coordinates (this coordinate frame will be represented with 'hats') as

$$v^{\hat{r}} = \frac{U^{\hat{r}}}{U^{\hat{t}}} = \frac{U}{U^t}\frac{1}{1-2M/r} = \frac{U}{(1-2M/r+U^2)^{1/2}}, \tag{4.20}$$

where in the last equality we used Equation (4.5). For a neutron star of mass $3\,\mathrm{M}_\odot$ and radius[3] 10 km, the solutions for the post-shock fluid four-velocity, three-velocity, density and pressure are presented respectively in the top-left, top-right, bottom-left and bottom-right panels in Figure 13; the ambient four-velocity – which implicitly establishes the physical location of the shock since the mass of the neutron star is set – for each curve is shown in the legend. In Figure 13, the radial coordinate is in km, while in Figure 14 it is normalized by the shock radius. In Figure 13, the location of the neutron star surface is shown with a black dashed line, and the location of the shock, appropriate to the specific ambient velocity, is shown by the respective colored dashed line. In Figure 14 we show the three-velocity as a function of r/R, in which case the shock is always at $r/R = 1$, represented by a black dashed line, while the neutron star surface now takes different r/R values and is shown with colored dashed lines. Figure 14 demonstrates that the relativistic solutions are not self-similar – each curve displays qualitatively different behavior as a function of the ambient velocity, whereas the Newtonian limit (shown by the black curve) is independent of this quantity once it is scaled out of the solution. Both of these figures show that the relativistic solutions approximately equal the Newtonian solution in the limit that the ambient speed is non-relativistic, which is not surprising. However, substantial deviations arise when the ambient speed reaches substantial fractions of the speed of light, and this is especially true deep in the interior of the flow where relativistic gravity is yet more important.

4.2.2 Impact of varying the adiabatic index

In addition to the magnitude of the infall velocity (relative to the speed of light), the solutions for the post-shock fluid variables depend on the adiabatic index of the gas. The $\gamma = 4/3$ adiabatic fluid is likely a reasonable approximation of the radiation-pressure dominated post-shock fluid accreting onto a neutron star [178, 30] over the expected temperature and density ranges [191]. Although in our model we neglected non-ideal effects (e.g., neutrino cooling), these can be roughly captured by using a softer equation

[3] We use 10 km for the neutron star radius for concreteness and simplicity, though [189] and [190] find that causality arguments require that the neutron star radius satisfy $R \gtrsim 2.823GM/c^2$, which is closer to 12.5 km for $M = 3M_\odot$. If we used 12.5 km, the maximum speed able to be achieved by the infalling fluid – obtained when the shock radius is comparable to the neutron star radius – would be $\sim 84\%$ c instead of $\sim 90\%$ c, as shown in Figure 13.

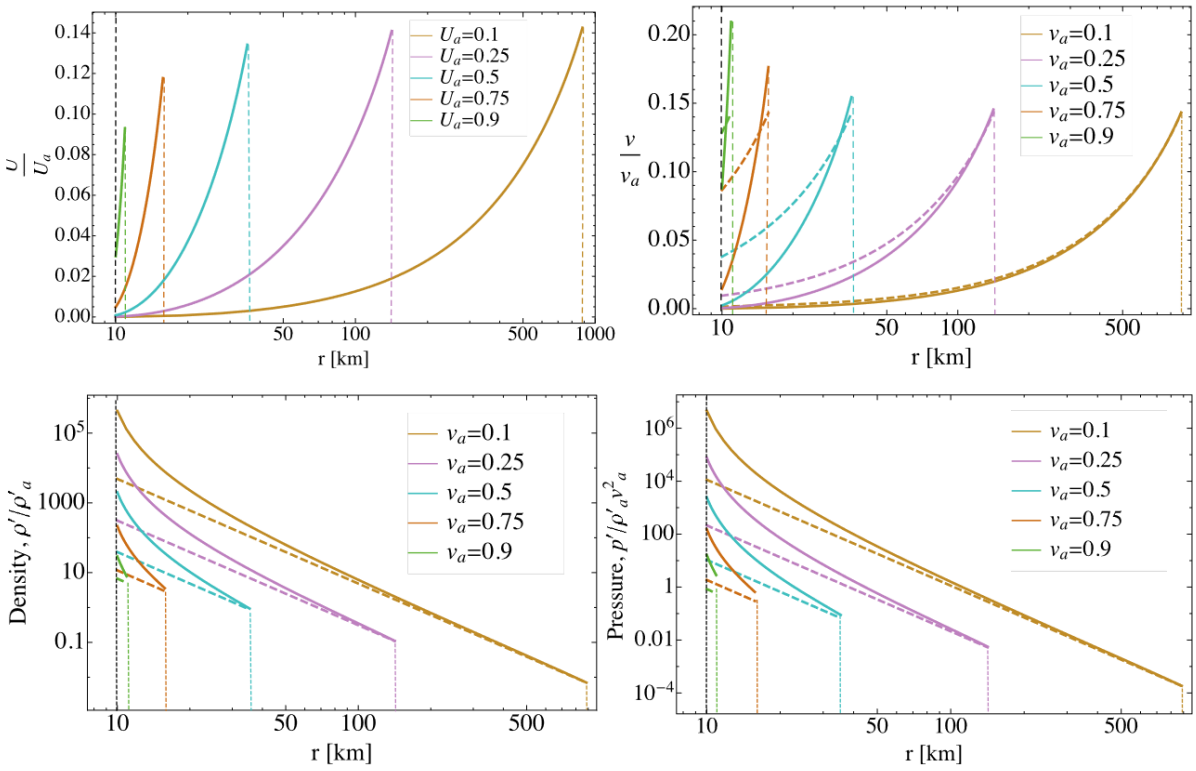

Figure 13: The normalized fluid velocity (the radial component of four-velocity in the top-left and the three-velocity as seen by local static observer in the top-right), comoving density (bottom-left), and comoving pressure (bottom-right) for the ambient speeds (at the location of the shock) shown in the legends as functions of radius (in km). Here we set the neutron star mass to be $3\,M_\odot$ to convert to physical units. The black dashed line indicates the surface of the neutron star whereas the colored dashed lines indicate the location of the stalled shock appropriate to the respective ambient velocity. Newtonian limits are given by the dashed curves in each panel.

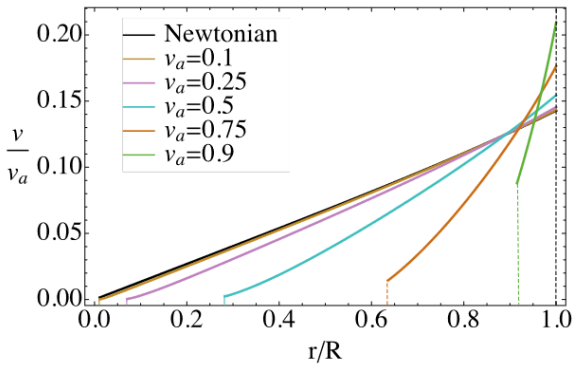

Figure 14: The normalized three-velocity as seen by a static and locally flat observer for the ambient speeds (at the location of the shock) shown in the legend as functions of normalized radial coordinate by the shock radius (r/R); the black dashed line at $r/R = 1$ indicates the fixed location of the shock in this coordinate and the colored dashed lines indicate the location of the neutron star surface, assumed to be at 10 km. The Newtonian solution, which is self-similar (i.e., it does not depend on $v_{\rm a}$), is shown by the solid black curve.

of state, i.e., reducing the value of the adiabatic index. While it is difficult to see how they are physically relevant, we also analyze the $\gamma = 5/3$ monoatomic ideal gas and one or two cases with even higher adiabatic indices, primarily to compare with [25].

The left panel of Figure 15 illustrates the absolute value of the velocity as a function of distance behind the shock in the Newtonian limit for the adiabatic indices in the legend. The solid curves show the solution to the Bernoulli equation in the non-relativistic limit (i.e., Equation 4.19 when the rest-mass energy far outweighs the internal energy and $GM/(rc^2) \ll 1$; see also Equation 4 in [25]), while the dashed curves give the asymptotic scaling near the origin[4]

$$\frac{U}{U_{\rm a}} = \left(\frac{4\gamma}{\gamma^2-1}\left(\frac{\gamma-1}{\gamma+1}\right)^{\gamma}\right)^{\frac{1}{\gamma-1}} \left(\frac{r}{R}\right)^{\frac{1}{\gamma-1}-2}. \tag{4.21}$$

This scaling can be derived from Equation (4.19) in the Newtonian limit and assuming that the internal energy far outweighs the kinetic energy near the origin, which is a valid assumption when $\gamma < 5/3$.

Equation (4.21) also shows, and the left panel of Figure 15 verifies that the velocity declines in absolute magnitude as one approaches the origin for $\gamma < 1.5$, while the gas accelerates (in terms of the magnitude of the velocity) for $\gamma > 1.5$; we believe that the value of $\gamma_{\rm c} = 1.522$ quoted in [25] that differentiates between these two limits is in error

[4]We have arbitrarily scaled the analytic, asymptotic solutions by a factor of 0.9 so that they can be distinguished from the exact solutions in this figure.

– it is only for $\gamma \equiv 1.5$ that the velocity approaches a finite value (i.e., neither zero nor infinite) near the origin. For $\gamma = 5/3$ the velocity satisfies $U/U_{\rm a} = 0.25(r/R)^{-1/2}$ and scales exactly with the freefall speed, as also found in [25]. For $\gamma > 5/3$, Equation (4.21) predicts that the fluid speed increases in a manner that exceeds the freefall scaling as the gas approaches the origin. However, this is not consistent with the assumption that the kinetic energy remains sub-dominant to the thermal energy, upon which the assumption Equation (4.21) is based. Instead, the blue curve in the left panel of Figure 15 demonstrates that this super-freefall acceleration is only maintained for a finite distance beneath the shock, and that the solutions terminate at a sonic point (i.e., the derivative of the velocity diverges at radius of $r/R \simeq 0.14$ for $\gamma = 1.75$, and solutions do not exist for radii smaller than this value). While this behavior is interesting from an academic standpoint, it is difficult to see how such stiff equations of state could be realized in nature, and hence we do not consider these solutions further here.

In the right panel of Figure 15, we present the solution to the relativistic Bernoulli equation (Equation 4.19) by solid curves, where the adiabatic index appropriate to each curve is given in the legend. We set the ambient fluid velocity to $0.2c$ for all solutions as a fiducial value. The dashed curves represent the corresponding Newtonian solutions. We see that the fluid "settles" at the event horizon, instead of conforming (approximately) to power-laws near the origin, as is the case in the Newtonian approximation. The Newtonian solutions display qualitatively different behavior above and below $\gamma = 1.5$, as illustrated in the left panel of Figure 3, with the gas decelerating (accelerating) for $\gamma < 1.5$ ($\gamma > 1.5$); on the other hand, the relativistic solutions all decelerate and settle as we approach the horizon, even though they closely match the Newtonian solutions near the shock. The asymptotic scaling of these solutions near the horizon is presented in the next subsection.

4.2.3 Asymptotic behavior of the general relativistic solutions near the horizon

The neutron star surface – where the fluid must physically stop – is always outside of the horizon, but it is instructive to discuss the extreme limit where the neutron star surface approaches the horizon. The fluid variables as measured by an observer in the comoving and locally flat frame either approach zero (velocity) or diverge (density and pressure) near the Schwarzschild radius, and it is straightforward to show from Equations (4.17), (6.5), and (4.19) that the rates at which they do so are

$$U \propto \left(1 - \frac{2M}{r}\right)^{\frac{1}{2(\gamma-1)}}, \tag{4.22}$$

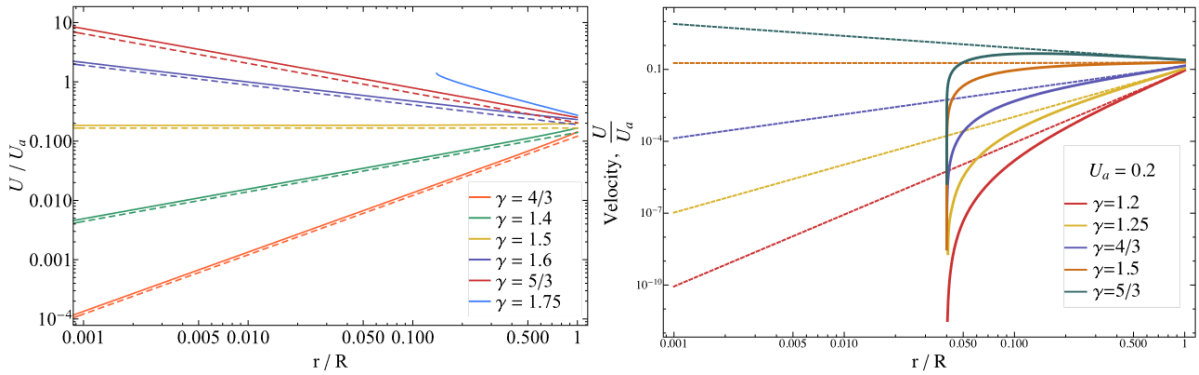

Figure 15: Left: The Newtonian solution for the fluid velocity as a function of radius normalized by the shock radius for the adiabatic indices in the legend; the solid curves show the numerical solution from the Bernoulli equation in the Newtonian limit, while the dashed curves give the analytic, asymptotic scalings, arbitrarily offset by a factor of 0.9 so that they can be differentiated from the exact solutions when $r/R \ll 1$. Right: The fluid velocity derived from the relativistic Bernoulli equation (solid curves) and the Newtonian Bernoulli equation (dashed curves) for an ambient velocity of $U_{\rm a} = 0.2$ and the adiabatic indices in the legend. The two solutions agree well near the shock front but disagree strongly near the horizon, which occurs at $r/R = 0.04$ in this case.

$$\rho' \propto \left(1 - \frac{2M}{r}\right)^{-\frac{1}{2(\gamma-1)}}, \tag{4.23}$$

and

$$p' \propto \left(1 - \frac{2M}{r}\right)^{-\frac{\gamma}{2(\gamma-1)}}. \tag{4.24}$$

Thus, in the general relativistic solutions presented here, the fluid velocity "settles" as in the Newtonian regime. However, instead of settling near the origin, the fluid velocity approaches zero near the event horizon. Similarly, the density and pressure diverge at small radii, but instead of following $\rho \propto r^{-\frac{5-3\gamma}{\gamma-1}}$ and $p \propto r^{-\frac{(5-3\gamma)\gamma}{\gamma-1}}$ as they do in the non-relativistic regime, they diverge as simple (and smaller) powers of $1 - 2M/r$.

Due to the presence of the strong shock, the fluid loses most of of its kinetic energy (gains equivalent thermal energy) and hence inevitably comes to rest interior to the shock. As it approaches the horizon it sees an unbounded gravitational field and can therefore only decelerate by developing an infinite pressure gradient as the event horizon is approached. We turn to the implications of these findings in the next section and our corresponding physical interpretations.

4.3 Physical Interpretation

The settling solutions obtained by [177], [178] and [25] in the Newtonian limit possess the feature that the velocity settles, or approaches zero, near the origin, which coincides with the location of the compact object in the Newtonian point-mass limit. This feature seems to imply that the Newtonian settling solutions describe the accretion of material onto the surface of an object and that these solutions apply to an accreting neutron star during the initial, stalled phase of the bounce shock, or at later times when weakly bound material falls back from the expulsion of the envelope in a successful explosion (e.g., [178]). The pressure and density of the gas also rise dramatically near the origin in the Newtonian settling solutions, which suggests that the pressure of the gas as it is brought to a halt at the surface of the neutron star provides the force that decelerates the flow.

However, while the velocity of the Newtonian solution approaches zero near the origin, the *mass flux* remains finite, as it must by virtue of the time-steady nature of the accretion through the shock. Similarly, the energy flux is conserved throughout the domain, and is given by the kinetic energy flux across the shock. Both of these quantities must effectively vanish at the surface of the neutron star where the velocity is (again, effectively) zero and the density and pressure retain finite values. Thus, if the solutions here are to describe accretion onto a neutron star (or any object with a "surface" at which the equation of state stiffens substantially), then the mass flux should not contribute substantially to the mass of the compact object, and there should be a mechanism for removing the incident energy flux. In core-collapse supernovae, both of these conditions are approximately upheld over the freefall time from the shock (i.e., conditions are roughly time-steady): the mass accumulated near the surface is small compared to the mass of the star, and neutrino losses from a very thin layer near the surface negate the incoming energy flux. Thus, the relativistic solutions here should apply to accretion onto a neutron star and become particularly relevant for scenarios in which the shock is pushed to small radii (see the additional discussion in Section 4.4 below).

In failed supernovae, the continued accretion onto the neutron star eventually pushes it over the TOV-limit, and the star collapses dynamically to a black hole [192, 193, 194, 169, 195, 196]. When the star collapses, an inward velocity must develop near the surface, and the pressure gradient must fall below the value necessary to retain hydrostatic balance. Thus, the solutions analyzed here cannot describe the entirety of the flow structure near the horizon when the black hole forms, which is also not expected because of the highly time-dependent nature of the interior of the flow as the core starts to collapse (i.e., the assumption of steady flow is clearly violated at this point). It is then possible that the shock is not supported by the reduced pressure in the interior and is correspondingly

swallowed by the black hole.

On the other hand, it seems possible that the adiabatic increase in the pressure of the gas as it nears the horizon (as evidenced from Figure 13 above) is sufficient to support the shock for at least a finite time, even though the divergence of the pressure is not physical (the true location of the horizon must increase to accommodate the large increase in the density predicted by our solutions, which would result in non-divergent values of fluid variables at the horizon). One could analyze the effects of imposing a more negative velocity at an inner radius (mimicking the effects of a true horizon) on the flow by using linear perturbation analysis [197], similar to what was done in [25] (though they used a smaller velocity, which caused the outward motion of the shock). The fading mass supply from the overlying envelope as less-dense regions of the progenitor are swallowed also implies that the ram pressure should be less capable of stifling the shock, which could allow the shock to remain quasi-stationary even in the absence of the strong pressure gradient in the interior that is predicted by the solutions here.

For these solutions to arise physically (i.e., in a setting in which the assumptions made here are relaxed), a steady-state must be reached by the flow. In general, this will take on the order of a sound-crossing time from the shock, which for a shock radius of $R = 150$ km and neutron star mass of $M = 2M_{\odot}$ is $\sim R^{3/2}/\sqrt{GM} \sim 3.5$ ms. If the neutron star collapses to a black hole on a timescale that is shorter than this, then these solutions will not be realized and the flow will be better approximated by pure freefall (e.g., Figure 7 of [196]).

4.4 Summary

In this work we analyzed the adiabatic accretion of gas through a stalled shock by modeling the gravitational presence of the compact body with the Schwarzschild geometry. The strong-gravitational effects (i.e., the inclusion of general relativity) is especially important in the case of weak or failed supernovae, where the shock wave launched by the bounce of the proto-neutron star could stall at much smaller, more relativistic radii, and during which a black hole forms. The black hole can continue to accrete at least as long as there remains supply from the host star, and we suggest that the solutions outlined here should also apply in this phase, i.e., while the black hole accretes through the stalled shock.

For a neutron star mass of $1.4M_{\odot}$ and a shock radius of 100 km, the freefall speed at the shock satisfies $\frac{v}{c} \sim 0.2$ and the differences between the relativistic and Newtonian solutions are at the level of $\sim$ 10 % (see the red curves in Figure 2). However, for failed supernovae (in which the shock is not revived), the shock can be pushed to smaller

radii and the mass of the neutron star increases to near the TOV limit (maximum mass limit for neuron stars $\lesssim 3M_\odot$ for most equations of state). For example, [194] find that the shock can stall at radii as small as 20 km; with a neutron star mass of $3M_\odot$, the freefall speed at this radius satisfies $\frac{v}{c} \simeq 0.66$, and relativistic effects become much more important (see the green and orange curves in Figure 2). Once the star exceeds the TOV limit, the mass increases to even larger values, while the shock can be compressed to even smaller radii, which necessitates the usage of our solution over the Newtonian one.

Relativistic effects will change the stability criteria and the corresponding growth of the standing accretion shock instability (SASI) (e.g., [25, 27, 198, 199]), and these effects can be important because the growth rate of the SASI has been found to be small (i.e., the e-folding time of the instability is many freefall times). For example, [32] find from their one- and two-dimensional simulations that the growth rate of SASI is between $\sim (0.1 - 0.22)$ in units of the freefall time (i.e., the instability grows as $\sim e^{(0.1-0.22)\tau}$, where τ is time relative to the freefall time; see their Figure 2). Their results agree well with those obtained analytically by [30]. [27] and [200] too find similar, small growth rates. Small changes in the background state can therefore change the stability of the system, and the solutions here present one such instance in which small changes arise from physical (relativistic) considerations.

Our solutions also have implications for gravitational wave signals from core-collapse supernovae. For example, [2] discuss the possibility that material that falls through the shock can impact the nascent neutron star and generate detectable gravitational wave signatures. Relativistic effects will modify the properties of the fluid as it rains down onto the neutron star surface, which could lead to pronounced differences in the gravitational wave signal owing to the fact that the neutron star radius is only marginally greater than the Schwarzschild radius.

In this work we assumed spherically symmetric, irrotational flow. If the progenitor does not contain a large reservoir of bulk angular momentum (which is likely, because stellar winds will carry away a substantial amount of angular momentum over the lifetime of the star), then angular momentum is important during the late stages of infall; this is because it is only in the outer envelope of the progenitor where random, convective motions can yield a specific angular momentum that exceeds the innermost stable circular oribit (ISCO) value [201]. If the progenitor does have significant net angular momentum, the gas can circularize outside of the ISCO and rotation can be dynamically important. The disc-like structure that forms in this case is likely optically and geometrically thick owing to the extremely high accretion rates, and we can integrate the equations over the scale height of the disc to obtain height-averaged Euler equations. The resulting disc solutions would be analogous to the advection-dominated accretion flow solutions of

[202] and the adiabatic inflow-outflow solutions of [203], but with the added constraint of satisfying the boundary conditions at a shock. We defer further investigation of this possibility to future work.

We assumed that the post-shock fluid is adiabatic and that the time-steady nature of the flow then ensures that the gas is isentropic. The gas is expected to be nearly isentropic because the fluid in the gain region is convectively unstable [175, 204, 205]. [178] justifies the adiabatic assumption by noting that neutrino losses become important in a very thin layer near the surface of the accreting body, and thus the post-shock flow is effectively adiabatic over most of its volume. [206] notes the neutrino cooling is not likely to result in a significant entropy gradient across the flow in the post-shock region. Furthermore, in his $3D$ simulations, he finds that mixing at the onset of convection and SASI largely reduce any entropy gradient. Nevertheless, some simulations in lower dimensions ($2D$) do find a more substantial entropy gradient, e.g., [207]. Interestingly, however, the numerical solutions of [207] appear to agree fairly well with the analytic solutions presented here. For example, in Figure 8 of [207], the density is shown to increase by ~ 6 orders of magnitude going from the location of the shock at ~ 200km to the origin, which agrees with what we find analytically (see the purple curve in the bottom left panel of Figure 13). The neutrino cooling in the thin layer acts effectively as a global sink on the energy, which balances the influx of energy from the material falling through the shock and allows the system to reach a steady state (i.e., the shock stalls). [178] also shows the ratio of thermal pressure to radiation pressure is

$$\frac{p_{\rm th}}{p_{\rm rad}} \approx 0.02 \left(\frac{\dot{M}}{M_\odot} \right)^{0.4} \tag{4.25}$$

for $\dot{M} = (0.01 - 100)\, M_\odot \text{ yr}^{-1}$ [191, 178] reinforcing the adiabatic claim further.

The time-steady nature of the solutions presented here requires specific ambient density and velocity profiles. More realistically, the mass infall rate will decline with time and the density profile of the accreting gas will change nontrivially as a consequence of the shells of nuclear ash in the progenitor star. The reduction in the mass supply rate and the ram pressure of the envelope then likely results in the outward motion of the stalled shock. We will analyze the consequences of a time-varying infall rate through a perturbative approach in future work.

Chapter 5

Asteroseismology on a proto-neutron star

Core-collapse supernovae are possible sources of gravitational-waves that could be detected by the proposed third-generation interferometric detectors, such as the Cosmic Explorer [208, 209] and the Einstein Telescope. These observatories will be able to detect a supernova within 100 kpc, which includes the Milky Way galaxy and its satellites [210]. The estimated rate of supernovae for a galaxy the size of Milky Way is 1-3 per century [211, 212, 213].

A number of studies have characterized the gravitational wave signal from the collapse and explosion of the core of a massive star [214, 215, 216, 217, 218, 219, 220, 221, 222, 223]. After decades of improvement in the numerical techniques, we are now much better able to account for the complex hydrodynamics in multi-dimensions, the neutrino interactions, and the hydrodynamical instabilities [224, 225, 226, 227, 228].

This rich and complex physics gives rise to a complex gravitational-wave signal, which in the time domain represents the stochastic nature of matter movements within the star. There is a sharp negative peak in the signal at the time of core bounce, and its amplitude depends on the rotation rate of the core of the progenitor. This is followed by the post-bounce oscillations of the core, that extend for 6-10 ms after the bounce, with an amplitude that depends interestingly on the rotation rate of the core of the progenitor star and its equation of state [229]. The end of post-bounce oscillations mark the onset of "prompt convection" due to the dynamical imposition of a negative entropy gradient as the shock stalls. Starting from $\sim$150 ms after the core bounce, there is a strong, stochastic signal. Moreover, an asymmetrical explosion is accompanied by a growing offset in the mean strain from zero due to "memory"[230, 231, 232].

Even though the signal is highly stochastic in the time domain, the time-frequency spectrogram of the gravitational-wave signal reveals that most of the power lies in a

narrow track in the time-frequency plane. Linear perturbation analysis of the proto-neutron star shows that this frequency corresponds to the quadrupolar $f-$mode of the proto-neutron star [222, 223], which starts approximately $100-400$ ms after the core bounce. These oscillations are excited by the downflows of matter accreted onto the proto-neutron star [216, 222].

Previously, Ref. [233] measured the frequencies associated with the g-mode oscillations of the proto-neutron star using the time-frequency spectrograms of the gravitational-wave strains obtained from simulations. Using frequency measurement and universal relations, they obtain measurement of the ratio $M_{\rm PNS}/R^2_{\rm PNS}$ of the proto-neutron star, where $M_{\rm PNS}$ is the mass and $R_{\rm PNS}$ is the radius of the proto-neutron star. Ref. [234] develop a phenomenological model of the gravitational-wave signal associated with the dominant mode and use the spectrogram of the strain to measure f-mode frequency evolution and energy. They use Bayesian parameter estimation to measure their model parameters, and then obtain frequencies and energies associated with the mode from the posteriors. More recently, Ref. [235] extended the work of Ref. [233] of measuring the f/g mode frequencies of the proto-neutron stars using the strains of 3D and 2D simulations. They use a network of current, and future, detectors to perform a coherent analysis of the detected signal.

In this work, we develop a model-independent method to measure the $f-$mode frequencies and the energy emitted in gravitational radiation of the proto-neutron star oscillations by analysing the spectrograms of the gravitational-wave strains obtained from state-of-the art three-dimensional core-collapse supernovae simulations.

Section 5.1 describes the numerical simulations used in this work, and describes the linear perturbation analysis used to determine the $f-$mode oscillation frequencies. In Section 5.3 we describe our method to construct the short-time Fourier transform and the spectrogram of the gravitational wave signal obtained from the simulations. In Section 5.4, we describe our main results from the analysis.

5.1 Simulations

In our analysis, we used the data obtained from two- and three-dimensional core-collapse supernovae simulations performed with the neutrino-radiation hydrodynamics code FORNAX [236, 237, 238]. The progenitors used in the simulations were calculated by Refs. [239] and [240]. Further details of the simulations can be found in Refs. [222, 225, 223].

We tabulate the models we consider in our works in Table 2. We show the mass of the progenitor, the equation of state of the proto-neutron star used in the simulations, and the core-rotation rate in columns 3, 4, and 5 of the table. We also indicate whether

the the shock is revived and the star explodes within the time of the simulation. For the three-dimensional simulation models, We use a wide range of progenitors with the ZAMS (Zero-Age Main Sequence) mass ranging from $9M_\odot - 60M_\odot$. We use SFHo equation of state, and all but the $13M_\odot, 14M_\odot$, and $15M_\odot$ explode within the time of the simulation. For the two-dimensional simulations with core rotation at the time of core bounce, we use a $15M_\odot$ progenitor. We have a total of 14 models with rotation rates ranging from 0.0 rad/sec -6.14 rad/sec. We also include 9 two-dimensional simulations with zero core rotation.

5.2 Linear Perturbation Analysis

In this section, we outline the method of the linear perturbation analysis of the angle-averaged data of the proto-neutron star profile (i.e. integrated over the solid angle Ω). The proto-neutron star is to be modeled with the energy-momentum tensor of a perfect fluid.

$$T_{\mu\nu} = \rho H u^\mu u^\nu + P g_{\mu\nu}, \tag{5.1}$$

where ρ denotes the rest-mass density, P the pressure, u^μ the fluid 4-velocity and $H := (1 + \epsilon + P/\rho)$ the specific enthalpy, ϵ the specific internal energy. Under the assumption of spherical symmetry [1], the space-time metric $g_{\mu\nu}$ in isotropic coordinates , using the (3 + 1) foliation, can be written as [241, 242, 224, e.g] ,

$$ds^2 = g_{\mu\nu} dx^\mu dx^\nu = -\alpha^2 dt^2 + \psi^4 f_{ij} dx^i dx^j \tag{5.2}$$

where α is the lapse function and the metric for spatial slices is approximated to be conformally related to the flat metric δ_{ij} with a conformal factor ψ^4, set to 1 in all simulations of Table 2.

We now perform perturbation analysis on top of this conformally-flat background by linearizing the equations of general relativistic hydrodynamics. In general, the three components of the Lagrangian fluid displacement field, $\boldsymbol{\xi}(\boldsymbol{r}, t) \equiv \xi^r \hat{r} + \xi^\theta \hat{\theta} + \xi^\phi \hat{\phi}$ representing the perturbation, can be resolved in terms of three scalar functions by virtue of the Helmholtz decomposition theorem. If one assumes that the radial component of the fluid vorticity equation vanishes at all points of the star, that is, $(\nabla \times \xi)_r = 0$, then one can show that the three components of ξ can now instead be resolved in terms of only two scalar functions. We now decompose these two scalar functions into purely radial functions $(\eta_r(r), \eta_\perp(r))$ supplemented with the spherical harmonics Y_{lm} and mode frequency

[1] The asymmetries are small enough and hence the angle-averaged background can well be approximated as spherically symmetric.

	Label	Progenitor mass ($M_\odot$)	Equation of state	Core rotation rate (rad/sec)	Explosion Status
Three-dimensional simulations	s9-3D	9	SFHo	-	Yes
	s10-3D	10	SFHo	-	Yes
	s11-3D	11	SFHo	-	Yes
	s12-3D	12	SFHo	-	Yes
	s13-3D	13	SFHo	-	No
	s14-3D	14	SFHo	-	No
	s15-3D	15	SFHo	-	No
	s17-3D	17	SFHo	-	Yes
	s18-3D	18	SFHo	-	Yes
	s19-3D	19	SFHo	-	Yes
	s20-3D	20	SFHo	-	Yes
	s25-3D	25	SFHo	-	Yes
	s60-3D	60	SFHo	-	Yes
Two-dimensional simulations with core rotation	0.0strain	15	SFHo	0.0	No
	0.05strain	15	SFHo	0.05	No
	0.1strain	15	SFHo	0.1	No
	0.2strain	15	SFHo	0.2	No
	0.25strain	15	SFHo	0.25	No
	0.3strain	15	SFHo	0.3	No
	0.4strain	15	SFHo	0.4	No
	0.5strain	15	SFHo	0.5	No
	0.75strain	15	SFHo	0.75	No
	1.0strain	15	SFHo	1.0	No
	2.0strain	15	SFHo	2.0	No
	pi.strain	15	SFHo	3.14	Yes
	4.0strain	15	SFHo	4.0	No
	5.0strain	15	SFHo	5.0	No
	2pi.strain	15	SFHo	6.28	No
Two-dimensional simulations without core rotation	M10-LS220	10	LS220	-	No
	M10-DD2	10	DD2	-	No
	M10-SFHo	10	SFHo	-	Yes
	M13-SFHo	13	SFHo	-	No
	M19-SFHo	19	SFHo	-	Yes
	gw-s11-2D	11	SFHo	-	No
	gw-s19-2D	19	SFHo	-	No
	gw-s25-2D	25	SFHo	-	No
	gw-s60-2D	60	SFHo	-	No

Table 2: The table summarizes the details of the simulations, including the progenitor mass, equation of state, initial core rotation, and explosion status within the simulated time interval.

σ as

$$\begin{aligned}\xi^r &= \eta_r Y_{lm} e^{-i\sigma t},\\ \xi^\theta &= \eta_\perp \frac{1}{r^2}\partial_\theta Y_{lm} e^{-i\sigma t},\\ \xi^\phi &= \eta_\perp \frac{1}{(r\sin\theta)^2}\partial_\phi Y_{lm} e^{-i\sigma t}.\end{aligned} \tag{5.3}$$

Here, any time dependence of the background state is assumed to be very small compared to the eigen value (i.e. the time derivative of any quantity f, $\partial f/\partial t << f/\sigma$). If σ is real, the system is neutrally stable (i.e. the modes are oscillatory in nature). As the background metric is assumed to be conformally flat, the perturbation of the metric is accomplished by perturbing the lapse function. Decomposing the perturbation to the lapse function in purely radial and spherical harmonics yields

$$\delta\alpha = \delta\hat{\alpha}(r) Y_{lm} e^{-i\sigma t}. \tag{5.4}$$

We define $f_\alpha \equiv \partial_r(\hat{\delta\alpha}/\alpha)$; together with $\hat{\delta\alpha}$ it represents the perturbation in the gravity sector. The timescale associated with neutrino heating and nuclear dissociation is typically $>> 1/\sigma$, hence the perturbations to the fluid properties to be adiabatic in nature, implying,

$$\frac{\partial P}{\partial \rho}|_{\text{adiabatic}} = H c_s^2 = \frac{P}{\rho}\Gamma_1, \tag{5.5}$$

c_s the relativistic sound speed in the fluid, and Γ_1 the adiabatic index. Now the equations of general-relativistic hydrodynamics together with the 00 component of the Einstein equation can be linearized to obtain the following system of equations:

$$\partial_r\eta_r + \left[\frac{2}{r} + \frac{1}{\Gamma_1}\frac{\partial_r P}{P} + 6\frac{\partial_r\psi}{\psi}\right]\eta_r + \frac{\psi^4}{\alpha^2 c_s^2}\left(\sigma^2 - \mathcal{L}^2\right)\eta_\perp - \frac{1}{\alpha c_s^2}\delta\hat{\alpha} = 0,$$

$$\partial_r\eta_\perp - \left(1 - \frac{\mathcal{N}^2}{\sigma^2}\right)\eta_r + \left[\partial_r \ln q - \tilde{G}\left(1 + \frac{1}{c_s^2}\right)\right]\eta_\perp - \frac{1}{\alpha\tilde{G}}\frac{\mathcal{N}^2}{\sigma^2}\delta\hat{\alpha} = 0,$$

$$\partial_r f_\alpha + 4\pi\left[\partial_r\rho - \frac{\rho}{P\Gamma_1}\partial_r P\right]\eta_r - \frac{4\pi\rho}{P\Gamma_1}q\sigma^2\eta_\perp + \left[\frac{4\pi\rho^2 h}{P\Gamma_1\alpha} - \frac{1}{\alpha}\frac{l(l+1)}{r^2}\right]\delta\hat{\alpha} = 0,$$

and

$$\partial_r\delta\hat{\alpha} = f_\alpha\alpha - \tilde{G}\delta\hat{\alpha}. \tag{5.6}$$

In Equations 6.37-6.40, we have collected the combination $\rho h\alpha^{-2}\psi^4$ as q, $\tilde{G}$ is the radial component of gravitational acceleration $\tilde{G} := -\partial_r \ln\alpha$, $\mathcal{N}$ is the relativistic Brunt-Väisälä frequency,

$$\mathcal{N}^2 = \frac{\alpha\delta_r\alpha}{\psi^4}\left(\frac{1}{\Gamma_1}\frac{\partial_r P}{P} - \frac{\partial_r e}{\rho H}\right) \tag{5.7}$$

and $\mathcal{L}$ is the relativistic Lamb shift,

$$\mathcal{L}^2 = \frac{\alpha^2}{\psi^4} c_s^2 \frac{l(l+1)}{r^2} \tag{5.8}$$

The system of equations 6.37-6.40 can be solved by incorporating appropriate boundary conditions: at the outer boundary, set at the radial coordinate where the density $\rho = 10^{10} g/cm^{-3}$ we consider the Lagrangian pressure to vanish and at the inner boundary (i.e. $r = 0$) use the regularity condition of [243]. Mathematically, this reads, at the outer boundary,

$$q\sigma^2 \eta_\perp - \frac{\rho H}{\alpha} \hat{\delta\alpha} + \partial_r P \eta_r = 0 \tag{5.9}$$

and at the inner boundary,

$$\eta_r = \frac{l}{r} \eta_\perp \propto r^{l-1}$$

$$\eta_r|_{r=0} = \eta_\perp|_{r=0} = 0$$

By discretizing the derivatives by means of trapezoidal rules, we can start integrating the set of equations 6.37-6.40 by inverting the 4×4 coefficient matrix at every step to solve for $(\eta_r, \eta_\perp, f_\alpha, \hat{\delta\alpha})$ and then using the bisection method to uniquely determine the solutions by satisfying the outer boundary condition Eq. 6.55. The eigenvalue corresponding to the unique solution thus obtained gives the frequency of oscillation as $\sigma/2\pi$. The lowest frequency oscillation mode is the fundamental oscillation mode (f-mode), with zero radial nodes. We find the f-mode starts few hundred ms after the core bounce for the simulations in Table 2 which confirms similar findings in [222]. The f mode thus obtained is then laid on the spectrogram and is found to contribute significantly to the strength of the GW signal after $\sim$ 400 ms. As noted in [222], the higher-order g- or p-modes are not found to be excited in these simulations.

5.3 Spectrogram Analysis

In this section, we describe the construction of the spectrogram of the gravitational-wave strain signal. We use the spectrogram to measure the properties of the fundamental quadrupolar $f-$mode oscillations of the protoneutron star. In particular, we are interested in measuring the frequency of the oscillations and the energy emitted in the gravitational-wave radiation. The analysis described here is for the fiducial case when the detector noise is not present. In the later sections we will discuss the effect of detector noise in the extraction of the features from the spectrogram and compare it with the output from the analysis described here.

Following [244, 245, 246, 221], the gravitational-wave strain $\mathbf{h_{ij}^{TT}}$ for a for a source at a distance D can be written as

$$\mathbf{h_{ij}^{TT}} = \frac{2G}{c^4 D}\frac{dq_{ij}}{dt}, \tag{5.10}$$

where q_{ij} is the time derivative of the mass quadrupole tensor $\mathcal{Q}_{ij} = \int d^3x\rho(x_i x_j - \frac{1}{3}r^2\delta_{ij})$. The strain amplitudes of the two polarizations, h_+ and $h_\times$, can be obtained in the slow-motion limit from the linear combinations of the second time derivatives of the components of the transverse traceless mass quadrupole tensor $\mathcal{Q}_{ij}$. The polarization strains as observed along the line of sight (θ, ϕ) are given by

$$h_+ = \frac{G}{c^4 D}\left(\frac{dq_{\theta\theta}}{dt} - \frac{dq_{\phi\phi}}{dt}\right), \tag{5.11}$$

$$h_\times = \frac{2G}{c^4 D}\left(\frac{dq_{\theta\phi}}{dt}\right). \tag{5.12}$$

Here, the time derivatives of the mass quadrupole in spherical coordinates, in terms of those in Cartesian coordinates, are given by

$$q_{\theta\theta} = (q_{xx}\cos^2\phi + q_{yy}\sin^2\phi + 2q_{xy}\sin\phi\cos\phi)\cos^2\theta + q_{zz}\sin^2\theta - 2(q_{xz}\cos\phi + q_{yz}\sin\phi)\sin\theta\cos\theta,$$

$$q_{\phi\phi} = q_{xx}\sin^2\phi + q_{yy}\cos^2\phi - q_{xy}\sin\phi\cos\phi,$$

$$q_{\theta\theta} = (q_{xx} - q_{yy})\cos\theta\sin\phi\cos\phi + q_{xy}\cos\theta(\cos^2\phi - \sin^2\phi) + q_{xz}\sin\theta\sin\phi - q_{yz}\sin\theta\cos\phi.$$

The total energy emitted in gravitational waves is given by [246]

$$E_{GW} = \frac{c^3}{5G}\int_0^t \sum_{ij}\left[\frac{d^3\mathcal{Q}_{ij}}{dt^3}\right]^2 dt, \tag{5.13}$$

which, in terms of gravitational-wave strain is given by

$$\begin{aligned} E_{GW} &= \frac{c^3 D^2}{16\pi G}\int_0^t dt \int_{4\pi} d\Omega \left[\left(\frac{dh_+}{dt}\right)^2 + \left(\frac{dh_\times}{dt}\right)^2\right] \\ &\approx \frac{c^3 D^2}{4G}\int_0^t dt \left[\left(\frac{dh_+}{dt}\right)^2 + \left(\frac{dh_\times}{dt}\right)^2\right], \end{aligned} \tag{5.14}$$

where the second approximation holds true if the strains are assumed to be nearly independent of line of observation and the integral over the solid angle gives a factor of 4π.

To compute the energy spectra of the gravitational wave signal we use the spectrogram of the signal

$$\begin{aligned} \frac{dE^\star_{GW}}{df} &= \frac{c^3 D^2}{4G}(2\pi f)^2\left[(\tilde{h}_+)^2 + (\tilde{h}_\times)^2\right] \\ &\approx \frac{c^3 D^2}{2G}(2\pi f)^2\left[\tilde{s}_{\text{eff}}\right]^2, \end{aligned} \tag{5.15}$$

where $\tilde{h}$ is the short-time Fourier transform, defined as

$$\tilde{h}(f) = \int_{-\infty}^{\infty} h(t)H(t-\tau_l)e^{-2\pi i f t}dt, \tag{5.16}$$

and $H(t-\tau_l)$ is the Hann window with offset time τ_l, indexed by l. A window function is applied to each segment to ensure that we don't get Gibb's junk when we take the Fourier transform of the segment. Equation 5.15 gives the energy per unit Hertz for a time-frequency block centered at time τ_l and frequency f. Thus, a spectrogram is the transformation of the short-time Fourier transform to represent the power content in a time-frequency block.

In practice, gravitational-wave strain h is a discrete function of time, obtained either from simulations, or via observations made by a gravitational-wave detector. In order to take the Fourier transform of the time-domain strain data, $h_j \equiv h_+(t_j)$, it must be evenly sampled at time intervals of $\Delta t = t_{j+1} - t_j$ seconds, $\forall j$. The sampling rate, or sampling frequency is given by $f_s = 1/\Delta t$. The data from the simulations is unevenly sampled since the size of each time step in the simulations is governed by the micro- and macro-physics at the time.

We re-sample the data at sampling rates ranging from $16,384$ Hz to $2,097,152$ Hz in powers of two and interpolate using one of the two interpolation schemes: linear interpolation and cubic spline interpolation. We then compute the energy using discretized versions of equations 5.11, 5.12 and 5.14, where now $h(t) \equiv h(t_j)$. We compute the third order time derivative of the the quadruple moment from the second order derivative using the central difference method. Fig. 16 shows the energies on the left ordinate for the model `s19-3D` computed via the two interpolation methods at various sampling rates. We see that the energy values converge with increasing sampling rate. The dashed curves show the difference between the energy values obtained between two consecutive sampling rates (shown on the right ordinate). This plot gives us a range of energy estimations for data sampled at different frequencies. We choose to use the Cubic spline interpolation and a sampling rate of $16,384$ Hz (or equivalently, sampling interval of $\Delta t = 6.1035 \times 10^{-5}$ seconds) since its is computationally less expensive and is a more realistic choice with regards to the sampling rate used by current and proposed gravitational-wave detectors.

In the next subsection we describe the construction of the short-time Fourier transform of the discretely-sampled signal, and measurement of the frequencies associated with the $f-$mode from the time-frequency representation. For this purpose, we use 50% overlap of Hann-windowed time-segments, since this configuration does not affect the amplitude of the signal.

In order to compute the short-time Fourier transform of the data, we need to divide the data into segments of equal length, say of $T_W = N_W \Delta t$ seconds, and multiply each

of these segments with a window function before we take its Fourier transform. There are a variety of windows available for this purpose [247]. In this study, we use the Hann window. We need to ensure that each data point of the waveform is equally weighted when we consider the sums of the windowed waveform segments. This presents a problem at the ends of the waveform, since Hann window starts from (or tapers to) zero. The solution is to first taper both ends of the waveform to zero, and then zero-pad the entire waveform on both ends by multiples of N_W points. Zero-padding the waveform does not change the total power content in the signal since we are only adding zeros to the ends of the data. We use the window size of $T_W = 40$ ms. For tapering, we use the 1024 data points at both ends of the waveform and apply a half cosine window. We zero-pad both ends of the tapered waveform by $N_W = 655$ points. For constructing the short-time Fourier transform of the signal, we use 50% overlap between two consecutive time segments that get multiplied by the Hann window.

The top panel of Fig. 17 shows the gravitational-wave strain data of the plus polarization as a function of time after core bounce for the simulation `s19-3D` in blue. This three-dimensional simulation uses a progenitor with ZAMS mass of $19M_{\odot}$. The equation of state used in the simulation is SFHo. The top panel shows evenly-sampled data in blue, and the data with both ends tapered for construction of the short-time Fourier transform is shown in orange. The bottom panel shows the short-time Fourier transform of the strain. The horizontal axis shows the time after bounce, the vertical axis shows the frequency. The color bar shows the modulus of the Fourier amplitude. We see the prompt convection signal after $\sim$ 50 ms after the core bounce. The prompt convection phase is followed by the $\sim$ 50 ms long quiescent phase. After this, the dominant part of the signal starts with frequency growing from $\sim$ 500 Hz to $\sim$ 1000 Hz 0.6 sec after core bounce. This signal is caused by matter accreting on the proto-neutron star and exciting its modes, including the $f-$mode. The $f-$mode frequencies obtained by the linear perturbation analysis are shown as red crosses in the bottom panel. The vertical orange line shows the time $t_0 = 200ms$ after the core bounce. The two orange parabolic curves define the frequency range within which the algorithm of [40] looks for the peak in the spectra.

5.4 Results

In this work, we have constructed the short-time Fourier transform of these signals to extract the $f-$mode frequencies. We then construct a spectrogram of the signal in a way that provides equal weights in power to all the data points of the signal. By performing linear perturbation analysis, we have shown that the $f-$mode frequency tracks down

the dominant component seen in the spectrogram of the gravitational wave strain. The vertical orange line in Fig. 17 shows the time $t_0 = 200$ ms after the core bounce. From the linear perturbation analysis we know that the $f-$mode starts around this time. We define a plausible range of the $f-$mode frequencies shown by the two orange quadratic curves in Fig. 17. This information is then used in the algorithm of [40] to measure the frequencies and energies of the gravitational strain merged into the detector noise. They find that the energy associated with the $f-$mode oscillations typically increases with the progenitor mass. The energy also depends on the delayed explosion times and the success of explosion. Simulations having higher shock stall times before the onset of explosion emit more gravitational-wave radiation since the oscillations are excited for a longer time. Additionally, the energy of the $f-$mode also increases monotonically with the rotation rate of the core, up to a certain value of core rotation rate. Centrifugal forces dominate for faster core rotations, and cease the activation of the oscillations of the proto-neutron star.

Measurement of the frequencies and energies of the $f-$mode oscillations can provide us more information about the mechanism of the supernova explosion. We can also infer the central density of the proto-neutron star and the turbulence energy within the system.

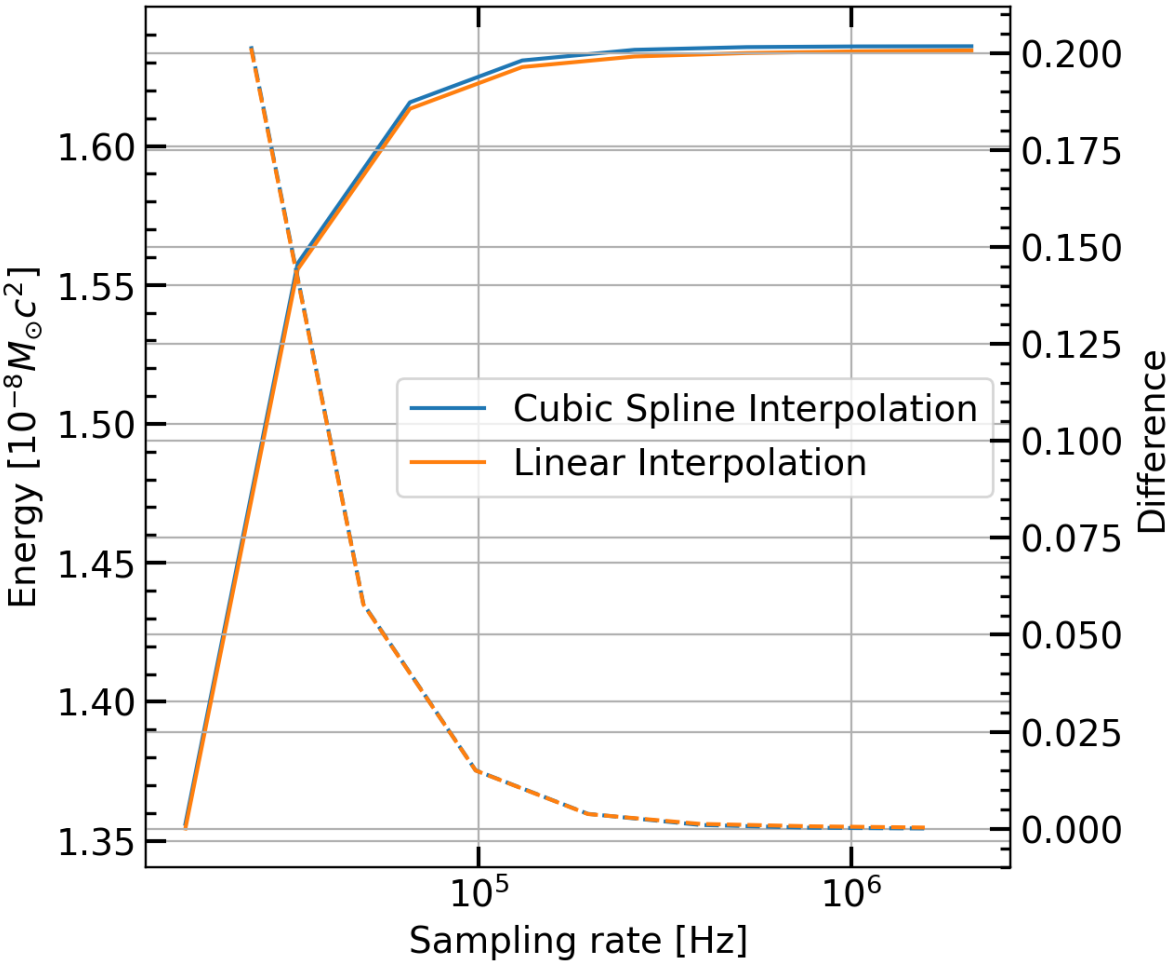

Figure 16: The figure shows the energy (in $10^{-8} M_\odot c^2$) obtained for the simulation `s19-3D` as a function of the sampling rate used to resample the data from the simulations. The solid blue curve represent the case when Cubic interpolation is used whereas the orange curve shows the case when Linear interpolation is used. The corresponding dashed curves show the difference between energy values obtained for a particular sampling frequency and the one lower. We can see that the values converge as the sampling frequency is increased.

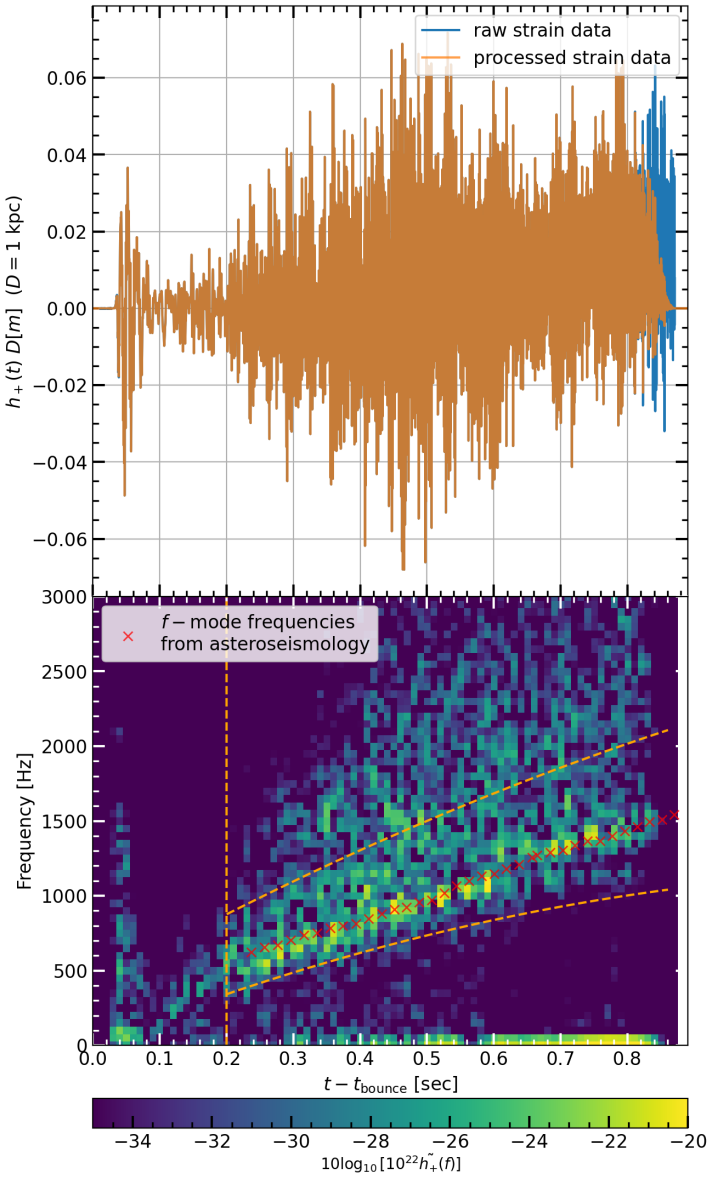

Figure 17: The figure shows the strain (top) and its spectrogram (bottom) of the 3D simulation `s19-3D`. The strain data has been uniformly sampled at 16,384 Hz. The ends have been tapered to zero by applying half cosine windows to the first and last 1024 points of the data. Then, the data are zero-padded by 0.04 seconds on either end. The spectrogram of this signal is shown on the bottom panel. The $f-$mode frequencies, obtained from linear perturbation analysis, start at 200ms and go from 500 Hz to 1000 Hz at 0.6 seconds after the core bounce, and are shown as red crosses in the bottom panel. The vertical orange line shows the time $t_0 = 200$ ms after the core bounce. The two orange parabolic curves define the frequency range within which the algorithm looks for the peak in the spectra.

Chapter 6

Standing Accretion Shock Instability

Accretion shocks are a ubiquitous phenomenon in astrophysics. They arise naturally in scenarios where compact objects (neutron stars, white dwarfs, and black holes) accrete material, typically from normal companion stars or accretion discs. Core collapse supernovae (CCSNe) are arguably the best example in which accretion shocks play a dominant role in the overall physics of the system if not dictating it. CCSNe results in the death of certain massive stars ($\gtrsim 8M_{\odot}$). At the end of their life, after their fuel reserves have been exhausted, the core of many of these stars becomes dynamically unstable and collapses. The collapse proceeds until the equation of state of the nascent neutron-rich inner core—of a typical mass of $1.4M_{\odot}$ and size of 10 km (proto-neutron star, PNS hereafter) stiffens sufficiently to stop further collapse. The onset of that moment, the so-called bounce of the PNS is proclaimed through the launch of a shock wave into the ambient stellar envelope. The shock propagates outward, loses energy by disassociating and ionizing the ambient material, and stalls at a radial distance of $\sim$ 100 km, as seen in numerous analytic and numerical studies [161, 163, 167], for a recent review, see [248]. The overlaying ambient stellar material keeps passing through the standing shock, gets compressed, slows down, and the thermal energy increases by the same amount of kinetic energy it loses and is accreted by the neutron star. The mechanism that revives this stalled shock, which would then power the energetic explosion seen in successful supernova events, remains illusive, while there are two viable proposals. The favored of this two, the neutrino mechanism, first proposed in the mid-1960s, argues that some fraction of the total neutrino flux radiated from the PNS deposits sufficient energy and momentum on the stalled shock to revive it [161, 164]. The other plausible mechanism emerged onto the scene in the early 2000s when some of the large-angle oscillation modes of the stalled shock were found to be strongly unstable in response to spherically asymmetric perturbations [25, 26, 32, 249, 250, 251]. This newly discovered hydrodynamic instability became known as the standing accretion shock instability (SASI) and is the main focus

of the present article.

However, the study of the hydrodynamics of spherical accretion onto compact objects has a rich history and was first initiated by [31] and subsequently advanced by [177, 179, 252], among others. A specific variety of the general problem, the study of spherical accretion onto compact objects–*matched to a standing shock*–specific to CCSNe gained momentum with the work of [253, 178, 254, 30]. In a major work, [178] achieved self-similar solutions for the post-bounce adiabatic fallback of stellar gas considering the mass flux approaching zero in the limit when the radius goes to zero. Then, these solutions became rightfully known as the "settling solutions". Subsequently, [30] (HC92 hereafter) modified these solutions considering the presence of a surface with a nonzero radius and nonadiabatic processes. They were focusing on a supernova remnant on timescales of hours to days, when the neutrino radiation carries away the gravitational energy through the envelope bounded by the shock wave, necessitating the need of modeling such a radiative process by means of a cooling function. The extra free parameters related to the cooling function in their problem allowed them to keep the shock standing at fixed location that they calculated in an iterative way. They studied the stability properties of their solutions analytically in linear perturbation theory for different values of adiabatic index and different strengths of cooling (by changing the form of the cooling function).

The stability of these solutions (i.e., settling solutions with cooling functions) has been studied by [30] and [34] analytically in perturbation theory and [26] (BM06, hereafter) in numerical simulations. The details of all these major works are presented in Table 3. The summary being that almost all the studies find the radial modes of oscillations to be stable; while some large-angle oscillations are found to be unstable. The $\ell = 1$ modes are the most unstable and epitomize the low-frequency instability– SASI. [34] has another interesting feature to add: They found that the real parts of the eigen modes (characterizing the growth of instabilities and termed growth rate) were found to oscillate as plotted against the complex part (charectering the radial osicllation of the modes and termed oscillation period), very clearly visible when the number of well-defined modes is large (see their Figure 7). We note that the particular study of [25] (BM03, hereafter), which revamped SASI, presented the result of the numerical stability analysis of the original "settling solutions" (i.e. without any cooling function) **but, as summarized in Table 3, to date there has been no analytic stability analysis performed on them**. In this work, we set out to do so and find some interesting results; specifically, we discover oscillations in the $l = 2$ eigenmode spectra, similar to the finding of [34] for $\ell = 1$ modes. We find a range of unstable modes–the maximum oscillation frequency (corresponding to the imaginary part of the eigen modes) of these modes is strikingly similar to the frequency associated with the free-fall time of the PNS, whereas SASI is

traditionally associated with relatively low-frequency oscillations. This makes us think whether these unstable $\ell = 2$ mode oscillations of the SASI cavity seed the fundamental mode (f-mode) oscillations of the neutron star seen in the gravitational wave signal of [2, 255, 256, 257, 258].

The mechanism driving SASI is yet unknown, and we are oblivious to it as well. One of the leading mechanisms is the "advective-acoustic mechanism" put forward by [34] identifies a loop of entropic and acoustic waves in the subsonic region between the shock and the accreting body as the source of this instability which was first presented to explain the isothermal flow accelerated towards a black hole [259, 33]. In this, the shock front generates an entropic wave that propagates inward, causing a pressure wave in the post-shock medium, which in turn propagates outward and completes the loop by creating further amplified entropic waves [260, 34, 35, 261, 262]. The other explanation, the "acoustic mechanism" –advocated by [32, 249] proposes that the instability is driven by acoustic waves generated from the oscillation modes of proto-neutron star excited by the infalling accretion plumes. In this model, the protoneutron star essentially transforms the gravitational energy into a sound wave and drives the SASI engine [249, 263]. Some studies have tried to settle the roles of each mechanism to power SASI, but it is wise to conclude that the issue is far from settled [264].

Despite uncertainty about its origin, SASI continues to be the subject of intense research. It is true that the initial hype with SASI to generate an asymmetric explosion has faded, but it is accepted that although SASI might not be able to generate the explosion independently, it plays a significant role in aiding the neutrino heating mechanism [176, 265]. Moreover, SASI activity was shown to generate gravitational waves that are speculated to be in the detectable band of the next generation gravitational wave detector [266, 267, 268], affect the emitted neutrino signatures [269, 270], possibly link the birth properties (i.e. spin, kick, and magnetic field) of pulsars [251, 271] and excites different oscillation modes of the protoneutron star [272, 273]. Hence, to date, SASI has always received significant attention from the supernovae community in numerous analytic and simulation works over the past decade [274, 275, 276, 277, 278, 279, 280, 206, 281, 282]. The results to be presented here promise that SASI has more to offer.

6.1 Background Flow and linearized equations

We assume that the infalling $\sim$ pressureless fluid passes through a radiation-dominated shock. We neglect the radiative losses below the shock; which is a very good approximation over most of its volume, the neutrino losses become important in a thin layer very close to the surface of the neutron star [178]. Therefore we characterize the post-shock

Study	Method	Cooling	l	γ	Stability	Notes
[178]	Analytic	not included	n/a	4/3	Stability analysis not performed	
HC92	Analytic	included	0	5/3	unstable	both the growth rates and oscillation period are sensitive to cooling
				4/3	mildly unstable	both the growth rates and oscillation period are almost independent to cooling
			1	5/3	unstable	$R_{\rm shock}/R_{\rm PNS} \gtrsim 2$; growth rate slower than radial oscillations
					stable	$R_{\rm shock}/R_{\rm PNS} < 2$
			2		stable	
			higher		stable	
BM03	Simulation	not included	0	4/3	stable	growth of instabilities slows down with smaller value of γ
			1, 2		unstable	
BM06	Simulation	included	0	4/3	unstable	$R_{\rm shock}/R_{\rm PNS} > 20$
					stable	$R_{\rm shock}/R_{\rm PNS} < 20$ unstable
			1, 2 and higher		unstable	
[34]	Analytic	included	qualitatively similar to BM06; quantitatively the growth rate and oscillation period they found showed $\sim 30\%$ discrepancies.			

Table 3: Summary of some of the major previous work investigating SASI.

flow by a single adiabatic index γ, and the gas is isentropic such that p/ρ^γ is constant [1]. We let the fluid be nearly spherically symmetric, so that the predominant dependence of the fluid variables is on the spherical radius r and the θ- and ϕ-components of the velocity are small. Considering the gravitational field of the neutron star described by the Newtonian potential $\Phi = -\mathrm{GM/r}$, where M is the mass of the neutron star, we write the fluid equations in spherical coordinates by keeping only the linear terms in θ and ϕ as

$$\frac{\partial \rho}{\partial t} + \frac{1}{r^2}\frac{\partial}{\partial r}\left[r^2 \rho v_{\rm r}\right] + \frac{1}{r\sin\theta}\frac{\partial}{\partial \theta}\left[\sin\theta \rho v_\theta\right] + \frac{1}{r\sin\theta}\frac{\partial}{\partial \phi}\left[\rho v_\phi\right] = 0, \tag{6.1}$$

$$\frac{\partial v_{\rm r}}{\partial t} + v_{\rm r}\frac{\partial v_{\rm r}}{\partial r} + \frac{1}{\rho}\frac{\partial p}{\partial r} = -\frac{GM}{r^2}, \tag{6.2}$$

$$\frac{\partial v_\theta}{\partial t} + v_{\rm r}\frac{\partial v_\theta}{\partial r} + \frac{v_{\rm r} v_\theta}{r} + \frac{1}{r}\frac{1}{\rho}\frac{\partial p}{\partial \theta} = 0, \tag{6.3}$$

$$\frac{\partial v_\phi}{\partial t} + v_{\rm r}\frac{\partial v_\phi}{\partial r} + \frac{v_{\rm r} v_\phi}{r} + \frac{1}{r\sin\theta}\frac{1}{\rho}\frac{\partial p}{\partial \phi} = 0. \tag{6.4}$$

$$\frac{\partial s}{\partial t} + v_{\rm r}\frac{\partial s}{\partial r} = 0. \tag{6.5}$$

In Equation (6.5) we identify, $S = \ln\left(p/\rho^\gamma\right)$ as the entropy of the gas, which is a conserved Lagrangian quantity in adiabatic process.

[1] We can nevertheless mimic radiative losses by considering softer equation of state, i.e. smaller values of the adiabatic index γ

6.1.1 Shock jump conditions

The overlying stellar envelope is assumed to freefall into the center of the star in a time-steady manner; the ambient velocity therefore satisfies

$$v_{\rm r}\frac{\partial v_{\rm r}}{\partial r} = -\frac{GM}{r^2} \quad \Rightarrow \quad v_{\rm a} = -\sqrt{\frac{2GM}{r}}. \tag{6.6}$$

Here the subscript-a denotes the fact that this velocity profile is appropriate to the ambient gas. The solution to the continuity equation is then

$$\frac{\partial}{\partial r}\left[r^2\rho v_{\rm a}\right] = 0 \quad \Rightarrow \quad \rho = \rho_0\left(\frac{r}{r_0}\right)^{-3/2}. \tag{6.7}$$

Here ρ_0 and r_0 are some scale density and radius, respectively.

In spherical coordinates, the equation describing the surface of the shock is

$$f = r - R(\theta,\phi) = 0. \tag{6.8}$$

Here $R(\theta,\phi)$ is the shock radius as a function of spherical angles θ and ϕ. The unit vector normal to the shock front is then

$$\frac{\nabla f}{|\nabla f|} = \frac{1}{\sqrt{1+\left(\frac{1}{R}\frac{\partial R}{\partial\theta}\right)^2+\left(\frac{1}{R\sin\theta}\frac{\partial R}{\partial\phi}\right)^2}}\left\{1, -\frac{1}{R}\frac{\partial R}{\partial\theta}, -\frac{1}{R\sin\theta}\frac{\partial R}{\partial\phi}\right\}. \tag{6.9}$$

In the co-moving frame of the shock the flux of mass, momentum, and energy must be conserved across the shock front; this gives the following three "jump conditions":

$$\rho_1\tilde{v}_1 = \rho_2\tilde{v}_2, \tag{6.10}$$

$$\rho_1\tilde{v}_1^2 = \rho_2\tilde{v}_2^2 + p_2, \tag{6.11}$$

$$\frac{1}{2}\tilde{v}_1^2 = \frac{1}{2}\tilde{v}_2^2 + \frac{\gamma}{\gamma-1}\frac{p_2}{\rho_2}. \tag{6.12}$$

Here tilde's denote the fact that we are in the co-moving frame of the shock, and hence

$$\tilde{v}_1 = v_1 - \frac{\partial R}{\partial t}, \quad \tilde{v}_2 = v_2 - \frac{\partial R}{\partial t}, \tag{6.13}$$

where $\frac{\partial R}{\partial t}$ is the shock speed. Solving the above three algebraic relationships gives

$$v_2 = \frac{2}{\gamma+1}\frac{\partial R}{\partial t} + \frac{\gamma-1}{\gamma+1}v_1, \tag{6.14}$$

$$p_2 = \frac{2}{\gamma+1}\rho_1\left(v_1 - \frac{\partial R}{\partial t}\right)^2, \tag{6.15}$$

$$\rho_2 = \frac{\gamma+1}{\gamma-1}\rho_1. \tag{6.16}$$

At the location of the shock we therefore have

$$v_{\rm r}(R) = \frac{2}{\gamma+1}\frac{\partial R}{\partial t} + \frac{\gamma-1}{\gamma+1}v_{\rm a}(R), \tag{6.17}$$

$$p(R) = \frac{2}{\gamma+1}\rho_a(R)\left(v_{\rm a}(R) - \frac{\partial R}{\partial t}\right)^2, \tag{6.18}$$

$$\rho(R) = \frac{\gamma+1}{\gamma-1}\rho_{\rm a}(R), \tag{6.19}$$

$$v_\theta(R) = -\frac{2}{\gamma+1}\left(\frac{\partial R}{\partial t} + v_{\rm a}(R)\right)\frac{1}{R}\frac{\partial R}{\partial \theta}, \tag{6.20}$$

$$v_\phi(R) = -\frac{2}{\gamma+1}\left(\frac{\partial R}{\partial t} + v_{\rm a}(R)\right)\frac{1}{R\sin\theta}\frac{\partial R}{\partial \phi}. \tag{6.21}$$

Now, we re-scale all the fluid quantities of interest, that is, (v_r, v_θ, v_ϕ), ρ, and p to dimensionless variables $(f_r, f_\perp)$, g, and h respectively [2]. Similarly, instead of working with the radial coordinate r and the time coordinate t, we choose to work with dimensionless variables ξ and τ, respectively. One of the main motivations behind all these re-definitions is to take advantage of the self-similarity property that the fluid equations enjoy. We would like to point out that to define ξ in Equation (6.22) we have normalized the radial coordinate r by the instantaneous shock location R(t) in the perturbed flow and not by the unperturbed shock location $\rm R_0(t)$ [3]. This means that the shock will always be at $\xi = 1$, whereas the fixed location of the neutron star surface will correspond to ξ_{ns}, a value that will change when the shock moves. The dimensionless time-like variable τ, on the other hand, is a measure of time in the unit of the dynamical timescale of the star.

$$t \to \tau, \quad \frac{d\tau}{dt} = \frac{\sqrt{2GM}}{R^{3/2}}, \quad r \to \xi, \quad \xi = \frac{r}{R}. \tag{6.22}$$

$$v_{\rm r} = \sqrt{\frac{2GM}{R}} = \sqrt{\frac{2GM}{R}} f_r(\xi,\tau) Y_\ell^m(\theta,\phi), \tag{6.23}$$

$$v_\theta = \sqrt{\frac{2GM}{R}} f_\perp(\xi,\tau)\frac{\partial Y}{\partial \theta}, \tag{6.24}$$

$$v_\phi = \sqrt{\frac{2GM}{R}} f_\perp(\xi,\tau)\frac{1}{\sin\theta}\frac{\partial Y_\ell^m}{\partial \phi}, \tag{6.25}$$

$$\rho = \rho_0\left(\frac{R}{r_0}\right)^{-3/2} g(\xi,\tau) Y_\ell^m(\theta,\phi), \tag{6.26}$$

$$p = \frac{2GM}{R}\rho_0\left(\frac{R}{r_0}\right)^{-3/2} h(\xi,\tau) Y_\ell^m(\theta,\phi). \tag{6.27}$$

[2] By mapping the functions v_θ and v_ϕ to a single function $f_\perp$ we implicitly assume the radial component of the vorticity equation to be identically zero at all points of the star [283].

[3] This is following [30].

Then (again to leading order) the fluid equations become

$$\frac{\partial g}{\partial \tau} - \frac{\frac{\partial R}{\partial t}}{\sqrt{\frac{2GM}{R}}}\left(\frac{3}{2}g + \xi\frac{\partial g}{\partial \xi}\right) + \frac{1}{\xi^2}\frac{\partial}{\partial \xi}\left[\xi^2 g f_{\rm r}\right] - \frac{\ell\left(\ell+1\right)}{\xi}g f_{\perp} = 0. \tag{6.28}$$

$$\frac{\partial f_{\rm r}}{\partial \tau} - \frac{\frac{\partial R}{\partial t}}{\sqrt{\frac{2GM}{R}}}\left(\frac{1}{2}f_{\rm r} + \xi\frac{\partial f_{\rm r}}{\partial \xi}\right) + f_{\rm r}\frac{\partial f_{\rm r}}{\partial \xi} + \frac{1}{g}\frac{\partial h}{\partial \xi} = \begin{cases} -\frac{1}{2\xi^2}, & \text{if } \ell = 0 \\ 0 & \text{if } \ell > 0. \end{cases} \tag{6.29}$$

$$\frac{\partial f_{\perp}}{\partial \tau} - \frac{\frac{\partial R}{\partial t}}{\sqrt{\frac{2GM}{R}}}\left(\frac{1}{2}f_{\perp} + \xi\frac{\partial f_{\perp}}{\partial \xi}\right) + \frac{1}{g}\left(-\frac{3}{2}\frac{1}{R}\frac{\partial R}{\partial \theta} - \frac{1}{R}\frac{\partial R}{\partial \theta}\xi\frac{\partial h}{\partial \xi} + h\right) = 0, \tag{6.30}$$

$$\frac{\partial f_{\perp}}{\partial \tau} - \frac{\frac{\partial R}{\partial t}}{\sqrt{\frac{2GM}{R}}}\left(\frac{1}{2}f_{\perp} + \xi\frac{\partial f_{\perp}}{\partial \xi}\right) + \frac{1}{g}\left(-\frac{3}{2}\frac{1}{R}\frac{\partial R}{\partial \theta} - \frac{1}{R}\frac{\partial R}{\partial \theta}\xi\frac{\partial h}{\partial \xi} + h\right) = 0, \tag{6.31}$$

$$\frac{\partial}{\partial \tau}\ln\left(\frac{h}{g^{\gamma}}\right) - \frac{\frac{\partial R}{\partial t}}{\sqrt{\frac{2GM}{R}}}\left(\frac{1}{2}\left(5-3\gamma\right) + \xi\frac{\partial}{\partial \xi}\ln\left(\frac{h}{g^{\gamma}}\right)\right) + f_{\rm r}\frac{\partial}{\partial \xi}\ln\left(\frac{h}{g^{\gamma}}\right) = 0. \tag{6.32}$$

6.1.2 Background Soluion

Let the shock be stationary such that $\frac{\partial R}{\partial t} = \partial R/\partial t \equiv 0$, and let the θ- and ϕ-components of the velocity be zero. Additionally, assume that all fluid variables depend only on the spherical radius r, and we will denote all fluid variables with a subscript 0. Then the fluid equations become

$$\frac{\partial}{\partial \xi}\left[\xi^2 f_0 g_0\right] = 0, \quad f_0\frac{df_0}{d\xi} + \frac{1}{g_0}\frac{dh_0}{d\xi} = -\frac{1}{2\xi^2}, \quad \frac{d}{d\xi}\ln\left(\frac{h_0}{g_0^{\gamma}}\right) = 0, \tag{6.33}$$

and the boundary conditions are

$$f_0(1) = -\frac{\gamma-1}{\gamma+1}, \quad g_0(1) = \frac{\gamma+1}{\gamma-1}, \quad h_0(1) = \frac{2}{\gamma+1}. \tag{6.34}$$

The solution to the above gives the following, algebraic equation to be solved for $f_{\rm r}$:

$$\frac{1}{2}f_0^2 + \frac{2\gamma}{\gamma^2-1}\left(\frac{\gamma-1}{\gamma+1}\right)^{\gamma}\left(\frac{-1}{\xi^2 f_0}\right)^{\gamma-1} - \frac{1}{2\xi} = 0. \tag{6.35}$$

We numerically solve that equation subject to the jump conditions Equation 6.34 and recover the "settling solutions" of [30, 25] for radiation-dominated $\gamma = 4/3$ fluid. We present them in Figure 18, which also illustrates the behavior of these solutions as we vary the adiabatic index γ. As γ decreases, the velocity (the modulus of which is shown in the left panel) more rapidly approaches zero as we move near the origin. This aspect of the solutions arises from the fact that the pressure (shown in the right panel) rises more rapidly toward the origin as the equation of state softens, the gradient of which is more capable of stopping the infall. The corresponding densities are shown in the middle panel.

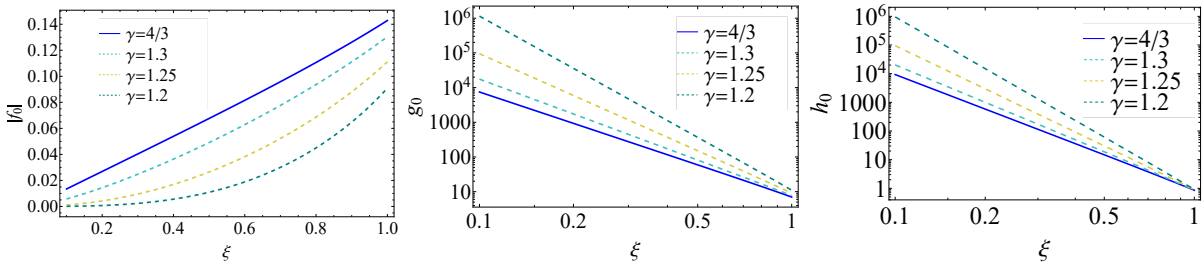

Figure 18: The modulus of the dimensionless, radial velocity ($f_{\rm r}$, left), the dimensionless density (g, middle), and the dimensionless pressure (h, right) as functions of $\xi = r/R$.

6.1.3 Linearized Equations for general ℓ

We perturb these background solutions by placing a rigid, spherically symmetric boundary in the interior of the flow that represents the surface of the neutron star. Physically we expect this location to coincide with where the density increases to the point that neutron degeneracy pressure and the repulsive nuclear force substantially stiffen the equation of state. We expect the sudden placement of this "wall" in the interior of the post-shock flow to generate an instantaneous response of the fluid and, in general, time-dependent and spherically asymmetric variations of the fluid variables

$$f_{\rm r}(\xi,\tau) = f_0(\xi) + f_1(\xi,\tau)Y_\ell^m(\theta,\phi), \quad g(\xi,\tau) = g_0(\xi) + g_1(\xi,\tau)Y_\ell^m(\theta,\phi), h(\xi,\tau) = h_0(\xi) + h_1(\xi,\tau)Y_\ell^m(\theta,\phi), R(\xi,\tau) = R_0\left(1+\alpha(\tau)Y_\ell^m(\theta,\phi)\right) \quad (6.36)$$

where subscript-0 functions are solutions to the background standing accretion shock problem, that is, those shown in Figure 18, subscript-1 functions (and α) are perturbations on top of these and $Y_\ell^m(\theta,\phi)$ is a spherical harmonic of degree $\{\ell, m\}$. Keeping only first-order terms in the fluid equations yields the following perturbation equations:

$$\frac{\partial g_1}{\partial\tau} - \frac{\partial\alpha}{\partial\tau}\left(\frac{3}{2}g_0 + \xi\frac{\partial g_0}{\partial\xi}\right) + \frac{1}{\xi^2}\frac{\partial}{\partial\xi}\left[\xi^2\left(f_0 g_1 + g_0 f_1\right)\right] - \frac{f_\perp g_0}{\xi}l(l+1) = 0, \quad (6.37)$$

$$\frac{\partial f_1}{\partial\tau} - \frac{\partial\alpha}{\partial\tau}\left(\frac{1}{2}f_0 + \xi\frac{\partial f_0}{\partial\xi}\right) + \frac{\partial}{\partial\xi}\left[f_0 f_1\right] + \frac{1}{g_0}\frac{\partial h_1}{\partial\xi} - \frac{g_1}{g_0^2}\frac{\partial h_0}{\partial\xi} = 0, \quad (6.38)$$

$$\frac{\partial f_\perp}{\partial\tau} + f_0\frac{\partial f_\perp}{\partial\xi} + \frac{1}{\xi}f_0 f_\perp - \frac{\alpha}{g_0}\frac{\partial h_0}{\partial\xi} - \frac{5\alpha}{2\xi}\frac{h_0}{g_0} + \frac{1}{\xi}\frac{h_1}{g_0} = 0, \quad (6.39)$$

$$\frac{\partial}{\partial\tau}\left[\frac{h_1}{h_0} - \frac{\gamma g_1}{g_0}\right] - \frac{\partial\alpha}{\partial\tau}\frac{1}{2}\left(5-3\gamma\right) + f_0\frac{\partial}{\partial\xi}\left[\frac{h_1}{h_0} - \frac{\gamma g_1}{g_0}\right] = 0. \quad (6.40)$$

The boundary conditions at the shock are

$$f_1(1) = \frac{2}{\gamma+1}\frac{\partial\alpha}{\partial\tau}, \tag{6.41}$$

$$h_1(1) = \frac{2}{\gamma+1}\left(2\frac{\partial\alpha}{\partial\tau} + \frac{\delta\rho}{\rho_{\rm a}}\right), \tag{6.42}$$

$$g_1(1) = \frac{\gamma+1}{\gamma-1}\frac{\delta\rho}{\rho_{\rm a}}. \tag{6.43}$$

$$f_\perp(1) = -\frac{2}{\gamma+1}\alpha. \tag{6.44}$$

Now, we take the Laplace transformation of various perturbations ($\tilde{f}_1$, $\tilde{g}_1$, $\tilde{h}_1$, and $\tilde{\alpha}$), where the Laplace transformation is defined as

$$\tilde{f}_1 = \int_0^\infty f_1(\xi,\tau)e^{-\sigma\tau}d\tau. \tag{6.45}$$

The Laplace-transformed equations are:

$$\sigma\tilde{g}_1 - \sigma\alpha\left(\frac{3}{2}g_0 + \xi\frac{\partial g_0}{\partial\xi}\right) + \frac{1}{\xi^2}\frac{\partial}{\partial\xi}\left[\xi^2\left(g_0\tilde{f}_1 + f_0\tilde{g}_1\right)\right] - \frac{\tilde{f}_\perp g_0}{\xi}l(l+1) = 0, \tag{6.46}$$

$$\sigma\tilde{f}_1 - \sigma\alpha\left(\frac{1}{2}f_0 + \xi\frac{\partial f_0}{\partial\xi}\right) + \frac{\partial}{\partial\xi}\left[f_0\tilde{f}_1\right] + \frac{1}{g_0}\frac{\partial\tilde{h}_1}{\partial\xi} - \frac{\tilde{g}_1}{g_0^2}\frac{\partial h_0}{\partial\xi} = 0, \tag{6.47}$$

$$\sigma\tilde{f}_\perp + f_0\frac{\partial\tilde{f}_\perp}{\partial\xi} + \frac{1}{\xi}f_0\tilde{f}_\perp - \frac{\alpha}{g_0}\frac{\partial h_0}{\partial\xi} - \frac{5\alpha}{2\xi}\frac{h_0}{g_0} + \frac{1}{\xi}\frac{\tilde{h}_1}{g_0} = 0, \tag{6.48}$$

$$\sigma\left(\frac{\tilde{h}_1}{h_0} - \frac{\gamma\tilde{g}_1}{g_0}\right) - \frac{1}{2}\sigma\alpha\left(5-3\gamma\right) + f_0\frac{\partial}{\partial\xi}\left[\frac{\tilde{h}_1}{h_0} - \frac{\gamma\tilde{g}_1}{g_0}\right] = 0. \tag{6.49}$$

with the following boundary conditions,

$$\tilde{f}_{1{\rm n}}(1) = \frac{2\sigma\alpha}{\gamma+1}, \tilde{f}_{\perp{\rm n}}(1) = -\frac{2\alpha}{\gamma+1}, \tilde{h}_{\rm n}(1) = \frac{4\sigma\alpha}{(\gamma+1)}, \quad \tilde{g}_{\rm n}(1) = 0. \tag{6.50}$$

The eigenvalues are specific values of the quantity σ, in general, complex, to be labeled as σ_n, are locations in the complex plane where the perturbation of the shock radius and the fluid variables diverge as a simple pole [150]. Next, we define

$$\tilde{f}_{\rm n} \equiv \frac{\tilde{f}_1}{\tilde{\alpha}} \tag{6.51}$$

and similarly for the other variables. The perturbation equations (6.46)-(6.49) now transform into:

$$\sigma\tilde{g}_{\rm n} - \sigma\left(\frac{3}{2}g_0 + \xi\frac{\partial g_0}{\partial\xi}\right) + \frac{1}{\xi^2}\frac{\partial}{\partial\xi}\left[\xi^2\left(g_0\tilde{f}_{\rm n} + f_0\tilde{g}_{\rm n}\right)\right] - \frac{f_\perp g_0}{\xi}l(l+1) = 0, \quad (6.52)$$

$$\sigma\tilde{f}_{\rm n} - \sigma\left(\frac{1}{2}f_0 + \xi\frac{\partial f_0}{\partial\xi}\right) + \frac{\partial}{\partial\xi}\left[f_0\tilde{f}_{\rm n}\right] + \frac{1}{g_0}\frac{\partial\tilde{h}_{\rm n}}{\partial\xi} - \frac{\tilde{g}_{\rm n}}{g_0^2}\frac{\partial h_0}{\partial\xi} = 0, \quad (6.53)$$

$$\sigma\left(\frac{\tilde{h}_{\rm n}}{h_0} - \frac{\gamma\tilde{g}_{\rm n}}{g_0}\right) - \frac{1}{2}\sigma\left(5-3\gamma\right) + f_0\frac{\partial}{\partial\xi}\left[\frac{\tilde{h}_{\rm n}}{h_0} - \frac{\gamma\tilde{g}_{\rm n}}{g_0}\right] = 0, \quad (6.54)$$

$$\tilde{f}_{\rm n}(1) = \frac{2\sigma}{\gamma+1}, \tilde{f}_{\perp{\rm n}}(1) = -\frac{2}{\gamma+1}, \tilde{h}_{\rm n}(1) = \frac{4\sigma}{\gamma+1}, \tilde{g}_{\rm n}(1) = 0. \quad (6.55)$$

6.1.4 Neutron star Boundary conditions

We now have three equations, the Laplace-transformed fluid equations, and four unknowns ($\tilde{f}_1$, $\tilde{g}_1$, $\tilde{h}_1$, and σ). To solve the system, we need a fourth boundary condition. For this boundary condition, we assume that very close to the surface of the neutron star the fluid velocity maintains its steady-state value. This condition is inspired by [284], where steady-state solutions are considered to continue beneath the neutrino sphere. This condition is expressed in Equation (6.59). Note that by imposing this boundary condition in the interior, we excite perturbations in the interior of the flow – establishing a wall in the interior of the self-similar solutions causes the shock to respond. We let the radius of the neutron star be $R_{\rm NS}$, which stays fixed in Eulerian space. We then have our fourth boundary condition

$$v(R_{\rm NS}) = \sqrt{\frac{2GM}{R}}\left(f_0\left(\frac{R_{\rm NS}}{R}\right) + f_1\left(\frac{R_{\rm NS}}{R}, \tau\right)\right) = \sqrt{\frac{2GM}{R_0}}f_0\left(\frac{R_{\rm NS}}{R_0}\right). \quad (6.56)$$

Therefore,

$$f_0\left(\frac{R_{\rm NS}}{R}\right) \simeq f_0\left(\frac{R_{\rm NS}}{R_0}\left(1-\alpha\right)\right) \simeq f_0\left(\xi_{\rm NS}\right) - f_0'\left(\xi_{\rm NS}\right)\xi_{\rm NS}\alpha, \quad (6.57)$$

where $\xi_{\rm NS} \equiv R_{\rm NS}/R_0$ is the ratio of the neutron star radius to the stationary shock radius.

$$f_1\left(\xi_{\rm NS}, \tau\right) = \alpha\left(\frac{1}{2}f_0 + \xi_{\rm NS}f_0'\left(\xi_{\rm NS}\right)\right). \quad (6.58)$$

Hence,

$$\tilde{f}_{\rm n}(\xi_{\rm NS}) = \frac{1}{2}f_0(\xi_{\rm NS}) + \xi_{\rm NS}f_0'\left(\xi_{\rm NS}\right) \quad (6.59)$$

6.1.5 Background Flow With Cooling Functions

Inclusion of the cooling function modifies the radial momentum and entropy equation. We write down those two modified equations with the inclusion of a cooling function of the form $\mathcal{L} \propto \rho^{\beta-\alpha} p^{\alpha}$ below:

$$\frac{\partial v_{\rm r}}{\partial t} + v_{\rm r}\frac{\partial v_{\rm r}}{\partial r} + \frac{1}{\rho}\frac{\partial p}{\partial r} = -\frac{GM}{r^2} + \frac{\mathcal{L}}{\rho v_r}, \tag{6.60}$$

$$\frac{\partial s}{\partial t} + v_{\rm r}\frac{\partial s}{\partial r} = \frac{\mathcal{L}}{p v_r}. \tag{6.61}$$

We employ the coordinate transformation of Equations (6.22) - (6.27) and obtain

$$\frac{\partial}{\partial \xi}\left[\xi^2 f_0 g_0\right] = 0, \quad f_0\frac{df_0}{d\xi} + \frac{1}{g_0}\frac{dh_0}{d\xi} = -\frac{1}{2\xi^2} + K_1 g_0^{\beta-\alpha-1} h_0^{\alpha} \quad , \quad \frac{d}{d\xi}\ln\left(\frac{h_0}{g_0^{\gamma}}\right) = K_2 g_0^{\beta-\alpha} h_0^{\alpha-1}, \tag{6.62}$$

Here, K_1, K_2 are two parameters arising from the proportionality factor used for the cooling factor and different normalization used in Equation (6.60) and (6.61).

6.2 Numerical determination of eigenfrequencies

We numerically solve the eigensystem (6.52) - (6.54) following way: by making a guess for the value of σ we start to integrate the above-mentioned system of equations inward from the location of the shock ($\xi = 1$) with the boundary condition of Equation (6.55). Then we calculate the value of $\tilde{f}_{\rm n}(\xi_{\rm ns})$ and plug this value into the fourth boundary condition (i.e. Equation (6.59)). We continue iterating the procedure by perturbing the value of σ until we find specific values of σ, to be denoted by $\sigma_{\rm n}$, for which the calculated $\tilde{f}_{\rm n}(\xi_{\rm ns})$ satisfies the fourth boundary condition of Equation (6.59). Therefore, the set of eigenvalues $\sigma_{\rm n}$ corresponds to those solutions that satisfy the boundary conditions at the location of the shock and at the surface of the neutron star. As the eigensystem (6.52) - (6.54) is not Hermitian, the eigenvalues $\sigma_{\rm n}$ are complex, which we will express with $\sigma_{\rm n} \equiv \sigma_r + i\sigma_i$. Due to the way we define the Laplace transformation in Equation (6.45) here, the real part σ_r dictates the stability of the solutions; $\sigma_r < 0$ corresponds to stable solutions, while $\sigma_r > 0$ gives unstable solutions. Although we are working in dimensionless units, the absolute value of σ_r determines how fast/slow the perturbations grow in time, and hence we will call this the "growth rate" associated with the instability. On the other hand, σ_i which we label as the "oscillation frequency", is roughly a measure of the radial nodes of *eigenfunctions*. In Table 4 we tabulate the eigenvalues corresponding to some

ℓ	σ_r	σ_i	ℓ	σ_r	σ_i	ℓ	σ_r	σ_i	ℓ	σ_r	σ_i
0	−0.201762	-2.55373×10^{-6}	1	0.0671051	0.315556	2	−0.0665241	0.332979	3	−0.142767	1.04364
	−0.266972	0.896751		0.0806943	2.28559		0.00535425	7.96419		−0.0852871	3.03898
	−0.312219	3.26877		0.01575	15.103		0.0444954	21.1379		−0.0197038	10.6595
	−0.31561	4.68161		−0.0582782	24.6993		0.00375948	25.7686		0.0248765	23.8486
	−0.316168	6.58475		−0.0700799	31.0231		−0.024543	34.3314		0.0353329	30.796

Table 4: The real and imaginary parts of eigenvalues corresponding to few representative eigenmodes of solutions specified by ℓ. We have set $\gamma = 4/3$ and $\xi_{ns} = 0.1$ for these results.

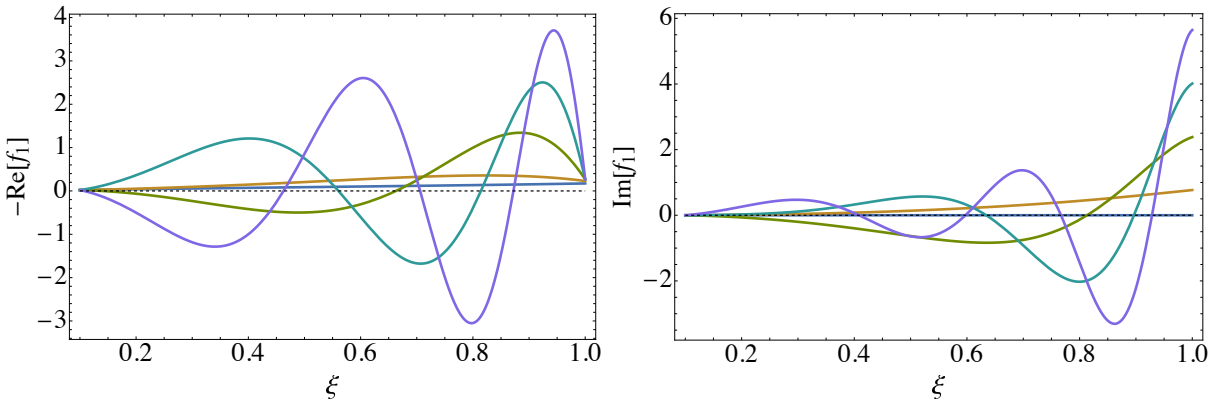

Figure 19: The real (left) and imaginary (right) parts of $\tilde{f}_{\rm n}$ for the first five radial ($l = 0$) eigenmodes with $\gamma = 4/3$ and $\xi_{\rm NS} = 0.1$.

representative *eigenmodes* for different values of ℓ with m $= 0$ [4]. Unless otherwise stated, the following results are obtained by setting $\gamma = 4/3$ and $\xi_{ns} = 0.1$.

6.2.1 $\ell = 0$, the radial modes

As can be seen from Table 4 and left panel of Figure 20, the real parts of the *eigenvalues* (σ_r) corresponding to $\ell = 0$ motion are all negative and hence all **the radial modes of oscillations are stable**. We plot the real (imaginary) component of the radial component of the post-shock fluid velocity corresponding to the five representative $\ell = 0$ *eigenvalues* presented in Table 4 in the left (right) panel of Figure 19.

6.2.2 Non-radial modes: Oscillation in the *eigenspectrum*

A striking feature of this particular problem is that we find that the growth rate (σ_r) oscillates when plotted against the oscillation frequency (σ_i), for **all non-radial modes of oscillations**, as we already point out that this phenomenon was first observed in the

[4] As we are assuming a spherically symmetric background, the results are independent of the choice of polar axis for the coordinate system, hence do not depend on the azimuthal order m

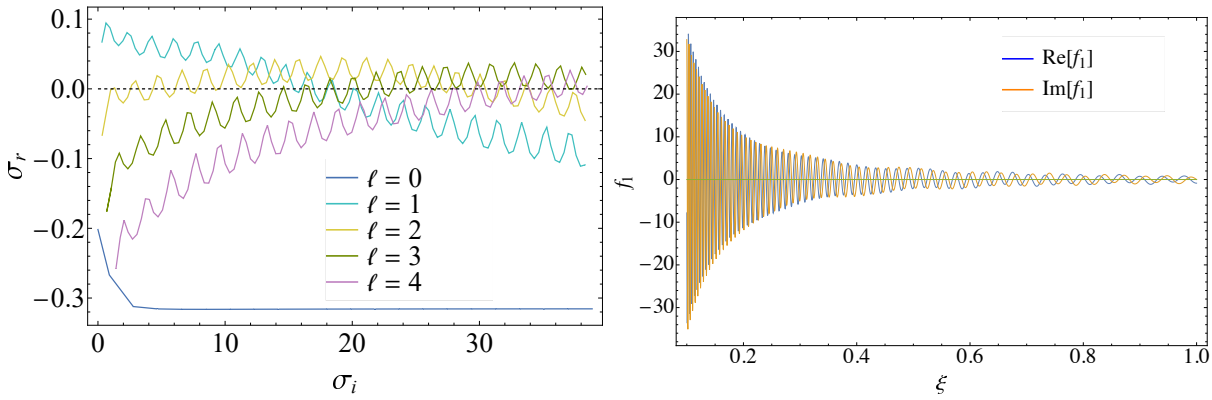

Figure 20: Left:The growth rate σ_r against the oscillation frequency σ_i for different values of ℓ as shown by the legends. Right: The real and imaginary parts of the first order perturbation to the post-shock fluid radial velocity corresponding to the maximally unstable mode with $\ell = 2$.

[34] although only for the $\ell = 1$ modes (see their Figure 7). We show the oscillating *eigenspectrum* for $\ell = 1 - 4$ in Figure 20, where we have calculated many closely spaced discrete modes and joined them with a continuous line.

6.2.3 $\ell = 1$, the *classic* SASI at low oscillation frequency

As discussed above, in all major previous SASI studies, the $\ell = 1$ oscillation modes are found to be the unstable; in-fact they are found to be the most unstable non radial modes. We also find the modes to be unstable for smaller values of the oscillation frequency σ_i, but they become stable for a sufficiently large value of σ_i ($\sigma_i \gtrsim 20$, in Figure 20). The maximum growth rate is found to be ~ 0.08, which is the **highest compared to other high-ℓ unstable modes**. These are indeed signatures of classic SASI.

6.2.4 $\ell = 2$, the surprise?

Now, the $\ell = 2$ comes with real surprise. In Figure 20 we see that although the solutions are stable at low values ($\sigma_i \lesssim 2$) of the oscillation frequency, there is **range of oscillation frequencies** ($5 \lesssim \sigma_i \lesssim 35$, in Figure 20) which the solutions are unstable.**This timescale associated with these frequencies are surprisingly very close to the frequency associated with the dynamical timescale of the neutron star (which is $\xi_{ns}^{-1.5}$ in this dimensionless unit we are using)**. This is one of our main results. The growth rates corresponding to these unstable modes are smaller compared to the unstable modes of $\ell = 1$, for example, the maximum growth rate for $\ell = 2$ we find is ~ 0.04, a factor of 2 reduced. The maximum instability also occurs at a large value of the oscillation frequency, i.e., at $\sigma_i \sim 20$. In the right panel of Figure 20, we present the

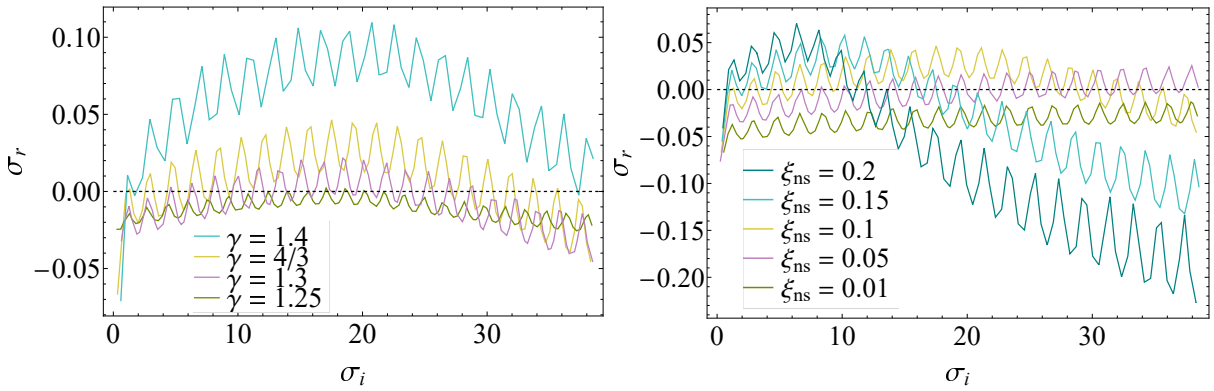

Figure 21: Left: $\ell = 2$ eigen spectrum while the adiabatic index γ is being varied while keeping ξ_{ns} fixed at 0.1. Right: $\ell = 2$ eigen spectrum, while the neutron star radius, ξ_{ns} is varied while the adiabatic index γ is kept fixed at 4/3.

real and imaginary components of the radial component of the post-shock fluid velocity corresponding to the maximally unstable mode. This mode oscillates wildly, and we see that, in contrast to the stable modes, here, any small perturbation that originated at the shock location amplifies significantly as it reaches the surface of the neutron star. This finding has previously unexplored implications for gravitational wave emission in CCSNes, which will be presented in Section 6.4.

6.2.4.1 Impact of Varying the Adiabatic index

In this subsection, we discuss the effect of changing the adiabatic index γ of the post-shock fluid while keeping the neutron star radius ξ_{ns} fixed at 0.1. We present the results of this effort in the left panel of Figure 21. **We see that as the value of γ decreases from 4/3 to 1.3, the shape of the *eigenspectra* remains similar but the whole curve shifts down (toward the negative Y- axis) and for $\gamma = 1.25$, the X- axis is almost tangent to the maximum of the curve; implying that this instability disappears if γ reduces any further. We note that reducing γ is an effective way of mimicking radiative losses. In their numerical simulation[25] also find that the instability weakens with a reduction γ value; this can be manifested by the following two considerations: if SASI arises due to some sort of vortical-accoustic feedback cycle [259, 33, 34], then neutrino cooling might dampen the feedback mechanism by dampening the pressure waves, or neutrino cooling can simply drive the shock away from the conditions leading to the instability by reducing the post-shock volume [25]. On the contrary, increases in the value of γ strengthen the instability, as is evident from the $\gamma = 1.4$ curve.**

6.2.4.2 Impact of Changing the Neutron Star Radius

In the right panel of Figure 21, for a $\gamma = 4/3$ post-shock fluid we vary the value of the neutron star radius and hence the value of ξ_{ns}. As can be seen, for an extended shock envelope (that is, low value of ξ_{ns}, the strength of the instability decreases (that is, magnitude of σ_r) while the instability shifts right to the X-axis, that is, the instability appears at a very high value of σ_i. On the contrary, as the size of the shocked envelope decreases, the magnitude of the instability increases, the band of frequencies over which the instability lives shortens, and the location of the maximum instability moves towards progressively lower values of σ_r.

6.2.4.3 Impact of Cooling function

To mimic the neutrino cooling mechanism in the context of core collapse, major SASI investigation studies have incorporated a parameterized cooling function of the form $\mathcal{L} \propto \rho^{\beta-\alpha} p^{\alpha}$ [30, 26, 261], where α and β are two parameters determining the cooling strength. In [26] two different choices for the cooling function have been discussed, one with $\alpha = 3/2, \beta = 5/2$ $(\alpha - \beta < 0)$ and the other with $\alpha = 6, \beta = 1$ $(\alpha - \beta > 0)$. With $\alpha - \beta < 0$ the cooling efficiency increases as the gas cools down, and the other way around for $\alpha - \beta > 0$. The inclusion of the cooling function modifies the background flow as a result of the modification of the radial momentum and entropy equation. These modified equations are given in Section 6.1.5. The background flow obtained by solving Equation (6.33) for the boundary condition (6.34). The solutions obtained for the two cooling functions mentioned above are presented alongside the original settling solutions in the left panel of Figure 22. We see that the velocity profiles are similar in the outer parts of the flow, but differ in the inner part. This is further clear when one looks at the first derivatives of the flow in the right panel of Figure 22. We see that while the $\alpha = 3/2, \beta = 5/2$ cooling causes the flow to decelerate near the accretor surface, the $\alpha = 6, \beta = 1$ causes the flow to accelerate.

6.2.5 $\ell > 2$

In Figure 20, we see for $\ell > 2$ while the *eigenspectra* continues to display similar oscillating characteristic shown by the $\ell = 2$ modes; the instability is weakened and onset of any such instability moves towards higher values of σ_r.

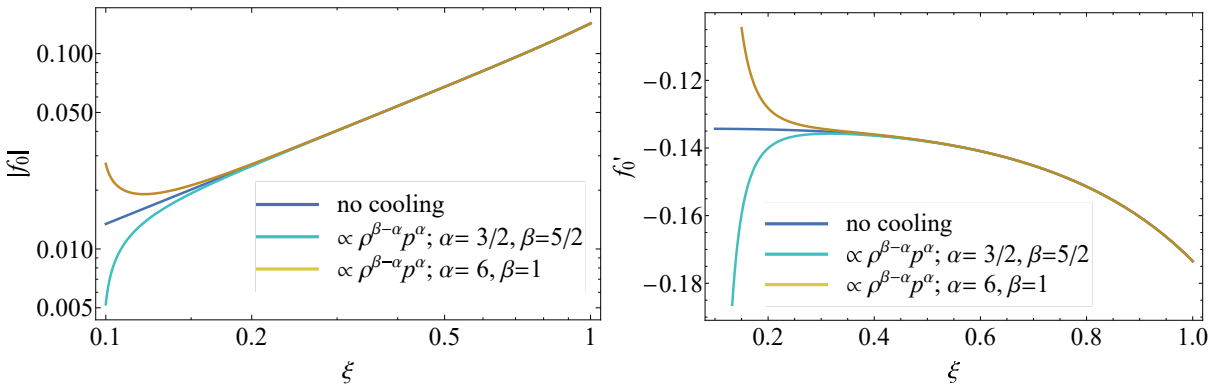

Figure 22: The modulus of the dimensionless, radial velocity ($f_{\rm r}$, left), the dimensionless density (g, middle), and the dimensionless pressure (h, right) as functions of $\xi = r/R$. With $\alpha < \beta$ ($\alpha > \beta$) the gas reaches the surface of the accretor in finite (infinite) time.

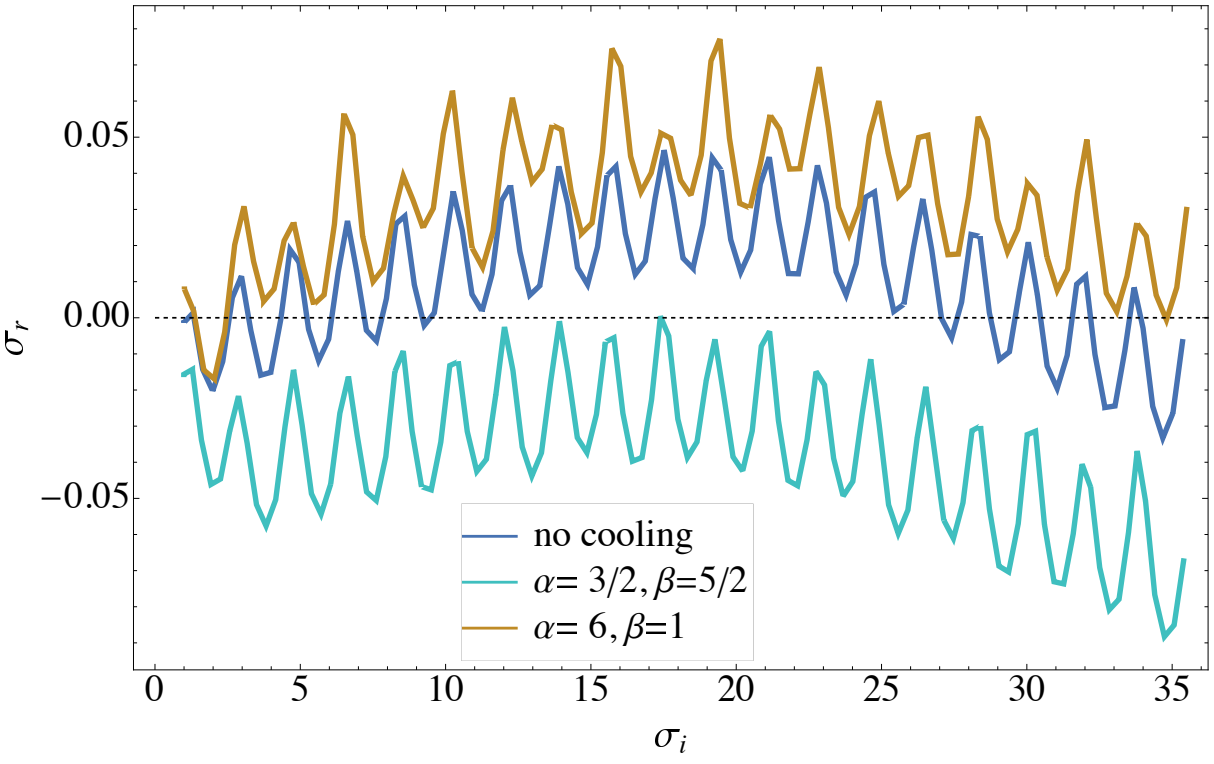

Figure 23: The modulus of the dimensionless, radial velocity ($f_{\rm r}$, left), the dimensionless density (g, middle), and the dimensionless pressure (h, right) as functions of $\xi = r/R$. Cooling with $\alpha < \beta$ ($\alpha > \beta$) boosts (weakens) the instability, which agrees well when we examined the same effect by varying the adiabatic index, γ.

6.3 Implications for explodability

The unstable $\ell = 2$ modes described here in the linear regime will grow and couple with each other. Moreover, as the oscillation timescale of the most unstable modes matches closely with the dynamical timescale of the neutron star, the unstable SASI modes will soon start ringing the oscillation of the neutron star. According to the addition rules of the spherical harmonics when the $\ell = 2$ modes couple, the power is divided into parts among lower order $\ell = 0$ modes, higher order $\ell = 4$ modes, and $\ell = 2$ modes. This process would soon cascade and provide power to all the other non-radial and radial modes. Once the amplitudes of these unstable oscillations grow, the process would delegate to the non-linear regime, and there would be coupling between different modes. Therefore, the cavity would soon undergo a turbulent motion. This turbulent motion further interacts with the shock and completes a feedback loop and a dramatic increase in the total turbulent energy in the cavity, where the turbulent energy is usually defined as:

$$E_{turb} = \frac{1}{2}\rho|\vec{\delta v}|^2 \tag{6.63}$$

where δv_i denotes the difference in the fluid velocity and the angle-averaged radial velocity of the flow [285, 186]. As shown by [36], this turbulent energy is more valuable than the thermal energy of the fluid to overcome the ram pressure of the infalling gas. [285] show the effective pressure support due to turbulent motion is 50% larger than the thermal pressure, and hence this added pressure support can cause an increase of the shock radius up to 25% [286]. Therefore, the variations in the shock radius caused by SASI would lead to radial entropy gradients from which turbulent convection will be further improved [249, 287]. Therefore, the ratio of turbulent energy to the thermal energy plays a crucial role in the asymmetric explosion seen in successful supernova explosions [36, 37, 38].

6.4 Implications for Gravitational Waves

Recently [258]([2]) have presented gravitational wave (GW) signal obtained from a set of three- (two)-dimensional multigroup neutrino radiation hydrodynamic simulations of CCSNe and [40] has discussed the measurability of this signal by third-generation gravitational wave detectors. The stellar progenitors they consider range from $9 - 60 M_{\odot}$ and are listed in Table 2. A summary of the simulation settings can be found in Section 5.1 of this thesis and further details can be found in [258, 2]. The simulation data specifies the fluid properties of interests to describe the progenitor from 0.1285 s before the core bounce to 1.2155s, in an interval of 0.0010s. The radial extension under inspection that extends from 25000.4 cm to 1.99021×10^9 cm is divided into 678 discrete points. The radial point where the density falls below 10^{10} gm/cm^3 is taken to be the surface of the

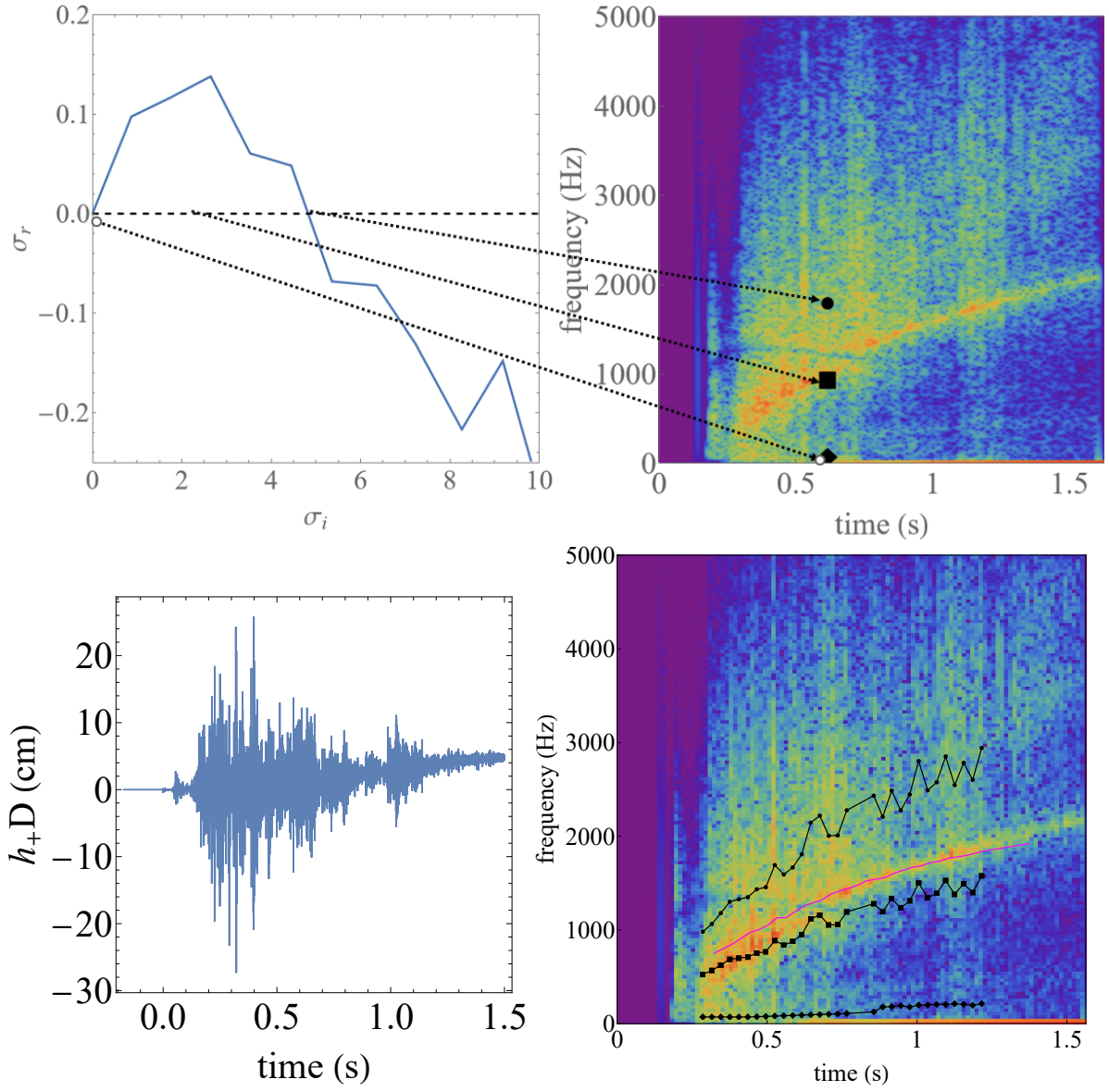

Figure 24: Data obtained from a 2-D simulation of a $10M_\odot$ progenitor of [2]. Top-Left: The oscillatory eigenspectrum of $\ell = 2$ modes at $t = 0.6155$s with $\xi_{NS} := R_{NS}/R = 0.394389$ and $\gamma_{mean} = 1.38631$ is calculated over the radial extent. Top-Right: The identification of the unstable modes with lowest, highest and the most unstable mode on the spectrogram. Bottom-Left: the strain times distance of GW, h_+D, bottom-right: the time-frequency representation (that is, spectrogram) of the strain signal. The pink line indicates the f-mode evolution obtained in asteroseismology, the black line with dots indicates the unstable SASI modes with the highest frequency, the black line with diamonds indicates the unstable SASI modes with the lowest frequency, and the black line with the squares on it indicates the unstable modes with maximum instability.

neutron star. On the other hand, the location of discontinuity in the velocity profile denotes the location of the shock. From this data, at each instant of time we calculate the value of ξ_{ns} as the ratio of the neutron star radius and the shock radius and γ_{mean} is the mean of the adiabatic index values γ specified at each radial point. This two data enables us to compute the *range* of $l = 2$ unstable SASI modes at each instant of time. To illustrate this procedure, in the top-left panel of Figure 24 we present the oscillation in the $\ell = 2$ eigenspectrum calculated for the $10M_{\odot}$ progenitor at 0.6155 s after the core bounce. Using the simulated data, we calculate $\xi_{NS} := R_{NS}/R = 0.394389$ and $\gamma_{mean} = 1.38631$ over the radial extent of the envelope at that instant. We then immediately find the frequency where the unstable region starts and the frequency where the unstable region ends along with the frequency corresponding to the mode that shows the maximum instability (with $Max(\sigma_r)$): These three frequencies are then mapped onto the spectrogram with black dots, diamonds, and squares, respectively. The specific algorithm used to generate the spectrogram is described in Section 5.3 of this thesis. By repeating this procedure for the entire duration of the data, we connect the points with lines and overlay them on the spectrogram in the bottom right panel of Figure 24. The fundamental modes of oscillations of the PNS as calculated in perturbation theory following [2, 258, 255] are also overlaid on the diagram in pink. We see that a few hundred milliseconds of core bounce, the GW signal is dominated by $l = 2$ oscillation modes of the PNS confirming the finding of [2] (see also [255] who run an independent set of simulations but make similar findings) and these frequencies match well with the frequencies of the most unstable $\ell = 2$ SASI modes. Therefore, we sense a strong possibility that the unstable $l = 2$ modes of the SASI oscillations act as a hammer to ring the PNS like a bell. This explains the fact that we do not see other oscillation modes of the PNS such as g-modes or p-modes (obtained in asteroseismology) that contribute to the gravitational wave signal, since only the $f-$mode frequencies match and hence are excited by the unstable SASI modes. The time-domain strain (times distance) GW signal is presented in the bottom right panel.

6.5 Summary

In this work, we have attempted to perform a linear perturbation analysis on the famous "settling solutions" –used famously as the background state for the work of [25] revamping SASI. Our major findings are:

1. We first confirm the *traditional* finding of SASI literature by finding unstable $\ell = 1$ modes at low-oscillation frequency compared to the frequency associated with the dynamic timescale of the accretor. The growth rate of these modes is highest in comparison to the other high-ℓ unstable modes.

2. We find an oscillation in the eigenspectrum of the $\ell = 2$ modes. A whole range of modes are found to be unstable, whose frequencies are high and very close to the frequency associated with the dynamical timescale of the neutron star.

3. We have examined the effect of cooling on these unstable modes-first by considering the low value of the adiabatic index γ and then incorporating two different cooling functions. As the cooling efficiency increases, the instability weakens.

4. The unstable modes that we find would couple with each other and with the oscillation modes of the neutron star, owing to being similar to the frequency associated with the dynamical timescale of the neutron star. This cascade effect will strengthen the turbulence in the SASI cavity and contribute to the ultimate revitalization of the shock.

5. The gravitational wave seen in state-of-art Supernovae simulations carry the signature of fundamental oscillation of the neutron star. We discuss the possibility of ringing the neutron star at the first place by the unstable $\ell = 2$ SASI modes that we present here.

The next step in extending our present analysis is to carry out perturbation analysis on the general relativistic extension of the Newtonian settling solutions presented in Chapter 4. The other avenue would be to investigate the origin of this instability. The WKB approximation near the surface of the neutron star might hint into the origin and will be explored in the future.

Chapter 7

Star crushed by black hole

Tidal disruption events occur when a star gets so close to a supermassive black hole (SMBH) that the tides imparted by the latter tear the star apart [51, 52, 53, 110, 54, 55]. The observation of these events has received an impetus in the last decade, and current (e.g., Chandra, Swift, SRG/eROSITA) and upcoming high-cadence wide-field all-sky surveys (e.g. SKA, LSST, Einstein probe) promise an exciting time ahead (see [288] for a detailed review of the observational status).

The outcome of a TDE depends largely on how close the star comes to the SMBH, which is implicitly defined via $\beta \equiv r_{\rm t}/r_{\rm p}$, where $r_{\rm t} \equiv R_\star \left(M_\bullet/M_\star\right)^{1/3}$, the tidal radius, is roughly the distance at which the SMBH tidal force equals the self-gravity of the star of radius $R_\star$ and mass $M_\star$, and $r_{\rm p}$ is the point of closest approach between the two bodies [51]. Events with $\beta \lesssim 1$ are partial TDEs, where a fraction of the star survives the encounter intact [84, 107, 160, 90]. In contrast, in events with $\beta \gg 1$ — "deep TDEs" — the gravity of the SMBH overwhelms the self-gravity of the star and the star is compressed by the vertical component of the tidal field of the SMBH [289, 290, 291, 292, 89, 93]. The degree of tidal compression suffered by a star in deep TDEs has been studied by, e.g., [109, 110, 108, 57, 3, 111, 4, 290, 293, 294].

[57, hereafter CL82] and [3, hereafter CL83] found that as the β of the encounter increases, the star experiences an increasing degree of adiabatic compression and its density increases to a maximum value $\rho_{\rm max}$ at roughly the time it reaches the pericenter. For radiative stars modeled with the Eddington standard model (e.g., [100]), in events with $\beta \gtrsim 5$ they claimed $\rho_{\rm max}/\rho_{\rm c} = 0.22\beta^3$, where $\rho_{\rm c}$ is the original, central stellar density. From Figure 13 of [4, LC86, hereafter], for a 3 $M_\odot$ standard-model star, the central density (temperature) increases by a factor of ~ 50 (10) for $\beta = 5$ and ~ 500 (50) when $\beta = 10$. As a consequence of this sharp increase in central density and temperature, these authors predicted that in $\beta \gtrsim 5$ encounters the energy released from the triple-α process ignites helium-burning reactions, which was supported by [295, 296, 297] and even a second

burst of nuclear energy release was postulated [298]. Almost immediate criticism of the work of Carter and Luminet came from [58], who used numerical techniques to refute the possibility of helium detonation as they found significantly milder compression. Despite many efforts, to date the degree of tidal compression in deep TDEs – and therefore the possibility of thermonuclear ignition – has not reached a consensus [289, 290, 294].

Recently, [92] and [5, hereafter CN22] analyzed the deep TDE regime using analytical and numerical methods, focusing mainly on a $\gamma = 5/3$ polytrope, and found that the β^3 scaling is generally not followed. However, they briefly considered a standard-model star *analytically* and concluded that these stars also do not adhere to the above scaling. To further understand the compression experienced by a radiative star during a deep tidal encounter, here we numerically analyze the maximum central density and temperature achieved by a Sun-like star modeled with the Eddington standard model during a deep TDE.

In Section 7.1 we recapitulate the analytical analysis of CN22 adapted for standard-model stars. In Section 7.2 we present the results of numerical simulations, and we make comparisons to, and demonstrate excellent agreement with, the analytical model; we also analyze the convergence of the simulations with respect to particle number and briefly consider the effects of general relativity. We summarize and conclude in Section 7.3.

In Section 7.1 we recapitulate the analytical analysis of CN22 adapted for standard-model stars. In Section 7.2 we present the results of numerical simulations, and we make comparisons to, and demonstrate excellent agreement with, the analytical model; we also analyze the convergence of the simulations with respect to particle number and briefly consider the effects of general relativity. We summarize and conclude in Section 7.3.

7.1 Analytic Estimates

In the present analysis, we consider a star of mass $M_\star = 1M_\odot$ and radii $R_\star = 1R_\odot$ (yielding avearage density, $\rho_\star = 3M_\star/\pi R_\star^3$) as a spherical cloud of classical perfect gas and radiation. To model such radiative stars, the Eddington standard model is a natural choice, and we choose a model with a polytropic index $\Gamma = 4/3$ (such that the pressure, p, is related to the density, ρ according to $p \propto \rho^\Gamma$) and an adiabatic index $\gamma = 5/3$ (the ratio between the specific heats). We assume the star to be in hydro-static equilibrium far away from the hole, i.e. the gas pressure perfectly balances the self-gravity at infinity. This assumption allows us to talk about a well-defined geometric center of the star, and we denote the density and the pressure at that center point of the star as ρ_c and p_c respectively. The ratio of the core density to the average density of such a star is $\rho_c/\rho_\star \simeq 54.2$. We combine the central density and pressure, ρ_c and p_c to define the

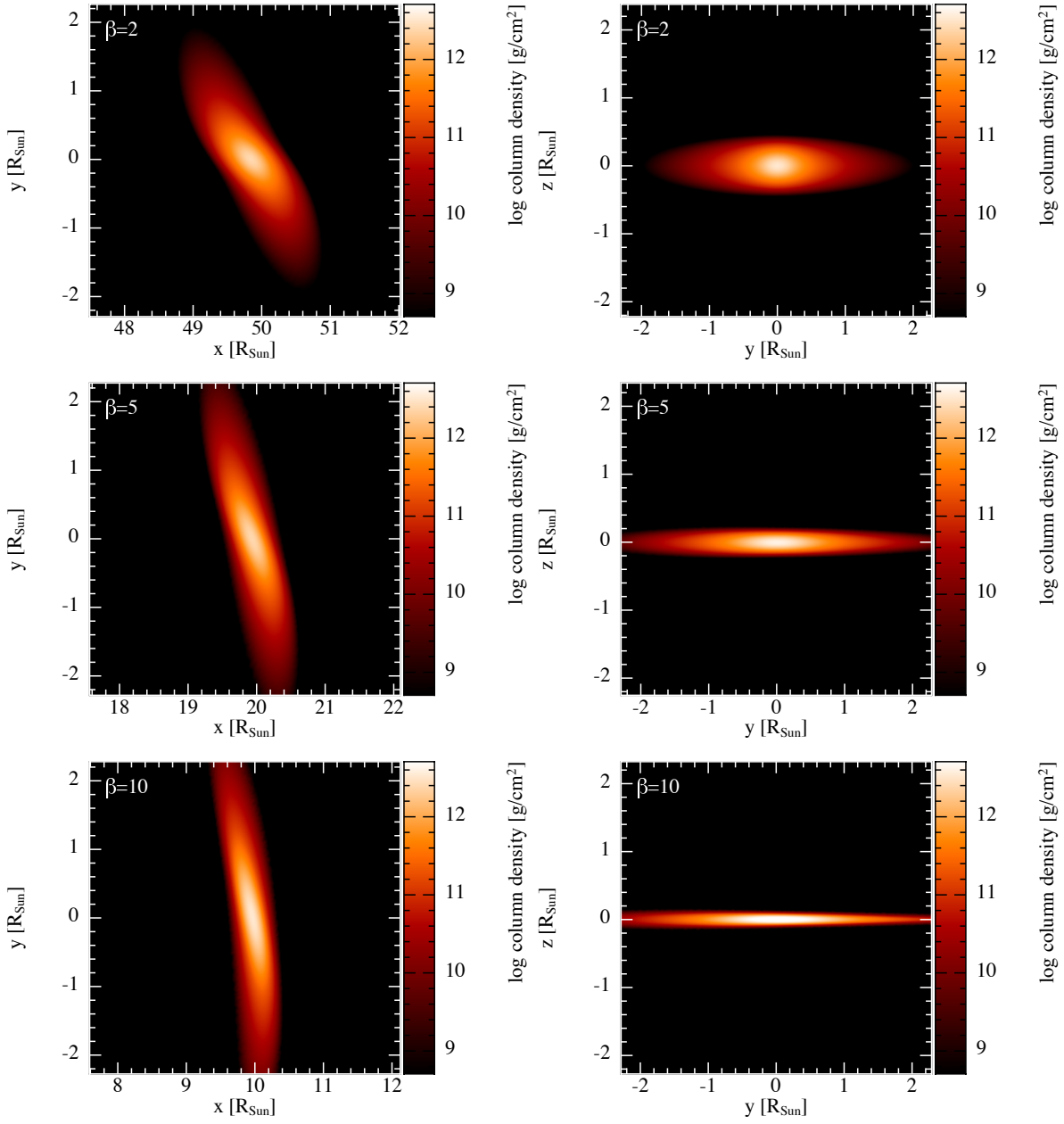

Figure 25: The integrated column density at the time when the center of mass of the star reaches pericenter. The value of β is shown in the top-left of each panel. The left panels show the distribution of stellar material in the orbital plane, and the corresponding right panels show the view perpendicular to that plane. In the convention we adopt, both the initial x, y coordinate of the center of mass of the star starts with negative values, and arrives the pericenter with a positive x-coordinate value and $y = 0$. Thus, any fluid element with a positive (negative) y-value has already (not yet) passed through its pericenter. Increasing β clearly leads to an increase in the flattening, or "crushing" of the star, into the orbital plane near pericenter.

following star-specific length scale α, to be used in normalization of the length scale in the problem as

$$\alpha^2 = \frac{6\gamma p_c}{\rho_c}\frac{1}{4\pi G\rho_c} \tag{7.1}$$

where G is the Newton's Gravitational constant.

We assume a star starting its journey from infinity with zero energy; the orbit of such a star is parabolic. To describe the tidal interaction between the black hole and the star, we adhere the "tidal-approximation" - which implies any internal, intra-body dynamics governed by hydro dynamical processes operating on $T_{int} \sim (R_\star^3/GM_{star})^{1/2} << $ the orbital time scale, $T_{orb} \sim (r_c^3)/GM_{star}$ when the size of the star $R_\star << $ the separation distance between the center of mass of the star and the black hole, r_c. This approximation considerably simplifies the calculation [299]. To analyze the tidal compression the star suffers, it suffices to focus only on the out-of-plane vertical compression while ignoring the compression the star suffers in the other two orthogonal in-plane directions, as they approximately nullify each other. We choose to work in a body-centered coordinate system whose origin coincides with the center of mass of the star. Due to the fact that the star is in parabolic orbit, the equation for the center-of-mass distance r_c is [300],

$$\frac{1}{2}\left(\frac{\partial r_c}{\partial t}\right)^2 + \frac{GM_\bullet r_p}{r_c^2} - \frac{GM_\bullet}{r_c} = 0 \tag{7.2}$$

where $r_p = r_t/\beta$, is the distance of closest approach (i.e. pericenter distance). We would like to introduce a natural time-scale τ in this problem, defining it as

$$\frac{\partial \tau}{\partial t} = \sqrt{\frac{GM_\bullet}{2r_c^3}} \tag{7.3}$$

The solution of Equation 7.2 can then be expressed as

$$r_c = r_p \cosh^2(\tau) \tag{7.4}$$

We assume a linear relationship between the perturbed and the original height of a particular fluid element, where the connection term only depends on the time coordinate and not on the spatial co-ordinates,

$$z = H(\tau)z_0 \tag{7.5}$$

Physically this means that we are assuming that the compression of the star is homologous. In a more realistic situation, this relationship should be thought of as the leading-order term in a power series expansion of the appropriate relation between the current and the original Lagrangian fluid position [4, 5]. In this one-dimensional out-of-plane

motion, the integrated mass to any position z above the plane is a conserved quantity in Lagrangian sense and hence,

$$\rho(z,\tau) = \frac{\partial z_0}{\partial z}\rho_0\big[z_0 = z_0(z,\tau)\big] = \frac{1}{H(\tau)}\rho_0\big[z/H(\tau)\big] \tag{7.6}$$

, ρ_0 being the density profile of the original configuration. Owing to our spherically symmetric approximation with a well-defined maximum density at the center, we can express the original density at any location within the star in terms of that central density.

$$\rho_0(z_0) \simeq \rho_c\left(1 - \frac{s_0^2 + z_0^2}{\alpha^2} + \mathcal{O}\left[(s_0^2 + z_0^2)^2\right]\right) \tag{7.7}$$

where s_0 is the cylindrical radial co-ordinate (i.e. distance from the vertical axes). Now, substituting Equation 7.7 into Equation 7.6 we get

$$\rho(z,\tau) = \rho_c\frac{\partial z_0}{\partial z}\left(1 - \frac{s_0^2 + z_0^2}{\alpha^2}\right) = \frac{\rho_c}{H(\tau)}\left(1 - \frac{s_0^2 + z_0^2}{\alpha^2}\right) \tag{7.8}$$

To further facilitate our calculation, we choose to introduce a new dimensionless variable u_0 as,

$$u_0 := \frac{z_0}{\alpha} \tag{7.9}$$

we rewrite Equation 7.8 in terms of u_0,

$$\rho(z,\tau) = \frac{\rho_c}{H(\tau)}\left(1 - (s_0'^2 + u_0^2)\right), \text{ where } s_0' := \frac{s_0}{\alpha} \tag{7.10}$$

We are not considering any source of energy injection or extraction in this process; the compression can be considered adiabatic, which implies,

$$p(z,\tau) = S_0(z_0)\rho^\gamma \tag{7.11}$$

where $S_0(z_0)$ is the entropy profile, - - a natural adiabatic invariant. Thus the pressure to the leading order is

$$p(z,\tau) \simeq p_c H^{-\gamma}\left(1 - \gamma(s_0'^2 + u_0^2)\right) \tag{7.12}$$

The internal gravitational potential of the star Φ, is to be solved for from the Poisson equation,

$$\nabla^2\Phi = 4\pi G\rho. \tag{7.13}$$

In spherical polar coordinate the solution of which reads

$$\Phi(t,r) = \frac{Gm(r,t)}{r} + 4\pi G\int_r^{R_\star}\rho(r',t)dr' \tag{7.14}$$

where $m(t,r)$ is defined as

$$m(t,r) := 4\pi\int_0^r \rho(r',t)dr' \tag{7.15}$$

In case of spherically symmetric stars in high-β encounter, where the pressure of the gas overwhelms the self gravity; instead of the full expression for the density ρ as in Equation 7.8, we use the leading order term (i.e. $\rho \simeq \rho_c/H$) in Equations 7.14 and 7.15. Doing so yields

$$\Phi = 4\pi G\rho_c\alpha^2 H^{-1}\frac{r^2}{6} + C(R_\star) \tag{7.16}$$

where $C(R_\star)$ is a constant term expressed in terms of the radii of the star and $r = \sqrt{s^2+z^2}$, the radial distance of the fluid element from the center of mass of the star. The equation of motion for such a fluid element located at a height z above orbital plane at time t is the z-component of the momentum equation, which reads

$$\frac{\partial^2 z}{\partial t^2} + \frac{1}{\rho}\frac{\partial p}{\partial z} = -\frac{GM_\bullet z}{r_c^3} - \frac{\partial \Phi}{\partial z} \tag{7.17}$$

We can substitute the expressions for r_c, p, Φ as in Equation 7.4, 7.12, 7.16 and the definitions of τ, z, u_0 as in Equation 7.3, 7.5, 7.9 in Equation 7.17 and equate the leading order terms in u_0 to arrive,

$$\mathcal{L}[H] - \frac{2}{\beta^3}\frac{\rho_c}{p_c}(H^{-\gamma}-1)\cosh^6(\tau) = 0 \tag{7.18}$$

where the operator $\mathcal{L}$ is

$$\mathcal{L} = \frac{\partial^2}{\partial\tau^2} - 3\tanh(\tau)\frac{\partial}{\partial\tau} + 2 \tag{7.19}$$

The last two terms in Equation 7.18 after the dynamical term (i.e. $\mathcal{L}[H]$) come from the contribution of gas-pressure and self gravity respectively. We note, in a model where self-gravity and gas-pressure is neglected (i.e. the gas free-falls in the tidal field), the governing equation of motion is

$$\mathcal{L}[H] = 0,\ \mathcal{L} \text{ is the same operator as expressed in Equation 7.19.} \tag{7.20}$$

Following [56, 293], we further assume that the star retains its hydro-static equilibrium until reaching the tidal radius; one can write the following closed-form solution for Equation 7.20,

$$\frac{z}{z_0} = \frac{1 - 2\sqrt{\beta-1}\sinh\tau - \sinh^2(\tau)}{\beta} \equiv H(\tau) \tag{7.21}$$

subject to the initial conditions $z(\tau_t) = z_0$ and $\dot{z}(\tau_t) = 0$, where z_0 is the initial height of the fluid element orthogonal to the orbital plane and $\tau_t = -\operatorname{arcsinh}(\sqrt{\beta-1})$ is the time when the center of mass reaches the tidal radius. On the other hand, to solve Equation (7.18), we must resort to numerical techniques. We do so by adopting the initial conditions $H(\tau \to -\infty) = 1$ and $\dot{H}(\tau \to -\infty) = 0$; again the star is assumed to maintain its hydro-static balance until it reaches the tidal radius.

We present the solutions, i.e. H as a function of the time coordinate τ, obtained for the range of $\beta = 2 - 10$ values, as shown by the legends, in the left panel of Figure 26.

Solid lines are the solutions obtained including pressure and self-gravity (i.e., solutions of Equation 7.18) and in dashed lines are the solutions when the gas free-falls in the tidal field (i.e., solutions of Equation 7.20). The pressureless solution goes to zero at a time of $\sinh(\tau_{cr}) = \sqrt{\beta} - \sqrt{\beta - 1}$, which can be calculated from Equation 7.21 and the plot confirms that. We note that the self-gravity and pressure become significant in modifying the solution H, much earlier times in comparison to the time when the star would be compressed to zero height, i.e. $H = 0$ in the free-fall case. And as β increases, the solution considering self-gravity and pressure starts to depart from the free-fall solutions at much earlier times; the amount of departure also increases. In the right panel of Figure 26, we show the density of the geometric center of the star normalized by the original density of the same point as a function of time normalized by the dynamical time of the star. We see that as β increases, the maximum density achieved increases and occurs at an earlier time (after the moment $t = 0$ when the center of much reaches the pericenter).

In Figure 27, we highlight the run of the maximum density (left) and maximum temperature (right) achieved during the tidal compression process in the geometric center of the star, normalized to its original value, with the run of the penetration factor β. The temperature is calculated assuming that the gas pressure dominates over the radiation pressure and thus can be well approximated as $T \propto p/\rho$. The blue dashed line, in each panel, shows the large-β ($\beta \gtrsim 20$) behavior which we find to scale as $\propto \beta^3$ for the maximum density and $\propto \beta^2$ for the maximum temperature. Although [3] predicted similar scalings, and we present their prediction with the black dashed lines on our plot; the proportionality factor that we find here is much smaller than what they predicted. For this $\Gamma = 4/3, \gamma = 5/3$ model, in the scaling relation of the maximum density and temperature with β, the proportionality factors in [3]'s works are respectively ~ 41 times and ~ 12 times larger than the factors we find here. This reduction of the proportionality factors is a direct consequence of the consideration of gas pressure; its clear that the gradient in gas pressure is able to counter the compression when the gas pressure becomes only a fraction of the free-fall ram pressure.

As a check of the above mentioned claim about the gas pressure, in the left panel of Figure 28 we display the ratio of the gas pressure to the ram pressure (calculated as the $density \times velocity^2$) of the freely falling fluid. We notice that for high β, the ratio approaches nearly a constant at the time of maximum compression and this constant is much smaller than 1. Next, in the right panel, we illustrate the velocity at the surface of the star calculated as

$$v_z = \frac{\partial z}{\partial t}(z_0 = R_\star) = V_\star \frac{\beta^{3/2}}{\cosh^3 \tau} \frac{dH(\tau)}{d\tau} \tag{7.22}$$

normalized to the escape velocity on the surface, $V_\star = (\alpha/R_\star)\sqrt{GM_\star/2R_\star}$, as a function

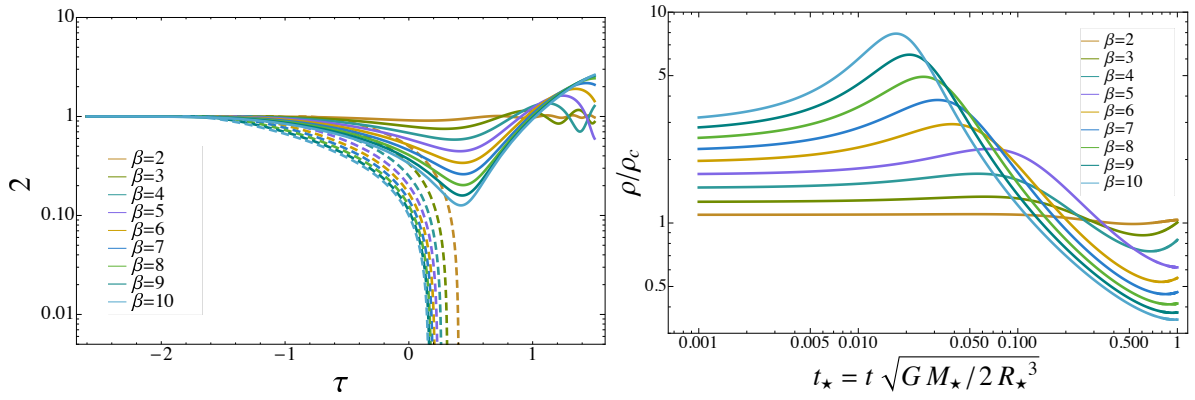

Figure 26: Left:The Solution for H, considering gas pressure and self gravity (solid curves) along with the solutions obtained when the gas free-falls in the tidal field (dashed curves). This shows that the self-gravity and pressure of the gas starts to play significant roles to counter the compression at much earlier times than when the star would be compressed to zero height ($H = 0$) in the free-fall case (i.e this time is to be read when the dashed curves goes vertical). Right: The ratio of the central density normalized to its original value as a function of time normalized by the dynamical time of the star. As β increases, the time of the maximum density achieved approaches 0, the time when the center of mass reaches the pericenter and the compression increases significantly.

of time, t. The velocity starts and remains negative approximately until the center of mass reaches the pericenter. At the pericenter, the velocity reaches its minimum with a value $v \simeq -2\beta V_\star$ agreeing with the free-fall solutions of [293]. The gas pressure then succeeds in reversing the compression, brings it to zero, and then increases to a positive maximum of $v \simeq 2\beta V_\star$ before decaying again.

7.2 Numerical simulations

7.2.1 Simulation setup

Here we present the results of numerical simulations of disruptions of Sun-like stars modeled with the Eddington standard model. We use the smoothed-particle hydrodynamics (SPH) code PHANTOM [301], which has been widely used for studying TDEs [85, 86, 90, 92, 302].

The Eddington standard model is implemented in our code in the following way: a discrete radial grid is constructed with a large number of sufficiently close points extending from the center of the star to the surface. We then assign to these points the appropriate density and pressure that are obtained by numerically integrating the Lane-Emden equation. The configuration is then "relaxed" in isolation (i.e., without the gravitational

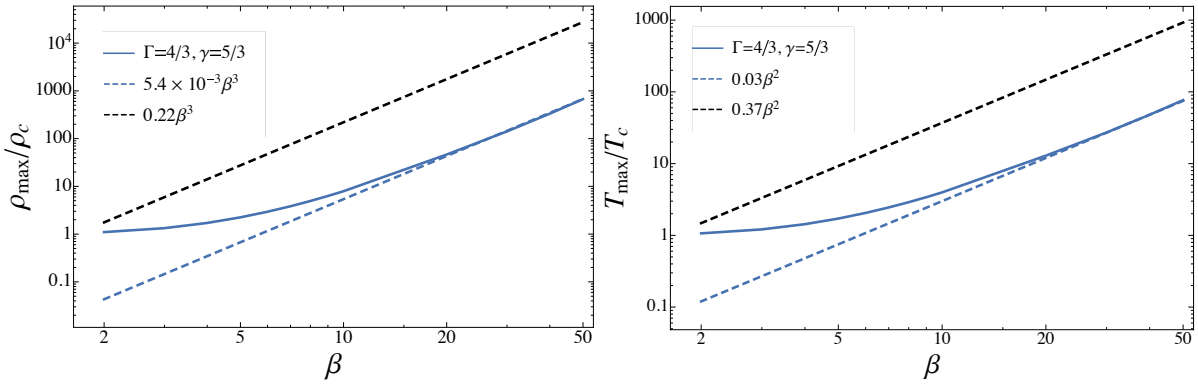

Figure 27: The maximum central density (temperature) normalized to the original density (temperature) at the center as a function of the penetration factor, β in the left (right) panel. The blue dashed lines indicate the large-β behavior of our solution while the black dashed lines indicate the corresponding scalings predicted by [3].

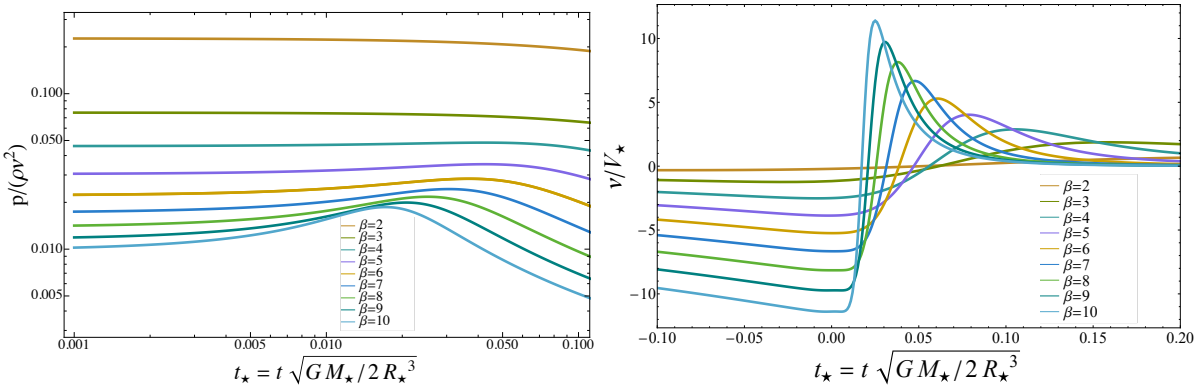

Figure 28: Left: The ratio of gas pressure to the ram pressure of the freely falling fluid as a function of time normalized by the dynamical time of the star. The ratio being much smaller to 1 indicates the fact that the gas pressure succeeds in resisting the compression much before it becomes comparable to the ram pressure. Right: The velocity of the fluid element normalized to the escape velocity as the function of time normalized to the dynamical time of the star.

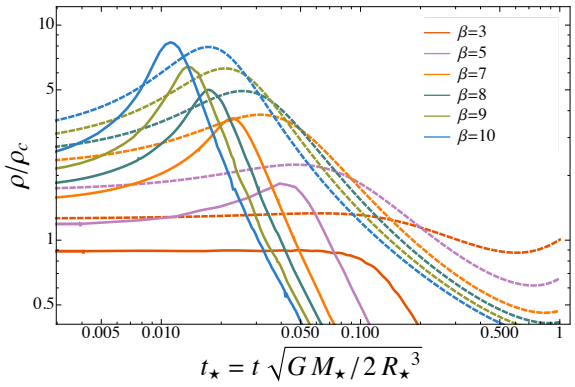

Figure 29: The central density normalized to its original value as a function of time normalized by the dynamical time of the star. The different curves are appropriate to the β in the legend, with solid (dashed) curves resulting from the numerical simulations (analytic model). The magnitude of the compression and time of the maximum compression agrees reasonably well between the SPH and analytic results.

field of the black hole) for ten sound crossing times to remove numerical perturbations. The center of mass of the relaxed star is then placed at a distance of $5r_{\rm t}$ from the black hole, so that all particles move with the center of mass, which is on a parabolic orbit with pericenter distance $r_{\rm p} = r_{\rm t}/\beta$. The self-gravity and viscosity switches are implemented through standard routines (see [92]). We simulate encounters with $2 \leq \beta \leq 10$ in integer steps.

7.2.2 Simulation Results

In the left (right) panel of Figure 25, we present the integrated column density as seen in the orbital plane (out of the orbital plane), when the center of mass of the star reaches the pericenter. The β of the encounter is shown in the top left of each panel. The pericenter is in the x-direction, the $x-y$ plane is the orbital plane, and the $y-z$ plane is orthogonal to the orbital plane. As seen in the figure, the star suffers a significant distortion in the process, and as β increases, it is compressed vertically into a small fraction of its original volume.

Figure 29 shows the central density normalized to its original value as a function of time normalized by the dynamical time of the star. Solid curves result from simulations, whereas dashed curves are the corresponding analytic predictions. As β increases, the magnitude of the maximum density achieved (that is, the height of the peak) during the encounter increases and the time at which the maximum density is achieved approaches zero. It is clear that the analytical and numerical results agree well with their prediction of the maximum density. The disagreement at other times is due to the fact that the homologous model presented here ignores both the in-plane stretching and nonlinear

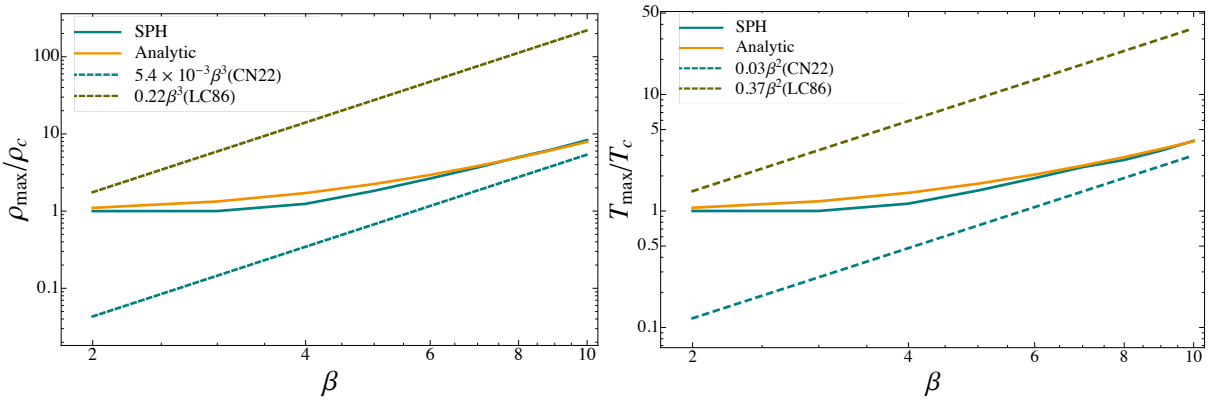

Figure 30: The maximum value of the central stellar density (left) and temperature (right) as a function of β normalized by their initial values. The dashed curves represent the scalings derived by [4] (olive) and [5] (teal), the solid, teal curves are from the analytic model (also in [5]), and the solid, orange curves are from the numerical simulations.

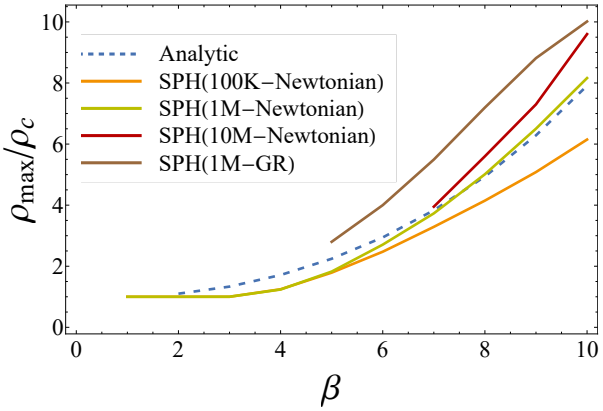

Figure 31: The ratio of the maximum to the original density at the geometric center of the star as a function of β. The different solid curves are obtained by varying the spatial resolution, with the corresponding number of particles shown in the legend. The analytic prediction is shown by the dashed curve.

(i.e., non-homologous) effects, which approximately negate one another as concerns the maximum density. We also note that the star spends a very short fraction of its dynamical time near the maximum density (and correspondingly near the maximum temperature).

In Figure 30 we show the maximum density (left) and temperature (right) against β obtained from the simulations alongside the corresponding analytic prediction. For small values of β the in-plane stretching is significant, and therefore the homologous model presented in Section 7.1, which ignores any in-plane dynamics, does not account for the decrease in density and overestimates the numerical value; overall, however, the agreement between the analytic model and numerical solution is good. In each panel the β^3 fit to the large-β behavior of our results is shown with a teal dashed curve and that of the LC86 with an olive dashed curve. In the β range of our investigation, we find that neither the maximum central density nor the maximum temperature follow any power-law scaling, in contrast to the prediction of LC86 (who claimed the β^3 scaling appears for $\beta \gtrsim 5$). We tabulate the maximum density and temperature as obtained from the simulations, along with their predicted values from Section 7.1 (and the homologous model of CN22) and LC86, in Table 5 for the full β range of our investigation. For $\beta = 1$ and 2, the in-plane stretching in the numerical simulation offsets the compression out of the plane, resulting in a monotonic decline in both the central density and temperature; hence these values are identically equal to 1.

By extrapolating our simulation (or analytic) results, one could argue that the $\propto \beta^3$ scaling would hold at a much higher value of β, on the order of $\beta \simeq 20$, and with a much smaller proportionality factor than that of LC86. However, the analytical model here is at the homologous level and does not permit the formation of shocks, and while the agreement between the analytical model and the numerical simulations for $\beta \leq 10$ suggests that shocks are not important over this β range, they likely do become important for larger β. For example, CN22 demonstrated that, for a $\gamma = 5/3$ polytrope, the maximum density never actually conforms to the β^3 scaling (in any β range) because a (weak) shock reaches the midplane prior to maximum adiabatic compression above $\beta \simeq 10$. A similar effect almost certainly occurs for this type of star as well, and hence it is likely inaccurate to extrapolate the homologous prediction and conclude that the β^3 scaling is eventually followed.

We tested the numerical accuracy of our results using three different resolutions, corresponding to 10^5, 10^6 and 10^7 SPH particles, which are shown in Figure 31 alongside the analytical results. It is clear that the simulations agree well with one another and the analytical results for small β, but disagree somewhat at large β where the higher-resolution simulations predict a greater degree of compression. Nonetheless, it is apparent from this figure that the relative change in $\rho_{\rm max}/\rho_{\rm c}$ is a decreasing function of resolution, with the

	$\rho_{\max}/\rho_c$			$T_{\max}/T_c$		
β	SPH (1M)	LC86	CN22	SPH (1M)	LC86	CN22
2	1	1.76	1.10	1	1.48	1.07
3	1	5.94	1.33	1	3.33	1.2
4	1.24	14.08	1.71	1.16	5.92	1.43
5	1.83	27.5	2.25	1.50	9.25	1.72
6	2.65	47.52	2.94	1.91	13.32	2.05
7	3.68	75.46	3.84	2.38	18.13	2.45
8	5.00	112.64	4.94	2.74	23.68	2.90
9	6.48	160.38	6.29	3.29	29.97	3.41
10	8.18	220.	7.91	4.01	37.	3.97

Table 5: The maximum central density and temperature, normalized to their original values, obtained from the SPH simulations, predicted by LC86, and predicted by CN22 for the β range analyzed here. For $\beta = 1$ and 2, the density and temperature at the center of the star monotonically decline with time in the numerical simulations, hence their values of identically 1 from the simulations.

β	$N_{\rm p}=10^5$	$N_{\rm p}=10^6$	% change	$N_{\rm p}=10^7$	% change
7	$\rho_{\rm max}/\rho_{\rm c}=3.3$	3.7	12.1	3.8	2.7
8	4.2	5.0	19.1	5.6	12
9	5.1	6.5	27.5	7.3	12.3
10	6.2	8.2	32.3	9.6	17.1

Table 6: For the β given in the first column, the maximum central density relative to its original value is given in columns 2, 3, and 5 for 10^5, 10^6 and 10^7 SPH particles, respectively. The relative error between successive resolutions, calculated as the difference between the higher and lower-resolution values normalized by the higher-resolution result, is shown in the fourth and sixth column.

specific values given in Table 6 (the % change columns are calculated as the difference between the higher and lower-resolution values normalized to the high-resolution value). We therefore conclude that while the results have not definitively converged at 10^7 particles for $\beta \gtrsim 8$, they are converging, and the amount of compression experienced by the star is an order of magnitude smaller than that predicted in previous works. We also note that a similar trend was found in [92], where even at 10^8 particles the results were not yet converged for $\beta \gtrsim 8$ (though they showed clear evidence that they were converging; see Figure 17 of [5]). Finally, while there is some disagreement between the 10^7-particle runs and the homologous prediction for $\beta \gtrsim 8$, [5] have shown that incorporating non-homologous terms in the analytical solution can bring these two into better agreement (see Figure 17 of [5] for a demonstration of this in the case of a convective star).

7.2.3 Effects of General Relativity

The analysis of Section 7.1 and the simulations presented so far have been performed in Newtonian gravity. This made the analysis simpler and the corresponding simulations computationally inexpensive. Furthermore, a Newtonian background has historically been preferred in almost all previous work investigating extreme tidal compression, specifically in CL82,83, LC86 and CN22 with which we compare our results.

However, the pericenter distance of the star in units of gravitational radii for a $10^6 M_\odot$ black hole is $r_{\rm p} \simeq 47/\beta$, and thus by $\beta = 10$ is very close to the direct capture radius (4 gravitational radii). Thus, general relativistic effects can modify the evolution of the compressing star nontrivially and, as argued in CN22, could increase the maximum-achieved density owing to the stronger tidal field of the black hole. To investigate this possibility, we performed general relativistic simulations in the (fixed-metric) Schwarzschild geometry

using the SPH algorithm described in [303]. The relativistic simulations were primarily performed using 10^6 SPH particles for $\beta = 5-10$ [1], though an additional simulation with 10^7 particles was performed for $\beta = 7$ to assess the convergence of the results.

The general relativistic results compared to the Newtonian values are shown by the brown curve in Figure 31. Compared to the green curve in this figure (which is at the same resolution), we see that general relativistic effects tend to increase the amount of compression by a factor of $\lesssim 1.5$. Interestingly, the relative change in the maximum-achieved density does not appear to be as pronounced for $\beta = 10$, which could be due to the fact that the direct capture radius for this configuration coincides with $\beta \simeq 11.8$. As the star nears the direct capture radius the tidal shear – responsible for reducing the density of the material – diverges, and one might therefore suspect that the overall degree of compression is reduced as the direct capture limit is reached. However, we make this interpretation with caution owing to the lack of complete convergence of the solutions for this value of β.

Figure 32 shows the central density as a function of coordinate time for the $N_{\rm p} = 10^6$ Newtonian, $N_{\rm p} = 10^6$ relativistic, and $N_{\rm p} = 10^7$ relativistic simulations for $\beta = 7$. Consistent with Figure 31, the maximum density attained in the relativistic simulations is $\lesssim 1.5$ times the Newtonian value. Additionally, the time at which the star is maximally compressed is slightly delayed (note that the horizontal axis is coordinate time relative to when the Newtonian, point-particle orbit would reach pericenter), and the overall duration of the compression (i.e., the amount of time that the star spends near its maximum-achieved density) is prolonged [2] in the general relativistic solutions compared to the Newtonian one. Both of these effects arise from relativistic time dilation. It is also evident that the results of the relativistic simulations with 10^6 and 10^7 SPH particles agree extremely well with one another.

7.3 Summary

To analyze the amount of tidal compression of a radiative, solar-like star (modeled with the Eddington standard model) during a tidal disruption event, we used an analytic model originally proposed by [5] that accounts for both the self-gravity and the pressure of the star during its tidal encounter with the black hole (Section 7.1). We then relaxed

[1] Note that we are still defining β by $\beta = r_{\rm t}/r_{\rm p}$, where $r_{\rm p}$ is the true pericenter distance the star would reach if it were a point particle in the relativistic gravitational field of the SMBH. We do not, in contrast, fix the angular momentum of the star to its Newtonian value and define $\ell^2 = 2GM_\bullet r_{\rm p}$, which would generally yield a smaller, true pericenter distance in the relativistic gravitational field of the SMBH; see [304].

[2] We thank Emilio Tejeda for pointing out this latter feature of the relativistic solutions.

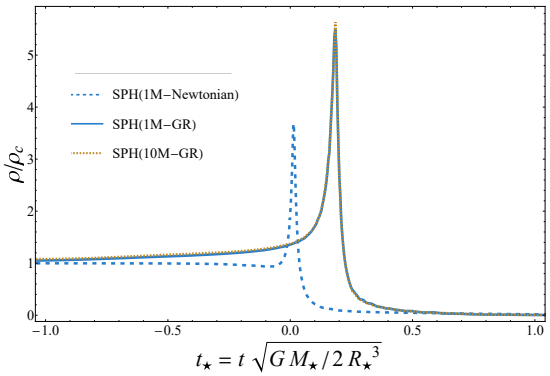

Figure 32: The ratio of maximum central density to the original central density against the dynamic time of the star with $\beta = 7$. The resolution and gravity are specified by the legend (solid-blue and dotted-orange use the Schwarzschild metric for the gravitational field of the SMBH). The compression is stronger (by a factor of $\lesssim 1.5$) with relativistic effects included, and the time of maximum compression occurs later in comparison to the Newtonian case; the latter effect arises from time dilation (note that the horizontal axis is coordinate time, i.e., time as measured by an observer at infinity) normalized by the dynamic time of the star.

the assumptions made within that model by performing three-dimensional simulations of deep TDEs that satisfied $2 \leq \beta \leq 10$, where $\beta = r_{\rm t}/r_{\rm p}$ with $r_{\rm p}$ the stellar pericenter distance and $r_{\rm t}$ the canonical tidal radius, verified the numerical accuracy of our results by varying the spatial resolution, and performed additional simulations in the Schwarzschild metric to assess the importance of general relativity (Section 7.2). We showed that the two methods – analytical and numerical – agree very well in their predictions for the maximum density and temperature reached during the disruption, and we therefore conclude that

1. The maximum density and temperature achieved by the star during its compression are significantly reduced (by over an order of magnitude for the density and nearly an order of magnitude for the temperature by $\beta = 10$) compared to the predictions of [57], [3], [111], [4] (see Figure 30).

2. Shocks are not important in this range of β, and therefore are not responsible for the lower degree of compression, although they are likely important for sufficiently large β ($\beta \gtrsim 10$; cf. [5]).

3. The predicted scaling $\rho_{\rm max} \propto \beta^3$ [57, 290, 293] is not realized over this range of β, and is lik ely not ever followed because of the eventual importance of shocks in reversing the compression of the star prior to reaching its maximum adiabatic value (see [5]).

4. General relativity modestly increases the maximum degree of compression of the star (by a factor of $\lesssim 1.5$; see Figures 31 and 32 and note that the general relativistic solutions are at 10^6 particles), and also induces a lag in the time at which the maximum compression occurs and the amount of time the star spends at increased density and temperature increases (according to an observer at infinity) as a result of time dilation.

5. The high temperatures and densities needed to ignite the triple-α process in the core of the star are not reached by $\beta = 10$, as the maximum temperature attained at this β is $T_{\rm max} \simeq 4 \times 10^7$ for an initial central temperature of 10^7 K (see right panel of Figure 30), and in general we expect the nuclear energy released to be minimal because of the small amount of time spent near maximum compression (see Figure 29). Nevertheless, this modest degree of compression could still be important for augmenting the importance of self-gravity in the compressing star and thus determining the critical β at which the star is completely destroyed, particularly for more massive stars where the critical β is $\gtrsim 3$ [305, 306].

.

Chapter 8

Conclusions

In this present era of multi-messenger astrophysics, routine observations–in electromagnetic, gravitational waves, or neutrions–are providing clues to unveil physics of the extreme universe. We need to take this opportunity to complement this tremendous progress and, at the same time, to trigger new observations by developing novel analytic and computational methods. This thesis aims to do this by studying the hydrodynamics in a few of the most intriguing astrophysical settings.

The formation of giant planets like gas giants in our own solar system is still not fully understood [307] and the results presented in this thesis point out the role of the solid core in stabilizing the configuration. This result complements the "core accretion" paradigm of giant planet formation, where during the rapid gas accretion phase, regions of the hydrogen envelope dissociate and ionize, which causes reduction in the adiabatic index of the gas. Naively, due to Chandrasekhar, one might expect the structure to become unstable; but we show that the addition of the solid core saves the structure from becoming dynamically unstable. The scope of the present work can be enhanced if used in conjunction with planetary evolutionary model; still it is very obvious from our results how a solid core dynamically stabilizes a Jupiter-like planet.

Core-collapse supernovae are considered one of the most promising multi-messenger sources [308]. In core-collapse supernovae all four fundamental forces are at work, and hence the understanding of the physics should enrich our understanding of fundamental physics, for example, how dense matter operates in extreme situations. Yet, at present we do not have a full understanding of the explosion mechanism. The present thesis studies core-collapse supernovae from a few different perspectives. By highlighting the importance of general relativity and the presence of a *hard* surface (such as the proto-neutron star), we provide a novel accretion solution through standing shock. These solutions clearly depict the orders of magnitude correction to the "settling solutions" obtained in Newtonian settings. Our results are important in the case of weak and failed

supernovae where the shock is pushed to smaller radii making use of general relativity indispensable. These solutions will impact the standing accretion shock instability (SASI) and because even the stable modes have very small eigen values, a modification in the background solution might make modes that were stable in Newtonian settings unstable with relativistic considerations. Future studies should target this. For this thesis, we have revisited the *traditional* SASI analysis with Newtonian background solutions and obtained some results that are *not found in the traditional analysis*. We see a range of $l = 2$ modes that are unstable whose frequencies go well with the dynamic timescale of neutron stars. These modes are never discussed in the traditional discussion of SASI, where SASI modes are always linked with low-frequency oscillations. The unstable modes can propagate in a cascade effect, and the eventual non-linear coupling between such unstable modes leads to strong turbulence, which in turn would aid the asymmetric explosion seen in supernovae [37, 38]. This thesis also studies the oscillation modes of neutron stars in perturbation theory and shows that the fundamental frequencies associated with neutron star oscillations supply a significant portion of the energy emitted as gravitational waves seen in state-of-the-art supernovae simulations [40, 2]. The frequency corresponding to the maximally unstable mode (among the newly found unstable $l = 2$ modes) of the SASI cavity oscillations matches well with the fundamental mode frequencies of the neutron star. Therefore, the SASI cavity might also be the *hammer* ringing the neutron star as a *bell*. The absence of other modes of oscillations of the neutron star such as the p-modes or g-modes in the gravitational wave bolsters our claim.

The advent of advanced computational methods enables us to make decisive comments on many disputed claims. In this thesis, we have presented such a dispute and (hopefully) provided a resolution. In the 1980s it was shown by Luminet & Carter through analytic work that a radiative star entering deep inside the tidal sphere of the supermassive black hole suffer such extreme tidal compression that the stellar core undergoes thermonuclear detonation [57, 3]. This conclusion has been doubted almost immediately as Bicknell et al. through a smoothed particle hydrodynamics simulation showed that the compression such a star would undergo in reality is much lower [58]. They ran their simulation with ~ 2500 SPH particles. This issue of whether thermonuclear detonation of a radiative star in deeply penetrating tidal disruption events is possible or not has been debated for the last four decades without any consensus. In this thesis, we have run high-resolution SPH simulations and shown that to resolve such instances soundly one needs $\sim 10M$ SPH particles (an $\sim 10^4$ order increase from [58])! Our results show few order of magnitude lesser compression than what was predicted; we have also run a set of general-relativistic simulations to show that even relativistic considerations does not increase the extent of compression by much, and therefore, we conclude any possibility of nuclear detonation is

highly unlikely in deep-TDEs.

This thesis portrays the role of hydrodynamics, stability, and accretion in a few exotic high-energy astrophysical scenarios. Our work will trigger further investigations, observations, and we anticipate that the precise knowledge thus developed will enhance our understanding of giant planet formation, the explosion mechanism of massive stars, and deeply penetrating tidal disruption events.

Bibliography

[1] M. Afrasiabi, H. Klippel, M. Roethlin, and K. Wegener. An improved thermal model for sph metal cutting simulations on gpu. *Applied Mathematical Modelling*, 100:728–750, 2021.

[2] Viktoriya Morozova, David Radice, Adam Burrows, and David Vartanyan. The Gravitational Wave Signal from Core-collapse Supernovae. *Astrophysical J.*, 861(1):10, July 2018.

[3] B. Carter and J. P. Luminet. Tidal compression of a star by a large black hole. I Mechanical evolution and nuclear energy release by proton capture. *Astron. and Astrophys.*, 121(1):97–113, May 1983.

[4] J. P. Luminet and B. Carter. Dynamics of an Affine Star Model in a Black Hole Tidal Field. *Astrophysical Journal, Supplement*, 61:219, June 1986.

[5] Eric R. Coughlin and C. J. Nixon. Stars Crushed by Black Holes. II. A Physical Model of Adiabatic Compression and Shock Formation in Tidal Disruption Events. *Astrophysical J.*, 926(1):47, February 2022.

[6] Cathie Clarke and Bob Carswell. *Principles of Astrophysical Fluid Dynamics*. Cambridge University Press, 2007.

[7] David N. Burrows, J. E. Hill, J. A. Nousek, J. A. Kennea, A. Wells, J. P. Osborne, A. F. Abbey, A. Beardmore, K. Mukerjee, A. D. T. Short, G. Chincarini, S. Campana, O. Citterio, A. Moretti, C. Pagani, G. Tagliaferri, P. Giommi, M. Capalbi, F. Tamburelli, L. Angelini, G. Cusumano, H. W. Bräuninger, W. Burkert, and G. D. Hartner. The Swift X-Ray Telescope. , 120(3-4):165–195, October 2005.

[8] Martin C. Weisskopf, Harvey D. Tananbaum, Leon P. Van Speybroeck, and Stephen L. O'Dell. Chandra X-ray Observatory (CXO): overview. In Joachim E. Truemper and Bernd Aschenbach, editors, *X-Ray Optics, Instruments, and Missions III*, volume 4012 of *Society of Photo-Optical Instrumentation Engineers (SPIE) Conference Series*, pages 2–16, July 2000.

[9] Jonathan P. Gardner, John C. Mather, Mark Clampin, Rene Doyon, Matthew A. Greenhouse, Heidi B. Hammel, John B. Hutchings, Peter Jakobsen, Simon J. Lilly, Knox S. Long, Jonathan I. Lunine, Mark J. McCaughrean, Matt Mountain, John Nella, George H. Rieke, Marcia J. Rieke, Hans-Walter Rix, Eric P. Smith, George Sonneborn, Massimo Stiavelli, H. S. Stockman, Rogier A. Windhorst, and Gillian S. Wright. The James Webb Space Telescope. , 123(4):485–606, April 2006.

[10] F. Jansen, D. Lumb, B. Altieri, J. Clavel, M. Ehle, C. Erd, C. Gabriel, M. Guainazzi, P. Gondoin, R. Much, R. Munoz, M. Santos, N. Schartel, D. Texier, and G. Vacanti. XMM-Newton observatory. I. The spacecraft and operations. *Astron. and Astrophys.*, 365:L1–L6, January 2001.

[11] B. P. Abbott, R. Abbott, R. Adhikari, P. Ajith, B. Allen, G. Allen, R. S. Amin, S. B. Anderson, W. G. Anderson, M. A. Arain, M. Araya, H. Armandula, P. Armor, Y. Aso, S. Aston, P. Aufmuth, C. Aulbert, S. Babak, P. Baker, S. Ballmer, C. Barker, D. Barker, B. Barr, P. Barriga, L. Barsotti, M. A. Barton, I. Bartos, R. Bassiri, M. Bastarrika, B. Behnke, M. Benacquista, J. Betzwieser, P. T. Beyersdorf, I. A. Bilenko, G. Billingsley, R. Biswas, E. Black, J. K. Blackburn, L. Blackburn, D. Blair, B. Bland, T. P. Bodiya, L. Bogue, R. Bork, V. Boschi, S. Bose, P. R. Brady, V. B. Braginsky, J. E. Brau, D. O. Bridges, M. Brinkmann, A. F. Brooks, D. A. Brown, A. Brummit, G. Brunet, A. Bullington, A. Buonanno, O. Burmeister, R. L. Byer, L. Cadonati, J. B. Camp, J. Cannizzo, K. C. Cannon, J. Cao, L. Cardenas, S. Caride, G. Castaldi, S. Caudill, M. Cavaglià, C. Cepeda, T. Chalermsongsak, E. Chalkley, P. Charlton, S. Chatterji, S. Chelkowski, Y. Chen, N. Christensen, C. T. Y. Chung, D. Clark, J. Clark, J. H. Clayton, T. Cokelaer, C. N. Colacino, R. Conte, D. Cook, T. R. C. Corbitt, N. Cornish, D. Coward, D. C. Coyne, J. D. E. Creighton, T. D. Creighton, A. M. Cruise, R. M. Culter, A. Cumming, L. Cunningham, S. L. Danilishin, K. Danzmann, B. Daudert, G. Davies, E. J. Daw, D. DeBra, J. Degallaix, V. Dergachev, S. Desai, R. DeSalvo, S. Dhurandhar, M. Díaz, A. Dietz, F. Donovan, K. L. Dooley, E. E. Doomes, R. W. P. Drever, J. Dueck, I. Duke, J. C. Dumas, J. G. Dwyer, C. Echols, M. Edgar, A. Effler, P. Ehrens, E. Espinoza, T. Etzel, M. Evans, T. Evans, S. Fairhurst, Y. Faltas, Y. Fan, D. Fazi, H. Fehrmenn, L. S. Finn, K. Flasch, S. Foley, C. Forrest, N. Fotopoulos, A. Franzen, M. Frede, M. Frei, Z. Frei, A. Freise, R. Frey, T. Fricke, P. Fritschel, V. V. Frolov, M. Fyffe, V. Galdi, J. A. Garofoli, I. Gholami, J. A. Giaime, S. Giampanis, K. D. Giardina, K. Goda, E. Goetz, L. M. Goggin, G. González, M. L. Gorodetsky, S. Goßler, R. Gouaty, A. Grant, S. Gras, C. Gray, M. Gray, R. J. S. Greenhalgh, A. M. Gretarsson, F. Grimaldi, R. Grosso, H. Grote, S. Grunewald, M. Guenther, E. K. Gustafson,

R. Gustafson, B. Hage, J. M. Hallam, D. Hammer, G. D. Hammond, C. Hanna, J. Hanson, J. Harms, G. M. Harry, I. W. Harry, E. D. Harstad, K. Haughian, K. Hayama, J. Heefner, I. S. Heng, A. Heptonstall, M. Hewitson, S. Hild, E. Hirose, D. Hoak, K. A. Hodge, K. Holt, D. J. Hosken, J. Hough, D. Hoyland, B. Hughey, S. H. Huttner, D. R. Ingram, T. Isogai, M. Ito, A. Ivanov, B. Johnson, W. W. Johnson, D. I. Jones, G. Jones, R. Jones, L. Ju, P. Kalmus, V. Kalogera, S. Kandhasamy, J. Kanner, D. Kasprzyk, E. Katsavounidis, K. Kawabe, S. Kawamura, F. Kawazoe, W. Kells, D. G. Keppel, A. Khalaidovski, F. Y. Khalili, R. Khan, E. Khazanov, P. King, J. S. Kissel, S. Klimenko, K. Kokeyama, V. Kondrashov, R. Kopparapu, S. Koranda, D. Kozak, B. Krishnan, R. Kumar, P. Kwee, P. K. Lam, M. Landry, B. Lantz, A. Lazzarini, H. Lei, M. Lei, N. Leindecker, I. Leonor, C. Li, H. Lin, P. E. Lindquist, T. B. Littenberg, N. A. Lockerbie, D. Lodhia, M. Longo, M. Lormand, P. Lu, M. Lubiński, A. Lucianetti, H. Lück, B. Machenschalk, M. MacInnis, M. Mageswaran, K. Mailand, I. Mandel, V. Mandic, S. Márka, Z. Márka, A. Markosyan, J. Markowitz, E. Maros, I. W. Martin, R. M. Martin, J. N. Marx, K. Mason, F. Matichard, L. Matone, R. A. Matzner, N. Mavalvala, R. McCarthy, D. E. McClelland, S. C. McGuire, M. McHugh, G. McIntyre, D. J. A. McKechan, K. McKenzie, M. Mehmet, A. Melatos, A. C. Melissinos, D. F. Menéndez, G. Mendell, R. A. Mercer, S. Meshkov, C. Messenger, M. S. Meyer, J. Miller, J. Minelli, Y. Mino, V. P. Mitrofanov, G. Mitselmakher, R. Mittleman, O. Miyakawa, B. Moe, S. D. Mohanty, S. R. P. Mohapatra, G. Moreno, T. Morioka, K. Mors, K. Mossavi, C. Mow Lowry, G. Mueller, H. Müller-Ebhardt, D. Muhammad, S. Mukherjee, H. Mukhopadhyay, A. Mullavey, J. Munch, P. G. Murray, E. Myers, J. Myers, T. Nash, J. Nelson, G. Newton, A. Nishizawa, K. Numata, J. O'Dell, B. O'Reilly, R. O'Shaughnessy, E. Ochsner, G. H. Ogin, D. J. Ottaway, R. S. Ottens, H. Overmier, B. J. Owen, Y. Pan, C. Pankow, M. A. Papa, V. Parameshwaraiah, P. Patel, M. Pedraza, S. Penn, A. Perraca, V. Pierro, I. M. Pinto, M. Pitkin, H. J. Pletsch, M. V. Plissi, F. Postiglione, M. Principe, R. Prix, L. Prokhorov, O. Punken, V. Quetschke, F. J. Raab, D. S. Rabeling, H. Radkins, P. Raffai, Z. Raics, N. Rainer, M. Rakhmanov, V. Raymond, C. M. Reed, T. Reed, H. Rehbein, S. Reid, D. H. Reitze, R. Riesen, K. Riles, B. Rivera, P. Roberts, N. A. Robertson, C. Robinson, E. L. Robinson, S. Roddy, C. Röver, J. Rollins, J. D. Romano, J. H. Romie, S. Rowan, A. Rüdiger, P. Russell, K. Ryan, S. Sakata, L. Sancho de la Jordana, V. Sandberg, V. Sannibale, L. Santamaría, S. Saraf, P. Sarin, B. S. Sathyaprakash, S. Sato, M. Satterthwaite, P. R. Saulson, R. Savage, P. Savov, M. Scanlan, R. Schilling, R. Schnabel, R. Schofield, B. Schulz, B. F. Schutz, P. Schwinberg, J. Scott, S. M. Scott, A. C. Searle, B. Sears, F. Seifert,

D. Sellers, A. S. Sengupta, A. Sergeev, B. Shapiro, P. Shawhan, D. H. Shoemaker, A. Sibley, X. Siemens, D. Sigg, S. Sinha, A. M. Sintes, B. J. J. Slagmolen, J. Slutsky, J. R. Smith, M. R. Smith, N. D. Smith, K. Somiya, B. Sorazu, A. Stein, L. C. Stein, S. Steplewski, A. Stochino, R. Stone, K. A. Strain, S. Strigin, A. Stroeer, A. L. Stuver, T. Z. Summerscales, K. X. Sun, M. Sung, P. J. Sutton, G. P. Szokoly, D. Talukder, L. Tang, D. B. Tanner, S. P. Tarabrin, J. R. Taylor, R. Taylor, J. Thacker, K. A. Thorne, A. Thüring, K. V. Tokmakov, C. Torres, C. Torrie, G. Traylor, M. Trias, D. Ugolini, J. Ulmen, K. Urbanek, H. Vahlbruch, M. Vallisneri, C. van den Broeck, M. V. van der Sluys, A. A. van Veggel, S. Vass, R. Vaulin, A. Vecchio, J. Veitch, P. Veitch, C. Veltkamp, A. Villar, C. Vorvick, S. P. Vyachanin, S. J. Waldman, L. Wallace, R. L. Ward, A. Weidner, M. Weinert, A. J. Weinstein, R. Weiss, L. Wen, S. Wen, K. Wette, J. T. Whelan, S. E. Whitcomb, B. F. Whiting, C. Wilkinson, P. A. Willems, H. R. Williams, L. Williams, B. Willke, I. Wilmut, L. Winkelmann, W. Winkler, C. C. Wipf, A. G. Wiseman, G. Woan, R. Wooley, J. Worden, W. Wu, I. Yakushin, H. Yamamoto, Z. Yan, S. Yoshida, M. Zanolin, J. Zhang, L. Zhang, C. Zhao, N. Zotov, M. E. Zucker, H. zur Mühlen, and J. Zweizig. LIGO: the Laser Interferometer Gravitational-Wave Observatory. *Reports on Progress in Physics*, 72(7):076901, July 2009.

[12] LIGO Scientific Collaboration, J. Aasi, B. P. Abbott, R. Abbott, T. Abbott, M. R. Abernathy, K. Ackley, C. Adams, T. Adams, P. Addesso, R. X. Adhikari, V. Adya, C. Affeldt, N. Aggarwal, O. D. Aguiar, A. Ain, P. Ajith, A. Alemic, B. Allen, D. Amariutei, S. B. Anderson, W. G. Anderson, K. Arai, M. C. Araya, C. Arceneaux, J. S. Areeda, G. Ashton, S. Ast, S. M. Aston, P. Aufmuth, C. Aulbert, B. E. Aylott, S. Babak, P. T. Baker, S. W. Ballmer, J. C. Barayoga, M. Barbet, S. Barclay, B. C. Barish, D. Barker, B. Barr, L. Barsotti, J. Bartlett, M. A. Barton, I. Bartos, R. Bassiri, J. C. Batch, C. Baune, B. Behnke, A. S. Bell, C. Bell, M. Benacquista, J. Bergman, G. Bergmann, C. P. L. Berry, J. Betzwieser, S. Bhagwat, R. Bhandare, I. A. Bilenko, G. Billingsley, J. Birch, S. Biscans, C. Biwer, J. K. Blackburn, L. Blackburn, C. D. Blair, D. Blair, O. Bock, T. P. Bodiya, P. Bojtos, C. Bond, R. Bork, M. Born, Sukanta Bose, P. R. Brady, V. B. Braginsky, J. E. Brau, D. O. Bridges, M. Brinkmann, A. F. Brooks, D. A. Brown, D. D. Brown, N. M. Brown, S. Buchman, A. Buikema, A. Buonanno, L. Cadonati, J. Calderón Bustillo, J. B. Camp, K. C. Cannon, J. Cao, C. D. Capano, S. Caride, S. Caudill, M. Cavaglià, C. Cepeda, R. Chakraborty, T. Chalermsongsak, S. J. Chamberlin, S. Chao, P. Charlton, Y. Chen, H. S. Cho, M. Cho, J. H. Chow, N. Christensen, Q. Chu, S. Chung, G. Ciani, F. Clara, J. A. Clark, C. Collette, L. Cominsky, Jr. Constancio, M., D. Cook, T. R. Corbitt, N. Cornish, A. Corsi, C. A. Costa, M. W.

Coughlin, S. Countryman, P. Couvares, D. M. Coward, M. J. Cowart, D. C. Coyne, R. Coyne, K. Craig, J. D. E. Creighton, T. D. Creighton, J. Cripe, S. G. Crowder, A. Cumming, L. Cunningham, C. Cutler, K. Dahl, T. Dal Canton, M. Damjanic, S. L. Danilishin, K. Danzmann, L. Dartez, I. Dave, H. Daveloza, G. S. Davies, E. J. Daw, D. DeBra, W. Del Pozzo, T. Denker, T. Dent, V. Dergachev, R. T. DeRosa, R. DeSalvo, S. Dhurandhar, M. D´ıaz, I. Di Palma, G. Dojcinoski, E. Dominguez, F. Donovan, K. L. Dooley, S. Doravari, R. Douglas, T. P. Downes, J. C. Driggers, Z. Du, S. Dwyer, T. Eberle, T. Edo, M. Edwards, M. Edwards, A. Effler, H. B. Eggenstein, P. Ehrens, J. Eichholz, S. S. Eikenberry, R. Essick, T. Etzel, M. Evans, T. Evans, M. Factourovich, S. Fairhurst, X. Fan, Q. Fang, B. Farr, W. M. Farr, M. Favata, M. Fays, H. Fehrmann, M. M. Fejer, D. Feldbaum, E. C. Ferreira, R. P. Fisher, Z. Frei, A. Freise, R. Frey, T. T. Fricke, P. Fritschel, V. V. Frolov, S. Fuentes-Tapia, P. Fulda, M. Fyffe, J. R. Gair, S. Gaonkar, N. Gehrels, L. Á. Gergely, J. A. Giaime, K. D. Giardina, J. Gleason, E. Goetz, R. Goetz, L. Gondan, G. González, N. Gordon, M. L. Gorodetsky, S. Gossan, S. Goßler, C. Gräf, P. B. Graff, A. Grant, S. Gras, C. Gray, R. J. S. Greenhalgh, A. M. Gretarsson, H. Grote, S. Grunewald, C. J. Guido, X. Guo, K. Gushwa, E. K. Gustafson, R. Gustafson, J. Hacker, E. D. Hall, G. Hammond, M. Hanke, J. Hanks, C. Hanna, M. D. Hannam, J. Hanson, T. Hardwick, G. M. Harry, I. W. Harry, M. Hart, M. T. Hartman, C. J. Haster, K. Haughian, S. Hee, M. Heintze, G. Heinzel, M. Hendry, I. S. Heng, A. W. Heptonstall, M. Heurs, M. Hewitson, S. Hild, D. Hoak, K. A. Hodge, S. E. Hollitt, K. Holt, P. Hopkins, D. J. Hosken, J. Hough, E. Houston, E. J. Howell, Y. M. Hu, E. Huerta, B. Hughey, S. Husa, S. H. Huttner, M. Huynh, T. Huynh-Dinh, A. Idrisy, N. Indik, D. R. Ingram, R. Inta, G. Islas, J. C. Isler, T. Isogai, B. R. Iyer, K. Izumi, M. Jacobson, H. Jang, S. Jawahar, Y. Ji, F. Jiménez-Forteza, W. W. Johnson, D. I. Jones, R. Jones, L. Ju, K. Haris, V. Kalogera, S. Kandhasamy, G. Kang, J. B. Kanner, E. Katsavounidis, W. Katzman, H. Kaufer, S. Kaufer, T. Kaur, K. Kawabe, F. Kawazoe, G. M. Keiser, D. Keitel, D. B. Kelley, W. Kells, D. G. Keppel, J. S. Key, A. Khalaidovski, F. Y. Khalili, E. A. Khazanov, C. Kim, K. Kim, N. G. Kim, N. Kim, Y. M. Kim, E. J. King, P. J. King, D. L. Kinzel, J. S. Kissel, S. Klimenko, J. Kline, S. Koehlenbeck, K. Kokeyama, V. Kondrashov, M. Korobko, W. Z. Korth, D. B. Kozak, V. Kringel, B. Krishnan, C. Krueger, G. Kuehn, A. Kumar, P. Kumar, L. Kuo, M. Landry, B. Lantz, S. Larson, P. D. Lasky, A. Lazzarini, C. Lazzaro, J. Le, P. Leaci, S. Leavey, E. O. Lebigot, C. H. Lee, H. K. Lee, H. M. Lee, J. R. Leong, Y. Levin, B. Levine, J. Lewis, T. G. F. Li, K. Libbrecht, A. Libson, A. C. Lin, T. B. Littenberg, N. A. Lockerbie, V. Lockett, J. Logue, A. L. Lombardi, M. Lormand, J. Lough, M. J. Lubinski, H. Lück, A. P. Lundgren, R. Lynch, Y. Ma,

J. Macarthur, T. MacDonald, B. Machenschalk, M. MacInnis, D. M. Macleod, F. Magaña-Sandoval, R. Magee, M. Mageswaran, C. Maglione, K. Mailand, I. Mandel, V. Mandic, V. Mangano, G. L. Mansell, S. Márka, Z. Márka, A. Markosyan, E. Maros, I. W. Martin, R. M. Martin, D. Martynov, J. N. Marx, K. Mason, T. J. Massinger, F. Matichard, L. Matone, N. Mavalvala, N. Mazumder, G. Mazzolo, R. McCarthy, D. E. McClelland, S. McCormick, S. C. McGuire, G. McIntyre, J. McIver, K. McLin, S. McWilliams, G. D. Meadors, M. Meinders, A. Melatos, G. Mendell, R. A. Mercer, S. Meshkov, C. Messenger, P. M. Meyers, H. Miao, H. Middleton, E. E. Mikhailov, A. Miller, J. Miller, M. Millhouse, J. Ming, S. Mirshekari, C. Mishra, S. Mitra, V. P. Mitrofanov, G. Mitselmakher, R. Mittleman, B. Moe, S. D. Mohanty, S. R. P. Mohapatra, B. Moore, D. Moraru, G. Moreno, S. R. Morriss, K. Mossavi, C. M. Mow-Lowry, C. L. Mueller, G. Mueller, S. Mukherjee, A. Mullavey, J. Munch, D. Murphy, P. G. Murray, A. Mytidis, T. Nash, R. K. Nayak, V. Necula, K. Nedkova, G. Newton, T. Nguyen, A. B. Nielsen, S. Nissanke, A. H. Nitz, D. Nolting, M. E. N. Normandin, L. K. Nuttall, E. Ochsner, J. O'Dell, E. Oelker, G. H. Ogin, J. J. Oh, S. H. Oh, F. Ohme, P. Oppermann, R. Oram, B. O'Reilly, W. Ortega, R. O'Shaughnessy, C. Osthelder, C. D. Ott, D. J. Ottaway, R. S. Ottens, H. Overmier, B. J. Owen, C. Padilla, A. Pai, S. Pai, O. Palashov, A. Pal-Singh, H. Pan, C. Pankow, F. Pannarale, B. C. Pant, M. A. Papa, H. Paris, Z. Patrick, M. Pedraza, L. Pekowsky, A. Pele, S. Penn, A. Perreca, M. Phelps, V. Pierro, I. M. Pinto, M. Pitkin, J. Poeld, A. Post, A. Poteomkin, J. Powell, J. Prasad, V. Predoi, S. Premachandra, T. Prestegard, L. R. Price, M. Principe, S. Privitera, R. Prix, L. Prokhorov, O. Puncken, M. Pürrer, J. Qin, V. Quetschke, E. Quintero, G. Quiroga, R. Quitzow-James, F. J. Raab, D. S. Rabeling, H. Radkins, P. Raffai, S. Raja, G. Rajalakshmi, M. Rakhmanov, K. Ramirez, V. Raymond, C. M. Reed, S. Reid, D. H. Reitze, O. Reula, K. Riles, N. A. Robertson, R. Robie, J. G. Rollins, V. Roma, J. D. Romano, G. Romanov, J. H. Romie, S. Rowan, A. Rüdiger, K. Ryan, S. Sachdev, T. Sadecki, L. Sadeghian, M. Saleem, F. Salemi, L. Sammut, V. Sandberg, J. R. Sanders, V. Sannibale, I. Santiago-Prieto, B. S. Sathyaprakash, P. R. Saulson, R. Savage, A. Sawadsky, J. Scheuer, R. Schilling, P. Schmidt, R. Schnabel, R. M. S. Schofield, E. Schreiber, D. Schuette, B. F. Schutz, J. Scott, S. M. Scott, D. Sellers, A. S. Sengupta, A. Sergeev, G. Serna, A. Sevigny, D. A. Shaddock, M. S. Shahriar, M. Shaltev, Z. Shao, B. Shapiro, P. Shawhan, D. H. Shoemaker, T. L. Sidery, X. Siemens, D. Sigg, A. D. Silva, D. Simakov, A. Singer, L. Singer, R. Singh, A. M. Sintes, B. J. J. Slagmolen, J. R. Smith, M. R. Smith, R. J. E. Smith, N. D. Smith-Lefebvre, E. J. Son, B. Sorazu, T. Souradeep, A. Staley, J. Stebbins, M. Steinke, J. Steinlechner, S. Steinlechner, D. Steinmeyer, B. C.

Stephens, S. Steplewski, S. Stevenson, R. Stone, K. A. Strain, S. Strigin, R. Sturani, A. L. Stuver, T. Z. Summerscales, P. J. Sutton, M. Szczepanczyk, G. Szeifert, D. Talukder, D. B. Tanner, M. Tápai, S. P. Tarabrin, A. Taracchini, R. Taylor, G. Tellez, T. Theeg, M. P. Thirugnanasambandam, M. Thomas, P. Thomas, K. A. Thorne, K. S. Thorne, E. Thrane, V. Tiwari, C. Tomlinson, C. V. Torres, C. I. Torrie, G. Traylor, M. Tse, D. Tshilumba, D. Ugolini, C. S. Unnikrishnan, A. L. Urban, S. A. Usman, H. Vahlbruch, G. Vajente, G. Valdes, M. Vallisneri, A. A. van Veggel, S. Vass, R. Vaulin, A. Vecchio, J. Veitch, P. J. Veitch, K. Venkateswara, R. Vincent-Finley, S. Vitale, T. Vo, C. Vorvick, W. D. Vousden, S. P. Vyatchanin, A. R. Wade, L. Wade, M. Wade, M. Walker, L. Wallace, S. Walsh, H. Wang, M. Wang, X. Wang, R. L. Ward, J. Warner, M. Was, B. Weaver, M. Weinert, A. J. Weinstein, R. Weiss, T. Welborn, L. Wen, P. Wessels, T. Westphal, K. Wette, J. T. Whelan, S. E. Whitcomb, D. J. White, B. F. Whiting, C. Wilkinson, L. Williams, R. Williams, A. R. Williamson, J. L. Willis, B. Willke, M. Wimmer, W. Winkler, C. C. Wipf, H. Wittel, G. Woan, J. Worden, S. Xie, J. Yablon, I. Yakushin, W. Yam, H. Yamamoto, C. C. Yancey, Q. Yang, M. Zanolin, Fan Zhang, L. Zhang, M. Zhang, Y. Zhang, C. Zhao, M. Zhou, X. J. Zhu, M. E. Zucker, S. Zuraw, and J. Zweizig. Advanced LIGO. *Classical and Quantum Gravity*, 32(7):074001, April 2015.

[13] F Acernese, M Agathos, K Agatsuma, D Aisa, N Allemandou, A Allocca, J Amarni, P Astone, G Balestri, G Ballardin, F Barone, J-P Baronick, M Barsuglia, A Basti, F Basti, Th S Bauer, V Bavigadda, M Bejger, M G Beker, C Belczynski, D Bersanetti, A Bertolini, M Bitossi, M A Bizouard, S Bloemen, M Blom, M Boer, G Bogaert, D Bondi, F Bondu, L Bonelli, R Bonnand, V Boschi, L Bosi, T Bouedo, C Bradaschia, M Branchesi, T Briant, A Brillet, V Brisson, T Bulik, H J Bulten, D Buskulic, C Buy, G Cagnoli, E Calloni, C Campeggi, B Canuel, F Carbognani, F Cavalier, R Cavalieri, G Cella, E Cesarini, E Chassande-Mottin, A Chincarini, A Chiummo, S Chua, F Cleva, E Coccia, P-F Cohadon, A Colla, M Colombini, A Conte, J-P Coulon, E Cuoco, A Dalmaz, S D'Antonio, V Dattilo, M Davier, R Day, G Debreczeni, J Degallaix, S Deléglise, W Del Pozzo, H Dereli, R De Rosa, L Di Fiore, A Di Lieto, A Di Virgilio, M Doets, V Dolique, M Drago, M Ducrot, G Endrőczi, V Fafone, S Farinon, I Ferrante, F Ferrini, F Fidecaro, I Fiori, R Flaminio, J-D Fournier, S Franco, S Frasca, F Frasconi, L Gammaitoni, F Garufi, M Gaspard, A Gatto, G Gemme, B Gendre, E Genin, A Gennai, S Ghosh, L Giacobone, A Giazotto, R Gouaty, M Granata, G Greco, P Groot, G M Guidi, J Harms, A Heidmann, H Heitmann, P Hello, G Hemming, E Hennes, D Hofman, P Jaranowski, R J G Jonker, M Kasprzack, F Kéfélian, I Kowalska, M Kraan,

A Królak, A Kutynia, C Lazzaro, M Leonardi, N Leroy, N Letendre, T G F Li, B Lieunard, M Lorenzini, V Loriette, G Losurdo, C Magazzù, E Majorana, I Maksimovic, V Malvezzi, N Man, V Mangano, M Mantovani, F Marchesoni, F Marion, J Marque, F Martelli, L Martellini, A Masserot, D Meacher, J Meidam, F Mezzani, C Michel, L Milano, Y Minenkov, A Moggi, M Mohan, M Montani, N Morgado, B Mours, F Mul, M F Nagy, I Nardecchia, L Naticchioni, G Nelemans, I Neri, M Neri, F Nocera, E Pacaud, C Palomba, F Paoletti, A Paoli, A Pasqualetti, R Passaquieti, D Passuello, M Perciballi, S Petit, M Pichot, F Piergiovanni, G Pillant, A Piluso, L Pinard, R Poggiani, M Prijatelj, G A Prodi, M Punturo, P Puppo, D S Rabeling, I Rácz, P Rapagnani, M Razzano, V Re, T Regimbau, F Ricci, F Robinet, A Rocchi, L Rolland, R Romano, D Rosińska, P Ruggi, E Saracco, B Sassolas, F Schimmel, D Sentenac, V Sequino, S Shah, K Siellez, N Straniero, B Swinkels, M Tacca, M Tonelli, F Travasso, M Turconi, G Vajente, N van Bakel, M van Beuzekom, J F J van den Brand, C Van Den Broeck, M V van der Sluys, J van Heijningen, M Vasúth, G Vedovato, J Veitch, D Verkindt, F Vetrano, A Viceré, J-Y Vinet, G Visser, H Vocca, R Ward, M Was, L-W Wei, M Yvert, A Zadro żny, and J-P Zendri. Advanced virgo: a second-generation interferometric gravitational wave detector. *Classical and Quantum Gravity*, 32(2):024001, dec 2014.

[14] Kagra Collaboration, T. Akutsu, M. Ando, K. Arai, Y. Arai, S. Araki, A. Araya, N. Aritomi, H. Asada, Y. Aso, S. Atsuta, K. Awai, S. Bae, L. Baiotti, M. A. Barton, K. Cannon, E. Capocasa, C. S. Chen, T. W. Chiu, K. Cho, Y. K. Chu, K. Craig, W. Creus, K. Doi, K. Eda, Y. Enomoto, R. Flaminio, Y. Fujii, M. K. Fujimoto, M. Fukunaga, M. Fukushima, T. Furuhata, S. Haino, K. Hasegawa, K. Hashino, K. Hayama, S. Hirobayashi, E. Hirose, B. H. Hsieh, C. Z. Huang, B. Ikenoue, Y. Inoue, K. Ioka, Y. Itoh, K. Izumi, T. Kaji, T. Kajita, M. Kakizaki, M. Kamizumi, S. Kanbara, N. Kanda, S. Kanemura, M. Kaneyama, G. Kang, J. Kasuya, Y. Kataoka, N. Kawai, S. Kawamura, T. Kawasaki, C. Kim, J. Kim, J. C. Kim, W. S. Kim, Y. M. Kim, N. Kimura, T. Kinugawa, S. Kirii, Y. Kitaoka, H. Kitazawa, Y. Kojima, K. Kokeyama, K. Komori, A. K. H. Kong, K. Kotake, R. Kozu, R. Kumar, H. S. Kuo, S. Kuroyanagi, H. K. Lee, H. M. Lee, H. W. Lee, M. Leonardi, C. Y. Lin, F. L. Lin, G. C. Liu, Y. Liu, E. Majorana, S. Mano, M. Marchio, T. Matsui, F. Matsushima, Y. Michimura, N. Mio, O. Miyakawa, A. Miyamoto, T. Miyamoto, K. Miyo, S. Miyoki, W. Morii, S. Morisaki, Y. Moriwaki, T. Morozumi, M. Musha, K. Nagano, S. Nagano, K. Nakamura, T. Nakamura, H. Nakano, M. Nakano, K. Nakao, T. Narikawa, L. Naticchioni, L. Nguyen Quynh, W. T. Ni, A. Nishizawa, Y. Obuchi, T. Ochi, J. J. Oh, S. H. Oh, M. Ohashi, N. Ohishi, M. Ohkawa, K. Okutomi, K. Ono, K. Oohara, C. P. Ooi, S. S. Pan, J. Park, F. E.

Peña Arellano, I. Pinto, N. Sago, M. Saijo, S. Saitou, Y. Saito, K. Sakai, Y. Sakai, Y. Sakai, M. Sasai, M. Sasaki, Y. Sasaki, S. Sato, N. Sato, T. Sato, Y. Sekiguchi, N. Seto, M. Shibata, T. Shimoda, H. Shinkai, T. Shishido, A. Shoda, K. Somiya, E. J. Son, A. Suemasa, T. Suzuki, T. Suzuki, H. Tagoshi, H. Tahara, H. Takahashi, R. Takahashi, A. Takamori, H. Takeda, H. Tanaka, K. Tanaka, T. Tanaka, S. Tanioka, E. N. Tapia San Martin, D. Tatsumi, T. Tomaru, T. Tomura, F. Travasso, K. Tsubono, S. Tsuchida, N. Uchikata, T. Uchiyama, T. Uehara, S. Ueki, K. Ueno, F. Uraguchi, T. Ushiba, M. H. P. M. van Putten, H. Vocca, S. Wada, T. Wakamatsu, Y. Watanabe, W. R. Xu, T. Yamada, A. Yamamoto, K. Yamamoto, K. Yamamoto, S. Yamamoto, T. Yamamoto, K. Yokogawa, J. Yokoyama, T. Yokozawa, T. H. Yoon, T. Yoshioka, H. Yuzurihara, S. Zeidler, and Z. H. Zhu. KAGRA: 2.5 generation interferometric gravitational wave detector. *Nature Astronomy*, 3:35–40, January 2019.

[15] David Reitze, Rana X. Adhikari, Stefan Ballmer, Barry Barish, Lisa Barsotti, GariLynn Billingsley, Duncan A. Brown, Yanbei Chen, Dennis Coyne, Robert Eisenstein, Matthew Evans, Peter Fritschel, Evan D. Hall, Albert Lazzarini, Geoffrey Lovelace, Jocelyn Read, B. S. Sathyaprakash, David Shoemaker, Joshua Smith, Calum Torrie, Salvatore Vitale, Rainer Weiss, Christopher Wipf, and Michael Zucker. Cosmic Explorer: The U.S. Contribution to Gravitational-Wave Astronomy beyond LIGO. In *Bulletin of the American Astronomical Society*, volume 51, page 35, September 2019.

[16] M. Punturo et al. The Einstein Telescope: A third-generation gravitational wave observatory. *Class. Quant. Grav.*, 27:194002, 2010.

[17] Christopher Reynolds, Rob Petre, Mike Corcoran, Keith Arnaud, Niel Brandt, Laura Lopez, Neil Cornish, Kristen Madsen, Gabriela Gonzales, and Laura Brenneman. High-Energy Astrophysics in the 2020s and Beyond. , 51(3):385, May 2019.

[18] Thomas Schäfer. Fluid Dynamics and Viscosity in Strongly Correlated Fluids. *Annual Review of Nuclear and Particle Science*, 64(1):125–148, October 2014.

[19] Gordon I. Ogilvie. Astrophysical fluid dynamics. *Journal of Plasma Physics*, 82(3), may 2016.

[20] Shoji Kato and Jun Fukue. *Fundamentals of Astrophysical Fluid Dynamics; Hydrodynamics, Magnetohydrodynamics, and Radiation Hydrodynamics*. 2020.

[21] Chris Reynolds. Lecture notes in astrophysical fluid dynamics, February 2021.

[22] T. P. Ray. Kelvin-Helmholtz instabilities in radio jets. *Mon. Not. Roy. Astr. Soc.*, 196:195–207, July 1981.

[23] A. P. Boss. Giant planet formation by gravitational instability. *Science*, 276:1836–1839, December 1997.

[24] Shu-Ichiro Inutsuka, Hiroshi Koyama, and Tsuyoshi Inoue. The Role of Thermal Instability in Interstellar Medium. In Elisabete M. de Gouveia dal Pino, Germán Lugones, and Alexander Lazarian, editors, *Magnetic Fields in the Universe: From Laboratory and Stars to Primordial Structures.*, volume 784 of *American Institute of Physics Conference Series*, pages 318–328, September 2005.

[25] John M. Blondin, Anthony Mezzacappa, and Christine DeMarino. Stability of Standing Accretion Shocks, with an Eye toward Core-Collapse Supernovae. *Astrophysical J.*, 584(2):971–980, February 2003.

[26] John M. Blondin and Samantha Shaw. Linear growth of spiral SASI modes in core-collapse supernovae. *Astrophys. J.*, 656:366–371, 2007.

[27] T. Foglizzo, P. Galletti, L. Scheck, and H.-Th. Janka. Instability of a stalled accretion shock: Evidence for the advective-acoustic cycle. *The Astrophysical Journal*, 654(2):1006–1021, jan 2007.

[28] J. E. Pringle. Accretion discs in astrophysics. *Annual Review of Astronomy and Astrophysics*, 19:137–162, January 1981.

[29] H.-Th. Janka, K. Langanke, A. Marek, G. Martínez-Pinedo, and B. Müller. Theory of core-collapse supernovae. *Physics Reports*, 442(1):38–74, 2007. The Hans Bethe Centennial Volume 1906-2006.

[30] John C. Houck and Roger A. Chevalier. Linear Stability Analysis of Spherical Accretion Flows onto Compact Objects. *Astrophysical J.*, 395:592, August 1992.

[31] H. Bondi. On spherically symmetrical accretion. *Mon. Not. Roy. Astr. Soc.*, 112:195, January 1952.

[32] John M. Blondin and Anthony Mezzacappa. Pulsar spins from an instability in the accretion shock of supernovae. , 445(7123):58–60, January 2007.

[33] Thierry Foglizzo and Pascal Galletti. Non-radial instability of stalled accretion shocks: advective-acoustic cycle. In *3-D Signatures in Stellar Explosions: A Workshop Honoring J. Craig Wheeler's 60th Birthday*, 8 2003.

[34] T. Foglizzo, P. Galletti, L. Scheck, and H. Th. Janka. Instability of a Stalled Accretion Shock: Evidence for the Advective-Acoustic Cycle. *Astrophysical J.*, 654(2):1006–1021, January 2007.

[35] T. Foglizzo. The Advective-Acoustic Instability in Numerical Simulations of Astrophysical Flows. In N. V. Pogorelov, E. Audit, and G. P. Zank, editors, *Numerical Modeling of Space Plasma Flows*, volume 385 of *Astronomical Society of the Pacific Conference Series*, page 85, April 2008.

[36] David Radice, Ernazar Abdikamalov, Christian D. Ott, Philipp Mösta, Sean M. Couch, and Luke F. Roberts. Turbulence in core-collapse supernovae. *Journal of Physics G Nuclear Physics*, 45(5):053003, May 2018.

[37] Ernazar Abdikamalov, César Huete, Ayan Nussupbekov, and Shapagat Berdibek. Turbulence Generation by Shock-Acoustic-Wave Interaction in Core-Collapse Supernovae. *Particles*, 1(1):7, May 2018.

[38] Ernazar Abdikamalov and Thierry Foglizzo. Acoustic wave generation in collapsing massive stars with convective shells. *Mon. Not. Roy. Astr. Soc.*, 493(3):3496–3512, April 2020.

[39] T. G. Cowling. The non-radial oscillations of polytropic stars. *Mon. Not. Roy. Astr. Soc.*, 101:367, January 1941.

[40] Chaitanya Afle, Suman Kumar Kundu, Jenna Cammerino, Eric R. Coughlin, Duncan A. Brown, David Vartanyan, and Adam Burrows. Measuring the properties of $f-$mode oscillations of a protoneutron star by third-generation gravitational-wave detectors. *Phys. Rev. D*, 107:123005, Jun 2023.

[41] A. G. W. Cameron. Physics of the Primitive Solar Accretion Disk. *Moon and Planets*, 18(1):5–40, February 1978.

[42] V. S. Safronov. Evolution of the protoplanetary cloud and formation of the earth and the planets. jerusalem, israel program for scientific translations. *Evolution of the protoplanetary cloud and formation of the earth and the planets. Jerusalem, Israel Program for Scientific Translations.*, 1972.

[43] D. J. Stevenson. *Planet. Space Sci.*, 30:755, 1982.

[44] S. Chandrasekhar and E. A. Milne. The equilibrium of distorted polytropes: (i). the rotational problem. *Monthly Notices of the Royal Astronomical Society, Volume 93, Issue 5, March 1933, Pages 390–406,*, 93, March 1933.

[45] M. Kafatos. Book-Review - Supermassive Black-Holes. , 76:639, December 1988.

[46] John Kormendy and Douglas Richstone. Inward Bound—The Search For Supermassive Black Holes In Galactic Nuclei. *Annual Review of Astronomy and Astrophysics*, 33:581, January 1995.

[47] Mitchell Begelman and Martin Rees. *Gravity's fatal attraction. Black holes in the universe*. Cambridge University Press, 1996.

[48] D. Richstone, E. A. Ajhar, R. Bender, G. Bower, A. Dressler, S. M. Faber, A. V. Filippenko, K. Gebhardt, R. Green, L. C. Ho, J. Kormendy, T. R. Lauer, J. Magorrian, and S. Tremaine. Supermassive black holes and the evolution of galaxies. , 385(6701):A14, October 1998.

[49] John Kormendy and Luis C. Ho. Coevolution (Or Not) of Supermassive Black Holes and Host Galaxies. *Annual Review of Astronomy and Astrophysics*, 51(1):511–653, August 2013.

[50] P. J. E. Peebles. Star Distribution Near a Collapsed Object. *Astrophysical J.*, 178:371–376, December 1972.

[51] J. G. Hills. Possible power source of Seyfert galaxies and QSOs. , 254(5498):295–298, March 1975.

[52] J. Frank and M. J. Rees. Effects of massive black holes on dense stellar systems. *Mon. Not. Roy. Astr. Soc.*, 176:633–647, September 1976.

[53] P. J. Young. The black tide model of QSOs. II. Destruction in an isothermal sphere. *Astrophysical J.*, 215:36–52, July 1977.

[54] J. Frank. Tidal disruption by a massive black hole and collisions in galactic nuclei. *Mon. Not. Roy. Astr. Soc.*, 184:87–99, July 1978.

[55] M. Kato and R. Hōshi. Possible Power Source and Time Variation of Quasars and Seyfert Galaxies. *Progress of Theoretical Physics*, 60(6):1692–1702, December 1978.

[56] J. H. Lacy, C. H. Townes, and D. J. Hollenbach. The nature of the central parsec of the Galaxy. *Astrophysical J.*, 262:120–134, November 1982.

[57] B. Carter and J. P. Luminet. Pancake detonation of stars by black holes in galactic nuclei. , 296(5854):211–214, March 1982.

[58] G. V. Bicknell and R. A. Gingold. On tidal detonation of stars by massive black holes. *Astrophysical J.*, 273:749–760, October 1983.

[59] Martin J. Rees. Tidal disruption of stars by black holes of 10^6-10^8 solar masses in nearby galaxies. , 333(6173):523–528, June 1988.

[60] Charles R. Evans and Christopher S. Kochanek. The Tidal Disruption of a Star by a Massive Black Hole. *Astrophysical J.*, 346:L13, November 1989.

[61] E.S. Phinney. Manifestations of a massive black hole in the galactic center. *Symposium - International Astronomical Union*, 136:543–553, 1989.

[62] Stefanie Komossa and Jochen Greiner. Discovery of a giant and luminous X-ray outburst from the optically inactive galaxy pair RX J1242.6-1119. *Astron. and Astrophys.*, 349:L45–L48, September 1999.

[63] Stefanie Komossa and Norbert Bade. The giant X-ray outbursts in NGC 5905 and IC 3599:() hfill Follow-up observations and outburst scenarios. *Astron. and Astrophys.*, 343:775–787, March 1999.

[64] D. Grupe, H. C. Thomas, and K. M. Leighly. RX J1624.9+7554: a new X-ray transient AGN. *Astron. and Astrophys.*, 350:L31–L34, October 1999.

[65] S. Gezari, S. Basa, D. C. Martin, G. Bazin, K. Forster, B. Milliard, J. P. Halpern, P. G. Friedman, P. Morrissey, S. G. Neff, D. Schiminovich, M. Seibert, T. Small, and T. K. Wyder. UV/Optical Detections of Candidate Tidal Disruption Events by GALEX and CFHTLS. *Astrophysical J.*, 676(2):944–969, April 2008.

[66] Suvi Gezari, Tim Heckman, S. Bradley Cenko, Michael Eracleous, Karl Forster, Thiago S. Gonçalves, D. Chris Martin, Patrick Morrissey, Susan G. Neff, Mark Seibert, David Schiminovich, and Ted K. Wyder. Luminous Thermal Flares from Quiescent Supermassive Black Holes. *Astrophysical J.*, 698(2):1367–1379, June 2009.

[67] S. Gezari, R. Chornock, A. Rest, M. E. Huber, K. Forster, E. Berger, P. J. Challis, J. D. Neill, D. C. Martin, T. Heckman, A. Lawrence, C. Norman, G. Narayan, R. J. Foley, G. H. Marion, D. Scolnic, L. Chomiuk, A. Soderberg, K. Smith, R. P. Kirshner, A. G. Riess, S. J. Smartt, C. W. Stubbs, J. L. Tonry, W. M. Wood-Vasey, W. S. Burgett, K. C. Chambers, T. Grav, J. N. Heasley, N. Kaiser, R. P. Kudritzki, E. A. Magnier, J. S. Morgan, and P. A. Price. An ultraviolet-optical flare from the tidal disruption of a helium-rich stellar core. , 485(7397):217–220, May 2012.

[68] Joshua S. Bloom, Dimitrios Giannios, Brian D. Metzger, S. Bradley Cenko, Daniel A. Perley, Nathaniel R. Butler, Nial R. Tanvir, Andrew J. Levan, Paul T. O'Brien, Linda E. Strubbe, Fabio De Colle, Enrico Ramirez-Ruiz, William H. Lee,

Sergei Nayakshin, Eliot Quataert, Andrew R. King, Antonino Cucchiara, James Guillochon, Geoffrey C. Bower, Andrew S. Fruchter, Adam N. Morgan, and Alexander J. van der Horst. A Possible Relativistic Jetted Outburst from a Massive Black Hole Fed by a Tidally Disrupted Star. *Science*, 333(6039):203, July 2011.

[69] K. Hryniewicz and R. Walter. Unbeamed tidal disruption events at hard X-rays. *Astron. and Astrophys.*, 586:A9, February 2016.

[70] T. Hung, S. Gezari, N. Blagorodnova, N. Roth, S. B. Cenko, S. R. Kulkarni, A. Horesh, I. Arcavi, C. McCully, Lin Yan, R. Lunnan, C. Fremling, Y. Cao, P. E. Nugent, and P. Wozniak. Revisiting Optical Tidal Disruption Events with iPTF16axa. *Astrophysical J.*, 842(1):29, June 2017.

[71] S. Komossa. Tidal disruption of stars by supermassive black holes: Status of observations. *Journal of High Energy Astrophysics*, 7:148–157, September 2015.

[72] R. D. Blandford and R. L. Znajek. Electromagnetic extraction of energy from Kerr black holes. *Mon. Not. Roy. Astr. Soc.*, 179:433–456, May 1977.

[73] M. C. Begelman, R. D. Blandford, and M. J. Rees. Massive black hole binaries in active galactic nuclei. , 287(5780):307–309, September 1980.

[74] S. Rosswog, E. Ramirez-Ruiz, and W. R. Hix. Tidal Disruption and Ignition of White Dwarfs by Moderately Massive Black Holes. *Astrophysical J.*, 695(1):404–419, April 2009.

[75] S. van Velzen. On the Mass and Luminosity Functions of Tidal Disruption Flares: Rate Suppression due to Black Hole Event Horizons. *Astrophysical J.*, 852(2):72, January 2018.

[76] T. Mageshwaran and A. Mangalam. Black hole demographics from TDE modeling. *arXiv e-prints*, page arXiv:1808.04531, August 2018.

[77] Dheeraj Pasham, Dacheng Lin, Richard Saxton, Peter Jonker, Erin Kara, Nicholas Stone, Peter Maksym, and Katie Auchettl. Probing the Cosmological Evolution of Super-massive Black Holes using Tidal Disruption Flares. , 51(3):27, May 2019.

[78] T. Wevers. TDE Black Hole Demographics. In *American Astronomical Society Meeting Abstracts #235*, volume 235 of *American Astronomical Society Meeting Abstracts*, page 332.06, January 2020.

[79] N. Roos. Galaxy mergers and active galactic nuclei. *Astron. and Astrophys.*, 104:218–228, December 1981.

[80] Hugo Pfister, Ben Bar-Or, Marta Volonteri, Yohan Dubois, and Pedro R. Capelo. Tidal disruption event rates in galaxy merger remnants. *Mon. Not. Roy. Astr. Soc.*, 488(1):L29–L34, September 2019.

[81] N. C. Stone, E. Vasiliev, M. Kesden, E. M. Rossi, H. B. Perets, and P. Amaro-Seoane. Rates of Stellar Tidal Disruption. , 216(3):35, March 2020.

[82] Eric R. Coughlin and Mitchell C. Begelman. Hyperaccretion during Tidal Disruption Events: Weakly Bound Debris Envelopes and Jets. *Astrophysical J.*, 781(2):82, February 2014.

[83] Samantha Wu, Eric R. Coughlin, and Chris Nixon. Super-Eddington accretion in tidal disruption events: the impactof realistic fallback rates on accretion rates. *Mon. Not. Roy. Astr. Soc.*, 478(3):3016–3024, August 2018.

[84] James Guillochon and Enrico Ramirez-Ruiz. Hydrodynamical Simulations to Determine the Feeding Rate of Black Holes by the Tidal Disruption of Stars: The Importance of the Impact Parameter and Stellar Structure. *Astrophysical J.*, 767(1):25, April 2013.

[85] Eric R. Coughlin and Chris Nixon. Variability in Tidal Disruption Events: Gravitationally Unstable Streams. *Astrophysical J.*, 808(1):L11, July 2015.

[86] Eric R. Coughlin, Chris Nixon, Mitchell C. Begelman, and Philip J. Armitage. On the structure of tidally disrupted stellar debris streams. *Mon. Not. Roy. Astr. Soc.*, 459(3):3089–3103, July 2016.

[87] Clément Bonnerot, Elena M. Rossi, Giuseppe Lodato, and Daniel J. Price. Disc formation from tidal disruptions of stars on eccentric orbits by Schwarzschild black holes. *Mon. Not. Roy. Astr. Soc.*, 455(2):2253–2266, January 2016.

[88] Yan-Fei Jiang, James Guillochon, and Abraham Loeb. Prompt Radiation and Mass Outflows from the Stream-Stream Collisions of Tidal Disruption Events. *Astrophysical J.*, 830(2):125, October 2016.

[89] Siva Darbha, Eric R. Coughlin, Daniel Kasen, and Chris Nixon. Ultra-deep tidal disruption events: prompt self-intersections and observables. *Mon. Not. Roy. Astr. Soc.*, 488(4):5267–5278, October 2019.

[90] Patrick R. Miles, Eric R. Coughlin, and C. J. Nixon. Fallback Rates from Partial Tidal Disruption Events. *Astrophysical J.*, 899(1):36, August 2020.

[91] Alexandra Spaulding and Philip Chang. The effect of impact parameter on tidal disruption events. *Mon. Not. Roy. Astr. Soc.*, 501(2):1748–1754, February 2021.

[92] S. M. J. Norman, C. J. Nixon, and Eric R. Coughlin. Stars Crushed by Black Holes. I. On the Energy Distribution of Stellar Debris in Tidal Disruption Events. *Astrophysical J.*, 923(2):184, December 2021.

[93] C. J. Nixon and Eric R. Coughlin. Stellar Revival and Repeated Flares in Deeply Plunging Tidal Disruption Events. *Astrophysical J.*, 927(2):L25, March 2022.

[94] G. Lodato, A. R. King, and J. E. Pringle. Stellar disruption by a supermassive black hole: is the light curve really proportional to $t^{-5/3}$? *Mon. Not. Roy. Astr. Soc.*, 392(1):332–340, January 2009.

[95] Giuseppe Lodato and Elena M. Rossi. Multiband light curves of tidal disruption events. *Mon. Not. Roy. Astr. Soc.*, 410(1):359–367, January 2011.

[96] Roseanne M. Cheng and Tamara Bogdanović. Tidal disruption of a star in the Schwarzschild spacetime: Relativistic effects in the return rate of debris. *Phys. Rev. D*, 90(6):064020, September 2014.

[97] Nicholas Stone and Abraham Loeb. Observing Lense-Thirring Precession in Tidal Disruption Flares. *Phys. Rev. Lett.*, 108(6):061302, February 2012.

[98] Tsvi Piran, Aleksander Sądowski, and Alexander Tchekhovskoy. Jet and disc luminosities in tidal disruption events. *Mon. Not. Roy. Astr. Soc.*, 453(1):157–165, October 2015.

[99] Nathaniel Roth and Daniel Kasen. What Sets the Line Profiles in Tidal Disruption Events? *Astrophysical J.*, 855(1):54, March 2018.

[100] C.J. Hansen, S.D. Kawaler, and V. Trimble. *Stellar Interiors: Physical Principles, Structure, and Evolution*. Astronomy and Astrophysics Library. Springer New York, 2012.

[101] A. Clerici and A. Gomboc. A study on tidal disruption event dynamics around an Sgr A*-like massive black hole. *Astron. and Astrophys.*, 642:A111, October 2020.

[102] Nicholas C. Stone, Michael Kesden, Roseanne M. Cheng, and Sjoert van Velzen. Stellar tidal disruption events in general relativity. *General Relativity and Gravitation*, 51(2):30, February 2019.

[103] W. Benz. Smooth Particle Hydrodynamics - a Review. In J. Robert Buchler, editor, *Numerical Modelling of Nonlinear Stellar Pulsations Problems and Prospects*, page 269, January 1990.

[104] Michael Gittings, Robert Weaver, Michael Clover, Thomas Betlach, Nelson Byrne, Robert Coker, Edward Dendy, Robert Hueckstaedt, Kim New, W. Rob Oakes, Dale Ranta, and Ryan Stefan. The RAGE radiation-hydrodynamic code. *Computational Science and Discovery*, 1(1):015005, October 2008.

[105] Volker Springel. E pur si muove: Galilean-invariant cosmological hydrodynamical simulations on a moving mesh. *Mon. Not. Roy. Astr. Soc.*, 401(2):791–851, January 2010.

[106] Elena M. Rossi, Nicholas C. Stone, Jamie A. P. Law-Smith, Morgan MacLeod, Giuseppe Lodato, Jane L. Dai, and Ilya Mandel. The Process of Stellar Tidal Disruption by Supermassive Black Holes. The first pericenter passage. *arXiv e-prints*, page arXiv:2005.12528, May 2020.

[107] Deborah Mainetti, Alessandro Lupi, Sergio Campana, Monica Colpi, Eric R. Coughlin, James Guillochon, and Enrico Ramirez-Ruiz. The fine line between total and partial tidal disruption events. *Astron. and Astrophys.*, 600:A124, April 2017.

[108] V. V. Lidskii and L. M. Ozernoi. Tidal triggering of stellar flares by a massive black hole. *Soviet Astronomy Letters*, 5:16–19, January 1979.

[109] J. Wheeler. Mechanism for Jets. In D. J. K. O'Connell, editor, *Study Week on Nuclei of Galaxies*, page 539, January 1971.

[110] J. G. Hills. Stellar debris clouds in quasars and related objects. *Mon. Not. Roy. Astr. Soc.*, 182:517–536, February 1978.

[111] B. Carter and J. P. Luminet. Mechanics of the affine star model. *Mon. Not. Roy. Astr. Soc.*, 212:23–55, January 1985.

[112] C.P. Dullemond and R. Kuiper. Lecture notes in numerical fluid dynamics, Summer 2008.

[113] P. Ledoux. Stellar stability and stellar evolution. In L. Gratton, editor, *Star Evolution*, page 394, January 1963.

[114] R. A. Gingold and J. J. Monaghan. Smoothed particle hydrodynamics: theory and application to non-spherical stars. *Mon. Not. Roy. Astr. Soc.*, 181:375–389, November 1977.

[115] J J Monaghan. Smoothed particle hydrodynamics. *Reports on Progress in Physics*, 68(8):1703, jul 2005.

[116] Daniel J. Price. Smoothed particle hydrodynamics and magnetohydrodynamics. *Journal of Computational Physics*, 231(3):759–794, February 2012.

[117] Volker Springel and Lars Hernquist. Cosmological smoothed particle hydrodynamics simulations: the entropy equation. *Mon. Not. Roy. Astr. Soc.*, 333(3):649–664, July 2002.

[118] J. J. Monaghan. SPH compressible turbulence. *Monthly Notices of the Royal Astronomical Society*, 335(3):843–852, 09 2002.

[119] Fred C Adams et al. Eccentric gravitational instabilities in nearly keplerian disks. *Astrophysical Journal*, 347:959, December 1989.

[120] K. M. Kratter. The Formation of Close Binaries. In L. Schmidtobreick, M. R. Schreiber, and C. Tappert, editors, *Evolution of Compact Binaries*, volume 447 of *Astronomical Society of the Pacific Conference Series*, page 47, September 2011.

[121] C. J. Nixon, A. R. King, and J. E. Pringle. The Maximum Mass Solar Nebula and the early formation of planets. *Mon. Not. Roy. Astr. Soc.*, 477(3):3273–3278, July 2018.

[122] F. Perri and A. G. W. Cameron. *Icarus*, 22:416, 1974.

[123] A. W. Harris. *Lunar and Planetary Science Conference*, page 459, 1978.

[124] Hiroshi Mizuno. Formation of the giant planets. *Progress of Theoretical Physics, Volume 64, Issue 2, August 1980, Pages 544–557*, 64, August 1980.

[125] D.J. Stevenson. Formation of the giant planets. *Planetary and Space Science*, 30(8):755–764, 1982.

[126] Peter Bodenheimer and James B. Pollack. Calculations of the accretion and evolution of giant planets: The effects of solid cores. 67(3):391–408, November 1986.

[127] James B Pollack et al. Formation of the giant planets by concurrent accretion of solids and gas. 124:62–85., November 1996.

[128] Andrew N. Youdin and Jeremy Goodman. Streaming instabilities in protoplanetary disks. *The Astrophysical Journal*, 620(1):459–469, feb 2005.

[129] E. Chiang and A.N. Youdin. Forming planetesimals in solar and extrasolar nebulae. *Annual Review of Earth and Planetary Sciences*, 38(1):493–522, 2010.

[130] A. Johansen, J. Blum, H. Tanaka, C. Ormel, M. Bizzarro, and H. Rickman. The Multifaceted Planetesimal Formation Process. In Henrik Beuther, Ralf S. Klessen, Cornelis P. Dullemond, and Thomas Henning, editors, *Protostars and Planets VI*, page 547, January 2014.

[131] P. Heinisch, H. U. Auster, B. Gundlach, J. Blum, C. Güttler, C. Tubiana, H. Sierks, M. Hilchenbach, J. Biele, I. Richter, and K. H. Glassmeier. Compressive strength of comet 67P/Churyumov-Gerasimenko derived from Philae surface contacts. *Astron. and Astrophys.*, 630:A2, October 2019.

[132] George W. Wetherill and Glen R. Stewart. Formation of planetary embryos: Effects of fragmentation, low relative velocity, and independent variation of eccentricity and inclination. *Icarus, Volume 106, Issue 1, November 1993, Pages 190-209*, 106, November 1993.

[133] Peter Goldreich, Yoram Lithwick, and Re'em Sari. Final stages of planet formation. *The Astrophysical Journal*, 614(1):497–507, oct 2004.

[134] C. W. Ormel and J. N. Cuzzi. Closed-form expressions for particle relative velocities induced by turbulence. *Astron. and Astrophys.*, 466(2):413–420, May 2007.

[135] Andrew N. Youdin and Scott J. Kenyon. *From Disks to Planets*, page 1. 2013.

[136] Beibei Liu, Chris W. Ormel, and Anders Johansen. Growth after the streaming instability. From planetesimal accretion to pebble accretion. *Astron. and Astrophys.*, 624:A114, April 2019.

[137] Ana-Maria A. Piso and Andrew N. Youdin. On the Minimum Core Mass for Giant Planet Formation at Wide Separations. *Astrophysical J.*, 786(1):21, May 2014.

[138] Eve J. Lee and Eugene Chiang. TO COOL IS TO ACCRETE: ANALYTIC SCALINGS FOR NEBULAR ACCRETION OF PLANETARY ATMOSPHERES. *The Astrophysical Journal*, 811(1):41, sep 2015.

[139] Masahiro N. Machida, Eiichiro Kokubo, Shu ichiro Inutsuka, and Tomoaki Matsumoto. Angular momentum accretion onto a gas giant planet. *The Astrophysical Journal*, 685(2):1220–1236, oct 2008.

[140] Takayuki Tanigawa, Keiji Ohtsuki, and Masahiro N. Machida. DISTRIBUTION OF ACCRETING GAS AND ANGULAR MOMENTUM ONTO CIRCUMPLANETARY DISKS. *The Astrophysical Journal*, 747(1):47, feb 2012.

[141] M. Lambrechts and E. Lega. Reduced gas accretion on super-Earths and ice giants. *Astron. and Astrophys.*, 606:A146, October 2017.

[142] Masahiro Ikoma, Kiyoshi Nakazawa, and Hiroyuki Emori. Formation of Giant Planets: Dependences on Core Accretion Rate and Grain Opacity. *Astrophysical J.*, 537(2):1013–1025, July 2000.

[143] S. H. Lubow, M. Seibert, and P. Artymowicz. Disk accretion onto high-mass planets. *The Astrophysical Journal*, 526(2):1001–1012, Dec 1999.

[144] Jack J. Lissauer, Olenka Hubickyj, Gennaro D'Angelo, and Peter Bodenheimer. Models of Jupiter's growth incorporating thermal and hydrodynamic constraints. , 199(2):338–350, February 2009.

[145] Sivan Ginzburg and Eugene Chiang. The endgame of gas giant formation: accretion luminosity and contraction post-runaway. *MNRAS*, 490(3):4334–4343, December 2019.

[146] D. Saumon, G. Chabrier, and H. M. van Horn. An equation of state for low-mass stars and giant planets. *Astrophysical Journal Supplement*, 99:713, August 1995.

[147] Richard B. Larson. Numerical calculations of the dynamics of collapsing proto-star. *Mon. Not. Roy. Astr. Soc.*, 145:271, January 1969.

[148] Günther Wuchterl. Hydrodynamics of giant planet formation III: Jupiter's nucleated instability. , 91(1):53–64, May 1991.

[149] Ana-Maria A. Piso, Andrew N. Youdin, and Ruth A. Murray-Clay. Minimum Core Masses for Giant Planet Formation with Realistic Equations of State and Opacities. *Astrophysical J.*, 800(2):82, February 2015.

[150] Eric R. Coughlin and C. J. Nixon. The Gravitational Instability of Adiabatic Filaments. *Astrophysical Journal, Supplement*, 247(2):51, April 2020.

[151] F. K. Liu. Polytropic gas spheres: an approximate analytic solution of the lane-emden equation. *Monthly Notices of the Royal Astronomical Society*, 281(4), August 1996.

[152] P. H. Chavanis. Gravitational instability of polytropic spheres and generalized thermodynamics. *Astronomy and Astrophysics*, 386:732–742, May 2002.

[153] Carl J. Hansen, Steven D. Kawaler, and Virginia Trimble. *Stellar interiors : physical principles, structure, and evolution.* 2004.

[154] John P. Cox. *Theory of stellar pulsation.* 1980.

[155] Ravit Helled and David Stevenson. The Fuzziness of Giant Planets' Cores. *The Astrophysical Journal Letters*, 840, April 2017.

[156] S. M. Wahl, W. B. Hubbard, B. Militzer, T. Guillot, Y. Miguel, N. Movshovitz, Y. Kaspi, R. Helled, D. Reese, E. Galanti, S. Levin, J. E. Connerney, and S. J. Bolton. Comparing Jupiter interior structure models to Juno gravity measurements and the role of a dilute core. , 44(10):4649–4659, May 2017.

[157] David J. Stevenson. Jupiter's Interior as Revealed by Juno. *Annual Review of Earth and Planetary Sciences*, 48:465–489, May 2020.

[158] John C. B. Papaloizou and Caroline Terquem. Critical Protoplanetary Core Masses in Protoplanetary Disks and the Formation of Short-Period Giant Planets. *Astrophysical J.*, 521(2):823–838, August 1999.

[159] William Béthune. Self-gravitating planetary envelopes and the core-nucleated instability. *Mon. Not. Roy. Astr. Soc.*, 490(3):3144–3157, December 2019.

[160] Eric R. Coughlin, Stephen Ro, and Eliot Quataert. Weak Shock Propagation with Accretion. II. Stability of Self-similar Solutions to Radial Perturbations. *Astrophysical J.*, 874(1):58, March 2019.

[161] Stirling A. Colgate and Richard H. White. The Hydrodynamic Behavior of Supernovae Explosions. *Astrophysical J.*, 143:626, March 1966.

[162] H.A. Bethe, G.E. Brown, J. Applegate, and J.M. Lattimer. Equation of state in the gravitational collapse of stars. *Nuclear Physics A*, 324(2):487–533, 1979.

[163] S. E. Woosley and T. A. Weaver. Theoretical Models for Type-I and Type-II Supernova. In J. Audouze and N. Mathieu, editors, *Nucleosynthesis and its Implications on Nuclear and Particle Physics*, volume 163 of *NATO Advanced Study Institute (ASI) Series C*, pages 145–166, January 1986.

[164] H. A. Bethe and J. R. Wilson. Revival of a stalled supernova shock by neutrino heating. *Astrophysical J.*, 295:14–23, August 1985.

[165] Marc Herant, Willy Benz, and Stirling Colgate. Postcollapse Hydrodynamics of SN 1987A: Two-dimensional Simulations of the Early Evolution. *Astrophysical J.*, 395:642, August 1992.

[166] Marc Herant, Willy Benz, W. Raphael Hix, Chris L. Fryer, and Stirling A. Colgate. Inside the Supernova: A Powerful Convective Engine. *Astrophysical J.*, 435:339, November 1994.

[167] H. A. Bethe. Supernova mechanisms. *Rev. Mod. Phys.*, 62:801–866, Oct 1990.

[168] Jeremiah W. Murphy and Adam Burrows. Criteria for Core-Collapse Supernova Explosions by the Neutrino Mechanism. *Astrophysical J.*, 688(2):1159–1175, December 2008.

[169] Marcella Ugliano, Hans-Thomas Janka, Andreas Marek, and Almudena Arcones. Progenitor-explosion Connection and Remnant Birth Masses for Neutrino-driven Supernovae of Iron-core Progenitors. *Astrophysical J.*, 757(1):69, September 2012.

[170] Ko Nakamura, Tomoya Takiwaki, Takami Kuroda, and Kei Kotake. Systematic features of axisymmetric neutrino-driven core-collapse supernova models in multiple progenitors. *Publications of the Astronomical Society of Japan*, 67(6), 10 2015. 107.

[171] Conrad Chan, Bernhard Müller, Alexander Heger, Rüdiger Pakmor, and Volker Springel. Black hole formation and fallback during the supernova explosion of a 40m$\odot$ star. *Astrophysical J.*, 852(1):L19, jan 2018.

[172] N Ohnishi, W Iwakami, K Kotake, S Yamada, S Fujioka, and H Takabe. Standing accretion shock instability: numerical simulations of core-collapse supernova. *Journal of Physics:Conference Series*, 112(4):042018, may 2008.

[173] Adam Burrows, Joshua C. Dolence, and Jeremiah W. Murphy. An Investigation into the Character of Pre-explosion Core-collapse Supernova Shock Motion. *Astrophysical J.*, 759(1):5, November 2012.

[174] W. David Arnett. Gravitational collapse and weak interactions. *Canadian Journal of Physics*, 44:2553–2594, January 1966.

[175] S. W. Bruenn. Stellar core collapse - Numerical model and infall epoch. *Astrophysical Journal, Supplement*, 58:771–841, August 1985.

[176] A. Marek and H. Th. Janka. Delayed Neutrino-Driven Supernova Explosions Aided by the Standing Accretion-Shock Instability. *Astrophysical J.*, 694(1):664–696, March 2009.

[177] M. L. Lidov. Automodel Motion of a Gas With Spherical Symmetry in the Field of a Gravitating Center. , 1:588, August 1957.

[178] Roger A. Chevalier. Neutron Star Accretion in a Supernova. *Astrophysical J.*, 346:847, November 1989.

[179] F. Curtis Michel. Accretion of Matter by Condensed Objects. , 15(1):153–160, January 1972.

[180] H. Bondi. On spherically symmetrical accretion. *Mon. Not. Roy. Astr. Soc.*, 112:195, January 1952.

[181] G. R. Blumenthal and W. G. Mathews. Spherical winds and accretion in general relativity. *Astrophysical J.*, 203:714–719, February 1976.

[182] Jun Fukue. Transonic disk accretion revisited. , 39(2):309–327, January 1987.

[183] Sandip K. Chakrabarti. Standing shocks in isothermal rotating winds and accretion. *Monthly Notices of the Royal Astronomical Society*, 240(1):7–21, 09 1989.

[184] Sandip K. Chakrabarti and Diego Molteni. Smoothed Particle Hydrodynamics Confronts Theory: Formation of Standing Shocks in Accretion Disks and Winds around Black Holes. *Astrophysical J.*, 417:671, November 1993.

[185] Wei-Min Gu and T. Foglizzo. Non-axisymmetric instabilities in shocked accretion flows with differential rotation. *Astron. and Astrophys.*, 409:1–7, October 2003.

[186] David Radice, Christian D. Ott, Ernazar Abdikamalov, Sean M. Couch, Roland Haas, and Erik Schnetter. Neutrino-driven Convection in Core-collapse Supernovae: High-resolution Simulations. *Astrophysical J.*, 820(1):76, March 2016.

[187] A. M. Anile. *Relativistic Fluids and Magneto-fluids: With Applications in Astrophysics and Plasma Physics*. Cambridge Monographs on Mathematical Physics. Cambridge University Press, 1990.

[188] Eric R. Coughlin, Eliot Quataert, and Stephen Ro. Weak shock propagation with accretion. i. self-similar solutions and application to failed supernovae. *Astrophysical J.*, 863(2):158, aug 2018.

[189] James M. Lattimer and Madappa Prakash. The equation of state of hot, dense matter and neutron stars. , 621:127–164, March 2016.

[190] P. Haensel, J. P. Lasota, and J. L. Zdunik. On the minimum period of uniformly rotating neutron stars. *Astron. and Astrophys.*, 344:151–153, April 1999.

[191] Paul J. Schinder, David N. Schramm, Paul J. Wiita, Steven H. Margolis, and David L. Tubbs. Neutrino Emission by the Pair, Plasma, and Photo Processes in the Weinberg-Salam Model. *Astrophysical J.*, 313:531, February 1987.

[192] K. Sumiyoshi, S. Yamada, and H. Suzuki. Dynamics and Neutrino Signal of Black Hole Formation in Nonrotating Failed Supernovae. I. Equation of State Dependence. *Astrophysical J.*, 667(1):382–394, September 2007.

[193] K. Sumiyoshi, S. Yamada, and H. Suzuki. Dynamics and Neutrino Signal of Black Hole Formation in Nonrotating Failed Supernovae. II. Progenitor Dependence. *Astrophysical J.*, 688(2):1176–1185, December 2008.

[194] Evan O'Connor and Christian D. Ott. Black Hole Formation in Failing Core-Collapse Supernovae. *Astrophysical J.*, 730(2):70, April 2011.

[195] Tuguldur Sukhbold, T. Ertl, S. E. Woosley, Justin M. Brown, and H. T. Janka. Core-collapse Supernovae from 9 to 120 Solar Masses Based on Neutrino-powered Explosions. *Astrophysical J.*, 821(1):38, April 2016.

[196] Takami Kuroda, Tobias Fischer, Tomoya Takiwaki, and Kei Kotake. Core-collapse Supernova Simulations and the Formation of Neutron Stars, Hybrid Stars, and Black Holes. *Astrophysical J.*, 924(1):38, January 2022.

[197] Prasun Dhang, Prateek Sharma, and Banibrata Mukhopadhyay. Spherical accretion: the influence of inner boundary and quasi-periodic oscillations. *Mon. Not. Roy. Astr. Soc.*, 461(3):2426–2439, September 2016.

[198] Rodrigo Fernández and Christopher Thompson. Stability of a Spherical Accretion Shock with Nuclear Dissociation. *Astrophysical J.*, 697(2):1827–1841, June 2009.

[199] Rodrigo Fernández and Christopher Thompson. Dynamics of a Spherical Accretion Shock with Neutrino Heating and Alpha-Particle Recombination. *Astrophysical J.*, 703(2):1464–1485, October 2009.

[200] Rodrigo Fernández, Bernhard Müller, Thierry Foglizzo, and Hans-Thomas Janka. Characterizing SASI- and convection-dominated core-collapse supernova explosions in two dimensions. *Mon. Not. Roy. Astr. Soc.*, 440(3):2763–2780, May 2014.

[201] E. Quataert, D. Lecoanet, and E. R. Coughlin. Black hole accretion discs and luminous transients in failed supernovae from non-rotating supergiants. *Mon. Not. Roy. Astr. Soc.*, 485(1):L83–L88, May 2019.

[202] Ramesh Narayan and Insu Yi. Advection-dominated Accretion: A Self-similar Solution. *Astrophysical J.*, 428:L13, June 1994.

[203] Roger D. Blandford and Mitchell C. Begelman. Two-dimensional adiabatic flows on to a black hole - I. Fluid accretion. *Mon. Not. Roy. Astr. Soc.*, 349(1):68–86, March 2004.

[204] Adam Burrows. Convection and the Mechanism of Type II Supernovae. *Astrophysical J.*, 318:L57, July 1987.

[205] Adam Burrows, John Hayes, and Bruce A. Fryxell. On the Nature of Core-Collapse Supernova Explosions. *Astrophysical J.*, 450:830, September 1995.

[206] Bernhard Müller. Hydrodynamics of core-collapse supernovae and their progenitors. *Living Reviews in Computational Astrophysics*, 6(1):3, June 2020.

[207] Bernhard Müller, Hans-Thomas Janka, and Harald Dimmelmeier. A New Multi-dimensional General Relativistic Neutrino Hydrodynamic Code for Core-collapse Supernovae. I. Method and Code Tests in Spherical Symmetry. *Astrophysical Journal, Supplement*, 189(1):104–133, July 2010.

[208] David Reitze et al. Cosmic Explorer: The U.S. Contribution to Gravitational-Wave Astronomy beyond LIGO. *Bull. Am. Astron. Soc.*, 51:035, 2019.

[209] Matthew Evans et al. A Horizon Study for Cosmic Explorer: Science, Observatories, and Community. 9 2021.

[210] Varun Srivastava, Stefan Ballmer, Duncan A. Brown, Chaitanya Afle, Adam Burrows, David Radice, and David Vartanyan. Detection Prospects of Core-Collapse Supernovae with Supernova-Optimized Third-Generation Gravitational-wave Detectors. *Phys. Rev.*, D100(4):043026, 2019.

[211] Scott M Adams, CS Kochanek, John F Beacom, Mark R Vagins, and KZ Stanek. Observing the next galactic supernova. *The Astrophysical Journal*, 778(2):164, 2013.

[212] E. Cappellaro, M. Turatto, D. Yu. Tsvetkov, O. S. Bartunov, C. Pollas, R. Evans, and M. Hamuy. The Rate of supernovae from the combined sample of five searches. *Astron. Astrophys.*, 322:431–441, 1997.

[213] G. A. Tammann, W. Loeffler, and A. Schroeder. The Galactic supernova rate. *apjs*, 92:487–493, June 1994.

[214] E. Mueller and H.-T. Janka. Gravitational radiation from convective instabilities in Type II supernova explosions. *Astron. Astrophys.*, 317:140–163, January 1997.

[215] K. Kotake, S. Yamada, and K. Sato. Gravitational radiation from axisymmetric rotational core collapse. *Phys. Rev. D*, 68(4):044023, August 2003.

[216] Jeremiah W. Murphy, Christian D. Ott, and Adam Burrows. A Model for Gravitational Wave Emission from Neutrino-Driven Core-Collapse Supernovae. *Astrophys. J.*, 707:1173–1190, 2009.

[217] Christian D. Ott, E. Abdikamalov, E. O'Connor, C. Reisswig, R. Haas, P. Kalmus, S. Drasco, A. Burrows, and E. Schnetter. Correlated Gravitational Wave and Neutrino Signals from General-Relativistic Rapidly Rotating Iron Core Collapse. *Phys. Rev. D*, 86:024026, 2012.

[218] K. Hayama, T. Kuroda, K. Kotake, and T. Takiwaki. Coherent network analysis of gravitational waves from three-dimensional core-collapse supernova models. *Phys. Rev. D*, 92(12):122001, December 2015.

[219] K. N. Yakunin, A. Mezzacappa, P. Marronetti, S. Yoshida, S. W. Bruenn, W. R. Hix, E. J. Lentz, O. E. Bronson Messer, J. A. Harris, E. Endeve, J. M. Blondin, and E. J. Lingerfelt. Gravitational wave signatures of ab initio two-dimensional core collapse supernova explosion models for 12 -25 $M_?$ stars. *Phys. Rev. D*, 92(8):084040, October 2015.

[220] Jade Powell, Sarah E. Gossan, Joshua Logue, and Ik Siong Heng. Inferring the core-collapse supernova explosion mechanism with gravitational waves. *Phys. Rev. D*, 94(12):123012, 2016.

[221] H. Andresen, B. Müller, E. Müller, and H.-T. Janka. Gravitational wave signals from 3D neutrino hydrodynamics simulations of core-collapse supernovae. *MNRAS*, 468:2032–2051, June 2017.

[222] Viktoriya Morozova, David Radice, Adam Burrows, and David Vartanyan. The gravitational wave signal from core-collapse supernovae. *Astrophys. J.*, 861(1):10, 2018.

[223] David Radice, Viktoriya Morozova, Adam Burrows, David Vartanyan, and Hiroki Nagakura. Characterizing the Gravitational Wave Signal from Core-collapse Supernovae. *Ap.J. Letters*, 876(1):L9, May 2019.

[224] A. Burrows, D. Vartanyan, J. C. Dolence, M. A. Skinner, and D. Radice. Crucial Physical Dependencies of the Core-Collapse Supernova Mechanism. *Space Science Revews*, 214:33, February 2018.

[225] Adam Burrows, David Radice, David Vartanyan, Hiroki Nagakura, M. Aaron Skinner, and Joshua Dolence. The Overarching Framework of Core-Collapse Supernova Explosions as Revealed by 3D Fornax Simulations. *Mon. Not. Roy. Astron. Soc.*, 491(2):2715–2735, 2020.

[226] M. A. Skinner, J. C. Dolence, A. Burrows, D. Radice, and D. Vartanyan. FORNAX: A Flexible Code for Multiphysics Astrophysical Simulations. *Ap.J. Suppl.*, 241:7, March 2019.

[227] Adam Burrows and David Vartanyan. Core-Collapse Supernova Explosion Theory. *Nature*, 589(7840):29–39, 2021.

[228] Chris L. Fryer and Kimberly C.B. New. Gravitational waves from gravitational collapse. *Living Rev. Rel.*, 14:1, 2011.

[229] Sherwood Richers, Christian D. Ott, Ernazar Abdikamalov, Evan O'Connor, and Chris Sullivan. Equation of State Effects on Gravitational Waves from Rotating Core Collapse. *Phys. Rev.*, D95(6):063019, 2017.

[230] D. Christodoulou. Nonlinear nature of gravitation and gravitational wave experiments. *Phys. Rev. Lett.*, 67:1486–1489, 1991.

[231] Kip S. Thorne. Gravitational-wave bursts with memory: The Christodoulou effect. *Phys. Rev. D*, 45(2):520–524, 1992.

[232] David Vartanyan and Adam Burrows. Gravitational Waves from Neutrino Emission Asymmetries in Core-collapse Supernovae. *Astrophys. J.*, 901(2):108, 2020.

[233] Marie-Anne Bizouard, Patricio Maturana-Russel, Alejandro Torres-Forné, Martin Obergaulinger, Pablo Cerdá-Durán, Nelson Christensen, José A. Font, and Renate Meyer. Inference of protoneutron star properties from gravitational-wave data in core-collapse supernovae. *Phys. Rev. D*, 103(6):063006, 2021.

[234] Jade Powell and Bernhard Müller. Inferring astrophysical parameters of core-collapse supernovae from their gravitational-wave emission. *Phys. Rev. D*, 105(6):063018, 2022.

[235] T. Bruel, M-A. Bizouard, M. Obergaulinger, P. Maturana-Russel, A. Torres-Forné, P. Cerdá-Durán, N. Christensen, J. A. Font, and R. Meyer. Inference of proto-neutron star properties in core-collapse supernovae from a gravitational-wave detector network. 1 2023.

[236] M. Aaron Skinner, Adam Burrows, and Joshua C. Dolence. Should One Use the Ray-by-Ray Approximation in Core-collapse Supernova Simulations? *apj*, 831(1):81, November 2016.

[237] A. Burrows, D. Vartanyan, J. C. Dolence, M. A. Skinner, and D. Radice. Crucial Physical Dependencies of the Core-Collapse Supernova Mechanism. *ssr*, 214(1):33, February 2018.

[238] David Vartanyan, Adam Burrows, David Radice, M. Aaron Skinner, and Joshua Dolence. A successful 3D core-collapse supernova explosion model. *mnras*, 482(1):351–369, January 2019.

[239] Tuguldur Sukhbold, T. Ertl, S. E. Woosley, Justin M. Brown, and H. T. Janka. Core-Collapse Supernovae from 9 to 120 Solar Masses Based on Neutrino-powered Explosions. *Astrophys. J.*, 821(1):38, 2016.

[240] Tuguldur Sukhbold, Stan Woosley, and Alexander Heger. A High-resolution Study of Presupernova Core Structure. *Astrophys. J.*, 860(2):93, 2018.

[241] F. Banyuls, J. A. Font, J. M. Ibáñez, J. M. Martí, and J. A. Miralles. Numerical {3 + 1} General Relativistic Hydrodynamics: A Local Characteristic Approach. *Ap.J.*, 476:221–231, February 1997.

[242] Irene Tamborra. Supernova Neutrinos: New Challenges and Future Directions. *J. Phys. Conf. Ser.*, 888(1):012040, 2017.

[243] Andreas Reisenegger and Peter Goldreich. A New Class of g-Modes in Neutron Stars. *apj*, 395:240, August 1992.

[244] Charles W. Misner, K. S. Thorne, and J. A. Wheeler. *Gravitation*. W. H. Freeman, San Francisco, 1973.

[245] Ken-ichi Oohara, Takashi Nakamura, and Masaru Shibata. A way to 3D numerical relativity. *Prog. Theor. Phys. Suppl.*, 128:183–249, 1997.

[246] E. Muller, H. Th. Janka, and A. Wongwathanarat. Parametrized 3D models of neutrino-driven supernova explosions: Neutrino emission asymmetries and gravitational-wave signals. *Astron. Astrophys.*, 537:A63, 2012.

[247] G Heinzel, A Rudiger, and R Schilling. Spectrum and spectral density estimation by the Discrete Fourier transform (DFT), including a comprehensive list of window functions and some new flat-top windows. page 84, February 2002.

[248] A. Burrows and D. Vartanyan. Core-collapse supernova explosion theory. , 589(7840):29–39, January 2021.

[249] A. Burrows, E. Livne, L. Dessart, C. D. Ott, and J. Murphy. A New Mechanism for Core-Collapse Supernova Explosions. *Astrophysical J.*, 640(2):878–890, April 2006.

[250] Naofumi Ohnishi, Kei Kotake, and Shoichi Yamada. Numerical Analysis of Standing Accretion Shock Instability with Neutrino Heating in Supernova Cores. *Astrophysical J.*, 641(2):1018–1028, April 2006.

[251] L. Scheck, T. Plewa, H. Th. Janka, K. Kifonidis, and E. Müller. Pulsar Recoil by Large-Scale Anisotropies in Supernova Explosions. *Phys. Rev. Lett.*, 92(1):011103, January 2004.

[252] J. I. Katz. X-rays from spherical accretion onto degenerate dwarfs. *Astrophysical J.*, 215:265–275, July 1977.

[253] R. A. Chevalier and J. N. Imamura. Linear analysis of an oscillatory instability of radiative shock waves. *Astrophysical J.*, 261:543–549, October 1982.

[254] James N. Imamura and Michael T. Wolff. On the Stability Properties of White Dwarf Radiative Shocks: Settling Solutions. *Astrophysical J.*, 355:216, May 1990.

[255] Alejandro Torres-Forné, Pablo Cerdá-Durán, Andrea Passamonti, Martin Obergaulinger, and José A. Font. Towards asteroseismology of core-collapse supernovae with gravitational wave observations - II. Inclusion of space-time perturbations. *Mon. Not. Roy. Astr. Soc.*, 482(3):3967–3988, January 2019.

[256] David Vartanyan, Adam Burrows, David Radice, M. Aaron Skinner, and Joshua Dolence. A successful 3D core-collapse supernova explosion model. *Mon. Not. Roy. Astr. Soc.*, 482(1):351–369, January 2019.

[257] David Radice, Viktoriya Morozova, Adam Burrows, David Vartanyan, and Hiroki Nagakura. Characterizing the Gravitational Wave Signal from Core-collapse Supernovae. *Astrophysical J.*, 876(1):L9, May 2019.

[258] David Vartanyan, Adam Burrows, Tianshu Wang, Matthew S. B. Coleman, and Christopher J. White. The Gravitational-Wave Signature of Core-Collapse Supernovae. *arXiv e-prints*, page arXiv:2302.07092, February 2023.

[259] T. Foglizzo. Entropic-acoustic instability of shocked Bondi accretion I. What does perturbed Bondi accretion sound like? *Astron. and Astrophys.*, 368:311–324, March 2001.

[260] P. Galletti and T. Foglizzo. The Advective-Acoustic instability in type II Supernovae. In F. Casoli, T. Contini, J. M. Hameury, and L. Pagani, editors, *SF2A-2005: Semaine de l'Astrophysique Francaise*, page 487, December 2005.

[261] T. Foglizzo. A Simple Toy Model of the Advective-Acoustic Instability. I. Perturbative Approach. *Astrophysical J.*, 694(2):820–832, April 2009.

[262] Jun'ichi Sato, Thierry Foglizzo, and Sébastien Fromang. A Simple Toy Model of the Advective-Acoustic Instability. II. Numerical Simulations. *Astrophysical J.*, 694(2):833–841, April 2009.

[263] A. Burrows, E. Livne, L. Dessart, C. D. Ott, and J. Murphy. Features of the Acoustic Mechanism of Core-Collapse Supernova Explosions. *Astrophysical J.*, 655(1):416–433, January 2007.

[264] Tatsuya Yamasaki and Shoichi Yamada. Stability of Accretion Flows with Stalled Shocks in Core-Collapse Supernovae. *Astrophysical J.*, 656(2):1019–1037, February 2007.

[265] Florian Hanke, Andreas Marek, Bernhard Müller, and Hans-Thomas Janka. Is Strong SASI Activity the Key to Successful Neutrino-driven Supernova Explosions? *Astrophysical J.*, 755(2):138, August 2012.

[266] Kei Kotake, Naofumi Ohnishi, and Shoichi Yamada. Gravitational Radiation from Standing Accretion Shock Instability in Core-Collapse Supernovae. *Astrophysical J.*, 655(1):406–415, January 2007.

[267] Jeremiah W. Murphy, Christian D. Ott, and Adam Burrows. A Model for Gravitational Wave Emission from Neutrino-Driven Core-Collapse Supernovae. *Astrophysical J.*, 707(2):1173–1190, December 2009.

[268] Chris L. Fryer and Kimberly C. B. New. Gravitational Waves from Gravitational Collapse. *Living Reviews in Relativity*, 14(1):1, January 2011.

[269] James P. Kneller, Gail C. McLaughlin, and Justin Brockman. Oscillation effects and time variation of the supernova neutrino signal. *Phys. Rev. D*, 77(4):045023, February 2008.

[270] Naofumi Ohnishi, Kei Kotake, and Shoichi Yamada. Inelastic Neutrino-Helium Scatterings and Standing Accretion Shock Instability in Core-Collapse Supernovae. *Astrophysical J.*, 667(1):375–381, September 2007.

[271] E. Endeve, C. Y. Cardall, R. D. Budiardja, A. Mezzacappa, and J. M. Blondin. Turbulence and magnetic field amplification from spiral SASI modes in core-collapse supernovae. *Physica Scripta Volume T*, 155:014022, July 2013.

[272] Shijun Yoshida, Naofumi Ohnishi, and Shoichi Yamada. Excitation of g-Modes in a Proto-Neutron Star by the Standing Accretion Shock Instability. *Astrophysical J.*, 665(2):1268–1276, August 2007.

[273] Nevin N. Weinberg and Eliot Quataert. Non-linear saturation of g-modes in proto-neutron stars: quieting the acoustic engine. *Mon. Not. Roy. Astr. Soc.*, 387(1):L64–L68, June 2008.

[274] Florian Hanke, Bernhard Müller, Annop Wongwathanarat, Andreas Marek, and Hans-Thomas Janka. SASI Activity in Three-dimensional Neutrino-hydrodynamics Simulations of Supernova Cores. *Astrophysical J.*, 770(1):66, June 2013.

[275] Chris L. Fryer. Compact object formation and the supernova explosion engine. *Classical and Quantum Gravity*, 30(24):244002, December 2013.

[276] Rodrigo Fernández, Bernhard Müller, Thierry Foglizzo, and Hans-Thomas Janka. Characterizing SASI- and convection-dominated core-collapse supernova explosions in two dimensions. *Mon. Not. Roy. Astr. Soc.*, 440(3):2763–2780, May 2014.

[277] Rodrigo Fernández. Three-dimensional simulations of SASI- and convection-dominated core-collapse supernovae. *Mon. Not. Roy. Astr. Soc.*, 452(2):2071–2086, September 2015.

[278] Stephen W. Bruenn, Eric J. Lentz, W. Raphael Hix, Anthony Mezzacappa, J. Austin Harris, O. E. Bronson Messer, Eirik Endeve, John M. Blondin, Merek Austin Chertkow, Eric J. Lingerfelt, Pedro Marronetti, and Konstantin N. Yakunin. The Development of Explosions in Axisymmetric Ab Initio Core-collapse Supernova Simulations of 12-25 M Stars. *Astrophysical J.*, 818(2):123, February 2016.

[279] John M. Blondin, Emily Gipson, Sawyer Harris, and Anthony Mezzacappa. The Standing Accretion Shock Instability: Enhanced Growth in Rotating Progenitors. *Astrophysical J.*, 835(2):170, February 2017.

[280] Prasun Dhang, Prateek Sharma, and Banibrata Mukhopadhyay. Magnetized SASI: its mechanism and possible connection to some QPOs in XRBs. *Mon. Not. Roy. Astr. Soc.*, 476(3):3310–3327, May 2018.

[281] Zidu Lin, Abhinav Rijal, Cecilia Lunardini, Manuel D. Morales, and Michele Zanolin. Characterizing a supernova's Standing Accretion Shock Instability with neutrinos and gravitational waves. *arXiv e-prints*, page arXiv:2211.07878, November 2022.

[282] A. C. Buellet, T. Foglizzo, J. Guilet, and E. Abdikamalov. Effect of stellar rotation on the development of post-shock instabilities during core-collapse supernovae. *arXiv e-prints*, page arXiv:2301.01962, January 2023.

[283] Paul Smeyers and Tim van Hoolst. *Linear Isentropic Oscillations of Stars: Theoretical Foundations*, volume 371. 2010.

[284] Rodrigo Fernández. Hydrodynamics of Core-collapse Supernovae at the Transition to Explosion. I. Spherical Symmetry. *apj*, 749(2):142, April 2012.

[285] Sean M. Couch and Christian D. Ott. The Role of Turbulence in Neutrino-driven Core-collapse Supernova Explosions. *Astrophysical J.*, 799(1):5, January 2015.

[286] Jeremiah W. Murphy, Joshua C. Dolence, and Adam Burrows. The Dominance of Neutrino-driven Convection in Core-collapse Supernovae. *Astrophysical J.*, 771(1):52, July 2013.

[287] Jérôme Guilet, Jun'ichi Sato, and Thierry Foglizzo. The Saturation of SASI by Parasitic Instabilities. *Astrophysical J.*, 713(2):1350–1362, April 2010.

[288] Suvi Gezari. Tidal Disruption Events. *Annual Review of Astronomy and Astrophysics*, 59:21–58, September 2021.

[289] Pablo Laguna, Warner A. Miller, Wojciech Zurek, and Melvyn B. Davies. Tidal disruptions by supermassive black holes - hydrodynamic evolution of stars on a schwarzschild background. *The Astrophysical Journal*, 410, 1993.

[290] Brassart, M. and Luminet, J.-P. Shock waves in tidally compressed stars by massive black holes. *A&A*, 481(2):259–277, 2008.

[291] Christopher Evans, Pablo Laguna, and Michael Eracleous. Ultra-close Encounters of Stars with Massive Black Holes: Tidal Disruption Events with Prompt Hyperaccretion. *Astrophysical J.*, 805(2):L19, June 2015.

[292] Emilio Tejeda, Emanuel Gafton, Stephan Rosswog, and John C. Miller. Tidal disruptions by rotating black holes: relativistic hydrodynamics with Newtonian codes. *Mon. Not. Roy. Astr. Soc.*, 469(4):4483–4503, August 2017.

[293] Nicholas Stone, Re'em Sari, and Abraham Loeb. Consequences of strong compression in tidal disruption events. *Monthly Notices of the Royal Astronomical Society*, 435(3):1809–1824, 09 2013.

[294] Emanuel Gafton and Stephan Rosswog. Tidal disruptions by rotating black holes: effects of spin and impact parameter. *Mon. Not. Roy. Astron. Soc.*, 487(4):4790–4808, 2019.

[295] B. Pichon. Helium detonation in pancake stars. *Astron. and Astrophys.*, 145(2):387–390, April 1985.

[296] J. P. Luminet and B. Pichon. Tidally-Detonated Nuclear Reactions in Stars-Black Hole Interactions. In S. Hayakawa and K. Sato, editors, *Big Bang, Active Galactic Nuclei and Supernovae*, page 361, January 1989.

[297] J. P. Luminet and B. Pichon. Tidally-detonated nuclear reactions in main sequence stars passing near a large black hole. *Astron. and Astrophys.*, 209(1-2):85–102, January 1989.

[298] J. P. Luminet and J. A. Marck. Tidal squeezing of stars by Schwarzschild black holes. *Mon. Not. Roy. Astr. Soc.*, 212:57–75, January 1985.

[299] Eric Poisson and Clifford M. Will. *Gravity: Newtonian, Post-Newtonian, Relativistic*. Cambridge University Press, 2014.

[300] Sergei A. Klioner. Basic Celestial Mechanics. *arXiv e-prints*, page arXiv:1609.00915, September 2016.

[301] Daniel J. Price, James Wurster, Terrence S. Tricco, Chris Nixon, Stéven Toupin, Alex Pettitt, Conrad Chan, Daniel Mentiplay, Guillaume Laibe, Simon Glover, and et al. Phantom: A smoothed particle hydrodynamics and magnetohydrodynamics code for astrophysics. *Publications of the Astronomical Society of Australia*, 35:e031, 2018.

[302] M. Cufari, Eric. R. Coughlin, and C. J. Nixon. The Eccentric Nature of Eccentric Tidal Disruption Events. *Astrophys. J.*, 924(1):34, 2022.

[303] David Liptai and Daniel J. Price. General relativistic smoothed particle hydrodynamics. *Mon. Not. Roy. Astr. Soc.*, 485(1):819–842, May 2019.

[304] Eric R. Coughlin and C. J. Nixon. On the Impact of Relativistic Gravity on the Rate of Tidal Disruption Events. *Astrophysical J.*, 936(1):70, September 2022.

[305] Jamie A. P. Law-Smith, David A. Coulter, James Guillochon, Brenna Mockler, and Enrico Ramirez-Ruiz. Stellar Tidal Disruption Events with Abundances and Realistic Structures (STARS): Library of Fallback Rates. *Astrophysical J.*, 905(2):141, December 2020.

[306] Eric R. Coughlin and Chris Nixon. A simple and accurate prescription for the tidal disruption radius of a star and the peak accretion rate in tidal disruption events. *arXiv e-prints*, page arXiv:2209.03982, September 2022.

[307] R. Helled, P. Bodenheimer, M. Podolak, A. Boley, F. Meru, S. Nayakshin, J. J. Fortney, L. Mayer, Y. Alibert, and A. P. Boss. Giant Planet Formation, Evolution, and Internal Structure. In Henrik Beuther, Ralf S. Klessen, Cornelis P. Dullemond, and Thomas Henning, editors, *Protostars and Planets VI*, pages 643–665, January 2014.

[308] C. D. Ott, E. P. O'Connor, S. Gossan, E. Abdikamalov, U. C. T. Gamma, and S. Drasco. Core-Collapse Supernovae, Neutrinos, and Gravitational Waves. *Nuclear Physics B Proceedings Supplements*, 235:381–387, February 2013.

Suman Kumar Kundu

315-243-0598 | skundu@syr.edu | sites.google.com/view/suman-kumar-kundu/home

Education

Syracuse University

Ph.D. in Physics **August 2023**
Theoretical and Computational Astrophysics
M.Sc. in Physics **December 2020**

Bangladesh University of Engineering & Technology

B.Sc. in Electrical & Electronic Engineering **September 2011**

Academic Experience **Aug 2018 – Dec 2020**

Teaching Assistant, Galactic Astronomy | Syracuse University | Syracuse, NY

- Designed and taught galactic astronomy laboratories to a diverse population of students
- Helped student to find and design their astronomy projects
- Worked with students to research on relation between astronomy and calendars
- Evaluated student writing based on the creativity and contexts
- Encouraged students to observe the motion of celestial bodies in the sky and relate it with what they learn
- Worked with students individually in dedicated office hours outside the classroom
- Used online student management system to grade and manage student assignments

Teaching Assistant, Extra-Galactic Astronomy | Syracuse University | Syracuse, NY

- Designed and taught extra galactic astronomy laboratories to a diverse population of students
- Designed online astronomy labs to be performed online (during COVID-19)
- Introduced students with telescopes and working in observatory
- Used online student management system to grade and manage student assignments

Teaching Assistant, Multi-messenger Astrophysics | Syracuse University | Syracuse, NY

- Wrote solutions for the assigned problem set.
- Present advanced research topics in multi-messenger astrophysics and cosmology to class.
- Helped students to present their class presentations.
- Graded the student exams.

Professional Experiences

System Engineer, Bangla Phone Limited, Dhaka, Bangladesh Sep 2011 — March 2014

- designed transmission networks used in the first-ever launch of 3G mobile communications in Bangladesh
- provided technical training newly introduced transmission multiplexers and optical fiber communications.

Assistant Engineer, Bangladesh Power Development Board April 2014 — July 2018

- researched efficient smart meters adapted to the need of a developing country in Landis & Gyr Lab, Guangzhou, China as a three-member national committee
- trained pros and cons of smart metering to the technical workforce
- regulation of cross-border power transmission
- served diverse grassroot communities in rural areas

Awards & Acknowledgements

Best TA, Extra-Galactic Astronomy, Department of Physics, 2019

College of Arts & Sciences summer fellowship 2019: in recognition of excellent work in first-year graduate courses.

Henry Levinstein fellowship 2020: outstanding performance as a graduate student

Dean’s award-2006: placed inside the first 100 in country wide merit list

Academic services

Reviewed scientific articles for the Astrophysical Journals (ApJ), Physics of Fluids

Outreach

Worked closely with neighboring high school students as part of the departments summer program intended to introduce state-of-the-art physics (astrophysics) research to high school students.

Media Coverage

Discover Magazine (a mass-market popular science magazine) has highlighted my recent work on Cosmological Constant in an article titled “How Exotic Atoms Can Transform Into Windows Into The Nature Of The Universe” (published in September, 2022)

Talks

Canadian – Cuban – American – Mexican Graduate Student Conference (C^2AM-APS): 2022

Poster presentation at High Energy Astrophysics Division (HEAD) meeting, 2022, Pittsburgh

Poster presentation for incoming graduate student, Department of Physics, 2021, 2022

Stonybrook University Astronomy Seminar, October 03, 2022

Frontier of Science lecture (a program designed to enrich the science backgrounds of area high school students), followed by observatory tour, March 06, 2022

Computational Skills

Coding:

C/C++: developed a project in palatini formulation of quantum gravity

Python: used in a project on gravitational wave from core collapse supernovae and data analysis in a project regarding vacuum energy

Fortran: employed in TDE research

Numerical packages: Mathematica, MATLAB

Simulation tools: Smoothed-Particle Hydrodynamics (SPH) code PHANTOM

Word Processors: Microsoft word, LaTex, Overleaf

Language Proficiency

Bengali: speak, read, write (excellent), English: speak, read, write (excellent), Hindi: speak (good)

Memberships

American Physical Society, American Astronomical Society

Research Interests

High energy Astrophysics, Cosmology

List of Publications

5. Measuring the properties of f-mode oscillations of a protoneutron star by third generation gravitation-wave detectors, Afle, C., **Kundu, S.K,** Cammerino, Jenna, Coughlin, E.R , Brown, D.A., Vartanyan, D., Burrows, A, PRD,107,12,123005 (2023), arXiv: 2304.04283

4. Stars Crushed by Black Holes. III. Mild Compression of Radiative Stars by Supermassive Black Holes, **Kundu, S.K**., Coughlin, E.R., Nixon, C.J., ApJ, 939, 2, 71 (2022), arXiv: 2210.01835

3. Spherically Symmetric Accretion onto a Compact Object through a Standing Shock: The Effects of General Relativity in the Schwarzschild Geometry, **Kundu, S.K**., Coughlin, E.R., MNRAS, 516, 4814-4821 (2022), arXiv: 2209. 00023

2. Does the Vacuum Gravitate? Rydberg Atoms Say, "Probably Not!", **Kundu, S.K**., Pradhan, Arnab, Rosenzweig, Carl, 2022, PRD, under review, arXiv: 2208.14192

1. Dynamical Stability of Giant Planets: the Critical Adiabatic Index in the Presence of a Solid Core **Kundu, S.K**., Coughlin, E.R., Youdin, A.N., Armitage, P.J., MNRAS, 507, 6215-6224 (2021) arXiv: 2108. 03160